University of Alberta

QUANTIFICATION OF LASER-INDUCED BREAKDOWN SPECTROSCOPY AT LOW ENERGIES

by

MICHAEL THOMAS TASCHUK

A thesis submitted to the Faculty of Graduate Studies and Research
in partial fulfillment of the requirements for the degree of

DOCTOR OF PHILOSOPHY

Department of Electrical and Computer Engineering

Edmonton, Alberta
Spring 2007

Library and
Archives Canada

Published Heritage
Branch

395 Wellington Street
Ottawa ON K1A 0N4
Canada

Bibliothèque et
Archives Canada

Direction du
Patrimoine de l'édition

395, rue Wellington
Ottawa ON K1A 0N4
Canada

Your file Votre référence
ISBN: 978-0-494-29755-1
Our file Notre référence
ISBN: 978-0-494-29755-1

NOTICE:
The author has granted a non-exclusive license allowing Library and Archives Canada to reproduce, publish, archive, preserve, conserve, communicate to the public by telecommunication or on the Internet, loan, distribute and sell theses worldwide, for commercial or non-commercial purposes, in microform, paper, electronic and/or any other formats.

The author retains copyright ownership and moral rights in this thesis. Neither the thesis nor substantial extracts from it may be printed or otherwise reproduced without the author's permission.

AVIS:
L'auteur a accordé une licence non exclusive permettant à la Bibliothèque et Archives Canada de reproduire, publier, archiver, sauvegarder, conserver, transmettre au public par télécommunication ou par l'Internet, prêter, distribuer et vendre des thèses partout dans le monde, à des fins commerciales ou autres, sur support microforme, papier, électronique et/ou autres formats.

L'auteur conserve la propriété du droit d'auteur et des droits moraux qui protège cette thèse. Ni la thèse ni des extraits substantiels de celle-ci ne doivent être imprimés ou autrement reproduits sans son autorisation.

In compliance with the Canadian Privacy Act some supporting forms may have been removed from this thesis.

While these forms may be included in the document page count, their removal does not represent any loss of content from the thesis.

Conformément à la loi canadienne sur la protection de la vie privée, quelques formulaires secondaires ont été enlevés de cette thèse.

Bien que ces formulaires aient inclus dans la pagination, il n'y aura aucun contenu manquant.

Canada

To my wife Heather and son Alexander.

Abstract

Laser-induced breakdown spectroscopy (LIBS) is an elemental characterisation technique using spectrally resolved emission from a laser-induced plasma to determine the composition of a sample. Due to limited quantitifcation of emission levels, in the literature, it is difficult to compare results between different lab groups, and only qualitative comparisons can be made with theory. As a result, understanding of the underlying physical processes which govern LIBS has lagged the growth of applications.

Most applications of the LIBS technique have employed laser pulse energies in the range of 10 - 100 mJ, focal spot sizes of $\sim$ 100 μm, and an accumulation of 10 - 100 spectra for a single measurement. The high energies, large focal spots and number of shots acquired improves the sensitivity of LIBS. The primary focus of this thesis is the quantification of the LIBS technique, LIBS equipment and the extension of LIBS to much lower pulse energies. This new regime, referred to as μLIBS, utilises pulse energies below 100 μJ.

In this thesis a theory of LIBS detector systems is developed, and used to define responsivity, noise-equivalent integrated spectral brightness and noise-equivalent spectral brightness in terms useful for the LIBS experimentalist. Four LIBS detection systems have been characterised.

Laser ablation plume dynamics and absolute emission levels from a millijoule energy LIBS system were studied and compared with simple physical models for shock wave expansion and stagnation. A simple model for the emission is compared with the absolute emission levels of the LIBS plasma.

The scaling of LIBS emission below 100 μJ pulse energies is investigated. The number of photons emitted is found to be a small fraction of the number of atoms ablated for the energy range between 100 nJ and 100 μJ. Using a thin film target, it is found that the ablated region which contributes to the LIBS emission is restricted to a layer much shallower than the ablation crater.

Finally, two applications of the μLIBS technique are presented. Surface mapping of Al alloys with sub-microjoule laser pulses is demonstrated. Latent fingerprint detection and imaging is demonstrated using the μLIBS technique.

Acknowledgements

This thesis would not have been possible without the supervision of Dr. Fedosejevs and Dr. Tsui. I would like to thank both of them for the opportunity to work on this project, the support for the numerous conferences I attended, and for the training I have received. Early guidance from Dr. Rieger was also extremely valuable. Excellent technical support from Blair Harwood and Rick Conrad has greatly eased the path.

Support and irritation from Mike Argument, Yogesh Godwal, James Gospodyn, Sean Kirkwood, Matt Reid and Craig Unick is gratefully acknowledged. Without them the work might have been faster, but certainly would have been less entertaining.

I would also like to thank Isabel Gibson for the detailed editing. Her help has greatly improved the quality of this thesis.

Finally, I would like to acknowledge funding from the Natural Sciences and Engineering Research Council of Canada, the Informatics Circle of Research Excellence, the University of Alberta, MPB Technologies, Inc. and the Canadian Institute for Photonic Innovations.

Contents

1 Introduction **1**

1.1 Introduction to Laser-Induced Breakdown Spectroscopy 1

1.2 LIBS Survey 3

1.2.1 Origin of LIBS: 1964 - 1969 3

1.2.2 LIBS Technique Develops: 1970 - 1980 3

1.2.3 LIBS with Multichannel Detectors: 1981 - 1997 5

1.3 Description of Project 6

2 μLIBS **9**

2.1 Introduction 9

2.2 Interaction Physics 9

2.2.1 Laser-Matter Interactions 10

2.2.2 Laser-Plasma Interaction 10

2.2.3 Laser-Induced Plume Expansion Dynamics 11

2.2.4 Plasma Emission Processes 12

2.3 Introduction to μLIBS 13

2.4 Microjoule Laser Sources 15

2.4.1 Microchip Lasers 15

2.4.2 Microjoule Fiber Lasers 18

2.5 Scaling LIBS to Microjoule Energies 19
  2.5.1 Plasma Emission and Lifetime 20
  2.5.2 Crater Size - Lateral and Depth Resolution 22
  2.5.3 Limits of Detection 28
  2.5.4 Signal Linearity with Concentration 30
2.6 μLIBS Applications 32
  2.6.1 Microanalysis of Small Volumes 33
  2.6.2 Scanning Microanalysis of Material Surfaces 35
  2.6.3 Liquid Samples 43
2.7 Conclusion 44

3 Experimental Methodology 47
3.1 Introduction 47
3.2 Spectrometers 47
3.3 Detectors 49
3.4 Calibration Procedures 51
  3.4.1 Energy Calibrations 53
  3.4.2 Temporal Calibrations 56
  3.4.3 Wavelength Calibrations 60
  3.4.4 Radiometric Calibrations 60
3.5 Optimisation Methodologies 69
  3.5.1 Focal Position 69
  3.5.2 Alignment of Plasma Imaging Optics 71
  3.5.3 Detector Conditions 71
3.6 LIBS Signal Analysis 72
  3.6.1 Description of Signals in LIBS Systems 73
  3.6.2 LIBS Signal Analysis: Method Definitions 73

3.7 LIBS Signal Model 78
  3.7.1 Scope of Model 79
  3.7.2 Cathode Noise Spike Characterisation 80

4 LIBS Detection Systems 87

4.1 Introduction 87
4.2 LIBS Detection System Theory 87
4.3 Systems Studied 92
4.4 LIBS System Responsivities 92
4.5 LIBS System Noise Characterisation 99
  4.5.1 Spatial Distribution of Cathode Spikes 99
  4.5.2 Cathode Spike Rate 101
  4.5.3 Area Distribution of Cathode Spikes 105
  4.5.4 Width Distribution of Cathode Spikes 107
  4.5.5 Cathode Spike Characterisation: Discussion 110
4.6 LIBS System Noise Equivalents 110
  4.6.1 Noise-Equivalent Integrated Spectral Brightness at Minimum Gain 111
  4.6.2 Noise-Equivalent Spectral Brightness at Maximum Gain 114
4.7 Conclusion 116

5 Quantification of the LIBS Process 119

5.1 Introduction 119
5.2 Experimental Setup 121
5.3 Experimental Results 123
5.4 Plume Expansion 130
5.5 Plume Emission 135

5.6 Conclusion 140

6 Scaling LIBS to μJ Energies **143**

6.1 Introduction 143

6.2 Experimental Setup 144

6.3 Absolute Emission Scaling of μLIBS Plasmas 148

6.3.1 Laser Pulse Width Scaling: Experimental Results 148

6.3.2 Laser Pulse Width Scaling: Discussion 148

6.3.3 Laser Wavelength Scaling 151

6.4 Ablation Efficiency of μJ Laser Pulses 156

6.5 Emission Efficiency of μLIBS Plasmas 158

6.6 Interaction Depth of fs μLIBS 159

6.7 Comparison with sub-millijoule results 161

6.7.1 Ablation Efficiency 163

6.7.2 Emission Efficiency 165

6.8 Conclusion 166

7 μLIBS Applications **169**

7.1 Introduction 169

7.2 Surface mapping of Al alloys by μLIBS 169

7.2.1 Introduction to Al Alloys 170

7.2.2 2D Mapping Methodology 170

7.2.3 Experimental Setup 175

7.2.4 Low Energy 2D Mapping of Al Alloys 177

7.2.5 Discussion and Future Work 184

7.2.6 Conclusion 185

7.3 Fingerprint Detection and Imaging 186

7.3.1 Introduction 186
7.3.2 Experimental Setup 187
7.3.3 Experimental Results 190
7.3.4 Discussion 195
7.3.5 Conclusion 196

8 Conclusions **199**
8.1 Summary of Thesis Results 199
8.2 Outlook for Future Work 200
8.2.1 μLIBS LOD Capabilities 200
8.2.2 Detector Characterisations 200
8.2.3 LIBS Modelling 201
8.2.4 μLIBS Physics 201
8.2.5 μLIBS Applications 201
8.3 Conclusion 202

References **203**

A Analysis Code **219**
A.1 Introduction 219
A.1.1 Code Requirements 219
A.2 Spectra 220
A.2.1 Introduction 220
A.2.2 File Listing 220
A.2.3 Testing the Code 221
A.2.4 Spectra Code Listing 223
A.3 Spectra Client Scripts 243
A.3.1 The Linefile 243

A.3.2 Spectra Client Script Code Listing 244
A.4 Taylor-RK 257
A.4.1 Introduction 257
A.4.2 Numerical Model 257
A.4.3 Runge-Kutta Equations 257
A.4.4 Comparison with Taylor 258
A.4.5 Conclusion 258
A.5 Emission Simulation Code 263
A.5.1 Emission Code Listing 263

List of Tables

2.1 Nanosecond Ablation Efficiencies [μm^3 μJ^{-1}] 27

2.2 Picosecond Ablation Efficiencies [μm^3 μJ^{-1}] 27

2.3 LOD for minor elements in aluminum alloys. All values are scaled to equivalent single shot acquisition values, using an $N_{shots}{}^{-1/2}$ scaling. 31

4.1 Summary of Manufacturer Data 93

4.2 Summary of optical characteristics for the systems under study 93

4.3 Standards applied to responsivity calibrations 96

4.4 Comparison of NEISB results and contributing parameters for minimum operating gain. 114

4.5 Comparison of NESB results and contributing parameters. . . . 116

5.1 Simplified Na atomic model. Values obtained from the NIST Atomic Spectra Database (Version 2.0) 138

6.1 Femtosecond Laser Characteristics 147

6.2 Target Reflectivities and Observation Wavelengths 147

6.3 Nanosecond Ablation Efficiencies [μm^3 μJ^{-1}] 165

7.1 Weight % of elements in different phases of an Al 2024 sample. Values are averages and standard deviations from 16 measurements on the matrix material, 3 for each of the precipitate types. (Reproduced with permission from [69].) 172

List of Figures

1.1 Schematic diagram of the LIBS process. 2

2.1 Schematic of a UV harmonically converted passively Q-switched microchip laser. Entire device is about a cm across. (Reprinted from Zayhowski [52] with permission from Elsevier) 16

2.2 Background corrected spectrum of aluminum plasma emission using a single 50 ps, 8 μJ pulse at 248 nm, with a gate width of 200 ns and zero gate delay. The spectrum was obtained using a system for which an absolute calibration was performed. (Reprinted from Rieger et al. [65] with permission from Elsevier) 20

2.3 Filtered photomultiplier detection of silicon line emission at 288 nm as a function of laser pulse energy for (a) 10 ns and 50 ps pulses at 248 nm, and (b) $\sim$ 130 fs pulses at 800 nm. The focal spot diameter was approximately 5 μm in all cases, yielding a fluence of $\sim$ 3 J cm^{-2} for 1 μJ pulse energies. The horizontal lines represents the noise floor of the PMT. ((a) Reprinted from Rieger et al. [65] with permission from Elsevier) 21

2.4 (a) Smoothed and normalised time-resolved signal-to-background ratios of the silicon line at 251 nm at various excitation energies using a 308 nm laser. (b) Decay time for calcium and silicon signals at 422 nm and 251 nm respectively as a function of laser pulse energy. (Reproduced with permission from Häkkänen et al. [55]) 23

2.5 Decay time constant for silicon line emission at 288 nm as a function of pulse energy for 10 ns and 50 ps pulses at 248 nm. The horizontal line represents the rise time of the PMT used. (Reprinted from Rieger et al. [65] with permission from Elsevier) 24

2.6 μLIBS 1D scan using pulses in the range of 35 - 40 μJ at 266 nm across an Al-Cu interface for determination of lateral resolution. Special care was taken to prevent re-sampling of ablated material, and a lateral resolution of 6 μm was reported. (Reprinted from Geertsen et al. [56] with permission from Elsevier) 25

2.7 Single-shot crater diameter as a function of energy for Al. Open circles represent shots using 248 nm pulses as described in [64]. Data from Cravetchi et al. [69], Geertsen et al. [56] and Salleé et al. [59] taken with $\sim$ 10 ns pulses at 266 nm and data from Gornushkin et al. [66] taken with 1064 nm are shown as solid points. 26

2.8 Single-shot crater volume as a function of energy for Al. Open circles represent shots using 248 nm pulses as described in [64]. Data from Geertsen et al. [56] and Salleé et al. [59] taken with $\sim$ 10 ns pulses at 266 nm. The line is a linear regression to the 248 nm data points which are above 25 μJ and below 300 μJ. . . 28

2.9 LOD as function of gate delay for Cu emission at 324.8 nm in Al 7075 alloy for 100 μJ (open squares) and 200 μJ (solid circles) laser pulse energy. (Reproduced with permission from Rieger et al. [64]) 29

2.10 Calibration curve of copper in aluminum matrix. Each point is an average of ten 240 μJ pulses at 248 nm. Gate width is 300 ns and gate delay is 200 ns. The 3σ LOD is 12 ppm, and the straight line is a linear fit to the averaged data points below 1000 ppm. (Reproduced with permission from Rieger et al. [64]) 32

2.11 Scanning electron microscope image of precipitates on the surface of aluminum alloy and individual single-shot μLIBS craters produced with 7 μJ pulses at 266 nm. Matrix (dark area) shots are labelled M1 and M2, while μLIBS shots that sampled precipitates (bright areas) are labelled P1 and P2. (Reproduced with permission from Cravetchi et al. [69]) 34

2.12 Representative single-shot spectra from matrix and precipitate regions of the aluminum surface. Clear differences are observed with a pulse energy of 7 μJ. (Reproduced with permission from Cravetchi et al. [69]) 34

2.13 2D scan of a 10 mm by 10 mm piece of coated paper board. Laser-induced fluorescence of underlying paper at 422 nm (upper), and μLIBS scan at 251 nm for Si in paper coating (lower). (Reproduced with permission from Häkkänen et al. [55]) 36

2.14 μLIBS 2D depth profile scan of the composition of paper using 80 μJ pulses at 308 nm. Gray indicates top coat, composed of a 50:50 mix of calcium carbonate:kaolin. Black indicates precoat, composed of a 80:20 mix of calcium carbonate:kaolin. White indicates the base paper. (Reproduced from Häkkänen et al. [71] with permission from Elsevier) 36

2.15 Scanning μLIBS image of a single inclusion on the surface of steel as seen in the emission of elements Mn, Fe, Ti and Ni. (Reproduced with permission from Menut et al. [46]) 38

2.16 Correlation plots of peak intensity values for minor elements in aluminum alloys. (a) Mn vs Fe shows a positive correlation as they appear in the same precipitates, (b) Mn vs Mg yields a negative correlation in both lobes, as they do not appear in the same precipitates. Dashed lines are 3σ values from the non-linear Gaussian fit to all available data. Solid lines are linear regressions within their respective quadrants. (Reprinted from Cravetchi et al. [70] with permission from Elsevier) 39

2.17 Comparison of SNR achieved for Al with optimum gate delay time versus negative gate delay time (ungated). Data are an average of 100 single 1 μs gate width acquisitions. The solid line is a best linear fit to the data. (Reproduced with kind permission of Springer Science and Business Media from Fig. 8 of Cravetchi et al. [98]) 41

2.18 Measured SNR for the Al doublet using multiple pulses on a single spot. For the data at ~ 80 nJ, the SNR is at or below 3σ. (Reproduced with kind permission of Springer Science and Business Media from Fig. 12 of Cravetchi et al. [98]) 41

2.19 (a) Ratio of peak intensities of the Ti line measured at 626 nm from two adjacent points on the surface of a TiO_2 coated Si sample. A ratio of 1.0 indicates the second shot has sampled an undisturbed surface. (b) Silicon intensity of the first ablation layer of coated paper as a function of distance between sampling points and number of shots at each sampling point. In this case, Si is a contaminant from buried layers in a paper coating. ((a) Reprinted with permission from Romero et al. [68]. Copyright (1997) American Chemical Society; (b) Reprinted from Häkkänen et al. [71] with permission from Elsevier) 42

2.20 (a) Scanning electron microscopic image of macroscopic redeposition of Al_2O_3 and shock cleaning near the perimeter of a 2D μLIBS scan area 300 μm by 900 μm in size with probe spot separation of 10 μm. The edge of the scanned area is visible at the left edge of of the image. (b) Isolated crater created using single 1.5 μJ pulses at 266 nm. (Reprinted from Cravetchi et al. [70] with permission from Elsevier) 43

2.21 Surface scanning rate as a function of applied power. 1 = Taschuk Ph.D. Thesis (Sec. 7.2.4), 2 = Menut et al. [46], 3 = Cravetchi et al. [70], 4 = Vadillo et al. [67], 5 = Romero et al. [97], 6 = Romero et al. [68], 7 = Hakkanen et al. [71], 8 = Romero et al. [99], 9 = Mateo et al. [100], 10 = Mateo et al. [101], 11 = Rodolfo et al. [102]. For comparison, surface scans carried out using millijoule laser pulses in a line focus geometry are also shown in the upper right area of figure [100–102]. 44

3.1 Schematics of gratings (a) without blaze and (b) with blaze. . . . 48

3.2 Schematics of the operation of an echelle spectrometer (a) represents the diffraction of light into high orders which overlap in space, while (b) shows the order sorting by a prism. 50

3.3 Schematic of the image of the sorted orders generated by an echelle spectrometer. 50

3.4 Schematic diagram of a PMT. 52

3.5 Schematic diagram of an intensified CCD (ICCD) device. 52

3.6 Schematic diagram of the energy monitor setups for the experimental setups used in this thesis. A reflection energy monitor (top left) uses a wedge or window to measure a fraction of the beam. A transmission energy monitor (top right) measures leakage light through a mirror. 53

3.7 Energy calibration example for a transmitting energy monitor configuration. In this data set, the calibration factor was 112.8 ± 1.3 μJ/V. 55

3.8 Calibration factor for an energy monitor for one experimental setup over the course of $\sim$ 2.5 years. 57

3.9 Derivation of calibration factor for the PD5 energy monitor. The data set is a histogram of the various calibration factors presented in Fig. 3.8, and the solid line is a Gaussian fit to the distribution. The calibration for this energy monitor during the period in question is 104.7 ± 7.3 μJ/V. 57

3.10 Schematic diagram of one of the temporal calibration experiments performed in this thesis. 58

3.11 Temporal calibration of ICCD delay in the case where the gate can be opened and closed in advance of the laser arrival. In this case a gate width of 5 ns is used to measure the arrival of a Nd:YAG laser pulse at the target location. 59

3.12 Temporal calibration of ICCD delay in the case where the gate can only be opened before the arrival of the laser pulse. In this case a gate width of 1 μs was used to measure the arrival of a Ti:Sapphire laser pulse at the target location. 59

3.13 Wavelength calibration for a 600 line mm^{-1} grating at a central wavelength of 359 nm. The solid line is a linear best fit to the data set, giving a calibration equation of $\lambda\left(N_{channel}\right) = (271.95 \pm 0.17)\, nm + (166.56 \pm 0.27 pm) \cdot N_{channel}$ 61

3.14 Calibrated tungsten blackbody used as a broadband calibration source in these experiments. The black line is a best fit of the blackbody emission curve to the calibration data, giving a temperature of 2930 ± 20 K. 63

3.15 Schematic of a broadband calibration setup. In this case, the calibrated tungsten lamp (Eppley Laboratories) illuminates the spectrometer's entrance slit. 63

3.16 Responsivity of the Andor Mechelle at maximum gain. 64

3.17 Schematic of an angular calibration setup. The energy delivered to the barium sulphate plate was monitored in transmission mode with a photodiode. The barium sulphate plate was rotated to present different emission angles to the entrance slit of the spectrometer. 65

3.18 Sample data set from the angular calibration technique. In this case, the ICCD gain was found to be 0.29 ± 0.03 counts/photoelectron at minimum gain. 65

3.19 Combined calibration data for one of the ICCDs used in this thesis. The solid line is an exponential fit to the data points with a MCP gain of ≤ 125. Above this value, a slight saturation in detector gain is observed. 66

3.20 Measurement of plasma image size at the spectrometer's entrance slit for a setup similar to that in Fig. 3.10. The solid lines are a best fit of Gaussian functions to the unresolved Al doublets observed here. This data must be deconvolved with the slit width to arrive at the actual image size. 68

3.21 Focal runs (closed circles) and crater diameters (open squares) for single $\sim 20\ \mu J$ pulses with (a) 10 ns, (b) 50 ps, (c) 130 fs pulses. A 10X objective was used in all cases. Nanosecond and picosecond pulses are at 248 nm, and femtosecond pulses are at 800 nm. 70

3.22 SNR of the Al doublet at 394 nm and 396 nm as a function of gate delay for 750 μJ, 6 ns pulses at 266 nm. Each data point is an average and standard deviation of 5 data points. The solid line is a best fit to Eqn. 3.7. In this case, the optimal gate delay is ~ 350 ns. 72

3.23 Removal of (a) average, (b) linear and (c) parabolic backgrounds from LIBS spectra. 75

3.24 Definitions for the single-channel signal analysis methods. I_{peak} is the background corrected height of the signal, $I_{background}$ is the strength of the background, and Noise Region is the area used to estimate the variation in the background. 76

3.25 Definitions for the multiple-channel signal analysis methods. The shaded area is $\sum I(\lambda)$, $N_{channels}$ is the integrated width which is also used to scale the noise, and Noise Region is the area used to estimate the variation in the background. 77

3.26 (a) Typical spectrum under high gain conditions with no external light allowed into spectrometer. (b) Results of a peak finding algorithm applied to the data set in (a). (c) The residual between the original data set and the peak finding algorithm, indicating good detection and fitting of cathode noise spikes. . . 81

3.27 Average and standard deviation of the number of cathode spikes observed per spectrum (1 μs integration) for an ICCD as a function of MCP gain. The number of spikes expected depends strongly on MCP gain. 82

3.28 Distribution of cathode spikes in 10 channel wide bins on the sample ICCD. Dead areas on either side and hot channels are observed. 83

3.29 Distribution of cathode spike area for a MCP gain of 250. The solid line is a best fit of a log-normal distribution to the experimental data. 84

3.30 Scaling of the log-normal fit parameters μ and σ to the cathode area distribution with MCP gain. 84

4.1 Manufacturer quantum efficiency data for the intensified detectors in the (a) the IPDA/Czerny-Turner system, (b) ICCD/Czerny-Turner system and (c) the ICCD/Echelle system. 94

4.2 (a) Calibrated IPDA gain for IPDA/Czerny-Turner system, (b) Calibrated ICCD gain for ICCD/Czerny-Turner system and (c) Manufacturer data for ICCD gain for ICCD/Echelle system. The solid lines are best exponential fits to the data for gains below (a) 6, (b) 150 and (c) 150. 95

4.3 Responsivity of the IPDA/Czerny-Turner system using maximum gain and a 150 l/mm grating. 97

4.4 Responsivity of the ICCD/Czerny-Turner system using maximum gain and a 600 l/mm grating. 97

4.5 Responsivity of the ICCD/Echelle system at maximum gain. . . 98

4.6 Responsivity of Multichannel CCD system. 98

4.7 Spatial distribution of cathode noise spikes for (a) the IPDA/Czerny-Turner system, (b) ICCD/Czerny-Turner system and (c) the ICCD/Echelle system. The solid line in (a) and (b) are the relative detector response as a function of channel number. In the case of the ICCD/Echelle system, the distribution is across virtual channels. 100

4.8 Mean and standard deviation of the cathode spike arrival rate for the IPDA/Czerny-Turner system. The solid lines are a guide for the eye. 103

4.9 Mean and standard deviation of the cathode spike arrival rate for the ICCD/Czerny-Turner system. This ICCD exhibits a threshold in the cathode spike arrival rate at a gain of ~ 100. The solid lines are a best fit to the experimental data. 103

4.10 Mean and standard deviation of the cathode spike arrival rate for the ICCD/Echelle system. The ICCD/Echelle system has a much lower cathode spike rate than either the IPDA/Czerny-Turner or ICCD/Czerny-Turner systems. The solid lines are a guide for the eye. 104

4.11 Schematic of the echelle 'staircase' pattern observed on the ICCD detector when using the ICCD/Echelle system. Each line represents an order of the echelle grating. Unlike the Czerny-Turner, very few pixels are used per unit nm to acquire the spectral signal. 105

4.12 Characteristics of the log-area distribution for the IPDA/Czerny-Turner system. This analysis uses the arithmetic mean and summation form of the standard deviation, rather than a fit to the log-normal distribution. 106

4.13 Characteristics of the log-normal distribution for the area of the cathode noise spikes for the ICCD/Czerny-Turner system. The solid lines are best linear fits to the data. 106

4.14 Characteristics of the log-normal distribution for the area of the cathode noise spikes for the ICCD/Echelle system. No noise spikes were observed below a MCP gain of 200. The solid lines are best linear fits to the data. 108

4.15 Characteristics of the cathode spike width distribution for the IPDA/Czerny-Turner system. This analysis uses the arithmetic mean and summation form of the standard deviation, rather than a fit to the log-normal distribution. 108

4.16 Characteristics of the distribution of cathode noise spikes as a function of MCP gain for the ICCD/Czerny-Turner system. The solid lines are best fit of a logarithmic function to the average cathode spike width, and a parabolic function to the cathode spike width standard deviation. 109

4.17 Characteristics of the width distribution of cathode noise spikes as a function of MCP gain for the ICCD/Echelle system. The increase as one moves to lower gain is not considered reliable for this data set, but rather a result of the limited number of spikes. 109

4.18 NEISB for the IPDA/Czerny-Turner system at minimum gain, with a 150 l/mm grating and slit area of $2.5 \cdot 10^{-3}$ cm^2. A different grating or entrance slit would affect these values. . . . 112

4.19 NEISB for the ICCD/Czerny-Turner system at minimum gain, with a 600 l/mm grating and slit area of $4.0 \cdot 10^{-3}$ cm^2. A different grating or entrance slit would affect these values. . . . 112

4.20 NEISB for the ICCD/Echelle system at minimum gain. For this system the grating and entrance aperture are fixed. The entrance aperture is controlled by choice of fiber, and is at the maximum allowable value of $19.6 \cdot 10^{-6}$ cm^2 in this case. 113

4.21 NEISB for the multichannel CCD prototype. For this system the grating and entrance aperture are fixed. The entrance aperture is controlled by the combination of the fiber aperture and the slit size, and is $\sim 6 \cdot 10^{-5}$ cm^2 in this case. Use of a different fiber bundle would affect these results. The narrow spikes near channel boundaries are due to imperfect wavelength matching between the channels. 113

4.22 NESB for the IPDA/Czerny-Turner system at maximum gain, with a 150 l/mm grating and slit area of $2.5 \cdot 10^{-3}$ cm^2. A different grating or entrance slit would affect these values. . . . 115

4.23 NESB for the ICCD/Czerny-Turner system at maximum gain, with a 600 l/mm grating and slit area of $4.0 \cdot 10^{-3}$ cm^2. A different grating or entrance slit would affect these values. . . . 115

4.24 NESB for the ICCD/Echelle system at minimum gain. For this system the grating and entrance aperture are fixed. The entrance aperture is controlled by choice of fiber, and is at the maximum allowable value of $19.6 \cdot 10^{-6}$ cm^2 in this case. 117

5.1 Experimental setup for the detection of trace elements in water. A frequency tripled Nd:YAG (355 nm, 10 ns) is used as excitation source. Pulse energy is controlled using a half wave plate Glan-Taylor prism combination, and monitored using a calibrated calorimeter. Plasma emission is imaged 1:1 using two achromats onto the entrance slit of a 1/4 m spectrometer. Dispersed plasma light is detected with a 2D ICCD. 122

5.2 A spacetime contour map of the integrated Na emission line strength in units of photons Sr^{-1} cm^{-2}. Horizontal axis refers to the position of the slit image on the longitudinal axis of laser, with zero as the front of the water jet. The vertical axis is the delay of the gate in time, with zero time as the laser striking the water jet. The laser travels from right to left. Experimental conditions: N_{shots} = 5, 2200 ppm Na, Slit = 100 μm, Gate Width = 100 ns, Detector Gain = 0.81 counts/photon. 124

5.3 A spacetime contour map of the Na SNR. Horizontal axis refers to the position of the slit image on the longitudinal axis of laser, with zero as the front of the water jet. The vertical axis is the delay of the gate in time, with zero time as the laser striking the water jet. The laser travels from right to left. Experimental conditions: N_{shots} = 5, 2200 ppm Na, Slit = 100 μm, Gate Width = 100 ns, Detector Gain = 0.81 counts/photon. 125

5.4 (a) Na emission, background levels, and noise equivalent signal as a function of gate delay. Continuum levels decay below detector equivalent noise power by about 2.5 μs. (b) SNR as a function of gate delay. Optimal SNR with a long gate of 40 μs occurs with a delay of $\sim$ 2.5 μs. Experimental Conditions: N_{shots} = 100, E = 100 mJ, 972 ppm Na in water, T_{gate} = 40 μs, Slit = 10 μm. (Reproduced with permission from Taschuk et al. [118]) 126

5.5 A survey of detector gain and gate width for SNR from 20 ppm Na in water. As gain increases, the increased rate of noise from the ICCD cathode causes a decrease in SNR. Similarly, as the gate width increases, more noise events from the cathode are included in the integration. These two factors combine to yield optimal detection conditions at a gain of 6.3 counts/photon and a gate width of 18.5 μs. Experimental Conditions: N_{shots} = 5, E = 45 mJ, 20 ppm Na in water, T_{delay} = 2.5 μs 128

5.6 LOD of Na in water at optimal detection conditions. The 100-shot LOD at 45 mJ for Na is ≈ 25 ppb. Experimental conditions: N_{shots} = 100, E = 45 mJ, T_{delay} = 2.5 μs, T_{gate} = 18.5 μs, Responsivity = 6.3 counts/photon. 129

5.7 LOD of Pb in water at optimal detection conditions. The 100-shot LOD at 45 mJ for Pb is ≈ 7 ppm. Experimental conditions: N_{shots} = 100, E = 45 mJ, T_{delay} = 2.5 μs, T_{gate} = 22 μs, Responsivity = 4.5 counts/photon. 129

5.8 Current results compared to literature values for Na LOD as a function of energy. All values have been scaled to a 100-shot, 3σ LOD. 1 = Samek et al. [141], 2 = Present Result, 3 = Knopp et al. [140], 4 = Lo et al. [143], 5 = μLIBS result for comparison, Taschuk et al. [105]. 131

5.9 Current results compared to literature values for Pb LOD as a function of energy. All values have been scaled to 100-shot, 3σ LOD. 1 = Arca et al. [139], 2 = Samek et al. [141], 3 = Present Result, 4 = Knopp et al. [140], 5 = Lo et al. [143], 6 = μLIBS result for comparison, Godwal et al. [106]. 131

5.10 Predicted temperature isotherms from Taylor/Sedov strong shock theory overlaid on Na emission spacetime map. The overlaid curves represent (a) 20000 K, (b) 5000 K, (c) 2000 K, and (d) 300 K strong shock isotherms. Curve (e) is the radius of the strong shock. The regions with high Na emission are bounded by the shock front, but are not correlated with strong shock isotherms. 133

5.11 Comparison between strong and weak shock models for (a) temperature and (b) density for an ideal gas at a time of $\sim$ 3 μs. The numerical solution to the weak shock model predicts a larger radius than the strong shock for all time. The model also predicts physically reasonable temperatures near the shock front, a clear improvement over the strong shock case. Discretization noise occurs in the temperature for the strong and weak shock due to numerical and digitisation errors in the very low densities, respectively. 134

5.12 Predicted temperature isotherms from numerical solutions to the weak shock wave case overlaid on Na emission spacetime map. The overlaid curves represent (a) 20000 K, (b) 5000 K, (c) 2000 K, (d) the strong shock radius and (e) the weak shock radius. The temperature isotherms lags the weak shock wave, and stagnates after approximately $2\mu s$. The correlation between the weak shock isotherms and the regions of high Na emission is better than the strong shock model, but deviation occurs at $\approx$ 3 μs. 136

5.13 Predicted stagnation distances from the model by Dyer et al. [44] overlaid on the Na emission spacetime map. A number of expansion angles θ are compared to the space time expansion of the plasma plume produced in these experiments. 137

5.14 A schematic top view of the hemispherical expanding plasma plume with the planar chord viewed by the entrance slit of the spectrometer. The numerical model calculates the properties of dV as a function of R. The cylindrically symmetric integration for emitted energy for a slit width Δx is given by equation 5.6. . 139

5.15 Comparison between a simple emission model and the corresponding experimental data for a time of (a) 3 μs and (b) 6.8 μs after the laser arrives at the water jet. 141

6.1 Experimental set-up for nanosecond and picosecond results. KrF pulses at 10 ns and 50 ps are focused onto the target using 10X objective. The LIBS emission is captured by the same objective, and imaged onto the entrance slit of the 0.5 m spectrometer. LIBS emission is also measured using a PMT with various interference filters. 144

6.2 Experimental setup used for quantitative characterisation of emission levels from femtosecond laser-induced microplasmas. The fundamental (800 nm), 2nd harmonic (400 nm) and 3rd harmonic (266 nm) are delivered to the setup collinearly. Plasma emission is collected simultaneously by a PMT coupled with interference filters for the wavelength of interest, and a imaging spectrograph and ICCD combination. 146

6.3 Time integrated emission of Si I 288 nm as measured with a photomultiplier. For signals below approximately $3 \cdot 10^7$ on the vertical axis the arbitrary units correspond to total photons emitted per steradian. (Reprinted from Rieger et al. [65] with permission from Elsevier) 149

6.4 Time integrated emission of Si I 288 nm as measured with a photomultiplier for femtosecond pulses. The longer pulse data from Fig. 6.3 is plotted for comparison. The femtosecond data is similar to the nanosecond data. 149

6.5 Time integrated emission of Al I (394.4, 396.2 nm) as measured with a photomultiplier. For signals below $\approx 4 \cdot 10^7$ on the vertical axis the arbitrary units correspond to total photons emitted per steradian. (Reprinted from Rieger et al. [65] with permission from Elsevier) 150

6.6 Time integrated emission of Al I (394.4, 396.2 nm) as measured with a photomultiplier for femtosecond pulses. The longer pulse data from Fig. 6.5 is plotted for comparison. 150

6.7 Quantitative emission levels from Si plasmas induced by 800 nm pulses. The solid lines are power law fits. Si data points are single shot, while air breakdown points are an average of 16 shots. The horizontal line represents the noise equivalent intensity of the PMT at 290 nm. (Reproduced with permission from Taschuk et al. [94]) 152

6.8 Quantitative emission levels from Cu plasmas induced by 800 nm pulses. The solid lines are power law fits. Cu data points are single shot, while air breakdown points are an average of 16 shots. The horizontal line represents the noise equivalent intensity of the PMT at 324 nm. (Reproduced with permission from Taschuk et al. [94]) 153

6.9 Quantitative emission levels from Al plasmas induced by 800 nm pulses. The solid lines are power law fits. Al data points are single shot, while air breakdown points are an average of 16 shots. The horizontal line noise equivalent intensity of the PMT at appropriate 400 nm. (Reproduced with permission from Taschuk et al. [94]) 153

6.10 Wavelength dependence of Cu microplasmas. A strong dependence on the linear reflectivity is observed, with increased absorption yielding higher emission levels at lower incident pulse energies. 155

6.11 Wavelength dependence of Al microplasmas. Overall behaviour of the emission scaling is similar, except for the emission threshold for 800 nm being reached by about 1 μJ. As the focal spot for the UV pulses is smaller, the incident fluence is higher, allowing the energy scaling of emission to continue to $\sim$ 100 nJ. . 155

6.12 Wavelength dependence of Si microplasmas. The changes in incident reflectivity do not appear to affect the overall emission levels observed here. 156

6.13 Si crater volumes for a variety of conditions. Open symbols were taken with a 10 cm lens; closed with a microscope objective. 10 cm lens data is rolling off below a pulse energy of ~ 2 μJ. The solid line is a best fit, described in the text. 157

6.14 Si emission efficiency for different laser wavelengths and focal conditions. The solid line is a power law fit with a dependence of [illegible].85 ± 0.05. 159

6.15 Depth profiles of ablation craters in 100 nm of Cu on a Si wafer using (a) 0.60 μJ and (b) 3.72 μJ. The penetration energy for the 266 nm pulses is ~ 1.5 μJ. 160

6.16 Cu emission due to 266 nm, 130 fs laser pulses. The Si substrate is ablated for energies above ~ 1.5 μJ, yet the trend of the Cu emission continues unperturbed. This implies that the sensitivity depth of fs LIBS is significantly shallower than the crater depth. 161

6.17 Spectra obtained from the (a) first and (b) seventh shot on a Cu target using 25.1 μJ pulses at 266 nm. The energy used is well above the single-shot penetration energy for this laser wavelength, but no signal from the Si substrate is observed for the first shot (a). 162

6.18 Al crater volume for KrF laser pulses with (a) 10 ns and (b) 50 ps pulse width, using a 10X objective. In the case of the 10 ns pulses, a significant decrease in ablation efficiency above 300 μJ is observed, and is attributed to plasma shielding. The solid lines are best linear fits to the data sets, described in the text. . . 164

6.19 Integrated Al signal as a function of energy. 166

7.1 SEM image of an Al 2024 alloy surface taken in electron backscatter mode. The bright areas correspond to both precipitate types with high concentrations of high Z elements such as Cu, Mn, Fe compared with aluminum matrix (grey area). The black areas may correspond to surface defects such as holes or scratches. 171

7.2 Histogram of precipitate area for the image presented in Fig. 7.1. Precipitate areas range from ~ 2 μm to ~ 370 μm for the area sampled here, with precipitates below 36 μm^2 making up 90% of the total. 171

7.3 Representative single-shot spectra from (a) Al 2024 matrix, (b) Al_6(Cu,Fe,Mn) precipitate, and (c) Al_2CuMg precipitate regions of an aluminum surface. A single ~ 7 μJ, 7 ns shot at 266 nm was used in each case. Clear differences between the spectra are observed, allowing definitive classification of region type. . 173

7.4 Histogram of Mg SNR using ~ 7 μJ, ~ 130 fs pulses at 800 nm. The solid line is a nonlinear fit to the distribution, while the dashed line delineates precipitates with Mg signals greater than 3σ above the average. (Reproduced with kind permission of Springer Science and Business Media from Fig. 10 of Cravetchi et al. [98]) 174

7.5 Precipitate map on the Al 2024 alloy surface: black squares represent Al_2CuMg precipitates; white squares represent Al_6(Cu,Fe,Mn) precipitates. 3σ criterion is applied for all constituent elements except Al. Reproduced with permission from [70]. 175

7.6 Experimental setup for low-energy 2D mapping. A frequency tripled Ti:Sapphire beam (266 nm, ~ 120 fs FWHM) produces pulses with energies up to ~ 7 μJ on the target surface. Pulse energy is controlled with $\lambda/2$ plate combined with a Glan-Taylor prism (not shown). The LIBS emission is imaged 1:1 with achromatic 90° off-axis parabolic mirrors. A real-time imaging system allows positioning of the LIBS sample spot on the target with a precision of ~ 1 μm. 176

7.7 100-shot average spectrum from Al 2024 sample, using 0.87 μJ laser pulses. Each shot was on a fresh surface. Emission levels observed here are low, with an average of ~ 4500 photons observed in the Al doublet at 394.4 nm and 396.2 nm. 178

7.8 Effect of normalisation of spectral emission on correlation between two emission lines of the same species. (a) Emission strength for two Mg I lines. (b) The expected signature from the Mg precipitates is visible when the Mg lines are normalized to the Al doublet at 308.2 nm / 309.3 nm. 180

7.9 Correlation of the (a) Cu 324.7 nm and Cu 327.4 nm lines, and the (b) Mg 285.2 nm and unresolved Mg lines near 383 nm. The solid ellipses represents the 3 σ level for a fit of a bivariate Gaussian distribution to the dataset. Data points outside the ellipse can be deemed statistically significant. In the case of the two Cu lines, the data outside the ellipse is strongly anti-correlated. 181

7.10 Histograms of normalized (a) Mg signals, and (b) Mn signals. The solid line is a best fit of a Gaussian distribution to the data set, and the dashed lines represent detection thresholds for the Al_2MgCu and Al_6(Cu,Fe,Mn) precipitates. 183

7.11 2D precipitate map of a 200 μm by 1 mm region of an Al 2024 sample with a step size of 10 μm. The background alloy matrix is grey, while Al_2CuMg precipitates are black squares, Al_6(Cu,Fe,Mn) precipitates are white squares and locations identified as both are represented with a checkered square. 184

7.12 SNR scaling as a function of shot number for the Al doublet at 394 nm / 396 nm. Accumulating a number of shots reduces the energy required to get reasonable SNR. (Reproduced with kind permission of Springer Science and Business Media from Fig. 12 of Cravetchi et al. [98]) 185

7.13 Experimental setup for latent fingerprint detection and mapping. A frequency doubled Ti:Sapphire beam (400 nm, ~ 120 fs FWHM) produces pulses up to ~ 90 μJ on target. Pulse energy is controlled using a combination of a half-wave plate and Glan-Taylor prism (not shown). One reflection from the wedge is measured with a photodiode to monitor the pulse energy delivered to the target. LIBS emission is observed at an angle of 45 degrees from the laser axis. (Reproduced with permission from Taschuk et al. [149]) 189

7.14 Sample spectra with no background correction from a fingerprint scan. (a) A strong Na signal is visible in a shot located on a fingerprint ridge. (b) Second-order signal from the Si substrate from a shot taken between fingerprint ridges. Both spectra were generated with a single 84 μJ pulse at 400 nm with a gate delay of ~ 5 ns and a gate width of 1 μs. (Reproduced with permission from Taschuk et al. [149]) 191

7.15 1D scan of a latent fingerprint on a Si wafer using single-shot 84 μJ pulses at 400 nm and ~ 50 μm spacing between shots. Na signals (a) and Si signals (b) are periodic in space with a period of ~ 750 μm. Si signal levels are lower where a strong Na signal is observed, suggesting that the presence of a fingerprint is sufficient to suppress the LIBS signal from the Si substrate. (Reproduced with permission from Taschuk et al. [149]) 192

7.16 1D LIBS scans of control samples. Sample were imprinted with a fingerprint as described in the text. Sample was then rinsed with ethanol and wiped with lens paper. (a) After repeating the cleaning procedure twice Na was still detected at reduced levels, though fingerprint structure had been destroyed. (b) After a total of 4 cycles of the cleaning procedure, Na is no longer reliably detectable on average. On both the twice washed and quadruple washed sample (c) Si is visible at all spatial locations at SNR levels similar to those observed in the gaps in the fingerprint observed in Fig. 7.15b. (Reproduced with permission from Taschuk et al. [149]) 193

7.17 2D LIBS scan of a 1 mm by 5 mm area of a latent fingerprint from the right thumb of one of the authors using 84 μJ pulse energies. Ridges are clearly visible in both (a) Na SNR and (b) Si SNR signals. (Reproduced with permission from Taschuk et al. [149]) 194

A.1 Comparison of current results (line) with Taylor [41] (circles) for (a) normalized density, (b) normalized velocity and (c) normalized pressure. Dots from Taylor, line from Python RK. 259

List of Symbols

$\mathcal{D}_0$	Detector Geometry	μm channels^{-1}
$\mathcal{G}_{A/D}$	A/D Converter Gain	counts e^{-1}
$\mathcal{L}$	Spectrometer ideal luminosity	Sr cm^2 nm μm^{-1}
$\mathcal{R}$	Detector Responsivity	counts J^{-1}
$\mathcal{T}$	Spectrometer transmissivity	N
Φ	Integrated plasma brightness	J Sr^{-1} cm^{-2} nm^{-1}
$\sigma_{Cathode}$	Cathode Noise	counts
σ_{Dark}	Dark Current Noise	counts
$\sigma_{Readout}$	Readout Noise	counts
D	Detector Response	counts μm J^{-1} channels^{-1}
I	LIBS Signal	counts channels^{-1}
L	Spectral luminosity	Sr cm^2 nm μm^{-1}
M^2	M-squared, Beam Propagation Ratio	
CCD	Charge Coupled Device	

FOM	Figure of Merit	Varies
ICCD	Intensified CCD	
IPDA	Intensified Photodiode Array	
NEISB	Noise-Equivalent Integrated Spectral Brightness	J Sr^{-1} cm^{-2} nm^{-1}
NESB	Noise-Equivalent Spectral Brightness	W Sr^{-1} cm^{-2} nm^{-1}
E_o	Strong shock blast energy	J
ϵ_0	Dielectric constant	F m^{-1}
k_B	Boltzmann constant	J Ki^{-1}
λ	Wavelength	nm
LIBS	Laser-Induced Breakdown Spectroscopy	
LOD	Limit of Detection	
m_{ions}	Ion mass	kg
M_o	Strong shock initial mass	kg
MCP	Microchannel Plate	
n_a	Atom number density	cm^{-3}
n_e	Electron number density	cm^{-3}
PMT	Photmultiplier Tube	
P_o	Strong shock ambient pressure	Pa
q	Electron charge	C

r_o	Strong shock characteristic length	m
r	Radius	m
ρ_o	Strong shock ambient density	$\mathrm{kg\,m^{-3}}$
SMR	Surface Mapping Rate	$\mu\mathrm{m^2\,s^{-1}}$
SNR	Signal to Noise Ratio	
T_{ions}	Ion temperature	eV
t	Time	s
ω_o	Beam Waist	µm

Chapter 1

Introduction

1.1 Introduction to Laser-Induced Breakdown Spectroscopy

Laser-induced breakdown spectroscopy (LIBS) is an elemental characterisation technique that examines the spectrally resolved emission from a laser-induced plasma to determine the elemental composition of a sample. A short intense laser pulse is used to ionize a small area of a sample. The sample may be in the gas, liquid or solid phase. The hot dense plasma created by the laser pulse expands into the ambient gas and cools rapidly during the initial expansion. As the plasma cools, electrons and ions recombine, emitting electromagnetic radiation at wavelengths characteristic of the elemental composition of the original target. A schematic view of the LIBS process is given in Fig. 1.1.

The key advantages of LIBS are:

1. Measurement speed: A LIBS measurement can be performed in well under a millisecond
2. Universal sensitivity: LIBS can detect all conventional elements in solid, liquid or gaseous form
3. Limited sample preparation: little or no sample preparation is required.
4. Environmentally robust: LIBS can be performed under an extremely broad range of conditions
5. Portable: LIBS systems can be transported with a little effort, specially compared to alternative techniques

While LIBS has been a known technique since the mid-1960s [1], the development has been slow compared to techniques such as inductively-coupled plasma atomic emission spectroscopy (ICP-AES). In practice, the ease of LIBS

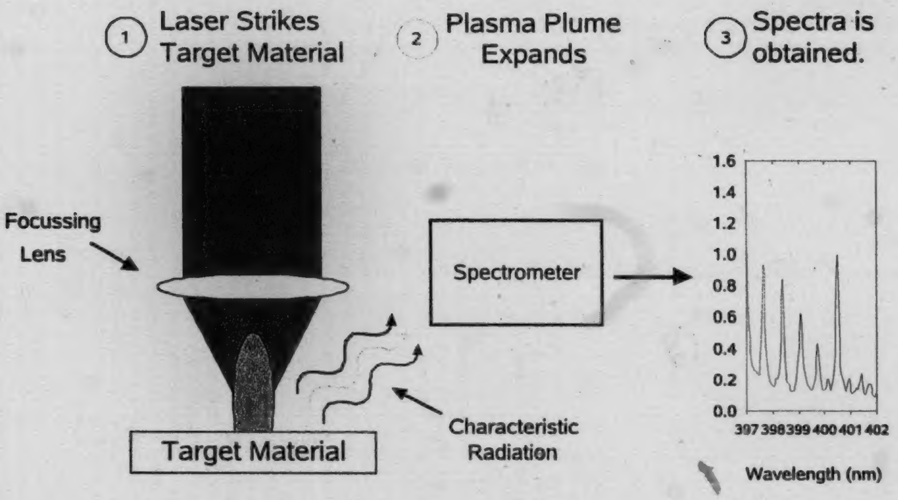

① Laser Strikes Target Material
② Plasma Plume Expands
③ Spectra is obtained.
Focussing Lens
Spectrometer
Characteristic Radiation
Target Material
1.6
1.4
1.2
1.0
0.8
0.6
0.4
0.2
0.0
397 398 399 400 401 402
Wavelength (nm)

Figure 1.1. Schematic diagram of the LIBS process.

has been outweighed by the poor analytic performance of the technique. As a result, LIBS has failed to become firmly established. However, in recent years there have been some promising developments with respect to industrial applications of LIBS [2]. The scientific activity in LIBS has also grown enormously over the past few years. Of particular note has been the publishing of three books devoted to LIBS [3–5]. A number of recent sub-fields of LIBS are:

Dual-Pulse LIBS uses a second pulse which interacts with the expanding plasma plume from the first pulse, further heating the expanding plasma plume. This reexcitation enhances the signal from the ablated atoms, improving the sensitivity of LIBS.

Resonant Dual-Pulse LIBS uses a second pulse which is tuned to a specific atomic transition for an element of interest. In this manner, the trace element is preferentially excited in the laser plume, and will emit a strong signal.

Remote LIBS takes advantage of the nature of the laser by ablating a target at a distance up to 10s of meters from the laser. Using a telescope it is possible to acquire spectra from the ablation event and characterise the material.

μLIBS reduces the energy requirements of LIBS. This reduction in energy requirements should speed the development of portable LIBS systems.

In the remainder of this chapter the history of LIBS will be reviewed, leading up to the development of μLIBS in the mid 1990s.

1.2 LIBS Survey

1.2.1 Origin of LIBS: 1964 - 1969

LIBS grew out of the related technique of laser-ablation spark optical emission spectroscopy (LA-SPARK-OES) in the mid 1960s. In LA-SPARK-OES, a laser is used to vaporise a small portion of a sample, which expands away from the target. As the laser-ablation plume expands, it passes through two electrodes which are held at a high voltage. The two electrodes discharge through the laser-ablation plume, further exciting the atoms in the plume. The atomic emission of the plume is recorded, and used to analyse the sample.

LA-SPARK-OES was first demonstrated in 1962 by Brech and Cross [6]. LA-SPARK-OES was considered to be an improvement over conventional arc-spectroscopy methods due to the ability to precisely localise the sample area and to sample non-conducting targets. While the brief report by Brech and Cross is often identified as the origin of LIBS , it is clear from contemporary literature that the technique used was in fact LA-SPARK-OES [1,7–9]

The first use of the LIBS technique, as we define it today, is reported by Runge et al. [1]. The authors used a Q-switched ruby laser which generated 50 - 75 mJ pulses, and recorded the resulting spectra with photographic plates. Calibration curves for Cr and Ni in stainless steels were obtained, with repeatability comparable to that achieved with spark spectroscopy methods [1].

This work was closely followed by Peppers, who integrated the LIBS technique with an optical microscope for the study of biological samples [10]. Spot sizes down to 2 μm were achieved in dried human blood cells, and 1 - 2 μm in a 'variety of metals'.

A comparison between LIBS and LA-SPARK-OES was performed by Rasberry et al. who found that LIBS signals were about 15 times less intense than those obtained with LA-SPARK-OES [8]. Further, LIBS spectra were much broader than those obtained by LA-SPARK-OES. This factor is also cited by Rosen et al. [11] as one of the advantages of the LA-SPARK-OES process. The chief disadvantages of the LA-SPARK-OES process are the presence of emission lines from the electrodes used to excite the laser ablation plume, and the minimum sample size of ~ 10 μm [12].

1.2.2 LIBS Technique Develops: 1970 - 1980

By the late 1960s, time-resolved measurements of laser-induced plasma emission had been made. Peipmeier et al. used a spinning parabolic mirror to sweep the plasma image along the entrance slit of a spectrometer [13]. Daibler et al. used photomultiplier tubes (PMT) to record the time history of emission from atoms and ionic species in a laser-induced plasma [14]. It was found that the peak emission was separate from the laser pulse, and that emission decay times varied with a species' degree of ionization. As a result of this work, it was clear that there were opportunities for improving the performance of LIBS with a time-resolved approach.

The time-resolved approach was applied by Scott et al. [15,16] and Treytl et al. [17]. Treytl et al. report an improvement in signal-to-background of 20 times with a drop of 40% in signal when using a time-resolved approach for minor constituents in polaroid film and Al foil. Ishizuka used LIBS for the detection of rare earth elements in different matrices [18]. The most intense signals were obtained with a NaCl matrix, resulting in limits of detection (LOD) as low as a few ppm.

The clinical applications of LIBS were studied by Glick et al. [19]. Applications include study of metal concentration in various tissues of the human body, and a study of the elemental differences between various cancerous tissues and normal tissue. The authors concluded that it should be possible to detect cancer, and possibly differentiate between types.

The effects of operating with different ambient gases and at reduced pressure was also investigated for the first time during this period by Tretyl et al. [20]. The signal-to-background observed varied with ambient gas, and was found to be enhanced at a background pressure of 5 torr. Operation in vacuum was also investigated by Kwong et al. [21], who report a minimisation of matrix effects at pressures of $\sim 10^{-3}$ torr. The work of Kwong et al. is also of note as it uses a second resonant pulse to excite emission from specific elements. However, it appears that the group was unable to significantly improve over the results of single pulse LIBS [22].

The use of multiple pulses was also considered during this era by Piepmeier et al. [13] and Scott et al. [15]. Scott et al. report a factor of 2 increase in signal intensity for two Q-switched laser pulses separated by 500 ns. Piepmeier et al. point out that since a large fraction of the laser pulse is absorbed by the plume, multiple pulses would be an efficient method of increasing the excitation of the ablated species. However, the authors conclude that reliable control of multiple spikes is too difficult to obtain, and that a single pulse is better for quantitative analysis.

From the perspective of μLIBS, the papers of Treytl et al. [17] and Allemand et al. [23] are of note. Treytl et al. report the use of 670 μJ pulses as part of their experiments, but the focus is on the time-resolved performance of their system. Allemand et al. perform a comparison of LIBS and LA-SPARK-OES under a variety of conditions, and study the performance of LIBS for energies down to 90 μJ. As a test sample, brass samples were used, and the ratio of Zn to Cu signal was observed. The ratio was constant for energies between 190 μJ and 2.3 mJ. This work represents the first study of μLIBS performance.

The period from 1970 to 1980 was a phase of extremely strong development in the understanding of the possibilities available in LIBS. With the exception of remote LIBS, every major subset of LIBS was investigated. The major limitation at this time was a matter of detector technology, rather than technique. The advent of multichannel detectors would improve the ability of LIBS to handle emission signals from multiple elements in a single acquisition.

1.2.3 LIBS with Multichannel Detectors: 1981 - 1997

This period is one in which LIBS is applied to a number of new applications. The following section covers a limited selection of the many reports of this period, and ends in the year 1997, which is approximately the time that μLIBS starts to fully develop as a sub-field of LIBS. A detailed survey of the μLIBS literature will be given in Chapter 2.

The work of Loree and Radziemski [24, 25] represents the first use of the term LIBS. In an independent discovery of the LIBS technique, Loree and Radziemski made use of an intensified photodiode array to investigate the performance of LIBS in time-integrated [24] and time-resolved [25] modes. This work was followed up by Cremers et al. [26], who studied the detection of C and F in air. The first application of LIBS to aerosols was reported in 1983 by Radziemski et al. [27].

In an effort to improve the relative standard deviation (RSD) of the LIBS process, normalisation of LIBS emission by the acoustic signal from the breakdown event was studied by Chen et al. [28]. Reasonable agreement over a few orders of magnitude was obtained between the acoustic signal and the emission peak area. The electron density and temperature of LIBS plasmas was investigated by Grant et al. [29], who went on to apply the technique to the study of iron ore [30, 31].

The absolute emission levels from LIBS plasmas were studied by Hwang et al. [32]. The results reported are integrated through the early time continuum and across a band from 250 nm to 400 nm. The authors also developed a model for ablated mass, and obtain reasonable agreement with their experimental results. This paper represents an important first step in quantifying the LIBS process.

Another interesting result from this period is the work of Lee et al. [33], who relate the intensity of continuum emission to the properties of an ablated metal target. The authors found that the strength of the emission from the background gas varied inversely with the specific heat, thermal conductivity and the density of the target:

$$I_B \propto \frac{1}{C_p C_T \rho} \tag{1.1}$$

The background gas was argon, and was observed at an emission wavelength of 763.59 nm. For Al, Cu, Fe, Pb and Zn good agreement was found with the above relationship.

Remote LIBS is first demonstrated by Davies et al. [34] in 1995, who used optical fibers to deliver the laser light to the target and to capture the LIBS emission. This technique was successfully applied to the case of a nuclear reactor. In a less hostile environment, LIBS was also applied to the study of art works by Anglos et al. [35] in 1997, who were able to discriminate between different pigment types. Depth resolution by LIBS was demonstrated by Vadillo et al. [36], who studied layered metal targets.

In general, the LIBS literature tends to be focused on specific applications. The results presented in the literature are almost entirely in arbitrary units, rather than physical ones. Thus, the values reported in the literature represent a combination of the behaviour of LIBS itself, and the detection systems that are being used. As a result, comparing between some researchers or with theory is very difficult. While lab groups are able to make progress as they refine a particular application using the same detection system, it is not possible for others to make full use of the data. This state of affairs has prevented the field from moving forward as efficiently as might otherwise have happened.

1.3 Description of Project

The project reported on in this thesis was focused on quantifying the LIBS process, while simultaneously reducing the energy requirements. By characterising the LIBS process in absolute terms, the understanding of the fundamental processes governing the performance of LIBS will be advanced. The fundamental limits to the LIBS technique are also investigated by reducing the energy used to excite the LIBS plasma. The use of lower pulse energies should also improve the practicality of the technique, as the equipment requirements will be smaller and less costly. The remainder of the thesis is outlined below.

Chapter 2 focuses on the emerging field of μLIBS, which makes use of low energy laser pulses. A review of the physics relevant to the LIBS process is given. The scaling of the LIBS process to μJ energies is explored in detail, with reference to recent literature results. A review of the current applications of μLIBS is given, and current status summarised.

Chapter 3 presents all aspects of the experimental methodology used in this thesis, with detailed examples.

Chapter 4 deals with the absolute characterisation of LIBS detection systems. A theory of LIBS detection systems is developed, and used to define detector system parameters of use to the LIBS experimentalist. A detailed characterisation of the noise sources in LIBS detector systems is performed, and used to evaluate the expected performance.

Chapter 5 investigates some of the dynamics and emission behaviour of millijoule energy LIBS in order to gain some insight into the fundamental physics of the LIBS process. A detailed characterisation of a millijoule energy LIBS event is performed in absolute terms. A global optimisation procedure is developed, and used to quantify the LOD for elemental contaminants in water. A simple model combining hydrodynamic and emission physics is developed and compared with experimental values.

Chapter 6 quantifies the μLIBS process in terms of absolute emission levels, ablation efficiencies and emission efficiency. These parameters are studied as functions of laser wavelength and pulse width for a few simple targets.

Chapter 7 reports on a few selected applications of the μLIBS technique developed during the course of this thesis. Application of the μLIBS technique to the 2D mapping of surface composition for Al alloy surfaces is presented. A new application of μLIBS to the detection and mapping of latent fingerprints is also reported.

Chapter 8 gives a summary of thesis results and outlines some avenues for future work.

Chapter 2

μLIBS

2.1 Introduction[1]

MicroLIBS (μLIBS) is a new growing area of LIBS which employs μJ energy laser pulses for excitation of plasma emission. Such μJ energy pulses are required to carry out 1D, 2D or 3D microanalysis of material surfaces with spatial resolutions approaching micron scale sizes laterally and nm scale sizes in depth. These pulses allow sampling of very small volumes (~ 10 - 1000 μm^3) and masses (~ 10 pg - ng). μLIBS is also applicable where low cost or portable systems are required. This chapter reviews the physics of LIBS and μLIBS and the capabilities of μLIBS as one scales to microjoule laser pulse energies.

2.2 Interaction Physics

This section will briefly introduce the physics relevant to the LIBS process. Laser-matter interactions, laser-induced plasmas, laser-induced plume expansion dynamics and plasma emission process are discussed.

The LIBS process begins with the interaction of a laser beam with a target of interest. The target can be composed of any element or mixture of elements, and be in solid, liquid or gaseous form. If the laser beam exceeds the breakdown threshold of the target material the atoms composing the target will be ionized, forming a plasma. The value of the breakdown threshold can be specified in terms of incident laser irradiance [W cm^{-2}], incident laser fluence [J cm^{-2}] or in laser pulse energy [J]. The breakdown threshold varies with the type and phase of the material being ablated, the type and pressure of the ambient atmosphere, and laser properties such as laser wavelength and pulse width.

---

[1] This chapter is an updated version of a book chapter to be published as Ref. [37]

2.2.1 Laser-Matter Interactions

The lasers typically used in LIBS have pulse widths ranging from 100 fs to 100 ns. The mechanisms which govern laser-matter interaction depend strongly on the length of the laser pulse and the response times of the materials under study.

In the case of femtosecond laser pulses of $\sim$ 100 fs, the pulse is short enough that the laser-solid interaction at low intensities is primarily an interaction between the laser pulse and the electrons in the solid. This interaction heats the electrons in the solid during the laser pulse, but the lattice will not react immediately. The electrons will transfer energy to the lattice through collisions on time scales of the order of 1 ps [38]. If sufficient energy has been deposited by the laser, the lattice temperature will exceed the melting or vaporisation threshold, and material removal will occur.

For nanosecond and picosecond laser pulses, ejection of electrons and initiation of a plasma occur more readily due to the longer laser pulses. The long pulse length allows more time for processes such as multi-photon ionization, avalanche ionization and interaction between the laser and expanding plasma plume. For nanosecond pulses, the formation of a significant plasma should occur very early in the pulse, allowing the interaction to be treated primarily as a laser-plasma interaction.

2.2.2 Laser-Plasma Interaction

The creation of a laser plasma requires the removal of electrons from atoms in the focal volume. Two mechanisms for electron generation are multi-photon ionization, and avalanche ionization. In cases where a single photon has insufficient energy to ionize an atom, a multi-photon process may substitute. The multi-photon ionization process is characterised by the number of photons, n, required to successfully ionize an atom. Since the probability of a multi-photon event is low, the laser pulse must be of relatively high intensity to ensure that a sufficient photon density exists. The rate of a multi-photon process varies with I^n, where I is the intensity of the laser, and n is the number of photons required for ionization.

Avalanche ionization occurs when free electrons are accelerated by the laser field to energies sufficient to ionize an atom during an impact. Both the original electron and the newly liberated electron will then interact with the laser field and be accelerated, and will potentially initiate further impact ionizations.

An important laser light absorption mechanism for LIBS plasmas is inverse Bremsstrahlung (IB). For IB to occur, there must be an interaction between the incident laser field, the electron to be accelerated and a collision with an ion in the plasma. In order to interact with the electrons in the plasma, the laser must be above the critical frequency, defined in Eqn. 2.1 [39].

$$f = \sqrt{\frac{n_e q^2}{2\pi m_e \epsilon_0}} \tag{2.1}$$

where n_e is the number density of electrons, q is the electron charge, m_e is the electron mass, and ϵ_0 is the dielectric constant. For laser light at frequencies above the critical frequency and plasmas with a high degree of ionization ($n_e gg n_a$, where n_a is the number density of atoms), the dominant absorption mechanism is inverse Bremsstrahlung (IB) [40]. This process interacts with free electrons, further accelerating them. This will provide an additional source of heating to the laser plasma.

For LIBS plasmas typical electron densities and temperatures in the range of 10^{16} - 10^{19} cm^{-3} and 0.3 - 10 eV are reported, depending on the time of observation. It is important to note that there is a selection bias in these densities and temperatures, as the measurement techniques used depend on the observation of atomic emission lines.

2.2.3 Laser-Induced Plume Expansion Dynamics

During the short-lived laser pulse, a laser-induced plasma is confined to a very small volume. The energy density of this volume, and thus the temperature and pressure, will be much higher than the surrounding atmosphere. As a result, the laser-induced plasma will expand rapidly into the background atmosphere. The thermal velocity of ions in a Maxwellian distribution with three degrees of freedom in a plasma is given by $\sqrt{3k_B T_{ions}/2m_{ions}}$. As discussed above, the typical LIBS plasma has a temperature of $\sim$ 10 eV at early times. The expected thermal velocity for a hydrogen ions comes to $\sim 3 \cdot 10^6$ cm s^{-1}, and $\sim 6 \cdot 10^5$ cm s^{-1} for aluminum ions. It is expected that the temperature of laser-induced plasmas exceeds 10 eV for early times in the evolution of the laser-induced plume. The velocities here are much greater than the speed of sound in ambient air, and the formation of a shock wave in the ambient atmosphere is expected. In μLIBS, tight focal points are often required to exceed the breakdown threshold due to the low energies used. The resulting expansion geometry can be considered to be spherical once the laser pulse has ended.

In the case of a strong shock where the background gas does not affect the propagation of a shock and where heat conduction, is neglected the work of Taylor [41] and Sedov [42] is applicable. In this case, the shock radius will scale with $t^{2/5}$, and the characteristic length is $r_o = (E_o/P_o)^{1/3}$, where E_o is the energy coupled into the blast wave, and P_o is the ambient pressure. The strong shock solution depends on an assumption of self-similarity, and is expected to be valid for the approximate range [43]:

$$\left(\frac{3M_o}{2\pi\rho_o}\right)^{1/3} \leq r \leq \left(\frac{E_o}{P_o}\right)^{1/3} \tag{2.2}$$

where M_o is the mass in the initial explosion, ρ_o is the ambient density, and the other symbols are as previously discussed. The case of a spherical shock when background gas pressure is significant is covered by Sedov [42], and is referred to here as a weak shock. Both the strong shock and weak shock solutions predict a shock that continues without stopping, though the magnitude of the shock steadily decreases. As the shock gets weaker, the effect of the background gas becomes more significant, slowing further expansion of the plasma plume. In time, the plume stops expanding completely. This effect has been studied by Dyer et al. for pulsed-laser deposition of superconducting films [44]. In a qualitative sense, the stagnation distance occurs when the energy of the expanding plume is equal to the work done in displacing the background atmosphere.

The stagnant plume continues to cool through radiation and conduction with the surrounding atmosphere, and is unable to maintain the volume that the once hot plume has expanded to. As the cooling continues, the plume begins to contract. In some cases, ablated material can redeposit on the target surface as the plume collapses.

2.2.4 Plasma Emission Processes

At early times, the laser plasma is much hotter than required for atomic emission lines. The spectrum emitted at this time is dominated by free-free transitions by the electrons in the plasma. In this state, the electron energies are a continuum and the photons emitted by the free-free transitions will exhibit a broad continuum spectrum. This emission process is Bremsstrahlung, and depends on collisions with ions or atoms to occur. This process is accompanied by free-bound transitions, in which upper levels of ions are populated by electrons. As in the case of the free-free transition, the electrons which populate the levels are in a continuum and generate a broad spectrum.

As the plasma temperature decreases line features are observed in the emission spectrum as electrons descend through the discrete levels of the atoms and ions. The lifetime of atomic states is of the order of 10 ns. However, it is clear from LIBS experiments that the available emission carries on for a time which is orders of magnitude longer. Due to the high temperature of the laser plume collisional reexcitation of ions and neutral atoms will occur, and is an important process in the long emission of the LIBS plasma. Atomic emission lines are characteristic of the emitting atom, and can be used to identify the emitting species. Atomic spectroscopy has been studied for many years, and National Institute of Standards and Technology (NIST) maintains a comprehensive database of atomic emission lines.

A few mechanisms in plasmas can interfere with the quality of the data obtained in LIBS. When the plasma is still at high densities, Stark broadening and shifting can make it difficult to identify lines accurately. However, careful analysis of the broadened spectral lines can give information about the plasma density [45]. At longer delay times, a large fraction of the ablated species will be in the ground state. If there is a large concentration of the species of interest, it is possible that the plasma will be optically thick, and the emission from that species will be reduced. As a result, the LIBS measurement will be somewhat saturated, which can lead to inaccuracies in quantitative LIBS measurements. In extreme cases, this can even lead to self reversal, where the emission from a hot emitting core is absorbed by a cooler layer surrounding the core.

2.3 Introduction to μLIBS

The development of μLIBS has been driven by two factors: 1) the desire to obtain higher spatial resolution when carrying out 2D scans of material surfaces and 2) the development of high repetition rate compact microchip lasers, ideal sources for μLIBS applications. It has been found that the plasma and continuum emission decreases significantly with lower pulse energies and thus one can obtain reasonable performance without using temporal gating. The term μLIBS has also been used in the context of applications with ablation spots of micron scale size [46,47]. In most cases, the definitions based on μJ energy and micron resolution spot sizes are equivalent. This chapter focuses on studies which have used pulse energies less than 1 mJ for nanosecond pulses, and below 100 μJ for femtosecond pulses.

In the early 1990s, Zayhowski developed the microchip laser [48–50] and he and other researchers started applying it to material analysis using both LIBS and laser-induced fluorescence detection [50–52]. Bloch et al. were able to achieve limits of detection (LOD) of the order of 100 to 1000 ppm without temporal gating for Pb, Cu and Fe in soils using pulse energies of several microjoules [51]. More recently, microjoule fiber laser sources with pulse lengths of 10 ps [53] to several nanoseconds [54] have been developed.

The first study of the capabilities of μLIBS came very early on in the history of LIBS, in a report from Allemand et al. [23]. However, it wasn't until the mid-1990s that several groups had started to investigate the application of microjoule pulses to LIBS in variety of studies [50,55–58]. In 1996, Geertsen et al. demonstrated the use of 30-70 μJ pulses for the microanalysis of aluminum alloys [56]. The authors used 266 nm pulses for various studies including LOD of minor elements down to 10 ppm, relative standard deviation (RSD) of $\sim$ 10% and lateral resolution to 6 μm. Sallé et al. [59,60] studied crater diameters, ablation volumes and expansion plumes for the interaction of 248 nm and 266 nm pulses with energies of 65 to 130 μJ and at 532 nm with energies of 10 μJ to 4 mJ. Semerok et al. extended these studies to look at the scaling of ablation craters with pulse length for durations of femtoseconds, picoseconds and nanoseconds and energies down to 10 μJ [61, 62]. μLIBS has also been combined with scanning probe fiber tip microscopy to achieve micron scale size ablation spots by Kossakovski et al. [63]. However, in the latter case the emission was not strong enough to give good species identification for sub-micron ablation spots using a non-gated and non-intensified camera. Rieger et al. [64] explored the scaling and optimisation of measuring trace constituents in aluminum alloy for 50 to 300 μJ laser pulses at 248 nm as a function of gate time. They achieved LODs of 2 to 450 ppm for elements of Mg to Fe for the case of optimised gate times and 200 μJ pulses. Further studies by the same group [65] compared LIBS signals for picosecond versus nanosecond 248 nm pulses. Scaling of line emission, continuum emission and emission lifetime with pulse energy were characterised with reported energy thresholds for observable line emission of 1 μJ for ns pulses and 0.1 μJ for 50 ps pulses. Above energies of 3 μJ the characteristics of the LIBS emission were reported to be comparable for both pulse lengths when identical laser and focusing conditions were used. Recent work by Gornushkin et al. [66], used 7 μJ 1064 nm microchip laser using a non-gated and non-intensified detector. The authors highlight many of the advantages of using microchip lasers, such as good mode quality of the beam, high shot-to-shot reproducibility, the high repetition rate, the low continuum emission and the possibility of using ungated detectors. Observation of line reversal in the emission spectra of Zn demonstrate that optically thick plasma conditions can exist for major constituents even for low energy microplasmas and observed signals and crater sizes for a several metals were reported [66]. LODs of the order of a few percent were obtained for metallic samples but poorer sensitivity was observed for pelletized graphite samples.

Studies of surface mapping using μLIBS also began in the mid 1990s. Häkkänen et al. [55] used 200 μJ 308 nm pulses to map Ca and Si concentrations in surface coatings of paper. They found good correlation with measurements of the surface using laser-induced fluorescence. The group of Laserna et al. started their studies on surface mapping using μLIBS with the investigation of depth profiling of a TiO_2 anti-reflection coating on silicon [57] and 2D mapping of carbon impurities [67] using 400 μJ pulses at 337 nm. Further investigations indicated depth resolution of the order of 40 nm for carbon impurity and demonstrated 3D scans of carbon contamination with 70 μm lateral resolution and 160 nm depth resolution [68]. Recently Menut et al. [46] demonstrated 2D surface scans with 3 μm spatial resolution using 5 μJ pulses at 266 nm and LODs in the percent range for mapping of the concentration of minor constituents on the surface of steel. They also reported that ablation probe spots down to 1 μm were possible but that there was insufficient signal to detect trace elements at the 1% level. Cravetchi et al. [69] studied crater size, line emission and RSD of signals from trace elements in aluminum demonstrating that μLIBS can resolve different types of micron scale size precipitates in aluminum. RSDs less than 10% were obtained with 7 μJ pulses at 266 nm. Full 2D scans mapping precipitate distribution in aluminum with a lateral resolution of 10 μm were subsequently demonstrated by the same group [70]. Redeposition of ablated material and cross contamination of a scanned surface has been noted by a number of different groups [56,60,63,66,68,70,71].

In the late 1990s, the analysis of elemental chemical content of liquid samples using microjoule pulses with the goal of measuring the elemental contents of single cells was demonstrated by Ho and Cheung et al. [58,72]. Using 80 - 250 μJ pulses at wavelengths of 532 nm and 193 nm they demonstrated a LOD of 50 ppm for Na in water. An acoustic normalisation which corrected for shot-to-shot variations in pulse energy and careful spatial sampling of the expansion plume improved sensitivity to the few ppm range.

During the first decade of work in the microjoule energy regime many features of μLIBS have been identified and characterised as described in more detail below. Microjoule laser sources and their application to μLIBS are briefly reviewed in Section 2.4, the scaling of LIBS to microjoule pulse energies is discussed in Section 2.5, and finally, a review of the demonstrated applications of μLIBS to date is given in Section 2.6.

2.4 Microjoule Laser Sources

While traditional lasers can be operated in the μJ range, one of the earliest sources specifically designed as a μJ pulse source was the microchip laser developed by the group at MIT [48–50,52,73–76]. Additional sources for the μJ energy regime have also been developed by other groups [54,77–81]. At the same time femtosecond laser sources were developed, many of which also operate at μJ energy levels. Recently, fiber optic oscillators and amplifiers have been developed to the point that μJ output energies are obtainable in pulsed operation mode and offer a potential new option for robust sources which can be used in field portable LIBS systems.

2.4.1 Microchip Lasers

In 1989 Zayhowski et al. reported on the development of a single frequency microchip laser in various different lasing materials [48]. Q-switched operation of the laser was developed using piezoelectric, electro-optic and pas-

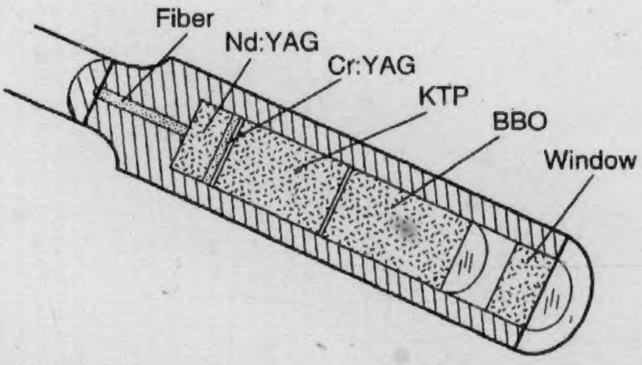

Figure 2.1. *Schematic of a UV harmonically converted passively Q-switched microchip laser. Entire device is about a cm across. (Reprinted from Zayhowski [52] with permission from Elsevier)*

sive techniques [49, 74, 75]. The output at the fundamental wavelength is polarised, allowing frequency conversion of the output and Nd:YAG laser harmonics down to 213 nm have been demonstrated [50]. When using ~ 1 W pump power, output pulse energies of 8 μJ at the fundamental wavelength, 3.5 μJ at 532 nm and 0.7 μJ at 266 nm were reported. Higher pulse energies have since been reported with 10 W of diode pump power resulting in pulse energies of up to 250 μJ and 310 ps pulse widths at the fundamental wavelength of 1064 nm and 12 μJ at 266 nm output with kHz repetition rates [52, 76]. The layout of a low power harmonically converted microchip laser is shown in Fig. 2.1. It is fabricated by bonding the gain medium to a saturable absorber and harmonic conversion crystals. In a typical configuration a 0.75 mm thick Nd:YAG gain medium is coupled to a 0.5 mm thick Cr:YAG saturable absorber [75]. Diode pump laser light of ~ 1 W at 808 nm is coupled to the gain medium by a butt coupled fiber. The resonator is formed between a dichroic dielectric mirror at the fiber input face, with a high reflectivity at the laser wavelength and high transmissivity at the pump wavelength, and a partially transmitting mirror at the output face of the saturable absorber. KTP and BBO crystals ~ 5 mm long are butt coupled to the output face to generate 2^{nd} and 4^{th} harmonic output respectively. The laser output is a single frequency TEM_{00} Gaussian mode with a diameter of the order of 50 μm. The short cavity length ensures single longitudinal mode operation since only one axial mode has sufficient gain to exceed the lasing threshold within the laser bandwidth.

Other groups have also developed similar microchip lasers with various gain media and geometries. Fluck et al. [82] passively mode-locked an

Er/Yb:Glass gain medium using a semiconductor saturable absorber mirror (SESAM) to achieve 4 μJ pulses at 1535 nm with a repetition rate of 320 Hz. Spuhler et al. [83] applied a SESAM to a Yb:YAG laser, producing 1.1 μJ pulses at 1030 nm with a repetition rate of 12 kHz. Feldman et al. [84] used a 4 mm Nd:YAG microchip crystal bonded to a 2 mm Cr:CaYAG saturable absorber crystal in a 31 mm external resonator to produce 50 μJ pulses at 1064 nm. Karlsson et al. [85] produced 12 μJ at 1535 nm with a 1 mm Er-Yb:Glass microchip laser with an external acousto-optic Q-switch and cavity mirror. Druon et al. [86] achieved ~ 9 μJ pulses at 1.06 μm and ~ 0.8 μJ pulses at 355 nm with pulse durations of 300 ps using a Nd:YAG microchip laser together with a double-pass microchip amplifier. Higher repetition rate picosecond to sub-nanosecond pulse width microchip lasers with sub-microjoule output energies have also been developed using SESAMs at 1.06 μm [87] and 1.34 μm [88]. Hansson et al. used a low voltage multiple quantum well electro-absorption Q-switch system applied to an Er-Yb:Glass laser to generate output pulses up to 0.47 μJ at a repetition rate of 10 kHz [89]. Further scaling in pump energy or addition of an amplifier chip should allow an increase in the output energy for some of these systems.

Microchip lasers have several attractive features for LIBS as pointed out by a number of authors [52,66]. They are compact, robust and relatively inexpensive. Because of the very short cavity length, the longitudinal mode spacing can be larger than the gain medium bandwidth and only a single narrow line width longitudinal mode will be generated. High repetition rates of 1 to 20 kHz can be obtained by passive Q-switching which can result in sub-nanosecond pulses making it easier to achieve the breakdown threshold for materials compared to several nanosecond pulses with the same energy. Active Q-switching can be used to set exact repetition rates and synchronise to external events at the cost of somewhat longer pulse durations. The pulse to pulse stability of microchip lasers is in the range of 0.05 to 0.5% [52, 90]. Single transverse TEM_{00} mode output is readily achieved via gain guiding and M^2 values of 1.0 to 1.3 have been obtained [73, 76]. This leads to low divergence output which can be focused to diffraction limited spot diameters. Various output wavelengths in the range of 1030 nm to 1550 nm have been demonstrated. With low energy pulses, 1550 nm pulses can fall in the eye safe operation range which is an important advantage for system use in public areas.

There remain some disadvantages of microchip lasers with respect to their use for μLIBS. When converted to UV wavelengths microchip lasers still have limited energies, on the order of 1 to 10 μJ per pulse. Further, when the simplest technique of passive Q-switching is used the laser output is free running, making it difficult to synchronise gated detectors. Additionally, the repetition rates of passively mode-locked microchip lasers may be too fast for some applications. It has been reported by Gornushkin et al. that in the case of graphite the damage from one pulse may modify the surface for the subsequent pulse, decreasing the reliability and sensitivity of the measurement [66].

Some initial work towards the design of a compact μLIBS system has been reported [91, 92]. In this work, 4 - 15 μJ 500 ps pulses at 1064 nm have been used to analyse minor constituents in aluminum alloys [91] and steel [92]. A compact CCD spectrometer was used as the detector, reducing the total footprint of the system. However, the compact CCD system cannot be gated and significant contributions from the continuum are observed [91]. The performance of this system is compared to other μLIBS techniques in Sec. 2.5.3.

2.4.2 Microjoule Fiber Lasers

High power mode-locked fibre lasers offer another potential laser excitation source for μLIBS. Fiber lasers have undergone intense development for applications in communications and recently with the advent of cladding-pumped large mode area (LMA) fibers it is possible to achieve microjoule to millijoule pulse energies. Erbium doped fibers at 1550 nm are of particular interest since they are eye safe at low microjoule pulse energies. Recently, acousto-optic Q-switching of LMA Er-doped [78] and Yb-doped fibers [79] have demonstrated close to diffraction limited transverse mode quality output pulses with pulse durations of 100 ns, pulse energies of 500 μJ and 700 μJ, and repetition rates of 400 Hz and 2 kHz, with output wavelengths of approximately 1550 nm and 1060 nm respectively. Passive Q-switching of Er-Yb co-doped fiber has also been demonstrated yielding shorter 3.5 ns, 60 μJ output pulses at around 1550 nm with 0.6 to 6 kHz repetition rates [54]. Active seeding with a pulsed CW diode laser injected into a multi stage erbium fiber amplifier has led to 118 μJ 1550 nm pulses with a duration of few nanoseconds [77] and more recently seeding with a thin disk laser source yielded longer but higher energy diffraction limited pulses of 4 mJ and 50 ns duration at 1060 nm from LMA Yb-doped fiber [81]. In the latter case undoped plain fused silica end caps were fused onto the ends of the fiber to allow the mode to expand before exiting to avoid damage on the fiber end faces. Harmonic conversion of the nanosecond output pulses from both acousto-optically mode-locked and CW diode-laser-seeded Er-doped fiber systems has also been demonstrated using periodically poled Lithium Niobate ~~crystals~~ yielding peak 2^{nd} harmonic conversion efficiencies to 768 nm pulses of 83% and 62% respectively, a peak 2^{nd} harmonic energy of 80 μJ in 45 ns pulses and 3^{rd} harmonic conversion efficiencies of 15% [93]. Generally the acousto-optically Q-switched systems have pulse lengths of tens of nanoseconds which is longer than the optimum pulse length of picoseconds to a nanosecond for μLIBS applications. The alternative approaches of passively mode-locking and amplification of a short seed pulse allow much shorter pulses. However, the damage fluence levels of the fibers in the nanosecond regime scale with the 0.5 power of pulse length given by heat diffusion scaling. Thus, shorter pulses are limited to lower maximum energies. Even so, the amplification of 0.8 ns pulses to 1.2 mJ has been demonstrated in a high power chirped-pulse-amplification femtosecond laser system at 1055 nm [80] and 60 μJ pulses have been generated by passive mode-locking at 1550 nm [54], indicating that sources with nanosecond duration are possible at the 100 μJ level. Recently work has started on the development of high-pulse-energy high-repetition-rate picosecond fiber sources with 0.6 μJ, 10 ps pulses at 1064 nm amplified at an 80 MHz repetition rate in a Yb-doped holey fiber system. These pulses were also frequency doubled with 50% efficiency to 532 nm. It is expected that by using lower repetition rate seed sources the pulse energy should increase leading to 10 ps pulse sources with energies in the range of microjoules.

Recently a guide fiber has been employed for coupling light to micron scale size spots onto a sample for μLIBS analysis [63]. While fiber laser systems have not yet been applied to μLIBS studies it is expected that they will soon become useful in LIBS microanalysis.

2.5 Scaling LIBS to Microjoule Energies

Over the past decade a basic understanding has been developed of the scaling of the performance of LIBS systems to microjoule energies. It has been found that the duration of the line and continuum emission along with the relative amount of continuum radiation decreases as one goes below 1 mJ excitation energy. In many cases the signal to noise ratio (SNR) is a weak function of energy and thus it is still possible to obtain good sensitivity if care is taken in collecting the emission light. This means that working with ungated detectors becomes possible which greatly simplifies the detector requirements and reduces system cost. However, the highest sensitivities are achieved using gated systems. Due to the submillimeter size of the plasmas obtained in μLIBS a large fraction of the plasma emission can be coupled to the narrow input slit of grating spectrometer systems. As the pulse energy decreases, the craters produced in μLIBS decrease in diameter and depth. The smaller sample areas achieved allow the probing of much smaller features approaching a micron in size for microanalysis applications. However, there is a tradeoff between sensitivity and sample area that must be taken into account for any given application. In the following section the scaling of these properties is discussed in detail.

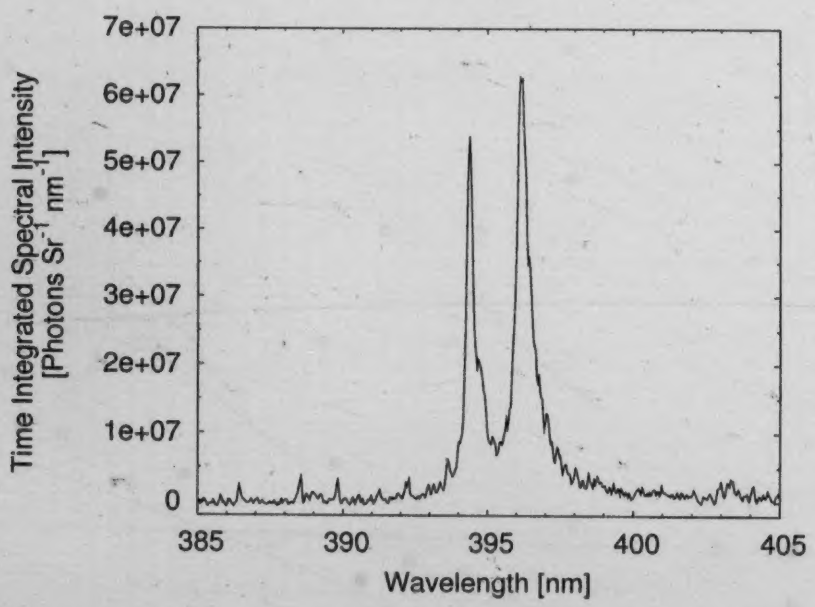

***Figure* 2.2.** *Background corrected spectrum of aluminum plasma emission using a single 50 ps, 8 μJ pulse at 248 nm, with a gate width of 200 ns and zero gate delay. The spectrum was obtained using a system for which an absolute calibration was performed. (Reprinted from Rieger et al. [65] with permission from Elsevier)*

2.5.1 Plasma Emission and Lifetime

Many materials have been examined using μLIBS, including Si photovoltaic cells, paper and paper coatings, and various metals. These studies have been performed across a range of energies from 400 μJ [57] down to 0.1 μJ [65]. A spectrum typical of what can be obtained using μLIBS is given in Figure 2.2. This spectrum of aluminum was taken using a single 8 μJ pulse with zero gate delay and a gate width of 200 ns.

Emission scaling with energy has been studied using a photomultiplier tube (PMT), a bandpass filter centred at 289 nm and a collection angle of ~ 0.4 Sr. Single line emission has been detected from Si down to 1 μJ using 10 ns 248 nm pulses and down to 0.1 μJ with 50 ps 248 nm pulses [65], and ~ 130 fs 800 nm pulses down to 0.1 μJ [94]. The resultant signal strengths are shown in Fig. 2.3 as a function of pulse energy for these three pulse lengths. It is seen that above an energy of approximately 3 μJ the signals are of the same strength. Only as the breakdown threshold is approached does one see a difference in the emission.

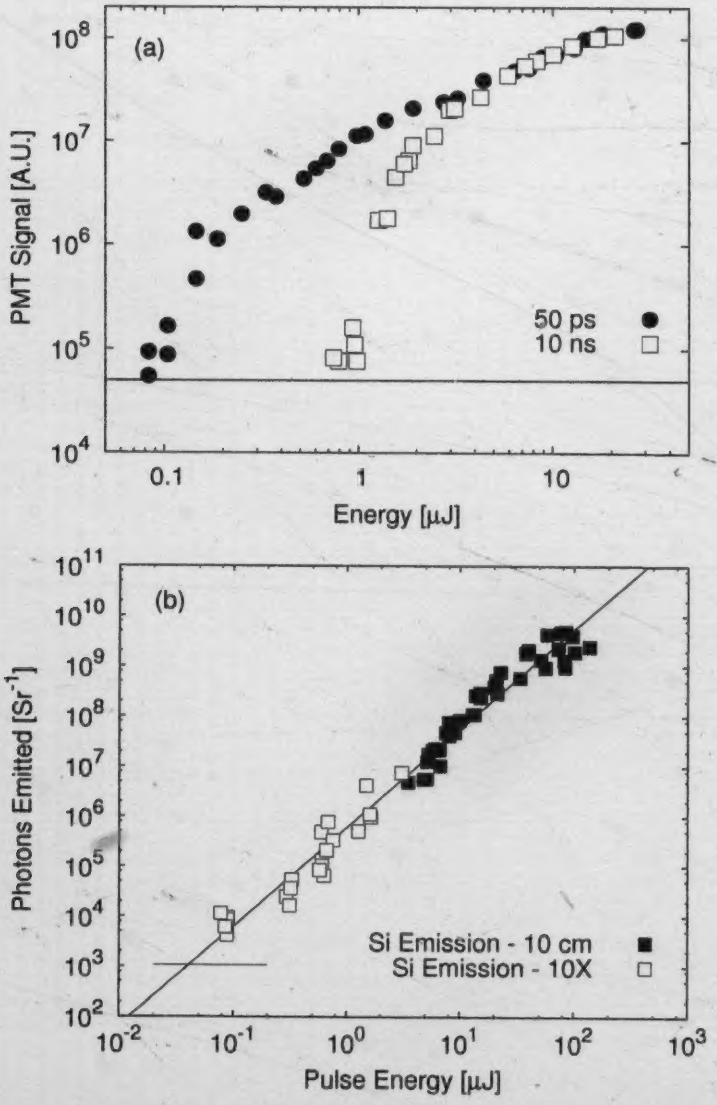

Figure 2.3. *Filtered photomultiplier detection of silicon line emission at 288 nm as a function of laser pulse energy for (a) 10 ns and 50 ps pulses at 248 nm, and (b) $\sim$ 130 fs pulses at 800 nm. The focal spot diameter was approximately 5 μm in all cases, yielding a fluence of ~ 3 J cm^{-2} for 1 μJ pulse energies. The horizontal lines represents the noise floor of the PMT. ((a) Reprinted from Rieger et al. [65] with permission from Elsevier)*

Emission is observed for shorter pulses at lower energies while emission disappears for longer pulses because the intensity is no longer sufficient to breakdown the target surface. Thus, above several microjoules the important variable appears to be energy fluence rather than intensity. The focal spot diameter was approximately 5 μm for these experiments leading to a fluence of approximately 3 J cm^{-2} for an energy of 1 μJ. The vertical scale units for Fig. 2.3a correspond approximately to photons per steradian except above $\sim 3 \cdot 10^7$ when the photomultiplier became weakly saturated. This work has recently been extended to 400 nm and 266 nm pulses, and is discussed in more detail in Sec. 6.3 of this thesis.

The scaling of peak emission time versus pulse energy has been studied by Häkkänen et al. [55] and Rieger et al. [65] for dielectric and metallic targets respectively. The scaling for the former case is shown in Fig. 2.4 indicating that optimum measurement times for peak signal to background ratio decreases to about 100 ns for 200 μJ pulses in line with the decrease in plasma emission decay time with pulse energy. The results of Rieger et al. [65] shown in Fig. 2.5 indicate that the emission decay time reduces further to a few nanoseconds as the pulse energy is reduced below 2 μJ for 10 ns pulses and below 0.3 μJ for 50 ps pulses. For energies above 3 μJ an expanding spherical plasma with a lifetime of tens of ns is formed for both ps and ns pulses leading to similar decay time constants for the emission. Similar observations have been reported by other authors with plasma emission decay times of 8 ns [66] to 15 ns [51] for 10 μJ 1064 nm sub-nanosecond microchip laser pulses. Gornushkin et al. also observed a prompt emission which was only slightly longer than the sub-nanosecond laser pulse [66].

It has been observed that the decreasing decay time of the line emission is matched by an even faster decay of continuum emission. As a result, the ratio of line to continuum emission improves as one reduces pulse energy and thus one can detect the LIBS signal even in the absence of a gated detector [57,65,66].

2.5.2 Crater Size - Lateral and Depth Resolution

One of the important advantages of μLIBS for microanalysis is the size of the ablation spot as compared to conventional LIBS. Several groups have studied the scaling of crater diameter or crater volume as a function of pulse energy [56,59,60,62,66,68,69,95]. However, one must distinguish between the detection region, which is ionized sufficiently to yield emission signals, and the total region, which is ablated by the laser pulse. Much of the ablated material is removed after the laser pulse by the shock wave and melt wave propagating into the target. The crater size will therefore represent an upper bound to the actual region probed in composition measurements.

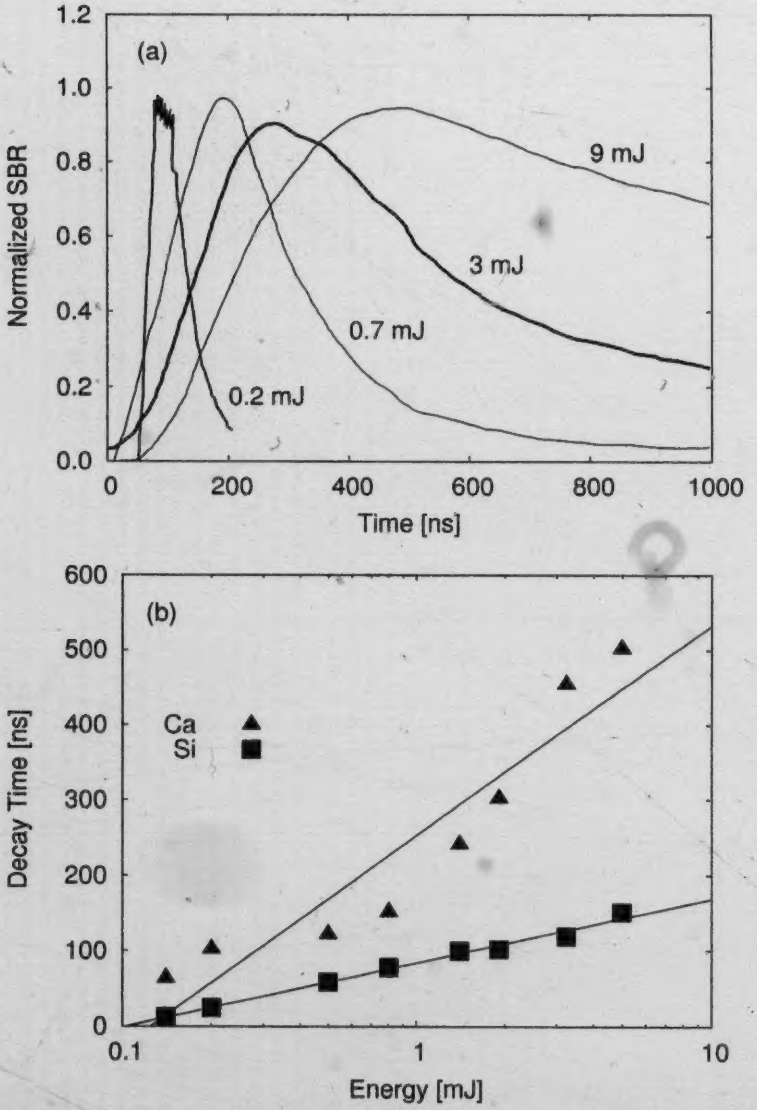

Figure 2.4. *(a) Smoothed and normalised time-resolved signal-to-background ratios of the silicon line at 251 nm at various excitation energies using a 308 nm laser. (b) Decay time for calcium and silicon signals at 422 nm and 251 nm respectively as a function of laser pulse energy. (Reproduced with permission from Häkkänen et al. [55])*

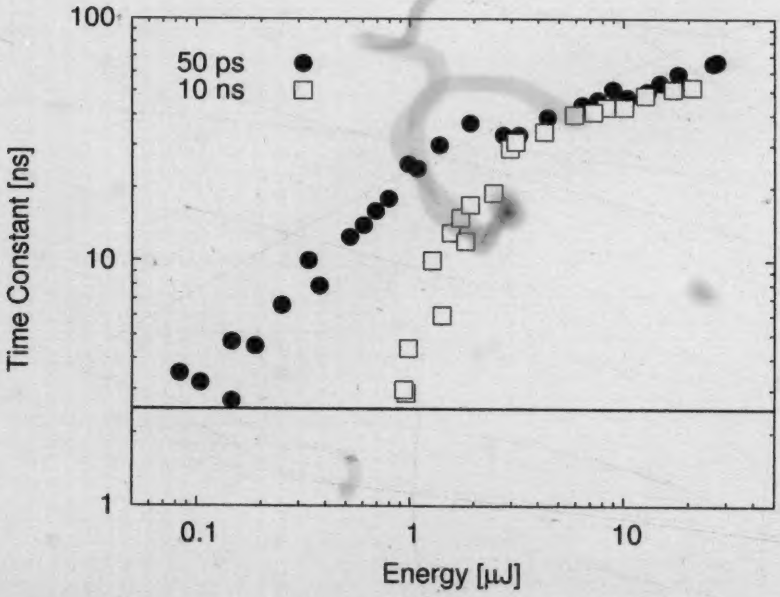

Figure 2.5. Decay time constant for silicon line emission at 288 nm as a function of pulse energy for 10 ns and 50 ps pulses at 248 nm. The horizontal line represents the rise time of the PMT used. (Reprinted from Rieger et al. [65] with permission from Elsevier)

A careful test of the lateral resolution obtainable by μLIBS was performed by Geertsen et al. [56] using a specially fabricated test sample with a sharp Cu/Al interface. Using pulse energies in the range of 35 - 40 μJ at 266 nm, a series of shots were spaced at 2 μm intervals measured perpendicular to the interface. The sample was displaced parallel to the interface by 15 μm between each shot to prevent previously ablated material from being re-sampled. The data from the experiment are shown in Fig. 2.6. The reported lateral resolution was ~ 6 μm.

Kossakovski et al. [63] used 12.5 μJ pulses at 337 nm coupled to an etched fiber probe tip in a scanning probe microscope to investigate the surface of basalt and meteorite samples. They were able to produce sub-micron ablation spot diameters but noted that the corresponding emission signals were too weak to obtain useful LIBS signals using a 20X microscope objective and viewing the emission plasma from the side. Useful LIBS signals were obtained when using spots greater than a micron in diameter.

The scaling of crater size and volume is an important variable in μLIBS applications. Aluminum is one of the most thoroughly studied materials in

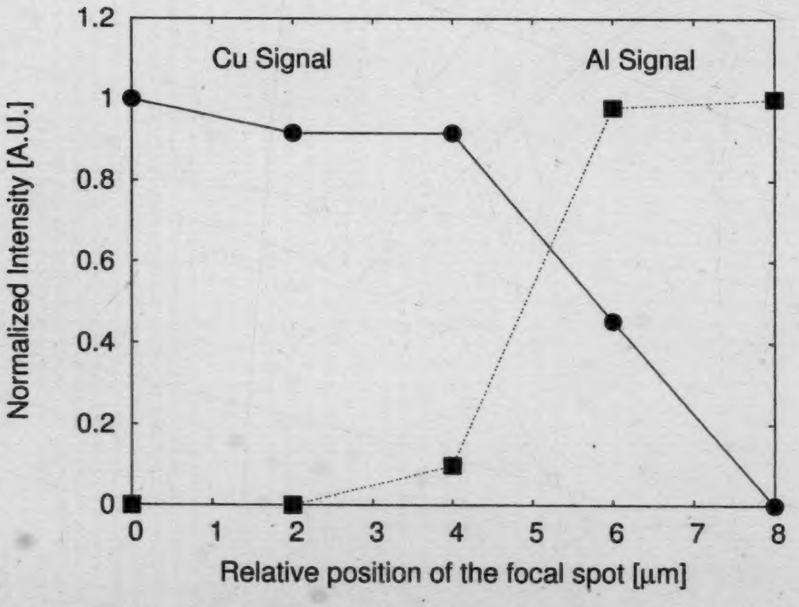

Figure 2.6. *μLIBS 1D scan using pulses in the range of 35 - 40 μJ at 266 nm across an Al-Cu interface for determination of lateral resolution. Special care was taken to prevent re-sampling of ablated material, and a lateral resolution of 6 μm was reported. (Reprinted from Geertsen et al. [56] with permission from Elsevier)*

the μLIBS literature, and probably represents the clearest data set with which to investigate the scaling laws for sample volume. Measured crater diameters and volumes for aluminum using nanosecond μJ pulses are shown in Fig. 2.7 and Fig. 2.8. Given the different methods of defining crater diameter and of measuring crater volume used in the literature the agreement between groups is quite good.

Ablation efficiency [$\mu m^3\ \mu J^{-1}$] has been measured for various metals under different conditions. Results which used nanosecond pulses are given in Table 2.1; picosecond results are given in Table 2.2. There are significant variations which may be due to the different focal geometries and intensities employed. Evidence for this interpretation is found in the two results reported from Sec. 6.7 of this thesis, which are taken at different intensities. The first result is at energies between 25 μJ and 300 μJ, and agrees with the results of Semerok et al. [61]. The second result is at higher intensities, with pulse energies between 300 μJ and 500 μJ. This value will not directly predict crater volumes for this energy, as the non-zero intercept for crater volumes must be

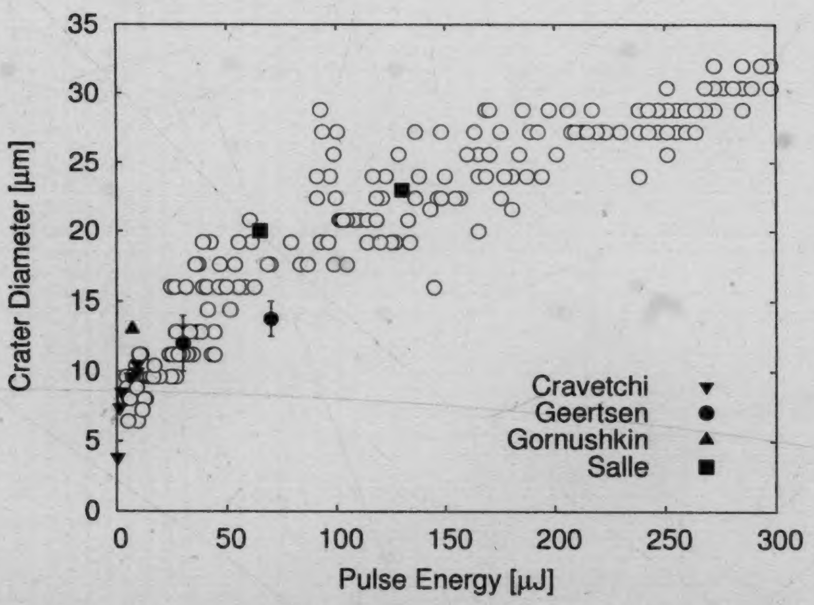

Figure 2.7. *Single-shot crater diameter as a function of energy for Al. Open circles represent shots using 248 nm pulses as described in [64]. Data from Cravetchi et al. [69], Geertsen et al. [56] and Sallée et al. [59] taken with ~ 10 ns pulses at 266 nm and data from Gornushkin et al. [66] taken with 1064 nm are shown as solid points.*

taken into account. For further discussion of the ablation efficiencies, see Sec. 6.7. While reasonable agreement for crater size scaling in the range applicable to μLIBS has been achieved in the literature between a number of groups, further work will be required to reach a consensus on the scaling of ablation efficiency.

As part of this thesis work, the absolute emission efficiency of the material ablated in μLIBS has been investigated, and is presented in Sec. 6.5. It has been shown that the number of photons emitted is significantly less than the number of atoms ablated from the target for femtosecond pulses at energies below 100 μJ. Further, the volume which actually contributes to LIBS emission has been demonstrated to be shallower than the final ablation crater.

Redeposition both immediately surrounding the crater and at further distances is an additional phenomenon which affects the effective lateral resolution that may be achieved by μLIBS. Under some conditions ablated material may redeposit and contaminate unsampled areas as discussed in Section 2.6.2

Table 2.1. *Nanosecond Ablation Efficiencies [$\mu m^3\ \mu J^{-1}$]*

Author	λ	Pulse Width	Al	Cu	Fe	Ni	Pb	Mo
Taschuk[a] [Sec. 6.7]	248 nm	10 ns	31 ± 1					
Taschuk[b] [Sec. 6.7]	248 nm	10 ns	18 ± 1					
Geertsen [56]	266 nm	6 ns	9.8					
Semerok [61]	266 nm	4 ns	29.3	6.5	3.1		45.7	
Semerok [62]	266 nm	6 ns	6	2	1	3	9	1.4
Salle [60]	532 nm	6 ns	4.9	1.93			6.11	
Semerok [61]	532 nm	4 ns	12.4	3.1	1.5		18.6	
Semerok [62]	532 nm	6 ns	5	2			6	
Gornushkin [66]	1064 nm	550 ps					200	
Semerok [62]	1064 nm	6 ns	5	2	0.9	0.7	6	0.6

[a] $25\ \mu J \leq E \leq 300\ \mu J$

[b] $300\ \mu J \leq E \leq 500\ \mu J$, see text.

Table 2.2. *Picosecond Ablation Efficiencies [$\mu m^3\ \mu J^{-1}$]*

Author	λ	Pulse Width	Al	Cu	Fe	Ni	Pb	Mo
Taschuk [Sec. 6.7]	248 nm	50 ps	11 ± 2					
Semerok [62]	266 nm	25 ps	5.7	2.8	0.6	0.9	21.3	0.5
Semerok [62]	532 nm	25 ps	4.0	0.9	0.4	0.7	12.5	0.7
Gornushkin [66]	1064 nm	550 ps					200	
Semerok [62]	1064 nm	25 ps	1	0.4	0.45	0.6	2.0	0.3

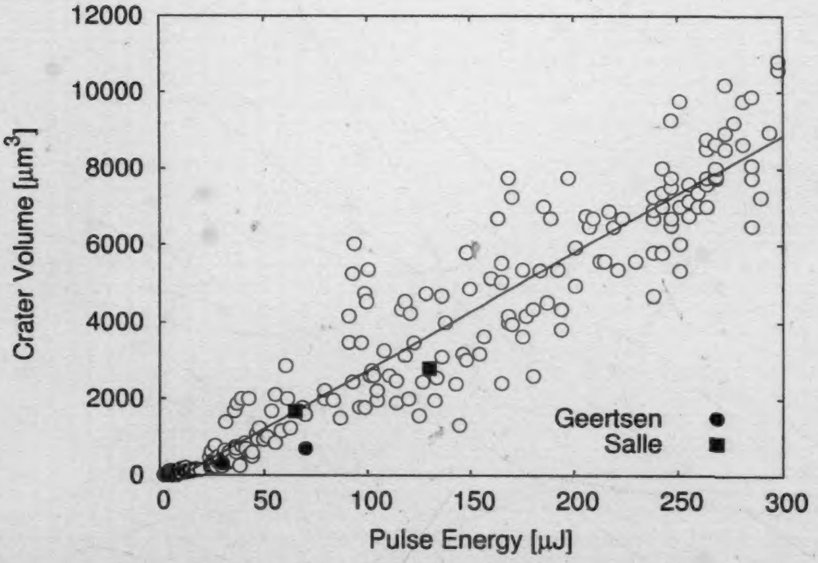

Figure 2.8. Single-shot crater volume as a function of energy for Al. Open circles represent shots using 248 nm pulses as described in [64]. Data from Geertsen et al. [56] and Salleé et al. [59] taken with ~ 10 ns pulses at 266 nm. The line is a linear regression to the 248 nm data points which are above 25 μJ and below 300 μJ.

below. Further work will be required to ascertain the ultimate spatial resolutions that will be possible in μLIBS.

2.5.3 Limits of Detection

Only a few studies have reported LODs for elements using μLIBS. Geertsen et al. used a frequency-quadrupled Nd:YAG with pulse energies of ~ 40 μJ to measure LODs of minor elements in specially prepared homogeneous aluminum targets [56]. Freedman et al. used a microchip laser which produced 14 μJ 500 ps pulses at 1064 nm, with a repetition rate of 7.8 kHz to measure LODs of minor elements in aluminum [91]. Commercially available aluminum alloys were used as samples.

In an alternative approach Rieger et al. [64] took advantage of the small probe spot size to probe only the matrix material in standard aluminum alloys for LOD measurements. The concentration of minor constituents in this matrix region was calibrated using electron probe microanalysis of the matrix region of the alloys. In the latter measurement the SNR was obtained by comparing peak line emission with to the 3σ noise in nearby regions of the spec-

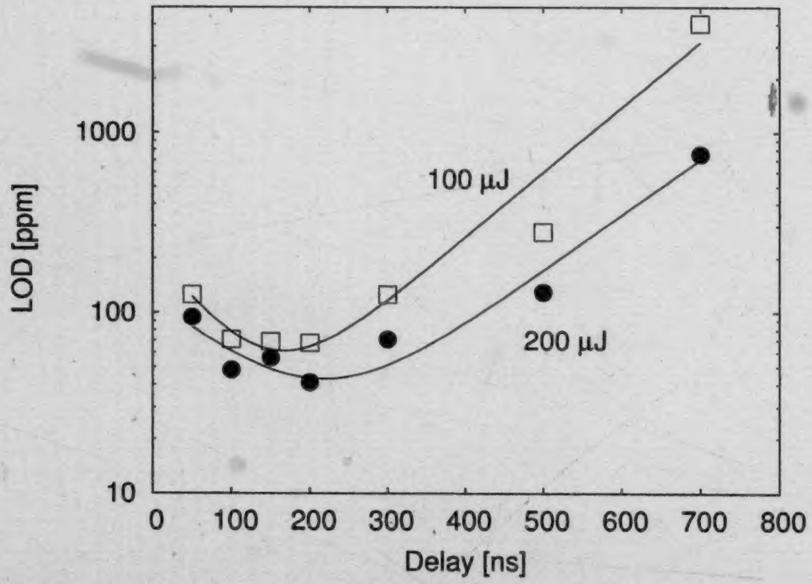

Figure 2.9. LOD as function of gate delay for Cu emission at 324.8 nm in Al 7075 alloy for 100 μJ (open squares) and 200 μJ (solid circles) laser pulse energy. (Reproduced with permission from Rieger et al. [64])

trum without line emission. For trace elements at concentrations below ~ 1% it was assumed that the signal scales linearly with concentration. A comparison with the traditional technique for determining LOD was performed and reasonable agreement between the techniques was obtained. The SNR was measured versus gate delay times and the optimum gate delay found for the given plasma conditions for several trace elements.

An example of the 3σ LOD for Cu in aluminum alloy as a function of pulse energy and gate delay is given in Fig. 2.9. It is seen that the LOD and optimum gate time are weak functions of pulse energy. The optimum LODs for several elements were determined and are presented in Table 2.3 together with values reported by Geertsen et al. [56] and Freedman et al. [91]. A typical set of values for millijoule energy LIBS measurements from Sabsabi et al. [96] is also given for comparison. To compare values taken with different number of shots it was assumed that the SNR scales with the inverse square root of the number of shots. The values presented have all been scaled to single shot values using this scaling.

It is seen that the optimised values reported by Rieger et al. are not greatly different from those reported for 60 mJ pulses, and single-shot LODs are mainly in the range of 20 to 400 ppm for 40 to 200 μJ pulses, depending on the element and line observed. Using more shots improves the LODs that are possible, as in the case of Geertsen et al. who report a LOD of 3 ppm for Mg using an accumulation of 150 shots [56]. In the case of the microchip laser and compact CCD system a total of 19500 shots were used, which improves the LODs reported in Table 2.3 by a factor $\sim$ 140.

The detector used in Rieger et al. [64] and Sabsabi et al. [96] were both similar gated intensified photodiode arrays, with similar spectrometer characteristics, including the slit widths. The only major difference in the experiments besides the energy is the laser wavelength used: Sabsabi et al. used 1064 nm where Rieger used 248 nm. The absorption will be better at 248 nm for metals, and plasma shielding will be a greater issue for the 1064 nm at higher energies which may affect the comparison somewhat. At still lower energies, Bloch et al. reported obtaining hundreds of ppm LODs for metals in soil [51].

In the case of a high energy LIBS emission plasma, the entrance slit of the spectrometer represents the limiting aperture for acceptance of light. The entrance slit and the collection optics limit the spatial region of the plasma plume that may be observed at any given time. In the case of μLIBS, the spatial expansion of the plasma is much smaller with a size comparable to the slit widths used for spectral measurements. Thus, a larger fraction of the plasma emission can be collected by the spectrometer as compared to traditional millijoule pulse energy LIBS. The result is that the LODs reported in the μLIBS literature are often comparable to those reported by more traditional LIBS systems using millijoule pulse energies.

The single shot LODs reported by Freedman et al. are not representative of the performance of the system. The microchip laser and compact CCD system is designed to integrate a large number of low energy laser pulses, taking advantage of the low continuum emission observed in μLIBS. In the actual operating conditions used by Freedman et al. LODs in the range of parts per thousand were achieved. A recent prototype from Ocean Optics has demonstrated that gating can be achieved for compact CCDs, though some issues remain to be resolved. If some form of gating can be used, the results from Freedman would be expected to improve by about a factor of 2, using the scaling given in Fig. 2.17.

2.5.4 Signal Linearity with Concentration

An important issue in the application of LIBS to analytical measurements is the scaling of the signal with concentration. For a small optically thin plasma it is expected that the line emission strength should scale linearly with con-

Table 2.3. *LOD for minor elements in aluminum alloys. All values are scaled to equivalent single shot acquisition values, using an* ${N_{shots}}^{-1/2}$ *scaling.*

		Geertsen [56]	Rieger [64]	Freedman [91]	Sabsabi [96]
	Emission	40 μJ	200 - 240 μJ	14 μJ	60 mJ
Element	Wavelength	266 nm	248 nm	1064 nm	1064 nm
Cr	425.4 nm		204 ppm		
Cu	324.8 nm		22 ppm		
	327.4 nm	245 ppm			71 ppm
	N/A			50%	
Fe	438.4 nm		447 ppm		
	N/A			20%	
Mg	285.2 nm	37 ppm	≤2 ppm		3 ppm
	N/A			15%	
Mn	279.5 nm		35 ppm		
	403.1 nm		67 ppm		14 ppm
	N/A			70%	
Ni	N/A			14%	
Si	251.6 nm				99 ppm
	288.2 nm		141 ppm		
	N/A			20%	
Zn	334.5 nm		281 ppm		
	N/A			14%	

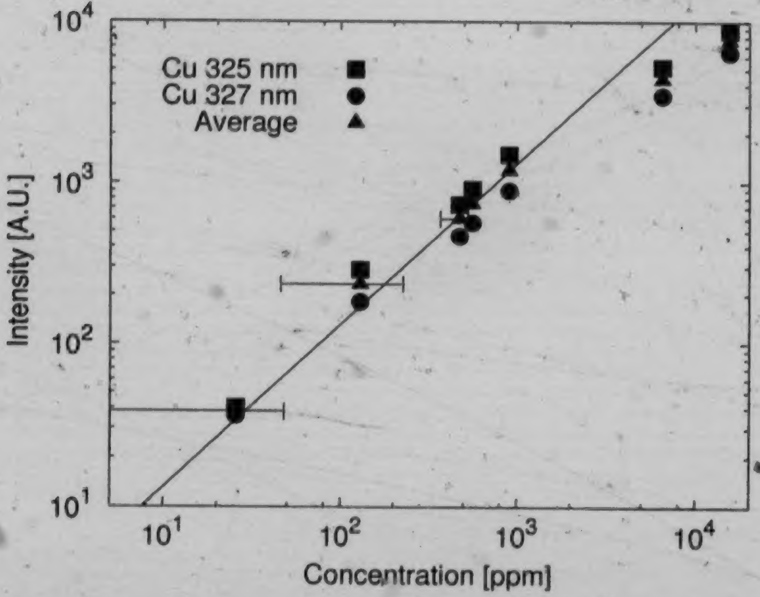

Figure 2.10. *Calibration curve of copper in aluminum matrix. Each point is an average of ten 240 μJ pulses at 248 nm. Gate width is 300 ns and gate delay is 200 ns. The 3σ LOD is 12 ppm, and the straight line is a linear fit to the averaged data points below 1000 ppm. (Reproduced with permission from Rieger et al. [64])*

centration for minor constituents. This linear scaling is observed in the emission of Cu in aluminum targets for concentrations below 0.1% as seen in Fig. 2.10. For the dominant species self reversal, indicating strong optical opacity, can be observed at energies as low as 7 μJ as reported by Gornushkin et al. [66]. Signal linearity depends on the characteristics of the line under observation, the focal conditions of the laser and the observation time. However, it appears that for many elements at concentrations less than ~ 1000 ppm signal linearity can be assumed.

2.6 μLIBS Applications

To date, the main application areas of μLIBS lasers have been in the analysis of very small sample volumes (~ 10 - 1000 μm^3) and in the scanning microanalysis of surface composition. Microanalysis can be carried out in 2D or 3D with depth resolution by using repeated scans over the surface. Initial reported results in these areas are presented below.

2.6.1 Microanalysis of Small Volumes

Microanalysis of metallic samples has been reported by Geertsen et al. [56], Rieger et al. [64,65], Cravetchi et al. [69] and Gornushkin et al. [66]. Geertsen et al. demonstrated the use of μJ pulses for the microanalysis of aluminum alloys [56]. The authors used 30 to 70 μJ pulses at 266 nm focused onto the samples using a 25X reflective microscope objective. Due to the very small focal spot used in these experiments, the signals obtained were very sensitive to inhomogeneity on the μm scale size. In studies reported by Cravetchi et al. [69,70] it was shown that the small probe spot could be positioned on individual precipitate crystals and used to analyse the composition of individual precipitates. The placement of a probe spot either on the precipitate or in the surrounding homogeneous matrix region is illustrated in Fig. 2.11. Representative spectra from locations on the matrix and the precipitate are given in Fig. 2.12.

It was shown that statistically significant determination of precipitate type could be made with single shot spectra by detecting emission lines which were more than 3σ higher than the same line for the homogeneous matrix [70]. It is essential for any application on the micron scale that the analysis be obtained in a single shot since the features being measured may be ablated in a single shot.

Broadband LIBS signals covering a large spectral range using μJ pulses have recently been demonstrated by Gornushkin et al. [66]. The use of broadband LIBS is seen as a major step forward for material analysis since one to two orders of magnitude more data can be obtained on each laser shot, thereby making optimum use of the limited photon emission from a single laser shot. A detailed characterisation of broadband spectrometer/detector combinations is presented in Chapter 4 of this thesis.

Using an ungated detector, Gornushkin et al. measured the μLIBS spectra of several metals with clear observation of emission lines but with significant continuum for the 1064 nm 7 μJ probe pulses. The authors observed that a moving target was necessary since the melting from previous laser shots left a more reflective surface and the LIBS signal would disappear after the first shot. This indicates that the use of 1064 nm wavelength is not optimum for measurements of many metals because of high reflectivity at this wavelength. For this reason many μLIBS investigations have been carried out using UV wavelength lasers to take advantage of the improved coupling.

Bloch et al. studied soil samples to detect Cu, Fe and Pb contamination using 10 μJ pulses at 1064 nm from a microchip laser. [51] The plasma emission was measured using an ungated and unintensified compact diode-array based spectrometer. The authors noted that the plasma continuum radiation decays quite rapidly with a time constant of $\sim$ 15 ns. As a result, they were able to measure concentrations at the hundreds of ppm level without the need

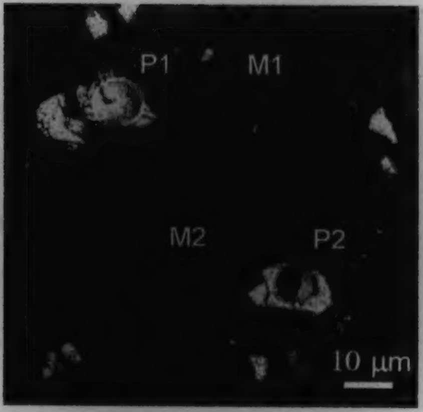

Figure 2.11. *Scanning electron microscope image of precipitates on the surface of aluminum alloy and individual single-shot μLIBS craters produced with 7 μJ pulses at 266 nm. Matrix (dark area) shots are labelled M1 and M2, while μLIBS shots that sampled precipitates (bright areas) are labelled P1 and P2. (Reproduced with permission from Cravetchi et al. [69])*

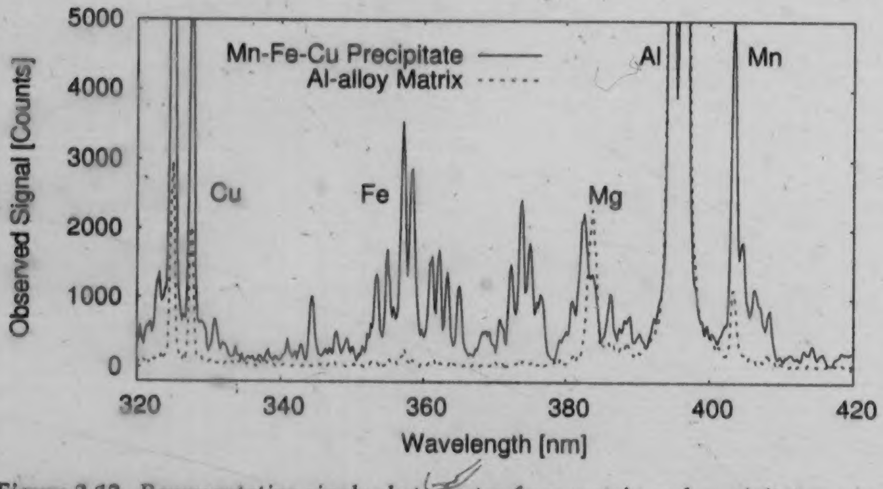

Figure 2.12. *Representative single-shot spectra from matrix and precipitate regions of the aluminum surface. Clear differences are observed with a pulse energy of 7 μJ. (Reproduced with permission from Cravetchi et al. [69])*

for temporal gating. Kossakovski et al. probed a meteorite sample comparing probing with a focal spot from a 50 mm quartz lens with that through an etched fiber probe showing the signals were similar for similar power densities [63]. In both cases light was collected from the side with a 20X microscope objective and an ungated unintensified spectrometer was used. Good signals were obtained when higher energies per pulse were used leading to probe craters on the order of 2 μm in diameter or greater. Pelletized graphite targets impregnated with magnesium hydroxide powder were studied by Gornushkin et al. using 7 μJ pulses with limited success [66]. They attributed the lack of success to the fragility and roughness of the target surface which eroded easily under the 5 kHz repetition rate laser. Due to the high repetition rate, the target was scanned in a spiral pattern in order to present a new spot to the sampling laser for every pulse.

2.6.2 Scanning Microanalysis of Material Surfaces

One main application of μLIBS is in the scanning microanalysis of material surfaces. To achieve high spatial resolution and small ablation depths, very small energies and small focal spots are desired. It has been reported that as the spot size approaches one micron, the signal becomes too weak for material composition analysis [46,63]. However, these observations were made for nanosecond pulses and without optical gating in one case. It may be possible that with shorter picosecond or femtosecond pulses and better light collection efficiency that LIBS signals can be obtained in cases where the ablation crater diameter is less than 1 μm.

Häkkänen et al. have studied the application of μLIBS to the mapping of surface coatings on paper [55,71]. This work also represents one of the earliest uses of LIBS as a surface mapping tool. The LIBS results were compared with laser-induced fluorescence (LIF) and found to give good agreement. The results of the 2D μLIBS scan and 2D LIF scan are presented here in Fig. 2.13. 2 μJ pulses at 308 nm were scanned over a 10 mm by 10 mm section of paperboard while monitoring the fluorescence signal at 422 nm. The same scan was performed after increasing the energy to 200 μJ pulses at a fluence of $\sim 10^9$ W cm^{-2}, leading to plasma emission. This fluence was sufficient to remove the paper coating, and generated craters 30 μm in diameter, and 2 μm deep. The Si I 251 nm line was monitored using a PMT with a delayed boxcar integrator. Eight shots, each displaced 32 μm, were averaged to generate a single data point corresponding to a pixel 30 μm by 250 μm. Forty pixels were taken to make a single row, and 40 rows make up the entire image presented in Fig. 2.13b. The LIF and LIBS images are expected to be negatives of each other since the Si line for the LIBS signal is sensitive to the coated regions of the paper while the fluorescence measurements are sensitive to organic compounds

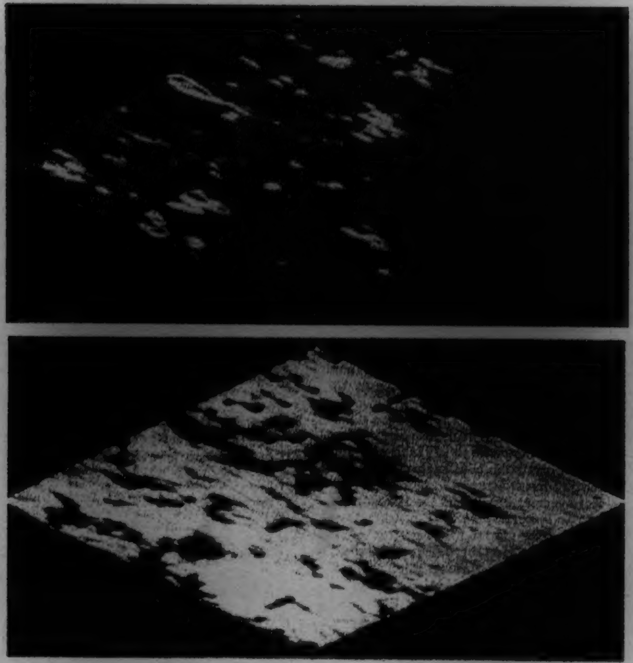

Figure 2.13. 2D scan of a 10 mm by 10 mm piece of coated paper board. Laser-induced fluorescence of underlying paper at 422 nm (upper), and μLIBS scan at 251 nm for Si in paper coating (lower). (Reproduced with permission from Häkkänen et al. [55])

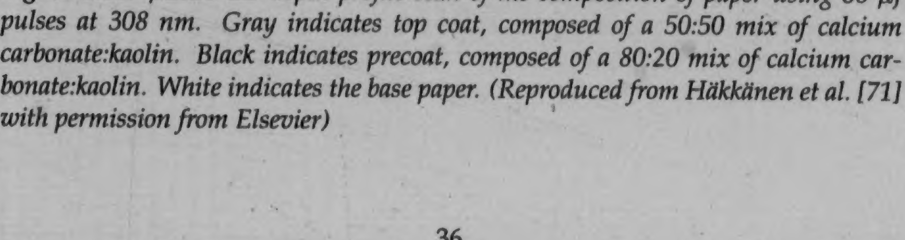

Figure 2.14. μLIBS 2D depth profile scan of the composition of paper using 80 μJ pulses at 308 nm. Gray indicates top coat, composed of a 50:50 mix of calcium carbonate:kaolin. Black indicates precoat, composed of a 80:20 mix of calcium carbonate:kaolin. White indicates the base paper. (Reproduced from Häkkänen et al. [71] with permission from Elsevier)

visible in the less coated regions.

Further improvements to the measurement technique were reported in a subsequent investigation [71]. Using a similar setup as previously the authors employed 80 μJ pulses at 308 nm and a 40 mm lens to generate focal spot sizes $\sim$ 100 μm in diameter. The resulting craters were also 100 μm in diameter and 0.5 μm deep. Using a series of 40 shots for each location on the target surface, the authors were able to measure the depth profile distribution of the pigment layers that make up the smooth surface of modern paper. A 2D depth resolved scan through the topcoat, precoat and into the base layer of paper, is shown in Fig. 2.14.

Scanning μLIBS of anti-reflection coated and uncoated silicon surfaces has been studied by Laserna's group in several reports [57,67,68,97]. In the initial investigation of Hidalgo et al. TiO_2 anti-reflection coatings for photovoltaic cells were studied using large, low fluence spots in order to achieve better depth resolution [57]. Using pulse energies of 400 μJ delivered to the target and focal spots of 160 μm by 40 μm, depth profiling of the TiO_2 coating was performed, and the coating was distinguishable from the Si substrate. However, a depth resolution was not estimated by the authors. One interesting feature noted by the authors was a dependence of the emission signal strength on the coating thickness which also correlated with the film reflectivity. The peak field strength in the coating which causes breakdown and emission depends on the interference between the reflected wave and incident wave and is a sensitive function of the layer thickness and thus a dependence on coating thickness is to be expected.

Using the same setup, Vadillo et al. applied μLIBS to a full 2D and 3D mapping of photovoltaic cell structures on silicon. The pulse energy was approximately 40 μJ [67]. Using these conditions, it was possible to produce a 2D surface map of carbon contamination distribution. By taking multiple shots to obtain depth profiling at each of the surface map locations, a 3D map was also produced, giving carbon distribution not only at the surface, but at layers further down.

The mapping work was extended to simultaneous monitoring of multiple wavelengths for mapping of Si photovoltaic cells in Romero et al. [68]. The setup was similar to that of Hidalgo et al. [57] where pulses of 100 to 400 μJ were used. Using this setup, the authors were able to generate a set of spectrally resolved images from their data, with a lateral resolution of about 80 μm. Moving on to a full three dimensional analysis of the photovoltaic cells Romero et al. studied the distribution of carbon in the solar cells, using a series of 2D scans over the same area [97]. The resulting lateral resolution obtained by Romero et al. was 70 μm, and the depth resolution was approximately 0.16 μm. In this work the goal was to achieve good depth resolution and thus the focal spot size was increased to give the low fluences necessary.

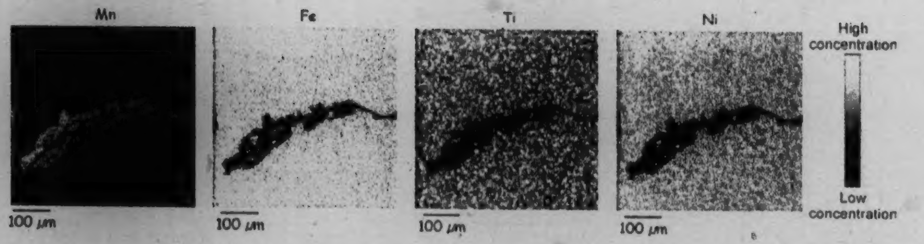

Figure 2.15. Scanning μLIBS image of a single inclusion on the surface of steel as seen in the emission of elements Mn, Fe, Ti and Ni. (Reproduced with permission from Menut et al. [46])

Menut et al. combined a LIBS system with an optical microscope and generated a 2D surface scanning instrument with a lateral resolution of 3 μm using an Ar buffer gas [46]. Crater sizes down to 1 μm are reported, though at such low energies the SNR was insufficient for analysis of minor constituents. The setup described by Menut et al. [46] detected signals at a pulse energy of 5 μJ, resulting in craters approximately 3 μm in diameter for their steel sample. The system was able to acquire signals at 20 Hz, and has been used to map the surface composition of various samples. In Fig. 2.15 a multi-elemental map of a single inclusion in a steel alloy is shown.

Cravetchi et al. reported 2D mapping of aluminum surfaces and identification of precipitates using 8 μJ pulses at 266 nm [70]. Particular attention was directed towards improving of the statistical validity of the precipitate identification technique. A Gaussian function was fit to the signal intensity distribution of all shots in the mapped region to derive the average and standard deviation for signals corresponding to the background matrix. Only signals 3σ above this level were deemed to be regions of precipitates. Correlations between various elements in a given type of precipitate can easily be observed as shown in Fig. 2.16. The densely populated region in the lower left hand corner of the plots represents the matrix background. Based on the standard deviation of signals observed, it was possible to set detection thresholds for various trace elements and map out the two dominant precipitates in Al 2024 alloy with 10 μm lateral resolution [70].

The application of 800 nm, ~ 130 fs pulses to μLIBS analysis of aluminum alloy surfaces has recently been studied by Cravetchi et al. [98]. The SNR achievable for the Al doublet for gated and ungated acquisition conditions for energies from 60 μJ down to 300 nJ is presented in Fig. 2.17. Over this range, gating improved the achievable SNR by a factor of 2.0 ± 0.1. While significant, the penalty for moving to an ungated acquisition system might be acceptable for some applications.

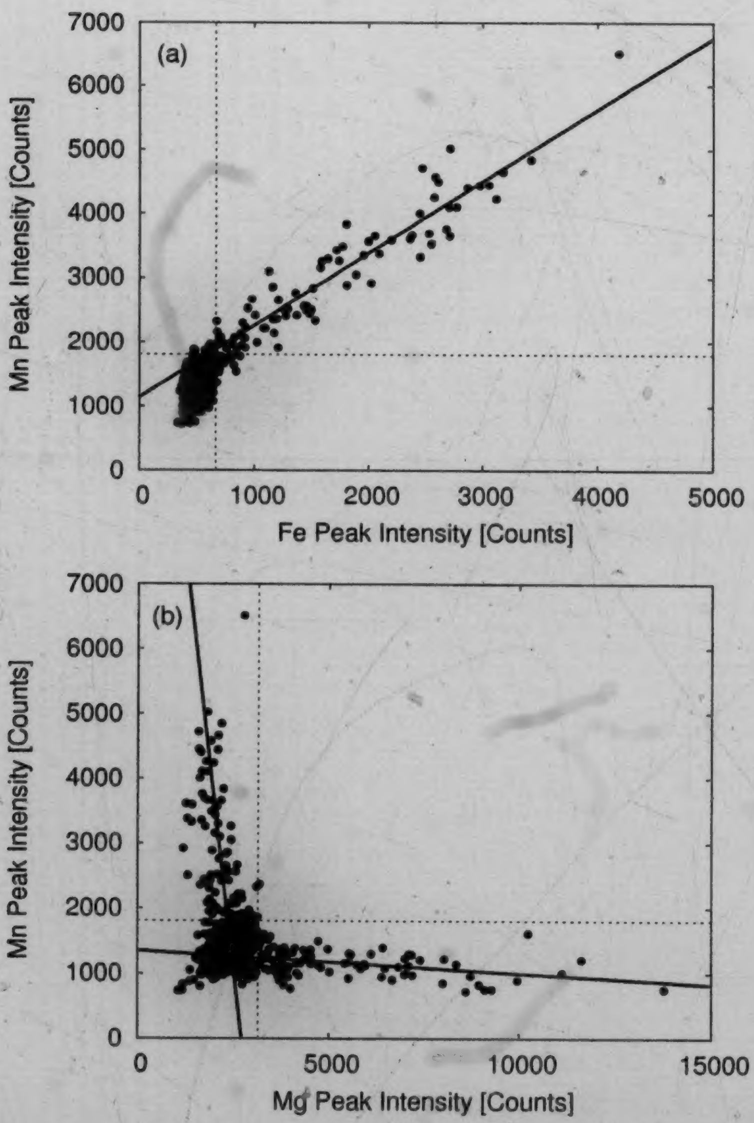

Figure 2.16. *Correlation plots of peak intensity values for minor elements in aluminum alloys. (a) Mn vs Fe shows a positive correlation as they appear in the same precipitates, (b) Mn vs Mg yields a negative correlation in both lobes, as they do not appear in the same precipitates. Dashed lines are 3σ values from the nonlinear Gaussian fit to all available data. Solid lines are linear regressions within their respective quadrants. (Reprinted from Cravetchi et al. [70] with permission from Elsevier)*

The possibility of very low energy shots was also investigated. Using energies below 1 μJ, multiple shots were fired upon a single spot. The resulting SNR for the Al doublet is presented in Fig. 2.18. Using this technique, the energy threshold for useful plasma emission was reduced from ~ 1 μJ to ~ 80 nJ, using a ICCD/Czerny-Turner combination as a detection system. The use of femtosecond pulses with energies below 1 μJ for 2D surface mapping of aluminum alloy was explored as part of this thesis, and is presented in Sec. 7.2.

A few of the groups studying μLIBS have noted the issue of cross contamination from material redeposited onto the surface from previous ablation spots. Romero et al. [68] and Häkkänen et al. [71] measured the single-shot contamination range from an ablated location for silicon and paper targets using the LIBS signal itself, giving values of 80 μm and 200 μm respectively. Their results are shown in Fig. 2.19. Several other groups also refer to visible redeposition of target material on the sample surface [56,59,63,66].

Clear evidence of material redeposition was found in the 2D mapping of aluminum surfaces experiment of Cravetchi et al. [70]. Redeposition of Al_2O_3 on the target surface was observed. The resulting coating of the target was quite pronounced when a large number of shots was taken, as can be seen in Fig. 2.20a. The left image is a SEM image which shows a smooth coating over the original aluminum surface. However, as can be seen in Fig. 2.20b, the redeposited layer ceases abruptly as one approaches the mapped area and around the isolated shots at the bottom of the images.

This can be understood by considering the blast wave in air and shock wave in the material created by the ablation plasma. As a LIBS plasma is created, it launches a shock wave that expands with a hemispherical symmetry and the force of this wave near the ablation spot is sufficient to remove the deposited material from the surface. The radius of this cleaned area is larger than the distance to the subsequent shot in the scanning analysis and thus the original target surface is probed by the scanning μLIBS measurement. The dynamics of material deposition and cleaning will depend on the sample being scanned and the conditions being employed. Redeposition may be reduced if one carries out the scans in vacuum but detailed studies need to be carried out to quantify the reduction.

In order to compare the various mapping experiments, I define a surface mapping rate (SMR) as the sample area per shot multiplied by the sample rate. In this case, the sample area per shot is defined by the crater diameter. These are plotted for published reports of μLIBS surface analysis in Fig. 2.21. Included for comparison is the use of line-focused beam scans with millijoule energy pulses, as applied by Mateo et al. [100, 101] and Rodolfo et al. [102]. In such line focused beams, the irradiance applied to the target can be in the same range as that of μLIBS. This plot demonstrates the current capabilities

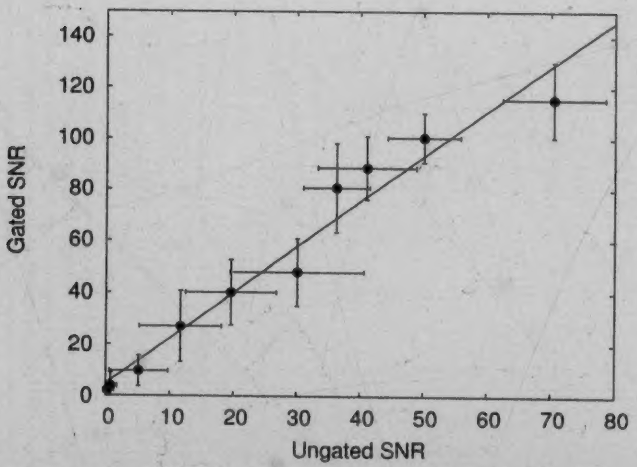

Figure 2.17. *Comparison of SNR achieved for Al with optimum gate delay time versus negative gate delay time (ungated). Data are an average of 100 single 1 μs gate width acquisitions. The solid line is a best linear fit to the data. (Reproduced with kind permission of Springer Science and Business Media from Fig. 8 of Cravetchi et al. [98])*

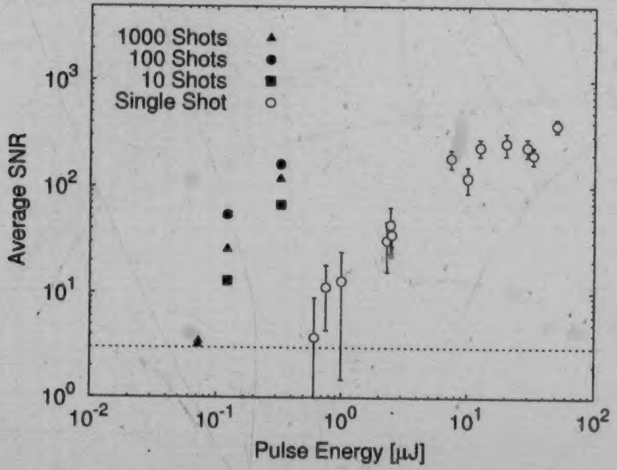

Figure 2.18. *Measured SNR for the Al doublet using multiple pulses on a single spot. For the data at $\sim$ 80 nJ, the SNR is at or below 3σ. (Reproduced with kind permission of Springer Science and Business Media from Fig. 12 of Cravetchi et al. [98])*

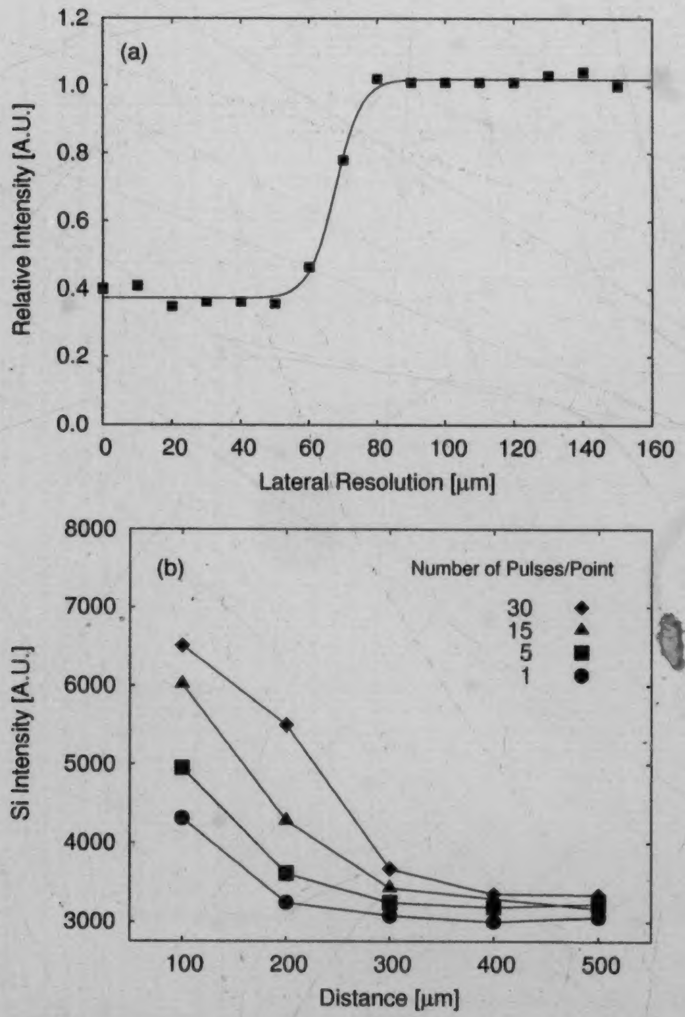

Figure 2.19. *(a) Ratio of peak intensities of the Ti line measured at 626 nm from two adjacent points on the surface of a* TiO_2 *coated Si sample. A ratio of 1.0 indicates the second shot has sampled an undisturbed surface. (b) Silicon intensity of the first ablation layer of coated paper as a function of distance between sampling points and number of shots at each sampling point. In this case, Si is a contaminant from buried layers in a paper coating. ((a) Reprinted with permission from Romero et al. [68]. Copyright (1997) American Chemical Society; (b) Reprinted from Häkkänen et al. [71] with permission from Elsevier)*

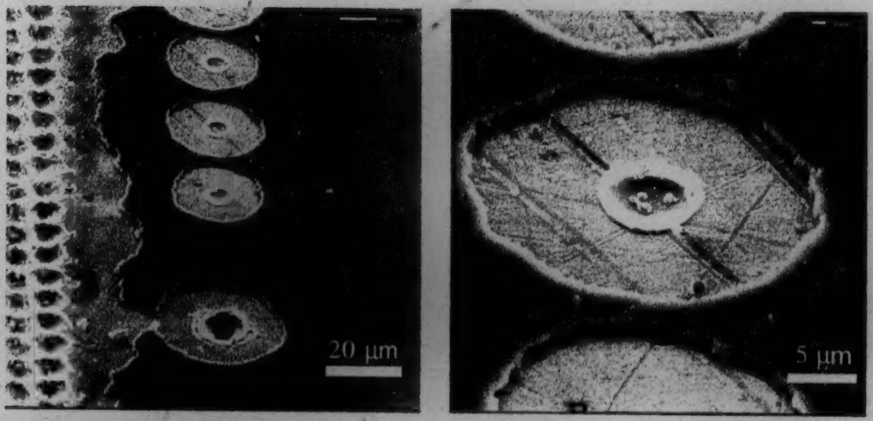

(a) (b)

Figure 2.20. (a) Scanning electron microscopic image of macroscopic redeposition of Al_2O_3 *and shock cleaning near the perimeter of a 2D μLIBS scan area 300 μm by 900 μm in size with probe spot separation of 10 μm. The edge of the scanned area is visible at the left edge of of the image. (b) Isolated crater created using single 1.5 μJ pulses at 266 nm. (Reprinted from Cravetchi et al. [70] with permission from Elsevier)*

of μLIBS scanning rates for 2D multi-elemental surface mapping.

2.6.3 Liquid Samples

In the early 1990s a series of experiments applying LIBS to the detection of elements in water jet samples were performed by Cheung et al. [103, 104]. This work has been extended to the μLIBS regime in more recent work by Ho and Cheung et al. [58, 72] for detection of Na and K. One of the goals was to demonstrate sufficient sensitivity to measure the chemical content of single cells. 532 nm and 193 nm laser pulses were used as excitation sources, with both a photomultiplier tube and ICCD detection. To increase the absorption of the liquid water, a solution of 12 mM methyl violet was used. Using 240 μJ pulses at 532 nm a detection limit of 50 ppm was achieved. The reported detection limit using the ArF excitation beam was 230 ppb. In further work by the same group, Cheung et al. note that the plasma generated by the ArF beam is significantly cooler than that generated by the 532 nm beam at short delay times. Plasma temperature and electron density were determined by line intensity ratios and line widths.

The analysis of liquid samples by μLIBS without an absorbing agent has been performed by our group for Na [105], Pb and Al [106]. The Na work

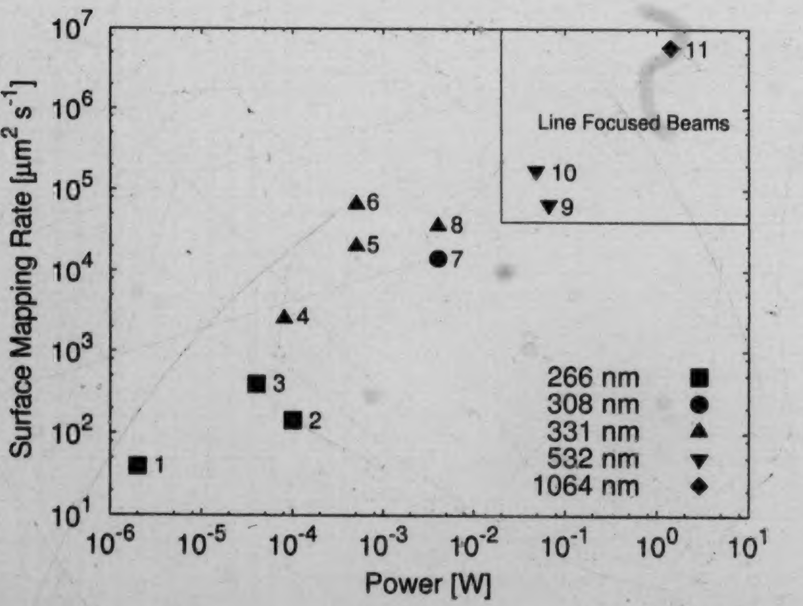

Figure 2.21. *Surface scanning rate as a function of applied power. 1 = Taschuk Ph.D. Thesis (Sec. 7.2.4), 2 = Menut et al. [46], 3 = Cravetchi et al. [70], 4 = Vadillo et al. [67], 5 = Romero et al. [97], 6 = Romero et al. [68], 7 = Hakkanen et al. [71], 8 = Romero et al. [99], 9 = Mateo et al. [100], 10 = Mateo et al. [101], 11 = Rodolfo et al. [102]. For comparison, surface scans carried out using millijoule laser pulses in a line focus geometry are also shown in the upper right area of figure [100–102].*

used ~ 200 μJ pulses at 355 nm and a IPDA/Czerny-Turner system; a 100-shot LOD of ≈ 50 ppm was obtained. For Pb and Al, a ICCD/Czerny-Turner system was used with 266 nm pulses. For Pb, a 100-shot LOD of 75 ppm was obtained using ~ 260 μJ. For Al, a 100-shot LOD of 125 ppm was obtained using ~ 200 μJ.

2.7 Conclusion

In the past decade there has been good initial progress in the development and understanding of μLIBS. Pulsed microchip laser sources with energies of 1 to 240 μJ have been demonstrated and are beginning to be commercially available. The primary sources demonstrated to date are in the infrared region while the optimum wavelength for μLIBS is most likely in the UV region to give smaller, diffraction limited focal spots and better target absorption.

The energy of harmonically converted UV sources is still limited to less than ~ 10 μJ. However, at 1550 nm (erbium based lasers) one also has the advantage of eye safe sources at microjoule energy levels making practical systems easier to implement. More work needs to be done on the wavelength scaling issues to determine how effective these mid infrared sources could be for μLIBS.

In microanalysis applications the ability to achieve single shot LODs of 10 to 100 ppm has been demonstrated with ~ 100 μJ energy pulses using gated detector systems and 100 to 10,000 ppm with ~ 10 μJ energy pulses using ungated detectors. The ability to analyse sample volumes of 10 to 1000 μm^3 has been demonstrated. 2D surface scans have been carried out with 3 μm lateral resolution on steel and 10 μm lateral resolution on aluminum. Microanalysis of water samples demonstrating sub-ppm sensitivities has also been demonstrated for optimised conditions.

Initial work characterising the exact region of LIBS emission sensitivity within the ablation volume has been performed. The cross contamination issue for scanning microanalysis systems will continue to be an issue and needs to be addressed in detail. It is likely that cross contamination is very much material and laser parameter dependent and particular attention should be paid to this issue in any scanning microanalysis system.

While there is much that remains to be done in the study of μLIBS, particularly in the area of wavelength and pulse length scaling of LODs achievable, the use of μLIBS already appears as a promising new regime which should lead to cost effective portable systems.

Chapter 3

Experimental Methodology

3.1 Introduction

This chapter gives an introduction to the key equipment and experimental methodologies used during the thesis work.

Spectrometers and grating theory for simple reflection gratings with and without blaze are introduced. The Echelle spectrometer principle is briefly discussed.

Optical Detectors used with spectrometers, such as photomultiplier tubes (PMT), charge-coupled devices (CCD) and intensified photodiode arrays (IPDA) and intensified CCDs (ICCD) are described.

Calibration procedures for laser pulse energy, ICCD timing, spectrometer wavelength positions and radiometric response are outlined. Experimental setups, procedures and analysis are described in detail.

Optimisation methods for target focal position, plasma imaging alignment and basic detector optimisation are described.

Signal Analysis methods for LIBS spectral data will be defined. A detailed characterisation of cathode noise spikes in intensified systems is performed.

3.2 Spectrometers

The spectrometers used in LIBS make use of reflection gratings, for which the governing grating equation is [107, 108]:

$$d\left(sin\theta_{observed} - sin\theta_{incident}\right) = m\lambda \tag{3.1}$$

where d is the distance between the grooves, $\theta_{observed}$ is the angle at which light is observed, $\theta_{incident}$ is the incident angle, m is the order of diffraction,

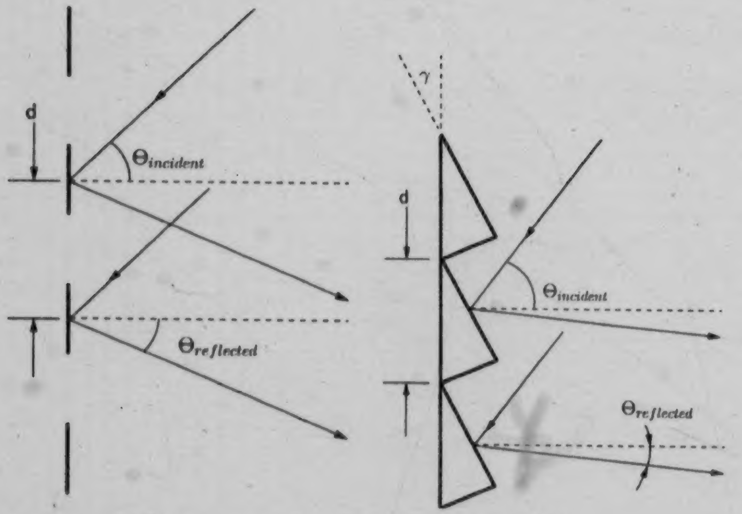

(a) (b)

Figure 3.1. *Schematics of gratings (a) without blaze and (b) with blaze.*

and λ is the wavelength of observation. If this equation is satisfied, constructive interference at a wavelength of λ will occur at an angle of $\theta_{observed}$.

A simple reflection grating is shown in Fig. 3.1a. In this case, there is no blaze angle, and the grating will therefore operate as a discrete array of little mirrors. Hence, the angle of reflection will be the same as the angle of incidence, and incident light at all wavelengths will tend to be reflected in one direction and the zeroth order ($m = 0$) of the grating. While some light will be diffracted into useful orders, this configuration is not efficient.

To improve the efficiency of gratings while maintaining spectral dispersion, the grating is blazed. A blazed grating has a sawtooth profile as shown in Fig. 3.1b, which allows the high-efficiency specular reflections to be directed to a particular diffraction order. The angular dispersion of a grating is given by [107, 108]:

$$\frac{d\theta_{reflected}}{d\lambda} = \frac{m}{d\cos\left(\theta_{incident}\right)} \tag{3.2}$$

The angular dispersion combined with the focal length of the spectrometer will determine the reciprocal linear dispersion of the spectrometer, which gives the spectral width per unit length at the exit of the spectrometer. The resolving power of a grating is defined as [108]:

$$R = \frac{\lambda}{\Delta\lambda} = mN \tag{3.3}$$

where λ is the wavelength of interest, $\Delta\lambda$ is the minimum resolvable wavelength difference, m is the diffraction order and N is the number of grooves on the grating. However, in practice the resolution of a spectrometer will depend not only on the grating, but also the size of the entrance slit and the characteristics of the detector used. The combined effects the spectrometer, grating and detector can be characterised using the technique described by Brodersen [109].

A typical spectrometer used in LIBS experiments is the Czerny-Turner configuration, which uses gratings with groove densities in the range of 150 lines/mm to 2400 lines/mm. These systems are usually blazed for use in the first order. Another type of spectrometer which has recently become more popular is the Echelle spectrometer, schematically shown in Fig. 3.2. This grating uses a very low groove density ($\leq$ 100) in very high orders ($\geq$ 50) to achieve high resolutions. However, due to the very high order used, the angular dispersion is also quite high. To make efficient use of limited detector surface area, an additional order sorting takes place using refractive optics to distribute the different orders across the detector face. The order sorting process is shown schematically in Fig. 3.2b. A schematic of the orders on a detector surface is given in Fig. 3.3. In this manner, an Echelle spectrometer can simultaneously offer high resolution with a high bandwidth.

3.3 Detectors

A CCD is an array of photosensitive areas, or pixels, on a semiconductor wafer that can be used to capture images. As photons strike a pixel, each has a chance of generating one or more electron-hole pairs. Once generated, the electrons are collected in 'wells' for the integration time of the CCD. The entire array of wells is moved by rows to a readout section of the CCD, in which each pixel in the row is read out. In this manner, the image collected by the CCD can be reconstructed. A detailed survey of the use of scientific CCDs can be found in the book by Janesick [110]. CCDs are not often used in LIBS since they are not gateable. Because of this the early continuum emission in LIBS is fully integrated with the signal of interest and the performance of LIBS suffers.

A PMT is a very sensitive detector of optical radiation that makes use of the photoelectric effect to convert incoming photons to electrons. These electrons are accelerated through a chain of dynodes held at descending voltages. At each dynode, each accelerated electron liberates multiple electrons, which are in turn accelerated to the next dynode. In this fashion, the initial few elec-

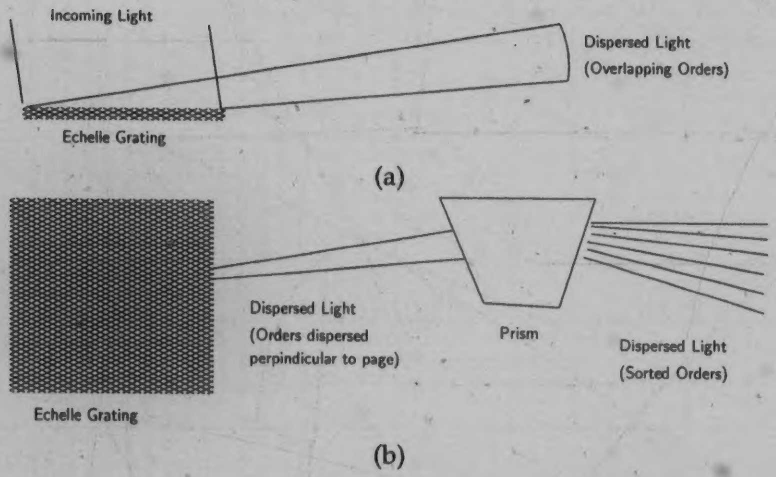
Incoming Light
Dispersed Light
(Overlapping Orders)
Echelle Grating
(a)
Prism
Dispersed Light
(Orders dispersed
perpindicular to page)
Dispersed Light
(Sorted Orders)
Echelle Grating
(b)

Figure 3.2. Schematics of the operation of an echelle spectrometer (a) represents the diffraction of light into high orders which overlap in space, while (b) shows the order sorting by a prism.

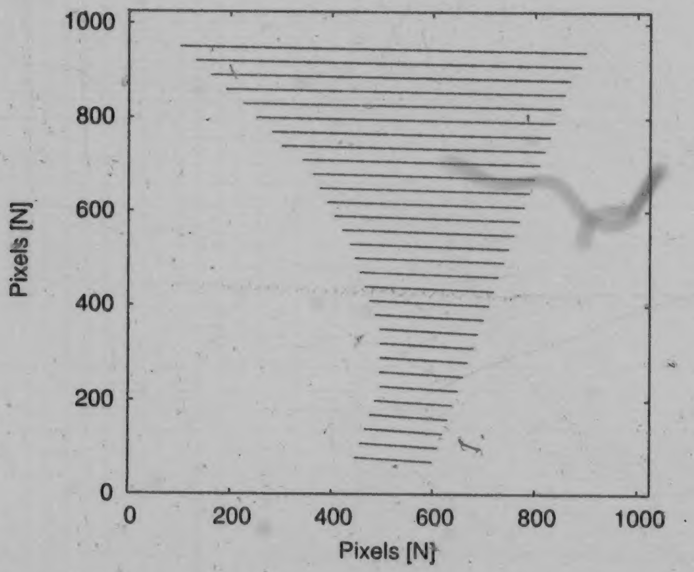

Figure 3.3. Schematic of the image of the sorted orders generated by an echelle spectrometer.

trons which are a direct response to incoming optical radiation are amplified to the point that they can be detected. A schematic view of a PMT is given in Fig. 3.4, along with a single photoelectron and the first few amplification stages. The key characteristics of a PMT are the quantum efficiency and the gain. The quantum efficiency, η, is the number of photoelectrons emitted per incident photons. The gain of the PMT is the number of electrons collected at the output per photoelectron generated at the input. Further details can be found in Chap. 9 of Ref. [111].

An ICCD is can be viewed as a combination of an array of miniature PMTs and a CCD. A schematic view of an ICCD is given in Fig. 3.5. The photocathode operates as in the case of a PMT, converting photons to electrons. The microchannel plate amplifies the electron signal, taking the place of the dynode chain in a PMT [111]. The microchannel plate can be thought of as an array of little PMTs, which preserves the image arriving at the photocathode. Once the microchannel plate has amplified the image, the electrons strike the phosphor, which emits light for subsequent capture by the CCD.

The ICCD has an additional feature that is very useful for LIBS, in that it can be switched on the nanosecond timescale by switching the voltage of the photocathode. In this manner the early continuum emission can be avoided, while the LIBS signal can be acquired with high sensitivity. An IPDA system was also used for parts of this thesis. An IPDA system is similar to a ICCD, except that instead of a CCD, a photodiode array is used.

3.4 Calibration Procedures

This section describes calibration procedures for four LIBS systems parameters.

Laser Pulse Energy is the laser pulse energy used to excite the LIBS plasma. Two types of energy monitors are discussed. The methods used to evaluate the overall precision and accuracy of energy calibration data are discussed, and the use of control charts to monitor LIBS system performance is described in Sec. 3.4.1.

Zero Time is the arrival of the laser pulse intensity peak at the target surface. Temporal calibrations are important in LIBS performance, because signal and noise levels depend strongly on the timing of acquisition. These issues become even more important in μLIBS, because the plasma evolves at a much faster rate than in conventional LIBS. Two methods for precisely calibrating laser arrival time at the sample surface are discussed in Sec. 3.4.2.

Observation Wavelength is the wavelength detected by a particular channel of a spectrally dispersive system. Making good use of LIBS spectral data observation wavelength calibration. A simple procedure for wavelength calibration is described in Sec. 3.4.3.

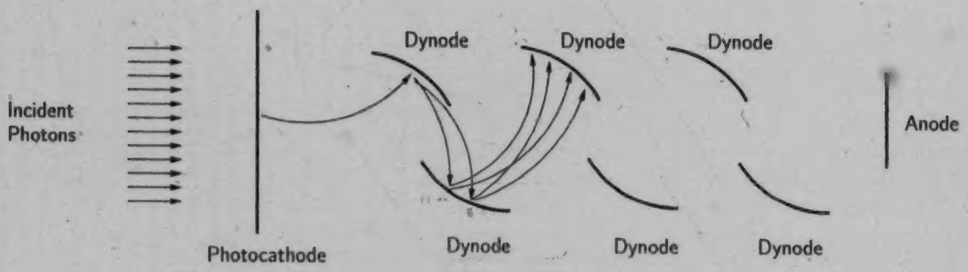
Incident
Photons
Photocathode
Dynode
Dynode
Dynode
Dynode
Dynode
Dynode
Anode

Figure 3.4. Schematic diagram of a PMT.

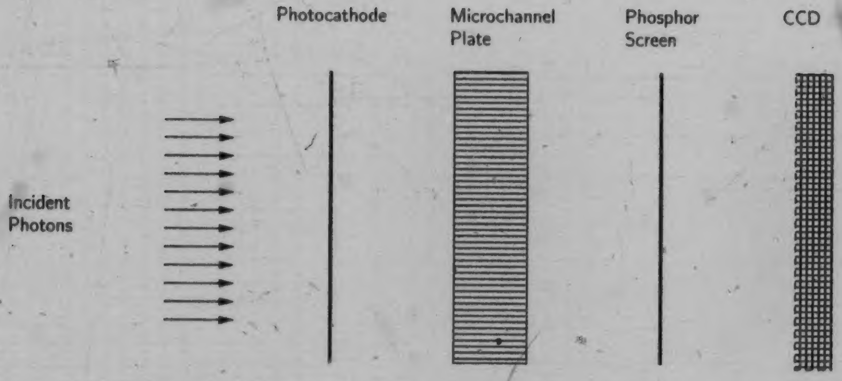
Photocathode
Microchannel Plate
Phosphor Screen
CCD
Incident
Photons

Figure 3.5. Schematic diagram of an intensified CCD (ICCD) device.

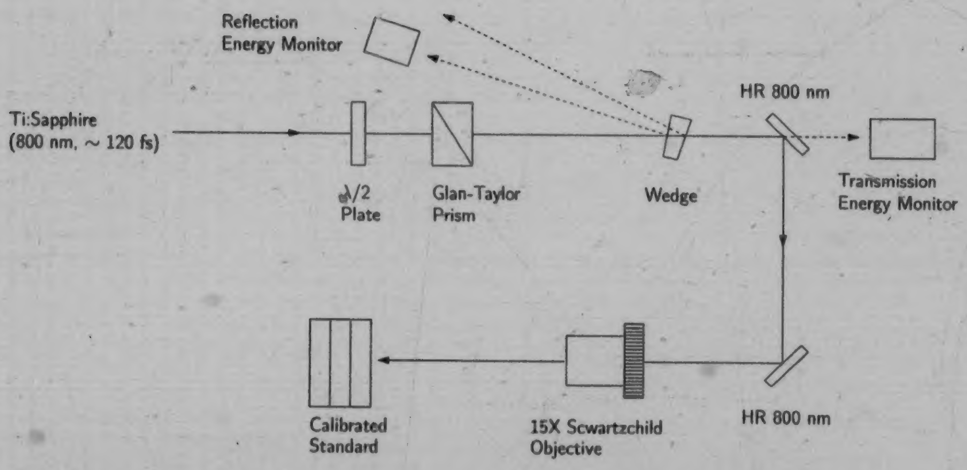
Reflection Energy Monitor
Ti:Sapphire (800 nm, ~ 120 fs)
λ/2 Plate
Glan-Taylor Prism
Wedge
HR 800 nm
Transmission Energy Monitor
Calibrated Standard
15X Scwartzchild Objective
HR 800 nm

Figure 3.6. *Schematic diagram of the energy monitor setups for the experimental setups used in this thesis. A reflection energy monitor (top left) uses a wedge or window to measure a fraction of the beam. A transmission energy monitor (top right) measures leakage light through a mirror.*

Radiometric Response is the number of counts recorded per Photon emitted from the LIBS plasma. Radiometric calibration is required to remove the characteristics of the detection system from LIBS data. Three methods have been used to calibrate radiometric responsivity LIBS systems, and are discussed in detail in Sec. 3.4.4.

3.4.1 Energy Calibrations

A key LIBS parameter is is the energy delivered to the target. The energy coupled to the target has been shown to be an extremely important parameter for the LIBS plasma emission [65, 94]. Online monitoring of the pulse energy delivered to the target is a simple diagnostic to implement.

During the work in this thesis, an online energy monitor was used to control and monitor energy being delivered to the target. A schematic view of the two types of energy monitor setups used in this thesis is given in Fig. 3.6. The first type is a 'reflection energy monitor', in which a wedge is used to reflect a small portion of the beam to a photodiode or calorimeter. The second type is a 'transmission energy monitor', in which leakage light through a dielectric mirror can be used in the same manner. So long as the laser intensity is low, such that the wedge or dielectric mirror is not perturbed, the reflected/transmitted energy will be linear with energy delivered to the target.

In the following discussion, the term 'split point' is used to denote the point in the laser path where the calibration beam is split from the beam which will ablate the target. The term 'upstream' refers to points along the optical path closer to the laser than the current point of interest, and the term 'downstream' refers to points closer to the target. Referring to Fig. 3.6, the split point for the reflection energy monitoring case is the wedge; for the transmission energy monitoring case it is the first dielectric mirror (HR 800 nm). In an energy monitoring setup of this kind the energy control mechanism (the half-wave plate and prism in Fig. 3.6) should be upstream of the split point.

The ideal case is that any limiting apertures along the laser path are upstream of the split point so that no change outside the setup affects the energy calibration. This situation can be achieved if one is using a lens with a diameter greater than the laser diameter to focus the laser light. However, if a microscope objective or other small diameter lenses are used this may not be possible. In such cases it is then possible that the amount of light delivered to the target will be affected by small variations in the alignment of the laser beam, and additional care must be taken.

Another potential source of difficulty is the laser light polarisation. Some of the dielectric mirrors used during the course of this thesis reflect S and P polarisations with different efficiencies. As a result, if these dielectric mirrors are downstream of the split point, a rotation in polarisation can affect the energy calibration. For example, if the Glan-Taylor prism shown in Fig. 3.6 were rotated, the energy delivered to the target would change. However, the relative fraction transmitted through the dielectric mirrors downstream of the split point will vary sinusoidally with the prism angle. As a result, the energy calibration will be affected. A factor of 5 difference in energy calibrations for S and P polarised light has been observed for the case where a 45° dielectric mirror is the split point. However, this represents an extreme case. Typical day to day variations were in the range of 15%.

To calibrate the energy at the target, a calibrated calorimeter or other energy measurement system should be placed at the target location. The energy delivered to the target can then be compared directly to the energy monitor signal. An example of this kind of calibration measurement is presented in Fig. 3.7. This particular case used the transmitting configuration, with a photodiode as energy monitor and calibrated calorimeter as standard. In this data set, the calibration factor was 112.8 ± 1.3 μJ/V, assuming the energy calibration of the calorimeter is perfect.

The calorimeters used during the course of this thesis were either calibrated against the lab standard calorimeter (Gentec ED-200), or in rare cases was the lab standard. The lab standard is calibrated by the manufacturer against a NIST calibrated standard, and has an accuracy quoted at 5%. A

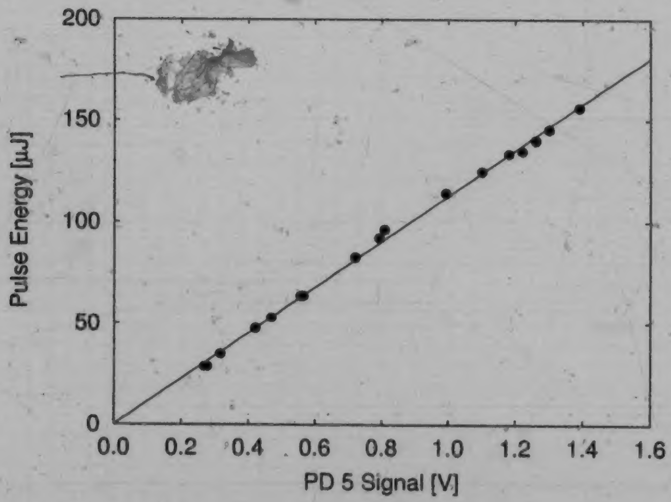

Figure 3.7. Energy calibration example for a transmitting energy monitor configuration. In this data set, the calibration factor was 112.8 ± 1.3 μJ/V.

number of different calorimeters were used during the course of this thesis, and it is therefore expected that any error in our in house cross calibration for each calorimeter would be averaged out as a result. Systematic error in our in house cross calibrated calorimeters is ruled out by the occasional use of the lab standard during energy calibration experiments.

Problems which can occur in the calibration procedure include nonlinear behaviour or a non-zero intercept for the best fit line. Nonlinear behaviour indicates that one of the detection systems being used is saturating and one may conclude that the linear range of the energy monitor has been exceeded. In the work performed for this thesis, it was common practice to use a dedicated attenuation filter which would keep the energy monitor photodiode in the linear range for the energies of interest. A more serious difficulty with the experiment is a non-zero intercept, indicated by a value outside the error bounds obtained for the best fit line. Such errors may indicate background light, stray laser light, an oscilloscope triggering error, or noise spikes in the energy monitoring system.

The energy calibration provides a monitor for the overall performance in time of the LIBS system, including features such as beam alignment, laser performance, cleanliness and damage to optics, and the position of nonlinear elements. An example of this sort of data is presented in Fig. 3.8. The value of the calibration as a function of time can provide feedback as to the performance of the system such as incremental damage to refractive objectives, which would show up as a slow decrease in the calibration factor for the energy monitor. A sharp change in the calibration factor is an indicator that the alignment of the system is incorrect, that sudden damage to the optics has occurred, or that the energy monitor or calibration standard has failed in some fashion. If the slope of a best fit line to data such as that presented in Fig. 3.8 is zero, it indicates that the experimental setup and alignment procedures are giving reproducible results.

It is possible to analyse the distribution of calibration factors obtained during the various calibration experiments to obtain an experimental precision which can be factored into estimates of the absolute uncertainty in the laser pulse energy delivered to the target in a LIBS system. Since the experiments performed in this thesis occur over many hours, it is expected that the energy calibration will drift somewhat during the course of the experiments due to variations in the laser alignment. Energy calibrations were usually performed at the start of experimental runs, but have also been taken during and at the end of experimental runs.

The energy calibrations obtained can therefore be viewed as a sampling of the alignments achieved using a particular setup. An analysis of the distribution of these energy calibration results therefore characterises the experimental setup in a manner that captures some of the experimental uncertainties. This analysis has been performed for the data set presented in Fig. 3.8, and is presented in Fig. 3.9. The various calibrations for the experimental setup has been fit with a Gaussian distribution. In this case the energy monitor calibration for this period of time is 104.7 ± 7.3 μJ/V. The error in this value should be added in quadrature to the accuracy of the lab standard to estimate the absolute accuracy of the energy monitoring system.

3.4.2 Temporal Calibrations

One difference between μLIBS and traditional LIBS is the short delay times required as energy is reduced below 100 μJ. In order to optimise the performance of LIBS generally, good control of the gate delay is required. However, in the case of μLIBS, this becomes much more difficult because the optimum delay times can be in the range of a ~ 10 ns or less. A sample setup for temporal calibrations is given in Fig. 3.10. In this case, a barium sulphate coated aluminum plate is used to scatter attenuated laser light. The scattered light is collected and imaged 1:1 by the off-axis parabolic mirrors. In general, it is necessary to strongly filter the laser light before it reaches the ICCD to prevent saturation.

Two temporal calibration methods were developed during the course of the thesis work. The first approach can be used for gateable systems, where the minimum reliable gate width and gate delay is such that the gate can

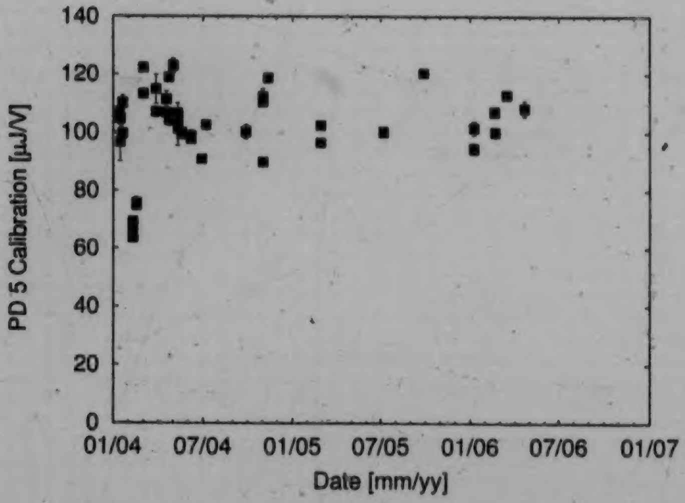

Figure 3.8. Calibration factor for an energy monitor for one experimental setup over the course of ~ 2.5 years.

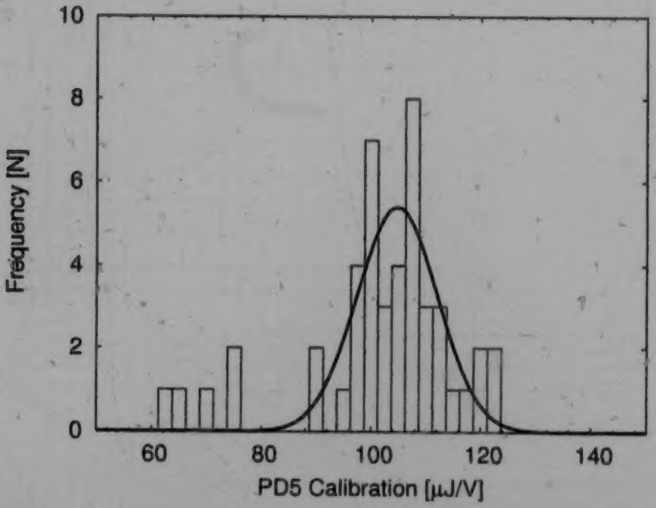

Figure 3.9. Derivation of calibration factor for the PD5 energy monitor. The data set is a histogram of the various calibration factors presented in Fig. 3.8, and the solid line is a Gaussian fit to the distribution. The calibration for this energy monitor during the period in question is 104.7 ± 7.3 µJ/V.

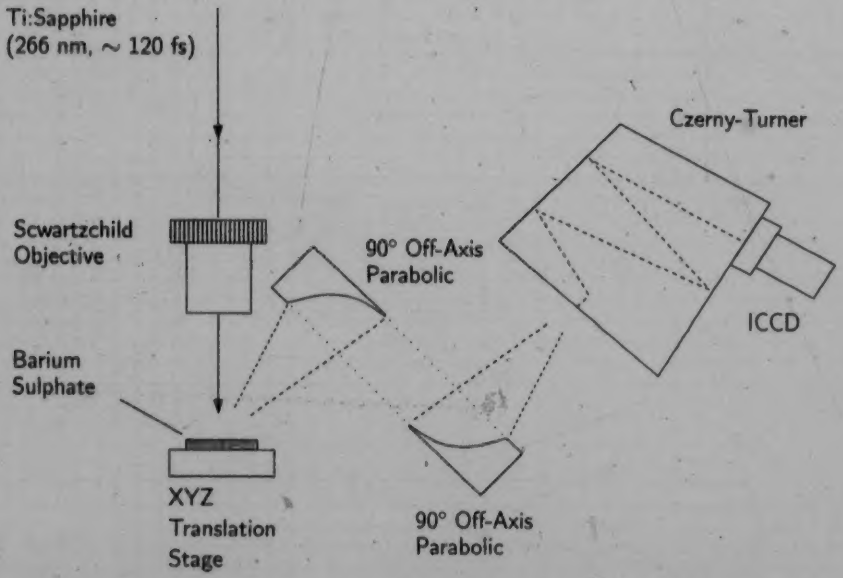

Figure 3.10. *Schematic diagram of one of the temporal calibration experiments performed in this thesis.*

be opened and closed, giving a short sampling cycle before the laser pulse arrives at the target. Gate delay can be increased, sweeping the gate through the laser's arrival. An example of data generated using this approach is given in Fig. 3.11. In this case, an ICCD and Nd:YAG laser were synchronised with a custom timing circuit that allowed the ICCD to be triggered well before the laser arrival. With this sort of data set the observed intensity can be fit with a Gaussian curve and the zero delay time (peak laser intensity) extracted.

The second case can be used for triggerable systems, and in situations where the timing only allows the gate to be opened before the laser pulse arrives at the target. This case applies to systems such as an Ocean Optics compact CCD (HR2000), which accepts an external trigger but does not have a fully controllable optical gate. For this method the gate is opened before the laser pulse, and then the gate delay is increased until the laser pulse is not observed. An example of the data generated from this approach is given in Fig. 3.12. In this case, an ICCD and Ti:Sapphire laser were used.

One final point of interest about this technique is that it can sometimes be used to measure the pulse width of the laser. In the case of Fig. 3.11 it is possible to estimate the laser pulse width based on the best fit and the known width of the optical gate. In this case, the gate pulse was 5 ns, and the

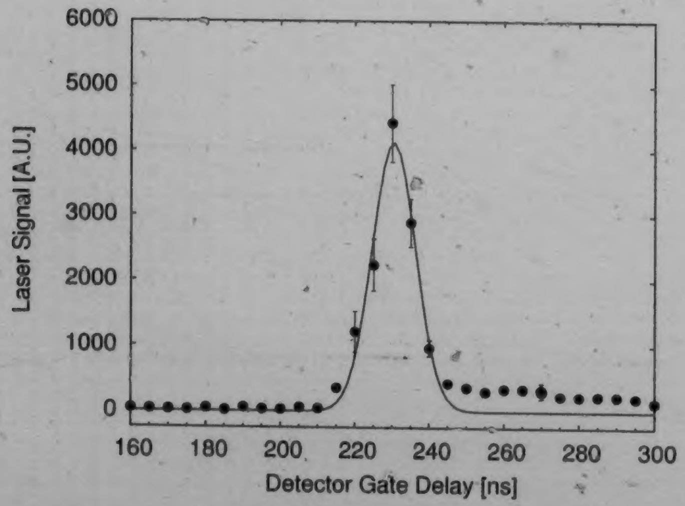

Figure 3.11. Temporal calibration of ICCD delay in the case where the gate can be opened and closed in advance of the laser arrival. In this case a gate width of 5 ns is used to measure the arrival of a Nd:YAG laser pulse at the target location.

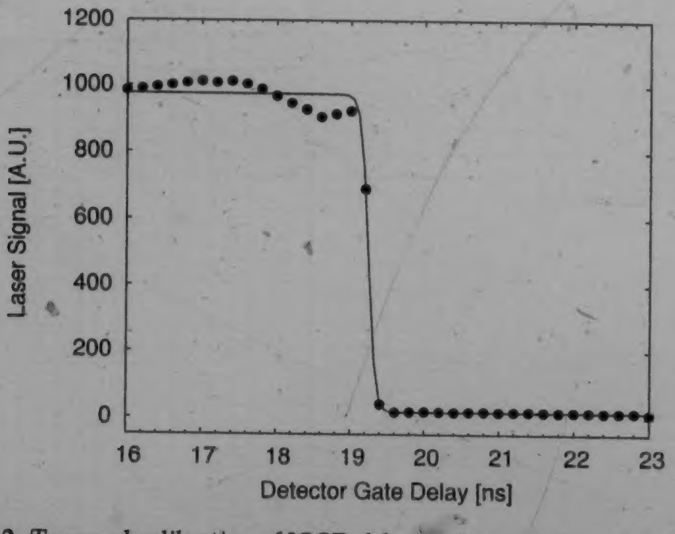

Figure 3.12. Temporal calibration of ICCD delay in the case where the gate can only be opened before the arrival of the laser pulse. In this case a gate width of 1 μs was used to measure the arrival of a Ti:Sapphire laser pulse at the target location.

estimated laser pulse width was 9 ns (FWHM). However, in the case of Fig. 3.12, the laser pulse width is far shorter than the precision of the delay time. The slight deviation from a vertical line in the transition region is not related to the laser pulse width, but rather the timing jitter inherent in the electronics used to synchronise the ICCD and laser, and the non-zero rise time of the ICCD gate.

3.4.3 Wavelength Calibrations

Making good use of LIBS spectral data requires an accurate wavelength calibration. For the work presented in this thesis, the most common wavelength calibration standard was a Hg lamp (Oriel 6035). While this particular lamp has not been calibrated, the class of pencil lamps has been characterised by a group at NIST [112]. Other sources include the various lasers used as LIBS excitation sources, HeNe and other low power lasers, Eu lines from fluorescent room lights, and the LIBS plasma itself in cases where the emitting species are known.

Sample data for a calibration experiment of a 600 line mm^{-1} grating at a central wavelength position of 359 nm using the Hg lamp are presented in Fig. 3.13. In this case 5 Hg lines were visible in a single acquisition. Each line was fit with a Gaussian profile to determine the line position and plotted against the wavelengths reported by Sansonetti et al. [112]. The solid line is a linear fit to the data set, which yields a fit of $\lambda\left(N_{channel}\right) = (271.95 \pm 0.17)\,nm + (166.56 \pm 0.27pm) \cdot N_{channel}$. The wavelength calibration procedure can be repeated for different grating positions, and the offset and channel width parameters analysed as a function of grating position.

3.4.4 Radiometric Calibrations

LIBS is fundamentally an optical observation and, as such, LIBS data can and should be reported in radiometric units. The applicable terminology for the quantities observed in LIBS measurements is brightness [W Sr^{-1} cm^{-2}], or intensity [W Sr^{-1}]. LIBS data is strongly dependent on the starting time of the observation and the total integration time. Thus, it may be more useful to report the total energy observed, rather than the power, while noting the gate delay and integration width. Spectrally integrated line intensities and equivalent noise power can then be reported in units of integrated brightness [J Sr^{-1} cm^{-2}] or integrated intensity [J Sr^{-1}]. The radiometric approach can be adapted to spectral measurements by correcting for the detector's reciprocal linear dispersion, reporting units in terms of spectral brightness [W Sr^{-1} cm^{-2} nm^{-1}] or spectral intensity [W Sr^{-1} nm^{-1}].

To present LIBS data in these units, it is necessary to have a good understanding of the optical properties of the experimental system. Every com-

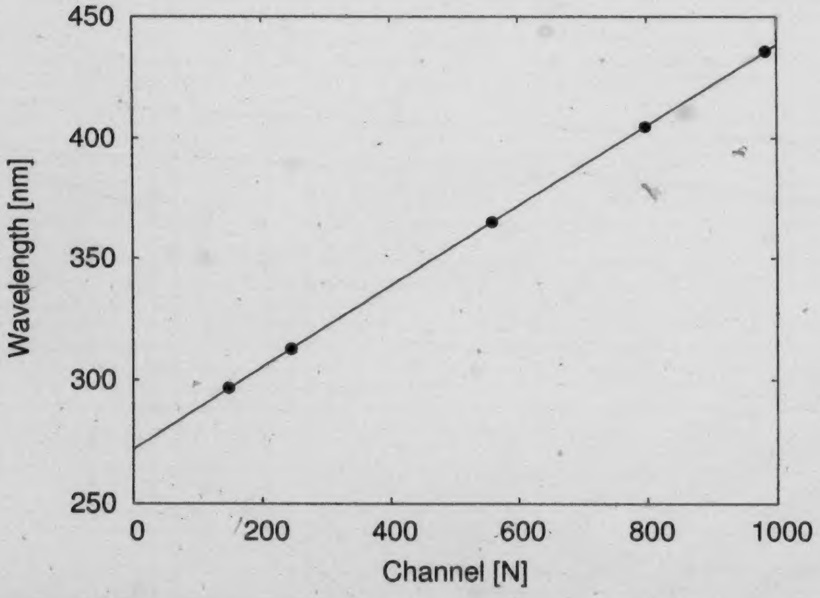

Figure 3.13. *Wavelength calibration for a 600 line mm^{-1} grating at a central wavelength of 359 nm. The solid line is a linear best fit to the data set, giving a calibration equation of* $\lambda\left(N_{channel}\right) = (271.95 \pm 0.17)\,nm + (166.56 \pm 0.27pm) \cdot N_{channel}$

ponent of a LIBS system possesses properties that vary with optical wavelength. However, once this characterisation has been made, it is possible to report data that reflect the behaviour of the LIBS plasma itself, rather than a combination of the LIBS plasma and experimental equipment which is more common in the literature. With data reflecting only the behaviour of the LIBS plasma, it will be possible to make detailed, absolute comparisons between different experimental groups and with theory. Fundamental understanding of the LIBS process will improve, and the true limits of the technique will be better understood.

This section describes the procedures used to calibrate detector system responsivity. To report units in terms of spectral brightness, further information about the collection optics used in a particular experiment is required. The radiometric calibration sources used were broadband radiometric sources and line emission sources. The broadband sources are a calibrated tungsten lamp (Eppley Laboratories) and a combination deuterium/halogen lamp (Ocean Optics DH2000). The line emission sources are a Hg lamp (Oriel 6035) and a variety of laser sources. The calibration procedures used with the two types of calibration sources are described below.

3.4.4.1 Broadband Responsivity Calibrations

The tungsten lamp is provided with a calibration from the manufacturer. A best fit of the blackbody equation to the calibration data is given in Fig. 3.14. The deuterium/halogen combination lamp is also calibrated by the manufacturer. Unlike the tungsten lamp, in this calibration the units were given in terms of spectral irradiance [W cm^{-2} nm^{-1}] for the calibration setup used at Ocean Optics, rather than spectral brightness. As a result, this calibration data depends on the solid angle of the experimental setup used by Ocean Optics. Despite several conversations with company personnel, including the person who performs the calibration, I was unable to ascertain what was done to arrive at the numbers in the provided calibration. Fortunately, the deuterium source and the tungsten lamp both radiate in the region between 300 nm and to 400 nm, allowing me to use the deuterium source as a relative source to extend calibration data down to about 200 nm.

An example of a setup used to calibrate the spectrometer systems with broadband sources is given in Fig. 3.15. During calibration operations, the tungsten lamp was operated with the filament of the lamp placed with its normal pointed at the spectrometer's entrance aperture at a distance of several meters. This distance ensures that the 60 mm^2 filament is well within the spectrometer's f/# allowing angular effects due to the size of the spectrometer's entrance slit to be neglected. Under these conditions, the filament can be converted to an equivalent point source, once the brightness in Fig. 3.14 has been corrected for filament area. The solid angle observed is defined by the area of, and distance to, the entrance slit. Once combined with the spectral dispersion of the spectrometer and the length of time observed, the number of photons delivered per spectrometer channel can be calculated.

It is then a simple matter to derive the absolute response of the instrument in terms of counts per photon. An example of this sort of data is given in Fig. 3.16 for an echelle spectrometer (Andor Mechelle 5000) using the tungsten lamp as a calibration source, and the deuterium/halogen lamp as a relative source to extend the calibration below 300 nm. This information is sufficient to report experimental data in terms of photons nm^{-1}, or J nm^{-1}, observed at the spectrometer's entrance slit. The remaining conversion to spectral brightness or spectral intensity is discussed in Sec. 3.4.4.4.

3.4.4.2 Line Emission Responsivity Calibrations

Different sources were used as line emission calibration sources during the course of this thesis work, including a Hg lamp, Nd:YAG laser, N$_2$ laser and a Ti:Sapphire laser. In practice, line emission techniques were used to calibrate

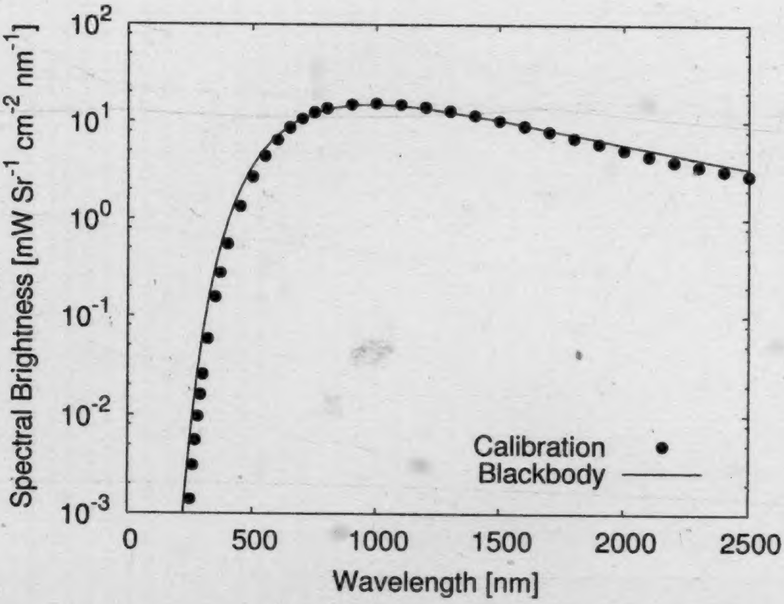

Figure 3.14. *Calibrated tungsten blackbody used as a broadband calibration source in these experiments. The black line is a best fit of the blackbody emission curve to the calibration data, giving a temperature of 2930 ± 20 K.*

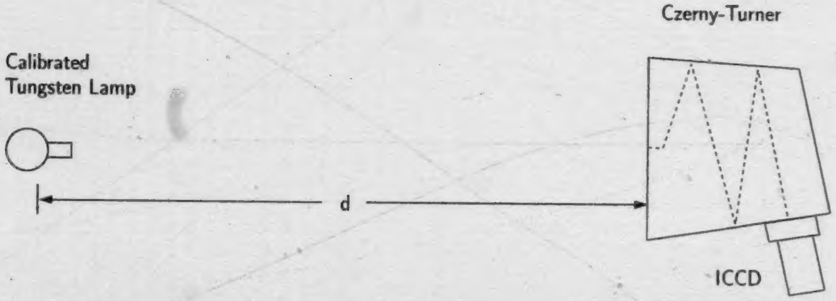
Czerny-Turner
Calibrated
Tungsten Lamp
d
ICCD

Figure 3.15. *Schematic of a broadband calibration setup. In this case, the calibrated tungsten lamp (Eppley Laboratories) illuminates the spectrometer's entrance slit.*

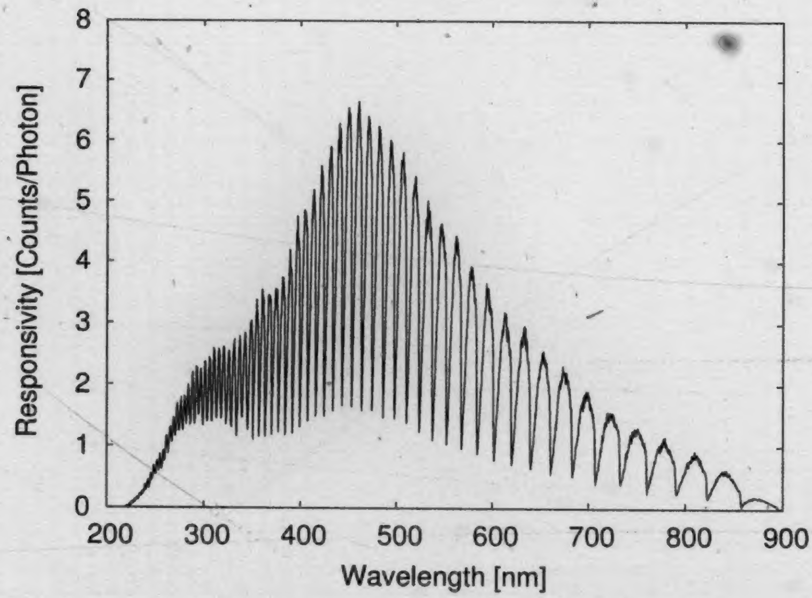

Figure 3.16. Responsivity of the Andor Mechelle at maximum gain.

the detection devices, rather than the combination of the spectrometer and ICCD as in the case of the broadband sources.

The class of Hg lamps has been characterised by a group at NIST [113], but the specific lamp used in the present work has not been calibrated. This lamp has known irradiances for several wavelengths at a given distance from the lamp. The experimental setup for calibrations using the lamp is similar to that given in Fig. 3.15. Manufacturer curves for the spectrometer transmission and photocathode quantum efficiency were used to calculate the number of photoelectrons presented to the ICCD MCP. Once this was done, the total number of counts for each Hg line observed was integrated, and the responsivity of the ICCD was calculated.

An alternative line emission technique is to make use of a lambertian emitter to scatter laser radiation to a spectrometer's entrance slit or PMT's photocathode. A sample setup is given in Fig. 3.17. Light scattered by such a lambertian source has the following emission pattern [108]

$$E = \frac{E_{input}}{\pi} cos\phi \tag{3.4}$$

In some cases, the barium sulphate plate was rotated to present different

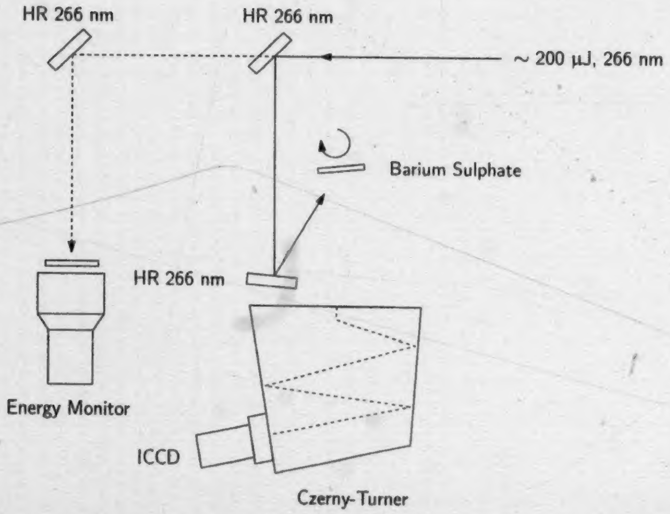
HR 266 nm
HR 266 nm
~ 200 μJ, 266 nm
Barium Sulphate
HR 266 nm
Energy Monitor
ICCD
Czerny-Turner

Figure 3.17. Schematic of an angular calibration setup. The energy delivered to the barium sulphate plate was monitored in transmission mode with a photodiode. The barium sulphate plate was rotated to present different emission angles to the entrance slit of the spectrometer.

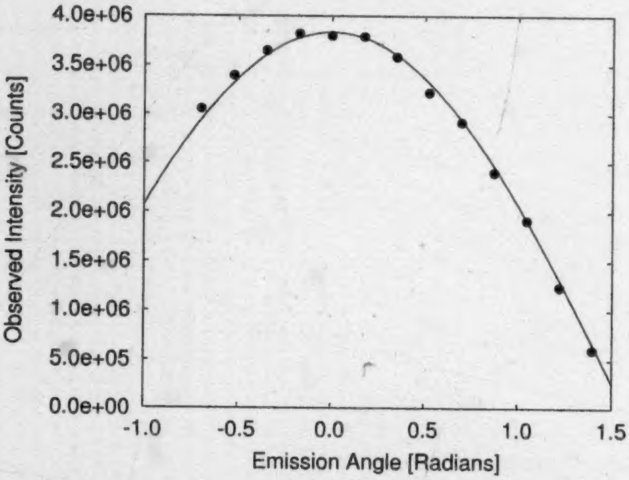

Figure 3.18. Sample data set from the angular calibration technique. In this case, the ICCD gain was found to be 0.29 ± 0.03 counts/photoelectron at minimum gain.

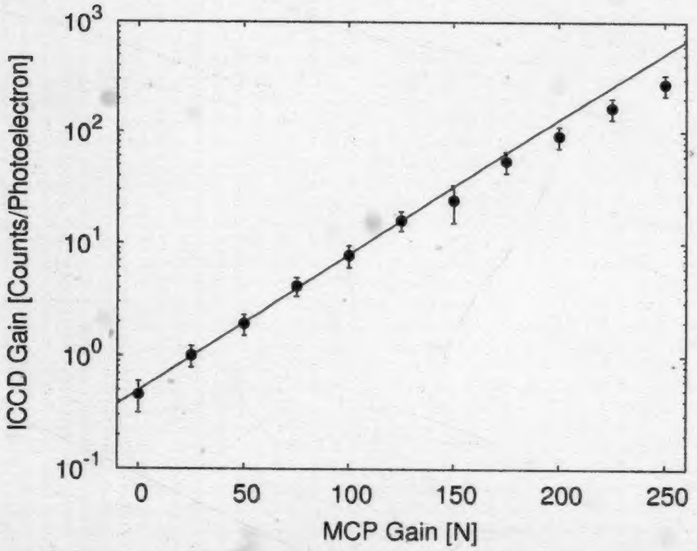

Figure 3.19. Combined calibration data for one of the ICCDs used in this thesis. The solid line is an exponential fit to the data points with a MCP gain of ≤ 125. Above this value, a slight saturation in detector gain is observed.

emission angles to the spectrometer's entrance slit. The scattered light varies in intensity with emission angle. Starting with a lambertian, it is possible to show that the number of counts expected as a function of angle is given by

$$N_{counts} = \frac{N_\gamma \Omega_{slit} T(\lambda)\, \eta(\lambda)\, G}{\pi} cos\phi \tag{3.5}$$

where N_γ is the number of photons scattered from the barium sulphate plate, Ω_{slit} is the solid angle observed by the spectrometer's entrance slit, $T(\lambda)$ is the spectrometer transmission, $\eta(\lambda)$ is the photocathode quantum efficiency, and G is the gain of the ICCD. In this case, everything is known except G, so it is a simple matter to fit Eq. 3.5 to the data set. An example of this analysis is given in Fig. 3.18.

3.4.4.3 Responsivity Calibration Accuracy

Over the course of the thesis work, the radiometric calibrations were performed many times. To assess the overall accuracy of the radiometric calibrations, the results for one of the ICCDs used are presented in Fig. 3.19.

There are three independent calibration sources used for the results presented in Fig. 3.19: the tungsten lamp, the Hg lamp and the angular calibration method. The data is dominated by the Hg lamp and angular calibration methods, as the tungsten lamp only enters into the above plot in the data point at a gain of 150. The RSD for this data point which combines calibration data from all three methods is $\sim$ 36%.

While the absolute accuracy of the tungsten lamp and Hg lamp are not known, the angular calibration method relies on the accuracy of the energy calibration of the energy delivered to the barium sulphate plate. The accuracy of this approach must include the error in the energy calibration factor, as described in Sec. 3.4.1. The lab standard calorimeter was recently recalibrated by the manufacturer, and exhibited less than 1% drift from the original calibration. It is expected that the angular calibration method is the most reliable of the methods used to calibrate the ICCD. However, if only the values obtained with the angular calibration method are used, the RSD value does not improve. The most data points for a single gain are 6 at a MCP gain of 0, and the RSD is $\sim$ 35%. Based on this analysis, the absolute photon values quoted in this thesis have an estimated accuracy of $\sim$ 36%. Errors involved in conversion to radiometric quantities are discussed in the next section.

3.4.4.4 Conversion to Radiometric Units

The calibration process described above yields the absolute number of photons detected, but not the number emitted by the LIBS plasma. LIBS plasmas are usually observed with slits smaller than size of the plasma. To correct for this factor, both the size of the plasma image at the entrance slit and the magnification of the optical imaging system which conveys plasma emission to the entrance slit are required. The limiting `f/#` of the setup must also be known in order to correct for the full angular emission of the plasma. Once these factors are well understood, it is possible to convert from counts to plasma brightness, and report experimental data in terms of $\mathrm{J\ Sr^{-1}\ nm^{-1}}$.

A measurement of the plasma image size for the setup given in Fig. 3.10 is presented in Fig. 3.20. This data can be used to measure the plasma image size at the entrance slit of the spectrometer, provided that the slit width is removed from the data, and that the relationship between the lens position and image position is well understood or calibrated. In addition, the magnification of the plasma imaging optics must be known. The signal presented in Fig. 3.20 is in fact a convolution of the slit and the plasma image, and therefore the slit width can be subtracted [114]. The focusing optic is a 90° off-axis parabolic mirror, moved along a plane parallel to the slit plane. In this case the position corresponds directly to the plasma image position. However, in a setup such as given in Fig. 6.1 the angle of last mirror must be carefully related to perpendicular distance at the entrance slit.

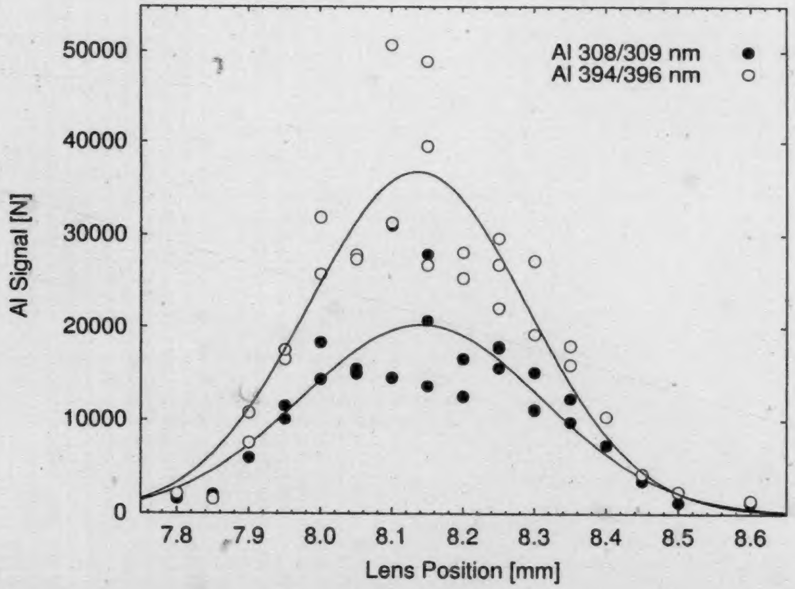

Figure 3.20. *Measurement of plasma image size at the spectrometer's entrance slit for a setup similar to that in Fig. 3.10. The solid lines are a best fit of Gaussian functions to the unresolved Al doublets observed here. This data must be deconvolved with the slit width to arrive at the actual image size.*

An additional complication for this kind of analysis is the nonuniform distribution of emitting species in the ablation plume [115–117]. However, plasma size in μLIBS is much smaller than in traditional LIBS. As a result, these effects will become less important for μLIBS, though they should not be ignored.

The values for the width parameters in the fits presented in Fig. 3.20 have an error of ~ 20%. Error in the reciprocal linear dispersion used to convert to spectral quantities are expected to be quite low, as seen in Fig. 3.13. As a result, this is not expected to be a significant source of error. Additional errors may exist in the magnification measurements, but these are not expected to be large. If they remain below 10%, the contribution will be low. Taking the plasma image area error as ~ 20%, combined with the absolute error in instrumental calibration of ~ 36%, it is estimated that the total absolute error in radiometric values quoted in this thesis is ~ 41%.

3.5 Optimisation Methodologies

In this section a few basic optimisation procedures used in LIBS are described:

Focal Position is the distance between the last laser focusing optic and the target sample. Laser spot size and intensity, crater diameter and LIBS emission signals will all vary with this distance. The procedure used to optimise focal position is described in Sec. 3.5.1.

Plasma Alignment describes the alignment of the plasma imaging optics which relay LIBS emission to the entrance slit. The techniques used to optimise alignment and thus coupling of LIBS emission to the spectrometer are described in Sec. 3.5.2.

Detector Conditions have a large impact on the overall performance of a LIBS system. This area has been the subject of much study during the course of this thesis, and only a brief introduction is presented here. A more detailed study of optimisation procedures is presented in Sec. 5.3. A basic technique for optimisation of the gate delay of a ICCD system is presented in Sec. 3.5.3.

3.5.1 Focal Position

Since the energies used in μLIBS are much smaller than typical LIBS experiments, attaining the breakdown threshold for a given sample requires a tighter focal spot. As a result, the depth of field will be smaller, and greater care must be taken to optimise the distance between the focusing lens and the sample surface. A related quantity is the size of the ablation spot on the sample surface as a function of the distance between lens and sample.

A set of experimental focal optimisation experiments are presented in Fig. 3.21 for 20 μJ pulses on aluminum targets. Pulse widths of 10 ns, 50 ps and 130 fs were used; the laser wavelength was 248 nm for the 10 ns and 50 ps data, 800 nm for the 130 fs data. Also plotted is the crater diameter. The solid lines are Gaussian fits for the emission signal, and the Gaussian beam propagation equation for the crater diameters as given in Eq. 3.6. In this case the quantity ω_0 and z_0 will represent the minimum crater size and location, respectively. However, the quantity M^2 will represent a combination of the beam propagation ratio and the material response, rather than just the beam propagation ratio.

$$\omega(z) = \omega_0 \sqrt{1 + \left(\frac{M^2 \lambda (z - z_0)}{\pi \omega_0^2} \right)^2} \tag{3.6}$$

It is clear from Fig. 3.21 that the maximum LIBS signal is closely associated with the minimum crater diameter. This agreement is quite convenient experimentally, allowing either to be used to ensure that the optimum sampling conditions for μLIBS have been achieved.

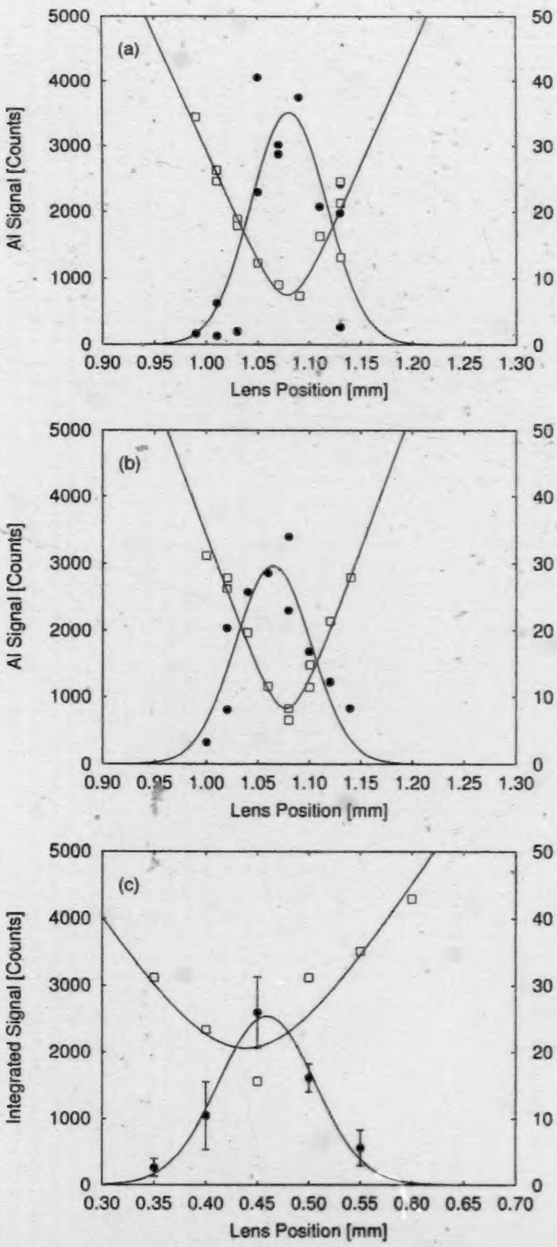

Figure 3.21. *Focal runs (closed circles) and crater diameters (open squares) for single ~ 20 µJ pulses with (a) 10 ns, (b) 50 ps, (c) 130 fs pulses. A 10X objective was used in all cases. Nanosecond and picosecond pulses are at 248 nm, and femtosecond pulses are at 800 nm.*

3.5.2 Alignment of Plasma Imaging Optics

The alignment of the plasma imaging optics was regularly checked by sweeping the image of the LIBS plasma across the entrance slit of the spectrometer. Sample experimental data from this type of experiment is presented in Fig. 3.20. The experimental data was fit with a Gaussian function, and the peak location is used.

In cases where more than one optic controls the position of the plasma image on the entrance slit of the spectrometer, this procedure was performed for each optic. During preliminary alignments, it was necessary to iterate this procedure. Once the system had been used for a while, it was determined that a single pass was sufficient, based on comparison of final optic positions with previous results. To monitor the stability of the experimental setup an approach similar to that presented in Fig. 3.8 could have been used, provided that experimental conditions were similar.

3.5.3 Detector Conditions

Detector parameters such as gate delay, gate width and gain are very important in determining the overall performance of a particular LIBS system. This area has been the subject of much study during the course of the thesis. As a brief introduction, a procedure for optimising gate delay will be presented here. In this case, a 750 μJ, 6 ns laser pulse at 266 nm was used on a piece of Al 2024 alloy, and the line of interest was the combined Al doublet at 394 nm and 396 nm. The experimental data is presented in Fig. 3.22.

The decay time of the Al emission was measured at $\sim$ 270 ns. In order to capture all of the emission, the gate width was set to 2 μs, which should be sufficient to capture the majority of the emission. Due to the high pulse energy the gain on the ICCD was set to the minimum available. Under these conditions, no significant detector noise is expected. The signal analysis technique defined in Sec. 3.6.2.7 was used to calculate SNR. A total of 5 shots at each delay were taken; the average and standard deviation are presented in Fig. 3.22.

In preliminary investigations of LIBS optimization techniques, it has been shown that the noise will fall in an approximately exponential manner to a minimum value given by the detector noise [118]. In many cases the atomic emission will also decay exponentially. A simple model for the time-resolved behaviour of SNR which combines these two behaviours is given in Eqn. 3.7.

$$SNR(t) = \frac{E_0 exp\left[-\frac{t}{\tau_{emission}}\right]}{N_0 exp\left[-\frac{t}{\tau_{noise}}\right] + N_{floor}} \qquad (3.7)$$

where E_0 and $\tau_{emission}$ are the strength and decay time of the line emis-

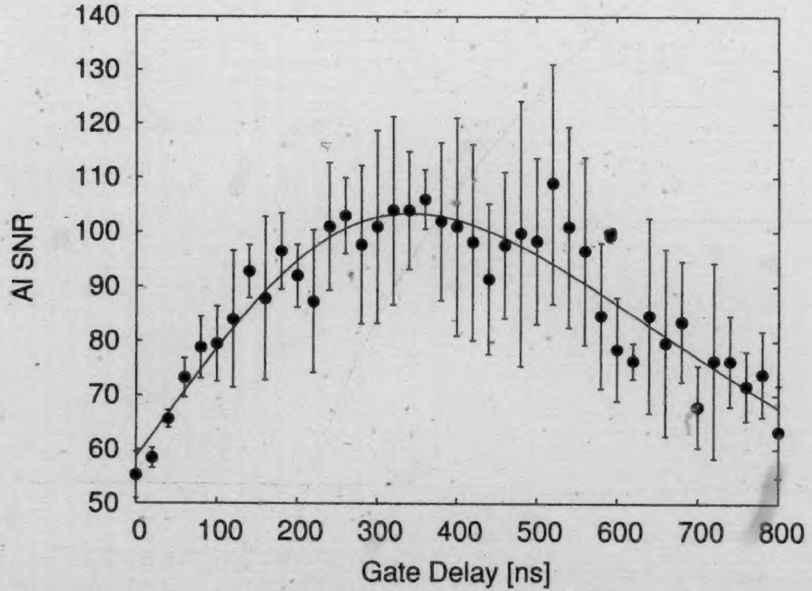

***Figure* 3.22.** *SNR of the Al doublet at 394 nm and 396 nm as a function of gate delay for 750 μJ, 6 ns pulses at 266 nm. Each data point is an average and standard deviation of 5 data points. The solid line is a best fit to Eqn. 3.7. In this case, the optimal gate delay is ∼ 350 ns.*

sion, N_0 and τ_{noise} are the strength and decay time of the noise, and N_{floor} is the detector noise floor. The model gives a reasonable fit to the experimental data presented in Fig. 5.4. Under these conditions, the optimum delay is ∼ 350 ns.

This kind of approach can be extended to gate delay, detector gain and other parameters that affect the SNR in a LIBS system. A more complete investigation of the various detector parameters is given in Sec. 5.3.

3.6 LIBS Signal Analysis

In this section, the signal analysis of LIBS data will be investigated using a model for line emission and ICCD noise sources. The signal analysis methods used in LIBS will be defined, and the effect of background removal techniques will be discussed. The noise sources relevant in the accurate assessment of emission line strength based upon a single spectral acquisition will be examined. A characterisation of ICCD noise sources will be carried out to allow the development of a suitable model of the various detector noise sources. The various signal analysis techniques will be tested against this model for accuracy, failure rate and processing time. A variety of emission line strengths and background noise levels will be used to investigate the full range of conditions which are found in LIBS data acquisition.

Techniques such as internal peak normalisation and multivariate analysis are specifically excluded from the following discussion. These techniques often improve the performance of LIBS, but are focused on dealing with the noise sources associated with the LIBS plasma across multiple emission lines from a single spectra and with noise between multiple LIBS spectra.

3.6.1 Description of Signals in LIBS Systems

For most detectors used in LIBS today, the signals generated are discrete both in wavelength and intensity. Such signals can be represented by a 2 by N matrix, where N is the number of channels in the detector. One column will represent channel number or wavelength, depending on the system and settings used; the other column represents the total integrated signal during the acquisition. Using the techniques described for wavelength calibration (Sec. 3.4.3) and radiometric calibration (Sec. 3.4.4) both columns can be converted to absolute units.

While 2D ICCD detectors are becoming common in LIBS, these detectors are typically binned over one dimension, and the resulting data will still fit the present formulation. In the case of an echelle spectrometer, which disperses the light spectrally in two dimensions, the situation is more complex. However, the observed pattern on the ICCD is usually converted to a spectrum by the manufacturer's software. In this case the system can be viewed as having a large number of virtual channels, and the proposed formulation would apply. A key exception would be a PMT, which integrates emission spatially and spectrally, but offers a time-resolved measurement.

For the following work, I will consider only discrete LIBS signals, which can be considered a 2 by N matrix, where N is the number of channels in the detector. In addition, detector specific effects such as dead channels or a variable response as a function of pixel are not considered here. In principle, it should be possible to categorise any LIBS reference by the signal analysis method used. However, it is not always clear how how the terms are intended, or what the exact methodology was.

3.6.2 LIBS Signal Analysis: Method Definitions

A number of different analysis techniques are used to reduce the spectral information obtained in a LIBS measurement to a single value (intensity or

SNR) per spectral line, including background removal and line strength estimation. This section defines the techniques used in the literature and in the thesis work. Each of the following methods has been implemented for the spectral analysis code given in Appendix A.2.1.

3.6.2.1 Background Correction

A few simple techniques are used to correct LIBS measurements for the effect of the background. Examples of three situations are given in Fig. 3.23. For a particular line of interest regions on either side are used to evaluate the background. In the case where the background is entirely devoid of other signals, or flat as a function of channel number, a simple average can be used to remove the background. In the case where the background contains a contribution from the continuum or a very strong line in the same region, it is sometimes possible to fit the line with a linear function. In cases where the contribution from a strong line which is very close, the background can sometimes be fit with a parabolic function.

Noise regions were often selected by inspection, especially in cases where the target was well known. In other cases, the standard deviation of each channel was calculated for $\sim$ 100 shots, and regions with flat minima in the standard deviation were used.

3.6.2.2 Peak Height

The *Peak Height* method is defined as:

$$Signal = I_{peak} \tag{3.8}$$

where I_{peak} is the background corrected height of the peak of interest, as shown in Fig 3.24.

3.6.2.3 Peak to Background

The *Peak-to-Background* method is defined as:

$$P/B = \frac{I_{peak}}{I_{background}} \tag{3.9}$$

where I_{peak} is the background corrected height of the spectral peak of interest and $I_{background}$ is the background light observed in the spectrum, both defined in Fig. 3.24. A variant of this technique uses an integration of the entire background in place of $I_{background}$ in an effort to normalise to the overall intensity of the LIBS plasma. However, this approach is very rare.

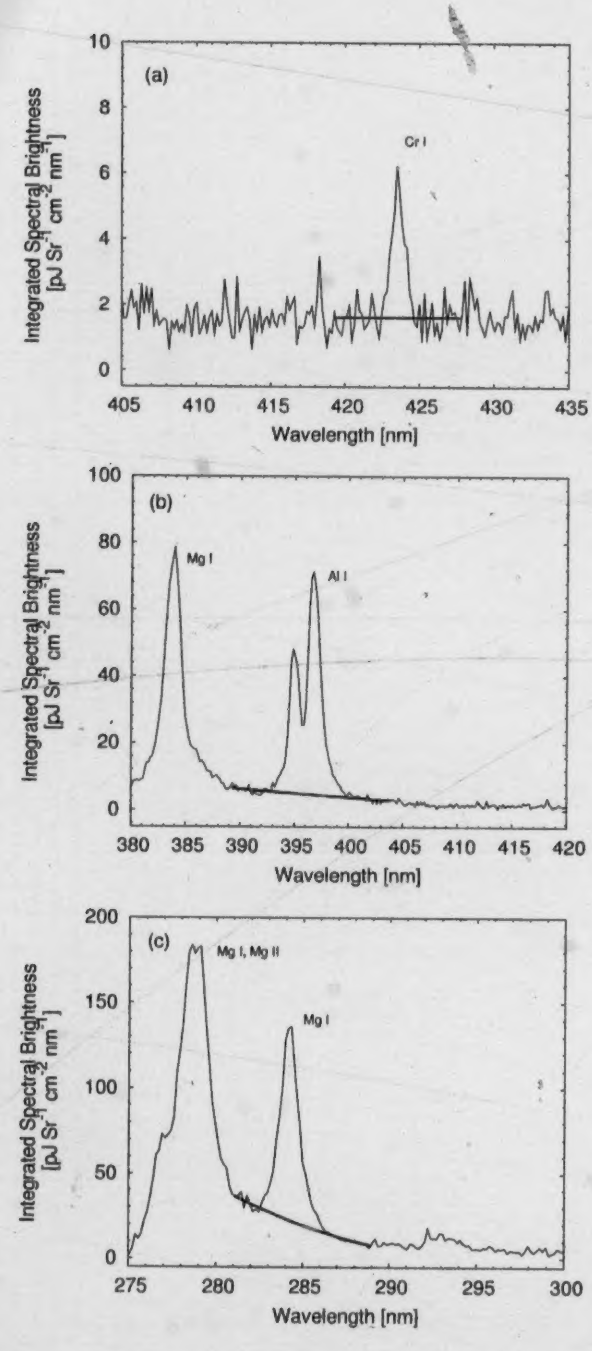

Figure 3.23. *Removal of (a) average, (b) linear and (c) parabolic backgrounds from LIBS spectra.*

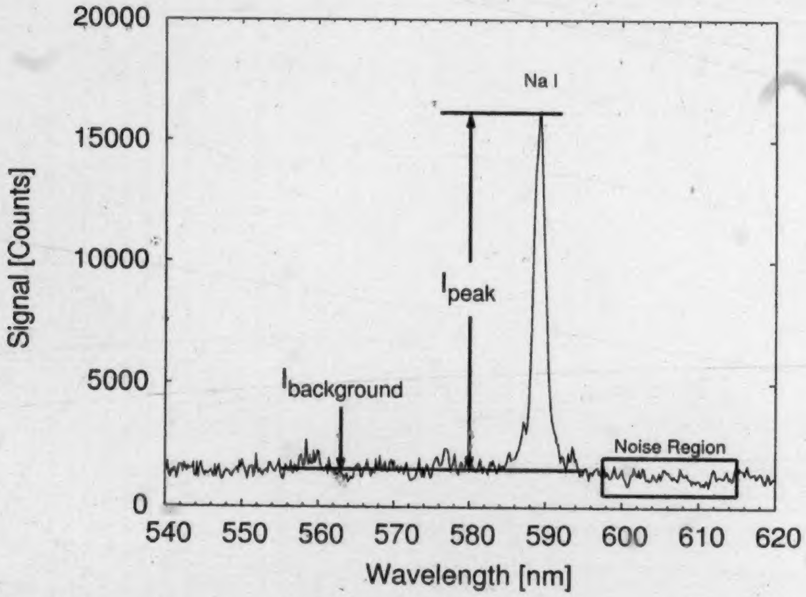

Figure 3.24. *Definitions for the single-channel signal analysis methods.* I_{peak} *is the background corrected height of the signal,* $I_{background}$ *is the strength of the background, and Noise Region is the area used to estimate the variation in the background.*

3.6.2.4 Peak Signal to Noise Ratio

The *Peak SNR* method is defined as:

$$SNR = \frac{I_{peak}}{\sigma_{background}} \tag{3.10}$$

where I_{peak} is the background-corrected strength of the line of interest in one channel, and $\sigma_{background}$ is the standard deviation of a spectrally quiet region away from the peak, once background correction has been performed.

3.6.2.5 Peak Area

The *Peak Area* method is defined as:

$$Signal = \sum I(\lambda) \tag{3.11}$$

where $I(\lambda)$ is the background corrected signal of interest. The integrated area is defined graphically in Fig. 3.25, with a width of $N_{channels}$. The chal-

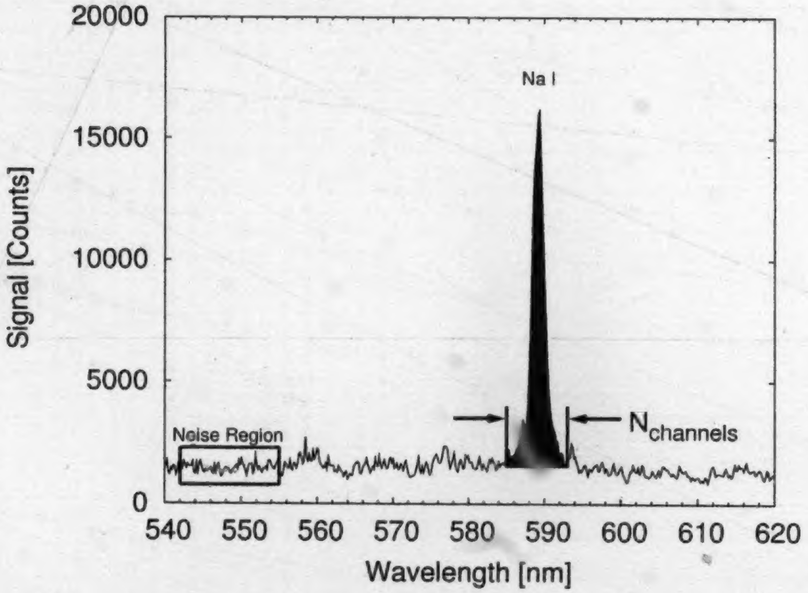

Figure 3.25. *Definitions for the multiple-channel signal analysis methods. The shaded area is* $\sum I(\lambda)$, $N_{channels}$ *is the integrated width which is also used to scale the noise, and Noise Region is the area used to estimate the variation in the background.*

lenge of this approach is to define an appropriate $N_{channels}$ for the peak summation. If the limits are too small, the results don't accurately reflect the strength of the signal. If the limits are too large, a little bit more noise is integrated into the signal. However, this is generally not a significant problem for this method. In practice, I considered the possibility of losing signal to be more serious, and defined the integration regions using a strong signal for the line of interest. Care was taken to ensure that contributions from other lines were avoided.

3.6.2.6 Area to Background

The *Area-to-Background* method is defined as:

$$A/B = \frac{\sum I(\lambda)}{I_{background}} \tag{3.12}$$

where $I(\lambda)$ is the background corrected signal of interest defined in Fig. 3.25, and $I_{background}$ is the background intensity, as defined in Fig. 3.24.

3.6.2.7 Area Signal to Noise Ratio

The *Area SNR* method is defined as:

$$SNR = \frac{\sum I(\lambda)}{\sigma_{background}\sqrt{N_{channels}}} \tag{3.13}$$

where $I(\lambda)$ is the background corrected signal of interest, $\sigma_{background}$ is the standard deviation of the spectrally quiet region away from the peak, and $N_{channels}$ is the number of channels over which the signal is integrated.

3.6.2.8 Gaussian Area

All of the previous methods are summation methods where the integration is carried out by adding the contributions from a number of discrete channels. An alternative approach is to use line fitting techniques, where a particular line profile is fit to the line region. For the work in this thesis, only gaussian profiles have been used. The *Gaussian* method is defined as:

$$SNR = \frac{\int I(\lambda)\, d\lambda}{\sigma_{background}\sqrt{N_{channels}}} = \frac{I_{peak}\sigma_{peak}\sqrt{2\pi}}{\sigma_{background}\sqrt{N_{channels}}} \tag{3.14}$$

where I_{peak}, $\sigma_{background}$ and $N_{channels}$ are as defined in Fig. 3.24 and Fig. 3.25, and σ_{peak} is the width parameter of the line in question. The challenge in this method is performing the fit. While a module has been written for Spectra which interfaces with GnuPlot to perform this fitting procedure, the method will not always converge. This is especially true in the case of weak signals near the noise limits of a particular system. Even worse, the nonlinear fitting procedure can fit noise spikes or large variations in the background if care to constrain the fit is not taken. The nice feature of the summation methods is that they will always return an answer, and do not diverge.

Defining a SNR using the gaussian fitting approach has proved to be quite difficult. Since the area of the peak is analytic, the width which should be used to scale the noise is not well defined. Some preliminary tests of this signal analysis function were made on blank spectra generated using the techniques described in the next section. However, the results were not clear and this technique has not been employed for the results of this thesis.

3.7 LIBS Signal Model

The objective of this section is to consider the problem of correctly estimating the emission strength observed by the spectrometer. Since one of the key advantages for µLIBS is the interrogation of a small area, the performance of LIBS signal analysis techniques on single shot data plays an important role in the performance of μLIBS. Further, under the low energy conditions of μLIBS, high gain on the detectors is often required. As a result, the background noise level in the detector system itself can begin to be the dominant source of noise for a LIBS acquisition [119]. In this section a generalised model of LIBS signals and noise sources will be developed. A discussion of the measurements required in order to apply the results of this work to any given detector will be given.

The model will consider only a single emission line, specified by $N_{emission}$, $C_{emission}$ and $\sigma_{emission}$; representing the number of counts produced by the line, the central channel of the line and the gaussian width parameter of the line, respectively. This model could easily be extended to multiple emission lines.

The noise sources that are considered for this model are variation in the background, Poisson statistics in the emission line, and noise spikes from an intensified detector system. Each of these sources will be quantified and defined below. In the current spectrum generation model, the background will be considered to be flat in all cases, though these results can be applied to the case of non-flat backgrounds if the caveats discussed in Sec. 3.6.2.1 are kept in mind.

3.7.1 Scope of Model

The standard deviation of the background, denoted $\sigma_{background}$, covers both normal detector dark current variability, and variation in the background from continuum radiation. As a result, the current model will be suitable for modelling the response of a LIBS system for all gate delays. In general, the noise in an experimental acquisition can be a function of wavelength. However, if regions close to the spectral line of interest are used, the local noise conditions can be considered constant under many conditions. Variation in the background is characterised by the standard deviation of a region without an emission line or cathode noise spikes, in units of counts.

In order to correctly simulate the effect of shot noise in the emission line as it is binned by a spectral detector, the emission line is constructed by selecting $N_{emission}$ random events from a gaussian distribution function, implemented in the standard Python libraries as **random.gauss**. This allows a line to be populated from a gaussian distribution, truly reflecting the behaviour of an emission line with a gaussian line shape. The emission line strength will be expressed in terms of the total number of counts emitted by the line.

The final component of the model comes from the noise spikes observed in intensified systems. A characterisation of the noise spikes from an ICCD is performed in order to determine the parameters that must be specified in the model. While these noise spikes can be represented in terms of radiometric units, using the calibration techniques described in Sec. 3.4.4, the natural units of the cathode noise spike is counts. Since the quantum efficiency of the detector will change as a function of wavelength, the radiometric equivalent will depend on the wavelength being observed. Our objective here is to develop a general model for the noise spikes, which can then be scaled to situations of interest for any detector. It is expected that the performance of the LIBS signal analysis techniques will depend on the number, area and width of cathode noise spikes.

3.7.2 Cathode Noise Spike Characterisation

A sample 1 μs acquisition from an ICCD at maximum gain with no external light is given in Fig. 3.26a. During these characterisations the entrance aperture was covered, and the slit and shutter were closed. It is therefore expected that the spikes must be a characteristic of the ICCD detector itself. Under these conditions, this ICCD has a an average dark current of $\sim$ 205 counts, and an average spike number per spectra of $\sim$ 19. For different integration times, one would expect the number of cathode spikes to change.

To characterise the cathode noise spike location, area and width distributions a peak finding and fitting routine was developed (code listing in Sec. A.3.2.3). This algorithm finds peaks by looking for regions more than 4σ above the background region, and fits such regions with a gaussian peak shape. When no cathode noise spikes are present, the background is known to have a gaussian distribution. For a normal distribution, the probability of observing an event more than 4 σ above the average is $\sim 3.2 \cdot 10^{-5}$. In a standard ICCD with 1024 channels the probability of observing such an event is $\sim 3.3 \cdot 10^{-2}$.

The code reports peak location, height, width and area for each peak which has a convergent gaussian fit. If the fit does not converge, no area is reported. Output from the peak finding routine was examined to ensure that it was correctly identifying and fitting the cathode noise spikes. An example of the output from this routine for the data set presented in Fig. 3.26a is given in Fig. 3.26b. The residuals between the original data set and the peak finding algorithm's output is given in Fig. 3.26c. The residual spectrum indicates that the line fitting algorithm has successfully located and fit the significant spikes in Fig. 3.26.

A set of 500 spectra with a 1 μs integration time were acquired for MCP gains ranging from 0 to 250 in steps of 50. For each of these spectra, the peak fitting algorithm was used to detect and analyse the peaks. The average and standard deviation of the number of peaks per spectra is presented in Fig. 3.27. It is clear that the number of spikes depends on the MCP gain of the ICCD, which is final confirmation that the spikes are related to the cathode

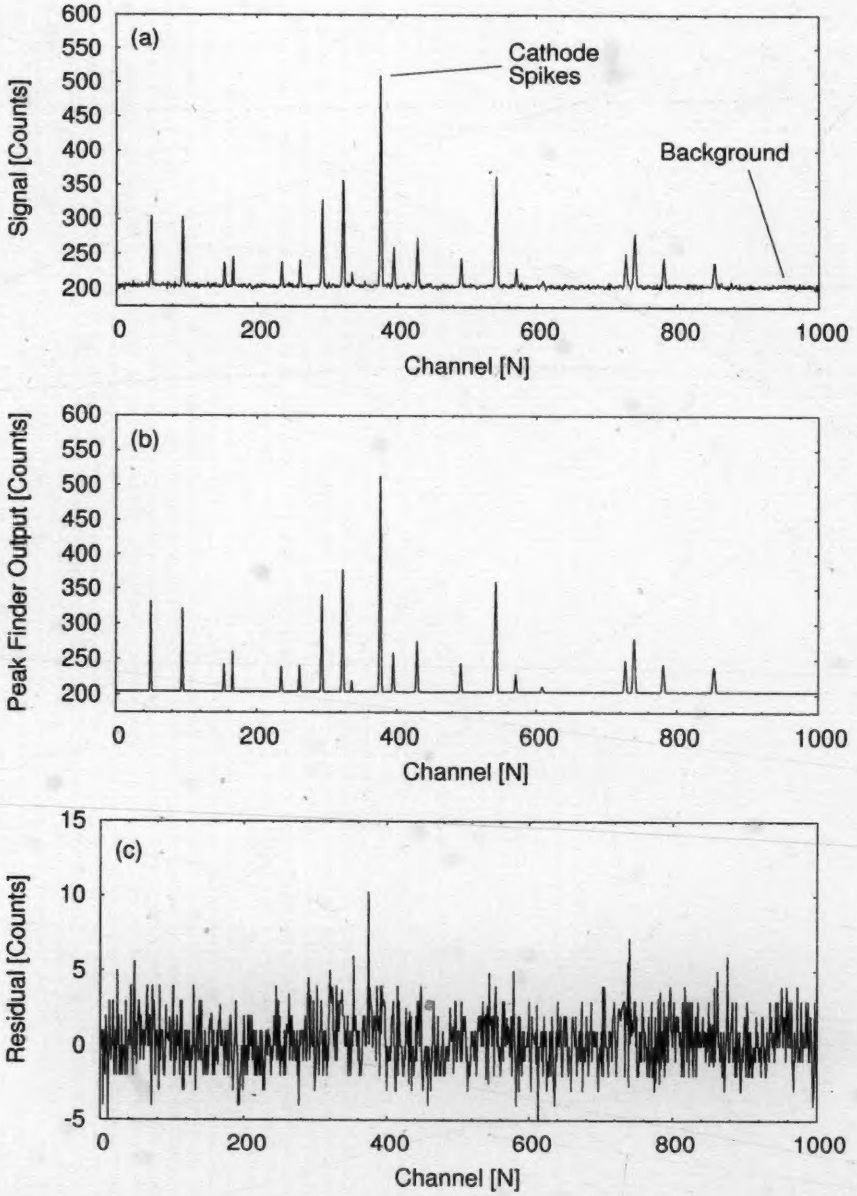

Figure 3.26. *(a) Typical spectrum under high gain conditions with no external light allowed into spectrometer. (b) Results of a peak finding algorithm applied to the data set in (a). (c) The residual between the original data set and the peak finding algorithm, indicating good detection and fitting of cathode noise spikes.*

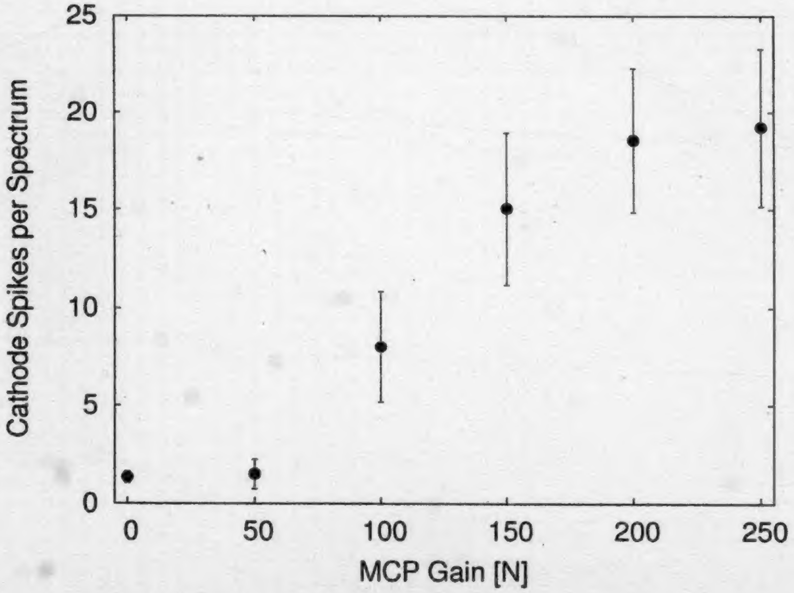

Figure 3.27. *Average and standard deviation of the number of cathode spikes observed per spectrum (1 μs integration) for an ICCD as a function of MCP gain. The number of spikes expected depends strongly on MCP gain.*

of the ICCD, rather than some external phenomena. The number of spikes expected per spectra also has a significant variability.

To characterise the spatial distribution of the cathode noise spikes, the highest gain data set was binned into a histogram of channel location, using 10 channel wide bins. The results of this analysis is presented in Fig. 3.28. This particular ICCD has 1024 channels, and has dead areas on either side which are visible in Fig. 3.28. Additionally, there is a hot channel at about 770. Over large regions of the ICCD, the distribution is flat. However, there is a clear tendency towards less cathode spikes towards the edges of the ICCD.

For further analysis I proceed under the assumption that the distribution is random spatially. While there are variations, overall it appears that a local spike rate could be defined for this detector, and presumably others as well. The spatial distribution of cathode spikes will be one of the characteristics that will need to be measured in order to extend the results presented here to any given detector.

It is clear from the spectra presented in Fig. 3.26 that the area, or intensity, of the spikes varies from spike to spike. The area distribution of spikes for

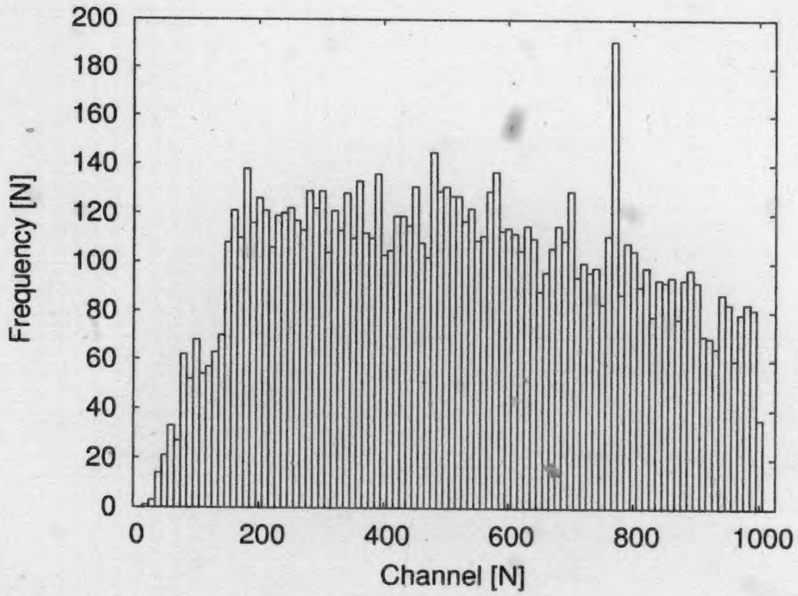

Figure 3.28. *Distribution of cathode spikes in 10 channel wide bins on the sample ICCD. Dead areas on either side and hot channels are observed.*

the high gain setting is presented in Fig. 3.29. The area distribution has been fit with a log-normal distribution, which has a probability density function given by:

$$f(x) = \frac{1}{x\sigma\sqrt{2\pi}} exp\left[-\frac{(log_{10}x - \mu)^2}{2\sigma^2}\right] \tag{3.15}$$

where $x > 0$, μ is the mean and σ is the standard deviation for this distribution. The log-normal distribution is used in cases where the logarithm of a variable is normally distributed. It presents as a normal gaussian when plotted with a horizontal scale that is logarithmic, as is the case in Fig. 3.29, where the solid line is a best fit of the log-normal distribution to the data set. This analysis has been performed for the different gains of the sample data set, and μ and σ have been found to be functions of gain. This result is presented in Fig. 3.30. Since the cathode noise spikes will be amplified by the microchannel plate, a dependence on gain is expected. In this case, μ and σ can be fit with linear equations as functions of MCP gain.

The distribution of cathode noise spikes has been characterised in terms of number per spectrum, area per spike and spike width. The cathode spike

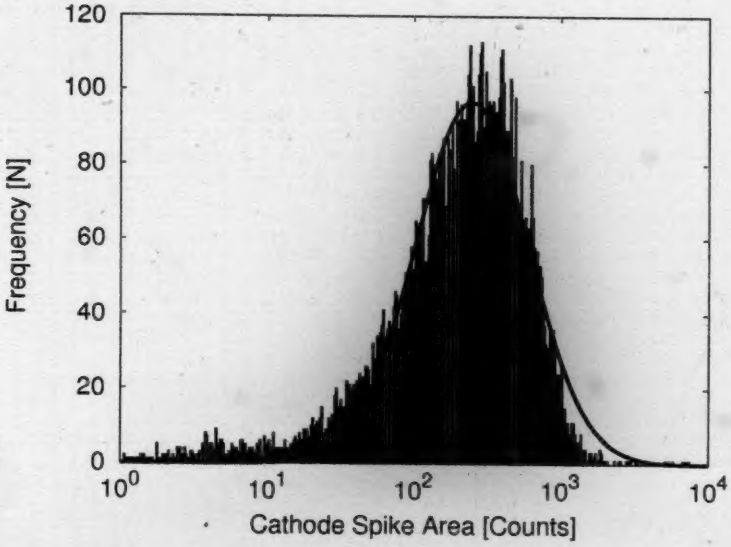

Figure 3.29. *Distribution of cathode spike area for a MCP gain of 250. The solid line is a best fit of a log-normal distribution to the experimental data.*

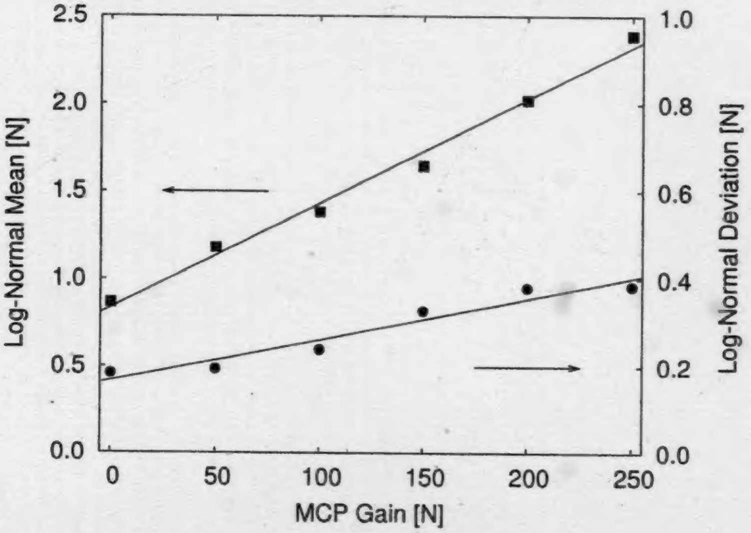

Figure 3.30. *Scaling of the log-normal fit parameters μ and σ to the cathode area distribution with MCP gain.*

characterisation that has just been performed has defined the range of conditions that the sample ICCD can exhibit for an integration time of 1 μs.

Chapter 4

Absolute Characterisation of LIBS Detection Systems

4.1 Introduction[1]

One of the goals of this thesis is to provide a framework for the engineering of LIBS systems. In this chapter, a number of LIBS detection systems are studied as complete units and characterised in terms of absolute responsivity, noise-equivalent integrated spectral brightness (NEISB) and noise-equivalent spectral brightness. A simple theory of LIBS detection systems is introduced, and used to define NEISB and NESB for spectral detectors. Experimental results for absolute responsivity are given, and a detailed characterisation of cathode noise sources in the intensified systems is presented. The detailed characterisation can be used to correctly simulate the performance of LIBS detector systems, and to provide sufficient statistical information to permit cathode spike removal from high gain spectra. Through the application of the methods described in this thesis, detailed feasibility studies requiring actual experimentation should become less necessary in the future, though verification exercises will be required as part of the normal engineering process.

4.2 LIBS Detection System Theory

In this section a theory of LIBS detection systems is developed to provide a framework for the absolute characterisation of LIBS systems studied in this chapter. This theory will provide definitions of responsivity, NEISB and NESB. These definitions will include the combined effects of any image relaying optics, the spectrometer properties, and performance of the detector system used.

---

[1] A version of this chapter has been submitted as Ref. [120]

While in many cases it would be possible to reliably distinguish between these components of a LIBS system, in experimental work or practical applications it is the performance of the combined system which is important. Further, in some cases such as an Ocean Optics system the detector and spectrometer are an integrated unit and changes cannot be easily made. In other cases, information about the spectrometer may be unavailable. As a result of these factors, it makes more sense to develop definitions which represent LIBS equipment as it is typically used. In the following discussion and equations, roman characters (L, D, Φ) represent overall characteristics of the spectrometer or detector units, while script characters ($\mathcal{L}, \mathcal{T}, \mathcal{R}$) refer to internal characteristics which combine to yield the external properties of the systems under study.

Integrated spectral plasma brightness is used to represent the plasma emission, as LIBS detectors are typically integrate over a set period and thus report energy rather than power. Integrated spectral plasma brightness, $\Phi(\lambda)$, has units of J Sr^{-1} cm^{-2} nm^{-1}. Effects such as different spatial extents for ion and atomic emission lines are assumed to be treatable as functions of wavelength, or negligible. Such functions could be rather complex, but in principle an effective emission size as a function of wavelength could be ascertained experimentally. In addition, any effects from the image relaying optics should be included in this factor.

Spectrometer luminosity can be thought of as a cross section for the spectrometer, and is well summarised in [121]. Spectrometer luminosity is synonymous with étendue. The entrance aperture and solid angle of the spectrometer define the maximum amount of plasma emission that can be coupled into the detector. The addition of the effect of the grating or other dispersing element which determines the dispersion at the exit plane of the spectrometer converts to spectral luminosity. Spectral luminosity, $L(\lambda)$, has units of Sr cm^2 nm $\mu\mathrm{m}^{-1}$, and can be written as

$$L(\lambda) = \mathcal{L}(\lambda)\,\mathcal{T}(\lambda) \tag{4.1}$$

where $\mathcal{L}(\lambda)$ represents only the geometric action of the spectrometer, and $\mathcal{T}(\lambda)$ captures the optical losses from the imperfections of the spectrometer.

Detector response includes factors such as gain, quantum efficiency, and effective pixel size of the CCD at the photocathode or other sensing surface. Detector response, $D(\lambda, G)$, is a function of wavelength and gain setting and has units of counts μm J^{-1} $\mathrm{channel}^{-1}$, and can be written as

$$D(\lambda, G) = \mathcal{D}_0\mathcal{R}(\lambda, G) \tag{4.2}$$

where $\mathcal{D}_0$ is a geometric constant which captures the pixel size for a given detector, and $\mathcal{R}$ is the responsivity of the detector alone. Note that gain includes not only signal amplification via a microchannel plate, but also factors such as pixel integration time, relative response of the various pixels and other signal gain mechanisms. Depending on the system used, different components setting will have to be included in this factor. In the limiting case, only the quantum efficiency of the detector will be used.

Using the functions defined above, the signal obtained using a LIBS system can be expressed as

$$I\,(channel) = \Phi\,(\lambda)\,L\,(\lambda)\,D\,(\lambda, G) \tag{4.3}$$

Where $\Phi\,(\lambda)$ is the integrated plasma brightness including the effects of any relaying optics, $L\,(\lambda)$ is the spectrometer spectral luminosity and $D\,(\lambda, G)$ is the detector response. Once these factors are combined, the result $I\,(channel)$ is the observed counts as a function of channel number, with units of counts channel^{-1}. This corresponds to the experimental observable for typical LIBS detector systems used today.

The responsivity of a optical system is typically defined in terms of the measured signal divided by the input optical power [110,121,122]. The input optical power will be the integrated plasma brightness multiplied by the geometric factors of the spectrometer and detector, and the measured signal is $I\,(channel)$. The resulting factor will have units of counts J^{-1}, or counts per photon. While counts are not directly a physical quantity, it is close to the day to day reality of the LIBS experimentalist. Thus, for the purposes of this chapter, the responsivity of a LIBS system will be defined as

$$R\,(\lambda, G) = \frac{I\,(channel)}{\Phi\,(\lambda)\,\mathcal{L}\,(\lambda)\,\mathcal{D}_0} = \mathcal{R}\,(\lambda, G)\,\mathcal{T}\,(\lambda) \tag{4.4}$$

As can be seen with this definition, it is possible to characterise the responsivity of a LIBS system by characterising the combined behaviour of the spectrometer transmissivity and detector response. However, this will only be true under conditions where the spatial and angular distribution of the radiation observed during a calibration experiment is less than that specified by the geometric luminosity $\mathcal{L}\,(\lambda)$.

For the work in this chapter, a single channel signal to noise ratio (SNR) will be used, defined as:

$$SNR = \frac{I\,(channel)}{\sigma_{noise}} \tag{4.5}$$

where $I\,(channel)$ is the background corrected signal, and σ_{noise} is the standard deviation of the background. This definition is very simple, but will serve to illustrate the differences in the detectors studied here. With the more sophisticated signal analysis techniques discussed in Sec. 3.6.2, noise in general will be less of a problem. However, this definition does not capture the effects of signal shot noise. Overall, these two competing factors will tend to cancel each other out, and the current results should be close to the final behaviour.

In general LIBS practice, both the signal and noise will be functions of channel number, since noise sources such as the continuum radiation vary with wavelength. However, it should always be possible to define a local noise for regions around and including the line of interest. Thus, SNR can be calculated with a single spectrum, provided a spectrally quiet neighbouring region can be found, or the noise estimated.

There are many sources of noise that are relevant to LIBS detection systems. For an unintensified CCD the primary noise sources are dark current, σ_{Dark}, read out noise, $\sigma_{Readout}$ [110,123]. Howell also considers the noise from the A/D converter, $\sigma_{A/D}$, in [123]. Note that the symbols used here have been modified from the original references. Many more sources of noise exist for the unintensified CCD [110, 122], but they are not included separately in the current model. In practice, any such effects can be integrated into one of the noise terms that is included.

Each of the σ_x is one standard deviation of the distribution of noise for the relevant quantity x, with units of electrons. To keep close to the experimental observables in a typical LIBS experiment, these quantities will be expressed with units of counts. As a result, it is also necessary to consider the gain of the A/D converter, $\mathcal{G}_{A/D}$, with units of counts per electron. Using these values, a single pixel from an unintensified CCD with no exposure to external light will have a noise, N, defined in Eqn. 4.6.

$$N^2 = \mathcal{G}_{A/D}^2 \left(\sigma_{Dark}^2 + \sigma_{Readout}^2\right) + \sigma_{A/D}^2 \tag{4.6}$$

This form of the noise would be sufficient for unintensified systems, but will not capture the full behaviour of intensified system. Intensified systems also exhibit cathode noise spikes, as described in Sec. 3.7.2. An additional term, $\sigma_{Cathode}$, must be added to Eqn. 4.6 to represent this behaviour. The average noise for a single pixel in an intensified system, $N_{intensified}$, with no exposure to external light will be as given in Eqn. 4.7.

$$N_{intensified}^2 = G_{A/D}^2 \left(\sigma_{Dark}^2 + \sigma_{Readout}^2 + \sigma_{Cathode}^2\right) + \sigma_{A/D}^2 \tag{4.7}$$

The quantity $\sigma_{Cathode}$ must be treated with care, as the the underlying distribution is not Gaussian [118]. This term is a strong function of the gain of the intensifier and type of spectrometer used for a particular LIBS detection system. A detailed characterisation of the noise spikes will be made in Sec. 4.5.

The shot noise due to the signal I must also be taken into account. The dominant source of shot noise as the signal is converted from photons to counts will occur at the point where the fewest countable particles occur. In the case of an intensified system, this will correspond to the number of photoelectrons in a single channel; in a CCD, to the number of electrons captured in a single channel. The observed signal I enters into the noise once it has been scaled by the A/D gain, $\mathcal{G}_{A/D}$, and the intensifier gain, $\mathcal{G}_I$. The signal to noise ratio (SNR) produced by a single channel in an intensified system observing a signal I can now be written as Eqn. 4.8 which is a variant of the 'CCD Equation' [123].

$$SNR = \frac{I}{\sqrt{G^2_{A/D}\left(\sigma^2_{Dark} + \sigma^2_{Readout} + \sigma^2_{Cathode}\right) + \sigma^2_{A/D} + I\mathcal{G}_I\mathcal{G}_{A/D}}} \tag{4.8}$$

Noise-equivalent power or noise-equivalent input is defined as the incident power or energy, respectively, required to generate a signal to noise of unity at the detector, with signal shot noise neglected [121, 122]. However, these definitions do not take into account the limited luminosity of the spectrometer. By following the same approach, quantities which do include the effect of the spectrometer can be defined. Analogous to noise-equivalent power will be noise-equivalent spectral brightness (NESB), and analogous to noise-equivalent input will be noise-equivalent integrated spectral brightness (NEISB). For the case of NESB, SNR can be expressed as

$$SNR \approx \frac{I_{NESB}}{N_{intensified}} \tag{4.9}$$

At the detector we can express the required signal as $I_{NESB}\,(channel)$, which corresponds to NESB through Eqn. 4.3. and the consideration of an integration width:

$$I\,(channel) = NESB\tau_{gate}L\,(\lambda)\,D\,(\lambda, G) \tag{4.10}$$

Solving algebraically yields a definition for NESB which includes the detector luminosity, which is more applicable to LIBS than a more conventional definition concerned only with the detector itself. NESB will depend on wavelength and any factors affecting the gain of the detector, and should be written as given in Eqn. 4.11. Unlike the responsivity of a LIBS system, the NESB requires inclusion of the spectrometer luminosity. Noise-equivalent spectral brightness has units of W Sr^{-1} cm^{-2} nm^{-1}.

$$NESB\,(\lambda, G) = \frac{N_{intensified}}{L\,(\lambda)\,D\,(\lambda, G)\,\tau_{gate}} \tag{4.11}$$

The use of NEISB is more appropriate when the noise in a system does not scale with integration time, but remains constant. In this case, it is the total integrated energy which is relevant, and τ_{gate} does not enter into the definition. Following the approach used above to derive NESB yields a definition of NEISB which includes the detector luminosity.

$$NEISB\,(\lambda, G) = \frac{N_{intensified}}{L\,(\lambda)\,D\,(\lambda, G)} \tag{4.12}$$

4.3 Systems Studied

A total of four spectrometer/detector combinations are studied in this chapter: an intensified photo-diode array (IPDA) coupled with a Czerny-Turner spectrometer, an intensified CCD (ICCD) coupled with a Czerny-Turner spectrometer, an ICCD coupled to an echelle spectrometer, and a multichannel compact CCD system. Manufacturer information is given in Table 4.1, and a summary of the optical characteristics is given in Table 4.2.

The quantum efficiencies of the intensified detectors are presented in Fig. 4.1. The quantum efficiency curves are supplied by the manufacturer for all three intensified systems, and is not known for the multichannel CCD prototype. The detector gain for the ICCDs is presented in Fig. 4.2. In the case of the ICCD on the echelle spectrometer, the detector gain is provided by the manufacturer and was not confirmed. For the ICCD on the Czerny-Turner, the gain data is the combined results of a large number of calibration experiments performed during the course of this thesis. For the IPDA/Czerny-Turner system the detector gain is provided by the manufacturer, and was not confirmed. According to the specifications, the maximum gain of the IPDA is 4 counts/photoelectron.

The multichannel CCD system is a prototype of a field portable spectrometer produced by Ocean Optics, composed of eight compact CCD spectrometers optimised for different spectral regions. Plasma emission light is imaged onto a multi-fiber bundle, which couples the light to the different CCDs. The system is externally triggerable and gateable, with a minimum gate width of 10 μs.

4.4 LIBS System Responsivities

Four types of calibration sources were used to characterise the responsivity , $R\,(\lambda, G)$ (combined detector response and spectrometer transmissivity, $\mathcal{R}\,(\lambda, G)\,\mathcal{T}\,(\lambda, G)$), for the systems studied here: a tungsten blackbody source, a combination deuterium/halogen broadband source, a Hg lamp and a variety of lasers scattered off a diffuse reflector. The procedures used to calibrate the systems are described in Sec. 3.4. The detector responsivitity calibrations were carried out with different subsets of available calibration sources.

Table 4.1. *Summary of Manufacturer Data*

System	Detector / Spectrometer
IPDA/Czerny-Turner	Princeton Applied Research (Model 1455R-700-G) Acton Research Corporation (SpectraPro 500)
ICCD/Czerny-Turner	Andor Technology (iStar DH720-25F-03) Oriel Instruments (MS 260i)
ICCD/Echelle	Andor Technology (iStar DH734-18U-03) Andor Technology (Mechelle 5000)
Multichannel CCD	Ocean Optics (Prototype for Field Portable Applications)

Table 4.2. *Summary of optical characteristics for the systems under study*

System	f/#	Focal Length [m]	Grating [lines/mm]	Reciprocal Linear Dispersion [nm/channel]	Spectral Resolution [nm]	Intensified
IPDA/Czerny-Turner	6.9	0.5	150	0.32	0.1[a]	✓
ICCD/Czerny-Turner	3.9	0.25	600	0.167	0.4[b]	✓
ICCD/Echelle	7	0.195	52.13	0.007 - 0.052	0.1[b]	✓
Multichannel CCD	4	0.1	Varies?	0.022 - 0.049	0.2[b]	

[a] Measurement of instrumental limit, 10 μm

[b] Measurement of instrumental limit, 100 μm

[c] Manufacturer specification, fixed slit width/aperture

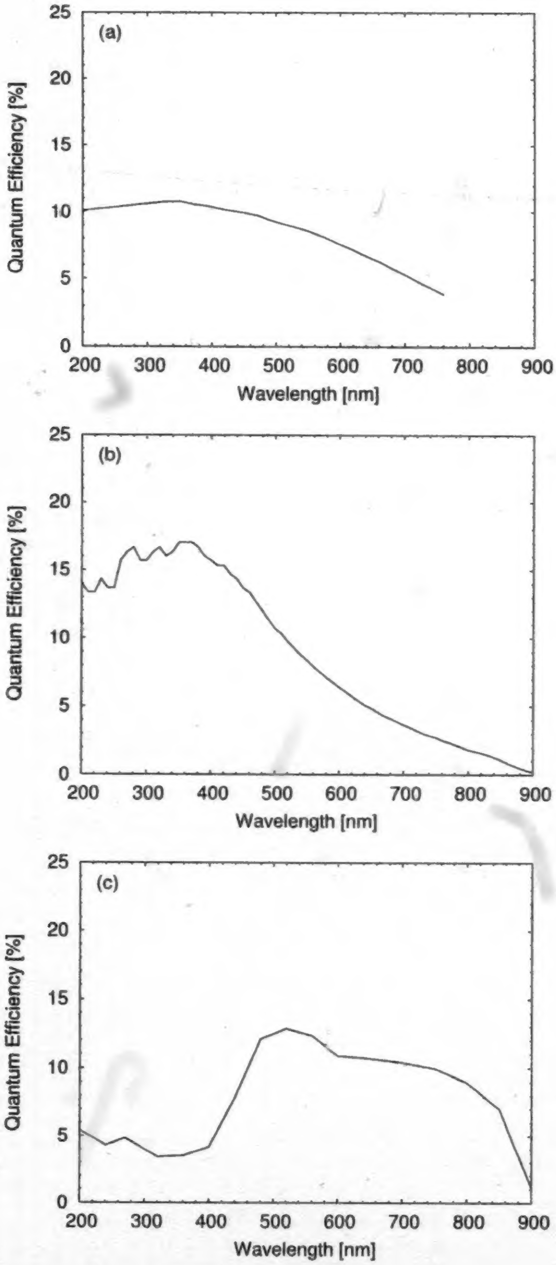

Figure 4.1. Manufacturer quantum efficiency data for the intensified detectors in the (a) the IPDA/Czerny-Turner system, (b) ICCD/Czerny-Turner system and (c) the ICCD/Echelle system.

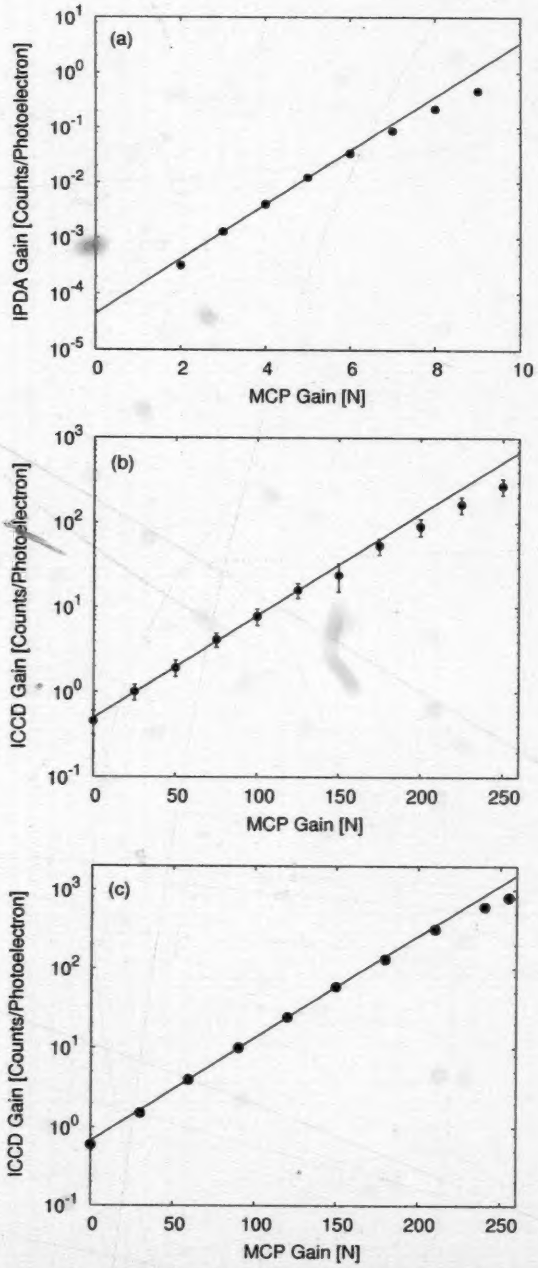

Figure 4.2. *(a) Calibrated IPDA gain for IPDA/Czerny-Turner system, (b) Calibrated ICCD gain for ICCD/Czerny-Turner system and (c) Manufacturer data for ICCD gain for ICCD/Echelle system. The solid lines are best exponential fits to the data for gains below (a) 6, (b) 150 and (c) 150.*

Table 4.3. *Standards applied to responsivity calibrations*

System	Tungsten Lamp	Deuterium/ Halogen	Hg Lamp	Angular Method
IPDA/Czerny-Turner	✓			
ICCD/Czerny-Turner	✓		✓	✓
ICCD/Echelle	✓	✓		
Multichannel CCD	✓	✓		

The standards applied to each system are given in Table 4.3. Note that the Deuterium/Halogen source was used as a relative extension to the tungsten lamp, and was not useable as a primary calibration source. Also, the calibration for the IPDA/Czerny-Turner system was performed a limited number of times. As a result, accuracy is estimated at a factor of ≈ 2. Since those early experiments, little further work was performed with this system to refine the calibration accuracy. For the other systems, the overall accuracy is estimated at $\sim 40\%$.

The absolute responsivity results for the systems are presented in Fig. 4.3 through Fig. 4.6. The ICCD/Czerny-Turner system was the most responsive of the systems studied, with a peak responsivity of ~ 27 counts per photon. The next most sensitive system is the ICCD/Echelle, with a peak responsivity of ~ 6.5 counts per photon. However, it must be noted that the ICCD used on the Echelle has a gain about a factor of 4 greater that that used on the Czerny-Turner. As a result, the peak responsivity of the Czerny-Turner could be much improved with a newer ICCD similar to the one used in the ICCD/Echelle system.

The IPDA/Czerny-Turner system falls below both ICCD systems in terms of overall responsivity, with a maximum of ~ 0.4 counts per photon. Finally, the Ocean Optics prototype was the least responsive, with a peak responsivity of $\sim 10^{-2}$ counts per photon. The low responsivity of the Ocean Optics prototype is not surprising, as the system is unintensified. The discontinuities observed in Fig. 4.6 are due to the transitions between the different responsivities of the compact CCD spectrometers which make up the Multichannel CCD spectrometer system.

One key caveat about the values presented for the Czerny-Turner systems is that the choice of grating can make a large difference in the both the magnitude and location of the peak responsivity. With a Czerny-Turner system, a good choice of grating is essential. For both the Echelle and multichannel CCD systems, rapid variations in responsivity as a function of wavelength

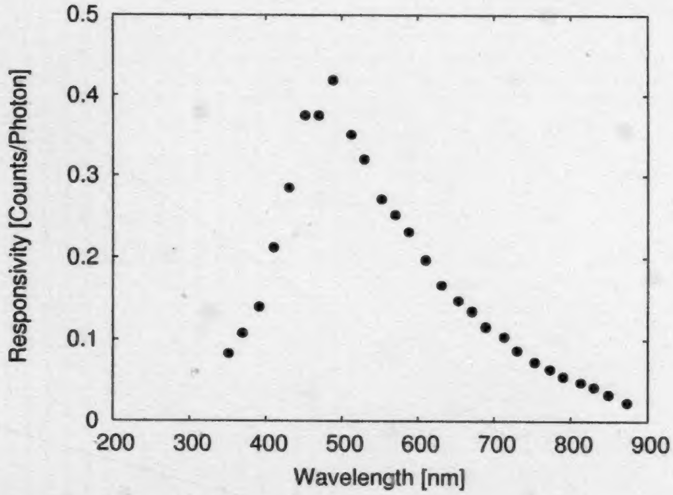

Figure 4.3. Responsivity of the IPDA/Czerny-Turner system using maximum gain and a 150 l/mm grating.

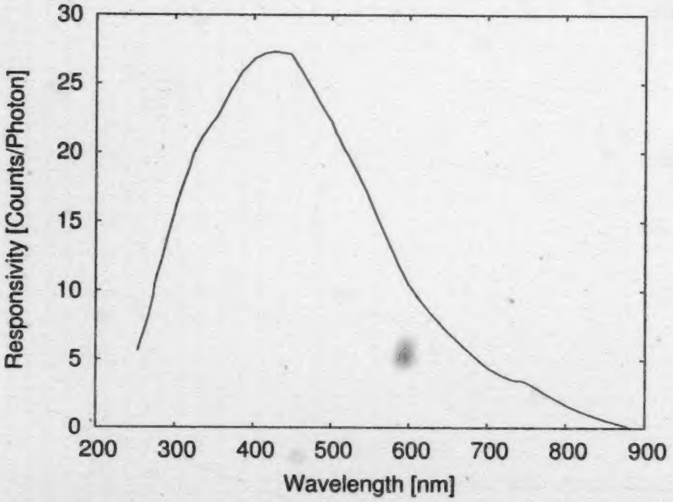

Figure 4.4. Responsivity of the ICCD/Czerny-Turner system using maximum gain and a 600 l/mm grating.

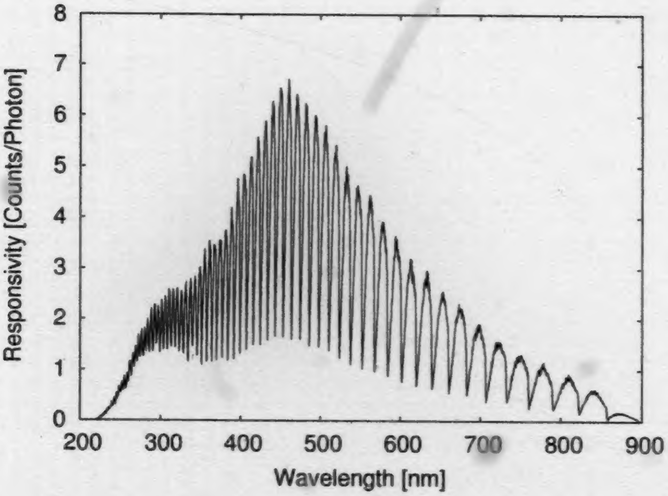

Figure 4.5. Responsivity of the ICCD/Echelle system at maximum gain.

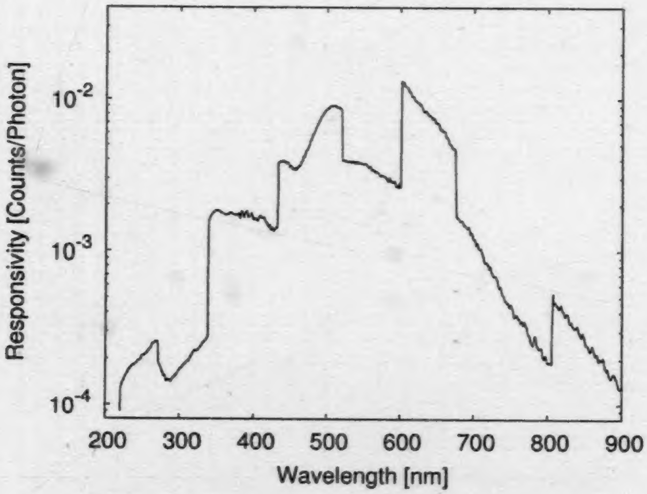

Figure 4.6. Responsivity of Multichannel CCD system.

are observed. While the calibration data presented in Fig. 4.5 and Fig. 4.6 can be used to remove these variations from spectral data, it will not always be possible to avoid regions of low sensitivity in LIBS experiments. Additionally, the effective dynamic range of the instruments will be a strong function of wavelength for both systems, which would require some care during experimental design.

4.5 LIBS System Noise Characterisation

The procedures described in Sec. 3.7.2 were used to characterise the noise of the intensified systems studied here. The cathode spike distributions were characterised as functions of detector gain for spatial distribution, rate, area and width. As the multichannel CCD is not intensified, no cathode noise spikes were observed, and this system is therefore not characterised in this section.

When characterising the systems for the cathode noise spikes, external light was blocked from the spectrometer. This means different things in each case as the design of the spectrometers varies. For the IPDA/Czerny-Turner system, a physical block was placed over the entrance slit, and a mirror which selects exit ports was moved to keep light from the IPDA. For the ICCD/Czerny-Turner system, the entrance slit was covered with an opaque cap, and the shutter and entrance slit were closed. For the ICCD/Echelle, an opaque end cap was placed over the fiber end.

Once the cathode noise spike characterisation has been completed, the behaviour of the cathode noise spikes can be predicted for any set of detector conditions. As a result, both the mean and standard deviations of the distributions will be reported, since the numerical values will be used to generate the test spectra with a population of noise spikes that reflects the detector performance as accurately as possible.

4.5.1 Spatial Distribution of Cathode Spikes

The spatial distribution of cathode noise spikes for the intensified systems is given in Fig. 4.7. For the IPDA/Czerny-Turner system, a limited number of noise characterisation shots were taken. As a result, the combined data from MCP gains above 7 was used to build up a histogram of the spatial distribution of cathode noise spikes. For the ICCD systems, the detector was run at maximum gain to obtain a large number of spikes for the histogram.

The spike locations are characterised in terms of channel numbers. In the case of the IPDA/Czerny-Turner and ICCD/Czerny-Turner system, these channel numbers correspond directly to physical location on the detector. In

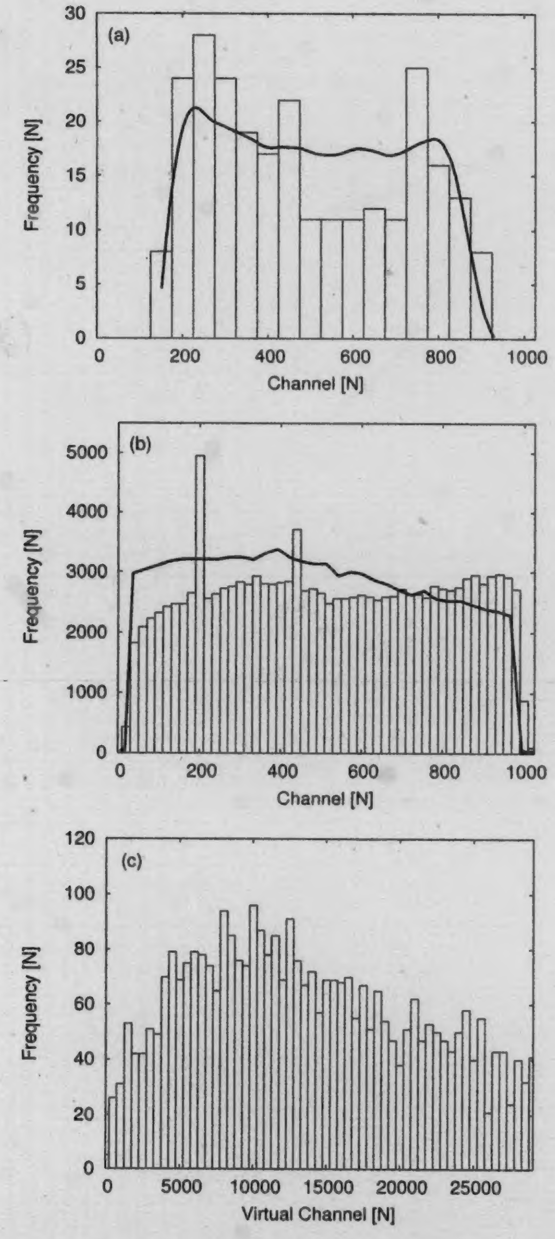

Figure 4.7. *Spatial distribution of cathode noise spikes for (a) the IPDA/Czerny-Turner system, (b) ICCD/Czerny-Turner system and (c) the ICCD/Echelle system. The solid line in (a) and (b) are the relative detector response as a function of channel number. In the case of the ICCD/Echelle system, the distribution is across virtual channels.*

the case of the ICCD/Echelle system the relationship between observed channel number and location on the detector is quite complicated. It is therefore necessary to report the ICCD/Echelle results in terms of virtual channels.

The solid line in Fig. 4.7a and 4.7b is the relative response of the detector. The responsivity of the channels in the detectors used here is not uniform. The relative response was measured by moving a spectral line with constant power over the detector surface. There is approximate agreement between the detector shape function and the spike distribution, especially pertaining to the active area of the two detectors.

With an echelle system it is not possible to control the grating position. As a result, a measurement of the shape function of the detector is not accessible while the ICCD remains attached to the echelle spectrometer. However, this does not present a difficulty for presenting absolutely calibrated data, since the contributions from such an effect will be captured by the broadband calibration technique used to measure the responsivity given in Fig. 4.5.

4.5.2 Cathode Spike Rate

The number of cathode spikes per unit channel and unit time was investigated for the systems studied here as a function of MCP gain. MCP gain is an arbitrary setting which is proportional to the voltage on the MCP. To normalise the arrival rate, the intensifier gate width was used in all cases. To normalise the spatial arrival density, the number of channels for which cathode spikes were observed is used. For the IPDA/Czerny-Turner and ICCD/Czerny-Turner systems, the number of active channels was estimated from the detector shape functions shown in Fig. 4.7. For the ICCD/Echelle system, each of the virtual channels is eligible for a cathode spike event and the total number of virtual channels is used. The results of this section will be presented in terms of channels rather than photocathode area as the channel is closer to the day to day experimental practice of a LIBS experimentalist. The results will be interpreted in terms of cathode area in Sec. 4.5.5.

In the case of the IPDA/Czerny-Turner system, the MCP gain ranges from 0 to 10. Using a step size of 1, the entire range was tested for arrival rate. Unfortunately, only 10 noise spectra were taken for each MCP setting. Cathode spikes were only observed for gains above 6. The gate width for these experiments was 5 μs, and the number of active channels is estimate at ~ 750. The mean and standard deviation of the cathode spike arrival rate for the IPDA/Czerny-Turner system is given in Fig. 4.8. The standard deviation was calculated using the standard summation equation [124]. The solid lines in Fig. 4.8 are best fits to the experimental data.

For the ICCD/Czerny-Turner, the MCP gain ranges from 0 to 255. The region above a gain of 100 was characterised with a step size of 25, while a step size of 50 was used below 100. A total of 10^4 spectra were acquired for each gain setting. The gate width for these experiments was 500 μs, and the number of active channels is estimated at $\sim$ 1000. The distribution of the number of spikes per spectrum was fit with a Gaussian distribution, and the mean and standard deviation are reported in Fig. 4.9. The solid lines are best fits of a logarithmic function to the experimental data. This ICCD displays a strong threshold in the spike arrival rate at a gain of $\sim$ 100.

The ICCD/Echelle system MCP gain also varies from 0 to 255. This region was characterised with a step size of 50. A total of 100 spectra were taken at each gain setting. The gate width for these experiments was 20 ms, and the number of active virtual channels is 29147. In practice this number was observed to depend on the wavelength calibration of the echelle, which was performed whenever the fiber was changed. The cathode spike arrival rate is much lower than in the previous two systems. Even with the much longer gate width used here, cathode spikes were only observed for gains above 150. As done previously, the distribution of the number of spikes per spectrum was fit with a Gaussian distribution, and the mean and standard deviation are reported in Fig. 4.10.

Only in the case of the ICCD/Czerny-Turner date is the cathode spike rate well characterised at all gains. For the IPDA/Czerny-Turner system and the ICCD/Echelle system the lack of spectra and the very quiet nature of the detector, respectively, limit the precision of the characterisation. However, the data set is of sufficient quality to compare the detector/spectrometer performance in high and low gain regimes for the various systems. At maximum gain, the IPDA/Czerny-Turner system has a cathode spike rate of $\approx 2000\ \mathrm{s}^{-1}$ channel^{-1}, the ICCD/Czerny-Turner system a rate of $\sim 25\ \mathrm{s}^{-1}$ channel^{-1}, and the ICCD/Echelle system a rate of $\approx 0.03\ \mathrm{s}^{-1}$ channel^{-1}.

The difference in the cathode spike rate for the two Czerny-Turner systems is attributed to the difference in the age, and the fact that the ICCD/Czerny-Turner system was cooled to - 10° C. The IPDA/Czerny-Turner system is $\approx$ 15 years older than the ICCD/Czerny-Turner, and it is reasonable to assume that photocathode materials were improved in this time. The photocathode area per channel is $650 \cdot 10^{-6}\ \mathrm{cm}^2$ for the IPDA/Czerny-Turner system, and $1730 \cdot 10^{-6}\ \mathrm{cm}^2$ for the ICCD/Czerny-Turner system. Combining the difference in cathode area with the cathode spike rate, the ICCD/Czerny-Turner outperforms the IPDA/Czerny-Turner by a factor of $\sim$ 425.

However, the same argument can not be made for the $\approx 10^3$ improvement in cathode spike rates demonstrated by the ICCD/Echelle system, as this system was also cooled to - 10° C. One reason the cathode rate for the ICCD/Echelle system is so much lower than the other systems is fundamental to the optics of the Echelle. A schematic of the 'staircase' pattern is given in Fig. 4.11. For this system, large areas of the ICCD are not used to construct

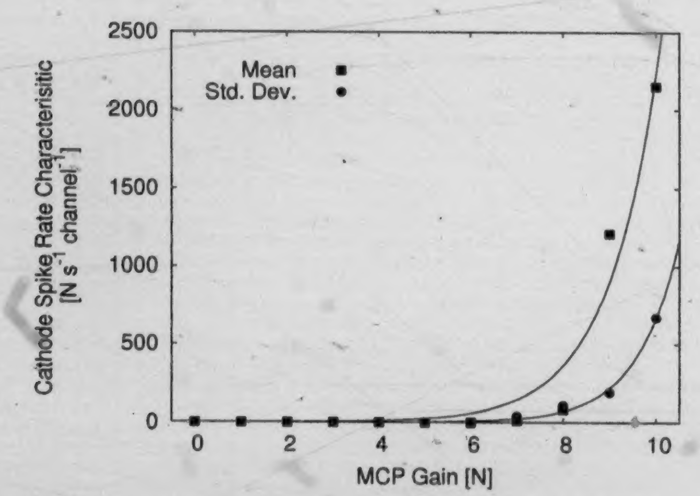

Figure 4.8. Mean and standard deviation of the cathode spike arrival rate for the IPDA/Czerny-Turner system. The solid lines are a guide for the eye.

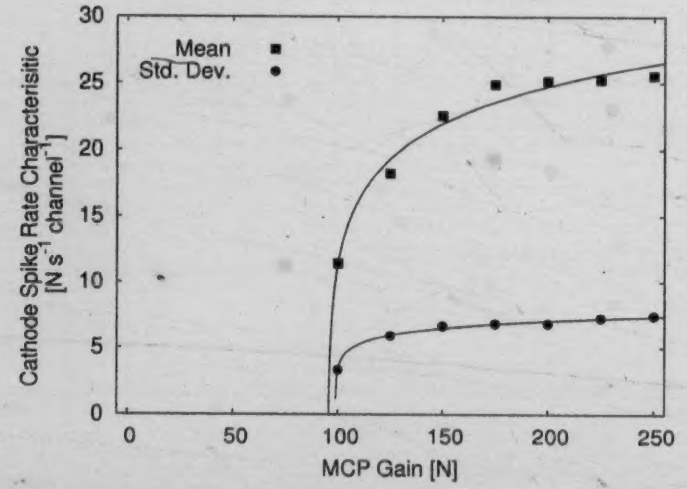

Figure 4.9. Mean and standard deviation of the cathode spike arrival rate for the ICCD/Czerny-Turner system. This ICCD exhibits a threshold in the cathode spike arrival rate at a gain of ~ 100. The solid lines are a best fit to the experimental data.

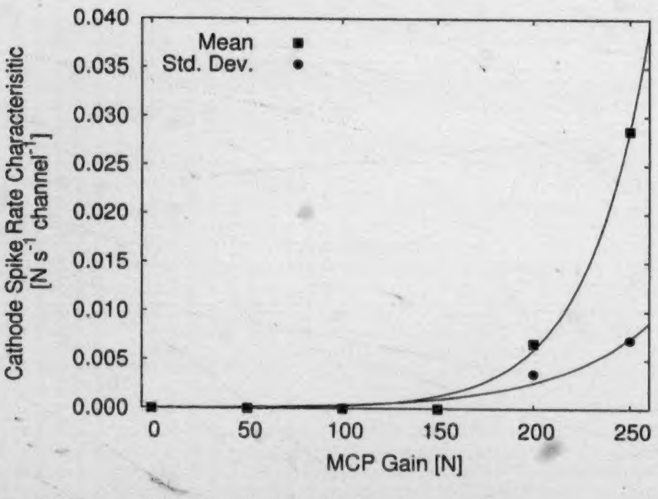

Figure 4.10. *Mean and standard deviation of the cathode spike arrival rate for the ICCD/Echelle system. The ICCD/Echelle system has a much lower cathode spike rate than either the IPDA/Czerny-Turner or ICCD/Czerny-Turner systems. The solid lines are a guide for the eye.*

the spectral signal. As a result, there are fewer opportunities for a cathode spike to interfere with the observed signal.

For the ICCD/Czerny-Turner system the full height of the ICCD was used, corresponding to a total of 256 pixels, each 26 μm by 26 μm. While the algorithm by which the ICCD/Echelle system constructs a spectrum is not known, the integration height is an option in the software. For the experiments performed here, this integration height was set to 5 pixels. If we assume that a single pixel width corresponds to a virtual channel, a total of 5 pixels are used, each 13 μm by 13 μm. The estimate for the cathode area used by the ICCD/Echelle for a single channel is then $\approx 9 \cdot 10^{-6}$ cm^{-2}.

The photocathode area used by the ICCD/Echelle for a single channel is about 200 times smaller than that used by the ICCD/Czerny-Turner system. It is therefore expected that the true difference in the cathode spike rate of the two ICCDs is a factor of ~ 4. Since this factor is associated with the ICCD themselves, a similar improvement in the cathode spike rate for the ICCD/Czerny-Turner system should be possible with a more recent ICCD.

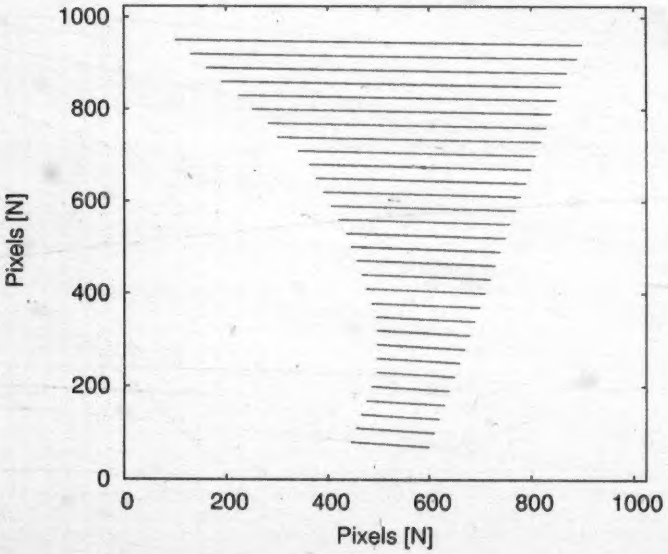

Figure 4.11. *Schematic of the echelle 'staircase' pattern observed on the ICCD detector when using the ICCD/Echelle system. Each line represents an order of the echelle grating. Unlike the Czerny-Turner, very few pixels are used per unit nm to acquire the spectral signal.*

4.5.3 Area Distribution of Cathode Spikes

As discussed in Sec. 3.7.2, the cathode noise spikes can be fit well with a Gaussian function. Since the location of the spikes is approximately random, area and width are sufficient to completely specify the cathode noise spikes. In this section, the area distribution of the cathode noise spikes will be characterised for the different systems under study.

Once again, due to the fact that only 10 shots were taken with the IPDA/Czerny-Turner system, the number of cathode spikes available for analysis is limited to $\sim$ 160 at a MCP gain of 10, and drops quickly to only 1 at a MCP gain of 7. While it is possible to fit the distribution of spikes at a gain of 9 and 10 to the log-normal distribution observed previously in Sec. 3.7.2, it is not possible for gains below that. In order to make the maximum use of the available data, the average and standard deviation were calculated for the data using the simple summation method. This analysis is presented in Fig. 4.12. At a MCP gain of 10, the simple approach agrees roughly with the fit of the Gaussian distribution.

Similar to the results presented in Sec. 4.5.1, the area distribution of the

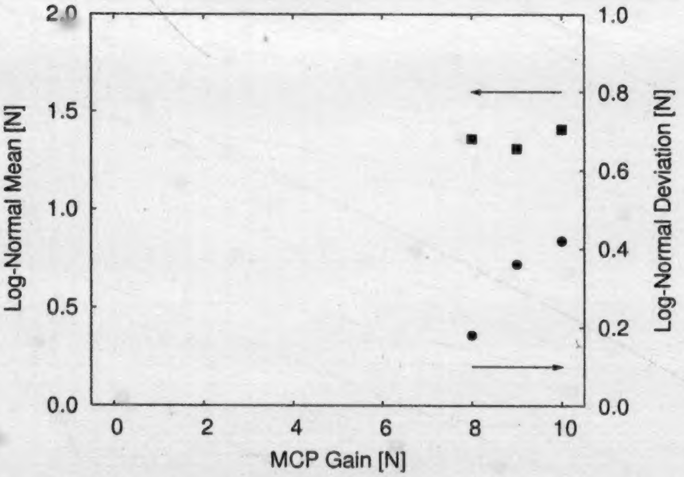

Figure 4.12. Characteristics of the log-area distribution for the IPDA/Czerny-Turner system. This analysis uses the arithmetic mean and summation form of the standard deviation, rather than a fit to the log-normal distribution.

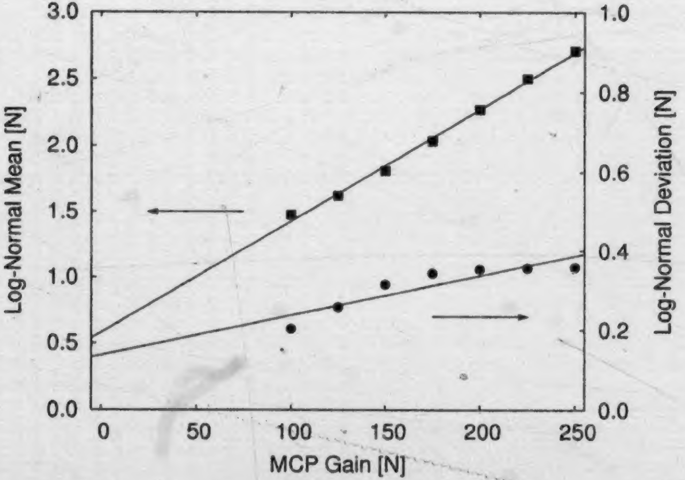

Figure 4.13. Characteristics of the log-normal distribution for the area of the cathode noise spikes for the ICCD/Czerny-Turner system. The solid lines are best linear fits to the data.

cathode spikes for the ICCD/Czerny-Turner system was found to be log-normal. The log-normal mean and standard deviation as a function of gain are presented in Fig. 4.13. The solid lines are a best linear fit to the data, which is deemed sufficient for the current comparison. While there appears to be some structure to the behaviour log-normal standard deviation, this has not been confirmed.

The area distribution for the ICCD/Echelle system was also log-normal. The log-normal mean and standard deviation as a function of gain are presented in Fig. 4.14. No cathode noise spikes were observed for gains below 200, despite the 20 ms gate width used for this data. While this data set can not be considered complete, it is sufficient to characterise the behaviour of the noise spikes in low and high gain conditions.

4.5.4 Width Distribution of Cathode Spikes

The last property of the cathode noise spikes that needs to be characterised is the width of the cathode noise spikes as a function of gain. Combined with the analysis presented in the previous three sections, this data will allow prediction of the noise behaviour of the systems studied here under a wide variety of acquisition conditions.

The cathode noise spikes have been fit with a Gaussian distribution, and the standard deviation of the best fit to each spike is considered to be the width. To characterise the cathode noise spike widths as a function of gain, the values are binned and fit with a Gaussian distribution. The mean and standard deviation of the best fit to the cathode spike width distribution is reported below.

Following the argument in the previous section for the limited data set available for the IPDA/Czerny-Turner system, the average and standard deviation were calculated for the data using the simple summation method. This analysis is presented in Fig. 4.15. The solid lines are best fits of a linear function to the data set. Due to the small number of cathode spikes available for analysis, this fit is considered to be an initial approximation only.

The mean and standard deviation of the cathode noise spike width distribution for the ICCD/Czerny-Turner system is given in Fig. 4.16. In this case, the cathode noise spike width was a weak function of MCP gain, varying ~ 15% over the range for which cathode spikes were observed. The solid lines are a best fit of a logarithmic function to the cathode spike width mean, and a best fit of a parabolic function to the cathode spike width standard deviation.

The distribution of cathode noise spike widths was also Gaussian for the ICCD/Echelle system. The average and standard deviation of the distribution are reported in Fig. 4.17. As in the previous sections, the quiet nature of the ICCD in this system limits the accuracy of this characterisation. The solid

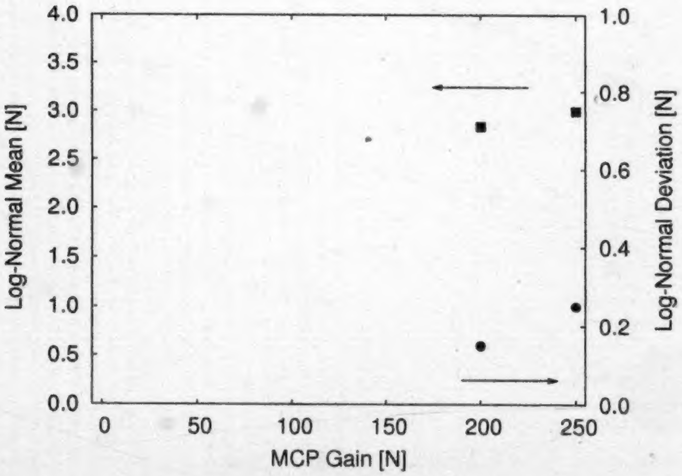

Figure 4.14. Characteristics of the log-normal distribution for the area of the cathode noise spikes for the ICCD/Echelle system. No noise spikes were observed below a MCP gain of 200. The solid lines are best linear fits to the data.

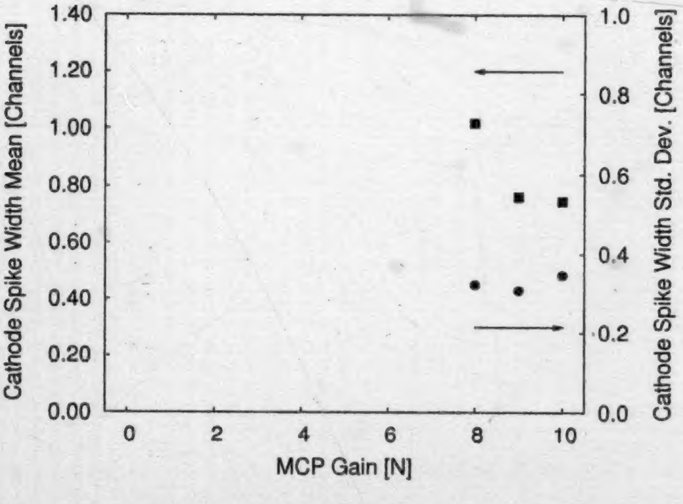

Figure 4.15. Characteristics of the cathode spike width distribution for the IPDA/Czerny-Turner system. This analysis uses the arithmetic mean and summation form of the standard deviation, rather than a fit to the log-normal distribution.

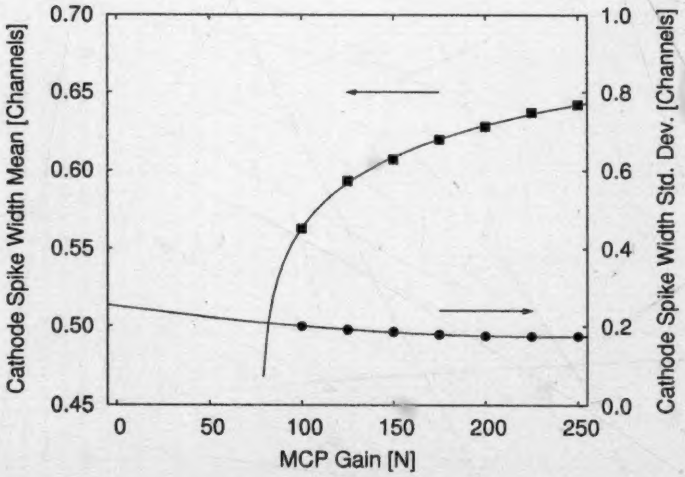

Figure 4.16. Characteristics of the distribution of cathode noise spikes as a function of MCP gain for the ICCD/Czerny-Turner system. The solid lines are best fit of a logarithmic function to the average cathode spike width, and a parabolic function to the cathode spike width standard deviation.

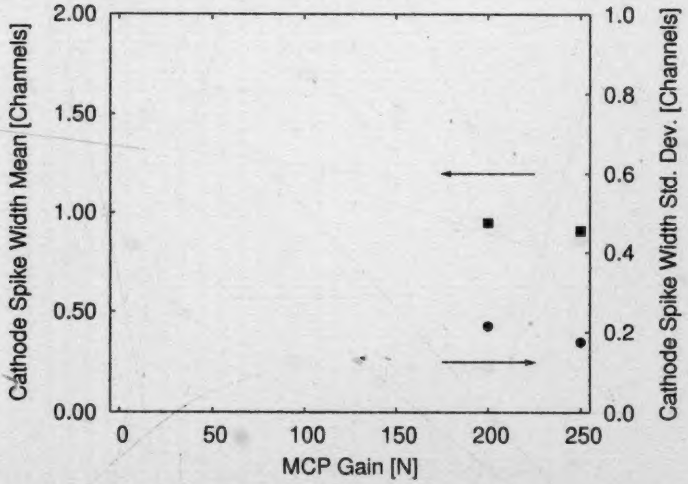

Figure 4.17. Characteristics of the width distribution of cathode noise spikes as a function of MCP gain for the ICCD/Echelle system. The increase as one moves to lower gain is not considered reliable for this data set, but rather a result of the limited number of spikes.

lines are best linear fits to the data set. For both data points a large number of cathode noise spikes have been fit with the Gaussian distribution. However, given the lack of corroborating data, any conclusions about the general trend of the cathode noise spike width would be premature at this time.

4.5.5 Cathode Spike Characterisation: Discussion

Overall, the lack of cathode spike data for the IPDA/Czerny-Turner system and ICCD/Echelle system is a weak point in the above analysis. The IPDA/Czerny-Turner system was used at the start of this thesis, before the cathode noise spike analysis was fully conceived, and has long since been disassembled. The ICCD/Echelle system was a loan from Andor Technologies, and was only available for a limited time. Unfortunately, at this time we must conclude that only the ICCD/Czerny-Turner can be considered well characterised at all gains. Despite these shortcomings, it is still possible to make use of this data set to characterise the behaviour of the cathode noise spikes in the regime of low and high gain for all three detectors. As a result, it is expected that with the current data set it will still be possible to draw some useful conclusions.

A final note is that for the ICCD/Czerny-Turner system, it is possible to reduce the vertical range which is integrated. However, this effect was not studied here, and further work would be required to ascertain to what degree an optimisation of the vertical integration range of the ICCD/Czerny-Turner system would reduce the number of cathode spikes observed.

4.6 LIBS System Noise Equivalents

We have seen that there are two modes of operation for the detectors studied here: one in which cathode spikes are observed, and one in which cathode spikes are not observed. In the case where cathode spikes are observed, an increase in gate width will increase the number of spikes which are observed. In this regime, it is appropriate to quote the noise equivalent in terms of NESB. In the case where no noise spikes are observed, it is more appropriate to quote the noise equivalent in terms of NEISB.

NESB and NEISB are quoted at the entrance slit of the spectrometer in terms of spectral brightness [W Sr^{-1} cm^{-2} nm^{-1}] and integrated spectral brightness [J Sr^{-1} cm^{-2} nm^{-1}], respectively. In order to calculate the NESB and NEISB, Eqn. 4.11 and 4.12 are used. The quantity $N_{intensified}$ is approximated by the standard deviation of the background signal when no light enters the LIBS detection system. This approach should capture the effects of all of the noise terms identified in Eqn. 4.7.

In order to calculate the spectrometer luminosity, the f-number and entrance aperture must be clearly defined. For all spectrometers, the full available f-number is used. To convert from channels to nm, the channel width of the detectors was used. For the Czerny-Turner systems, it is possible to alter these values significantly by changing the grating. In addition, the values presented here are single-channel values. The use of more sophisticated signal analysis methods will improve the performance of all of these systems.

In the case of the ICCD/Echelle and multichannel CCD system, the entrance aperture of the system is well defined by the optical fibers used and cannot be changed during use. It would be possible to change the fiber, though in both cases it is expected that the fiber aperture is already as large as possible to ensure good spectrometer luminosity.

In the case of the IPDA/Czerny-Turner and ICCD/Czerny-Turner systems, the slit width and slit height can be changed. For the noise study performed earlier, the full height of the detector was used. To remain consistent, the full available height of the detector will be used to calculate the spectrometer luminosity. The effective height of the IPDA/Czerny-Turner system is $\sim$ 2.5 mm (assuming unity magnification), and 4.1 mm for the ICCD/Czerny-Turner system. A typical slit width for my μLIBS experiments is 100 μm, and is used to define the area for the Czerny-Turner systems.

This analysis was first performed for the case where no cathode noise spikes were observed. The multichannel CCD prototype can be included in this analysis. In all cases, the minimum gain for the intensified systems was used. The standard deviation of all available low gain noise spectra was calculated, and the average used to evaluate NEISB. The intensified systems were then analysed for behaviour at high gain, and the same analysis carried out.

4.6.1 Noise-Equivalent Integrated Spectral Brightness at Minimum Gain

The NEISB for the various systems are presented in Fig. 4.18 through Fig. 4.21. The minimum NEISB, luminosity and maximum responsivity at minimum gain are tabulated in Table 4.4. In the case of the multichannel CCD system, the size of the pixels is not known. Based on personal communications with Ocean Optics personnel, the effective pixel width is estimated at $\approx$ 24 μm.

Overall, the NEISB is lowest for the ICCD/Czerny-Turner system, largely due to the large luminosity of the Czerny-Turner spectrometer. The next best performing system is the multichannel CCD system, followed by the IPDA/Czerny-Turner system. The very low responsivity of the IPDA/Czerny-Turner system is offset by the high luminosity of the Czerny-Turner spectrom-

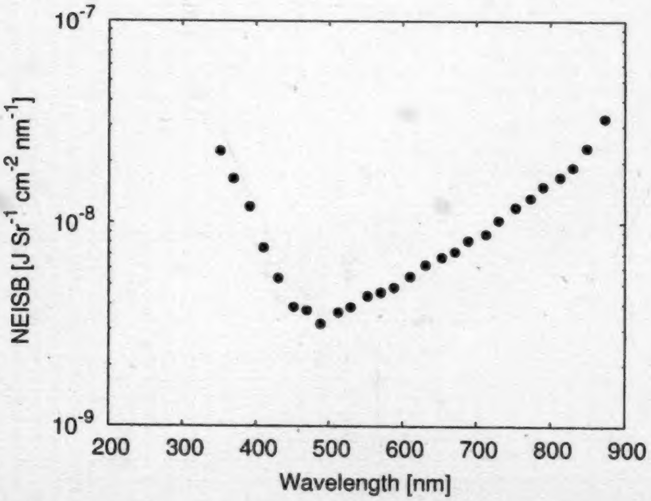

Figure 4.18. *NEISB for the IPDA/Czerny-Turner system at minimum gain, with a 150 l/mm grating and slit area of 2.5 $\cdot$ 10^{-3} cm^2. A different grating or entrance slit would affect these values.*

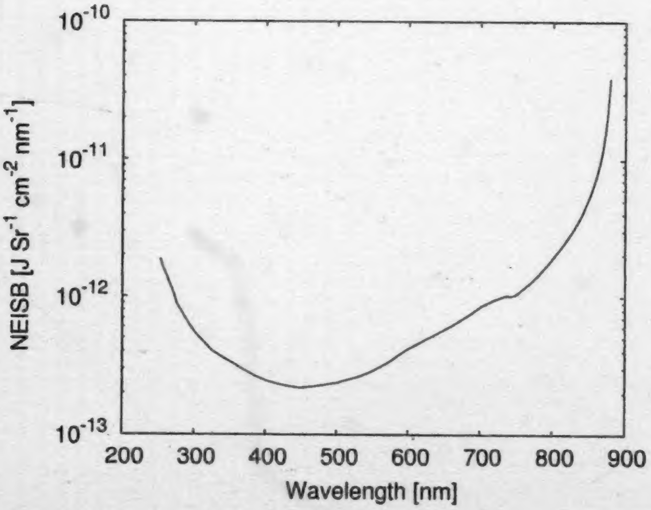

Figure 4.19. *NEISB for the ICCD/Czerny-Turner system at minimum gain, with a 600 l/mm grating and slit area of 4.0 $\cdot$ 10^{-3} cm^2. A different grating or entrance slit would affect these values.*

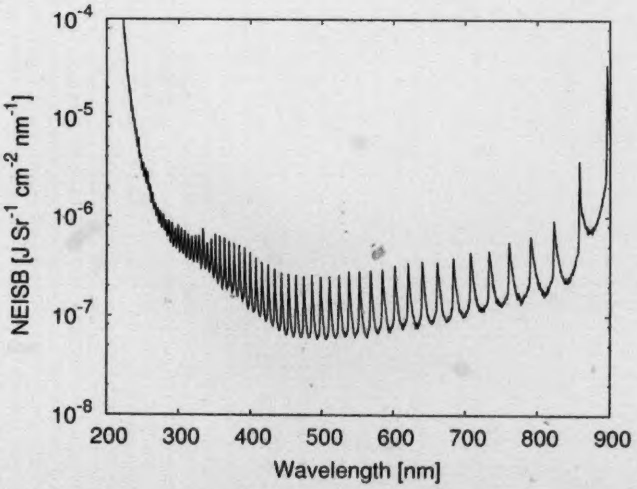

Figure 4.20. *NEISB for the ICCD/Echelle system at minimum gain. For this system the grating and entrance aperture are fixed. The entrance aperture is controlled by choice of fiber, and is at the maximum allowable value of* $19.6 \cdot 10^{-6}$ *cm*^{2} *in this case.*

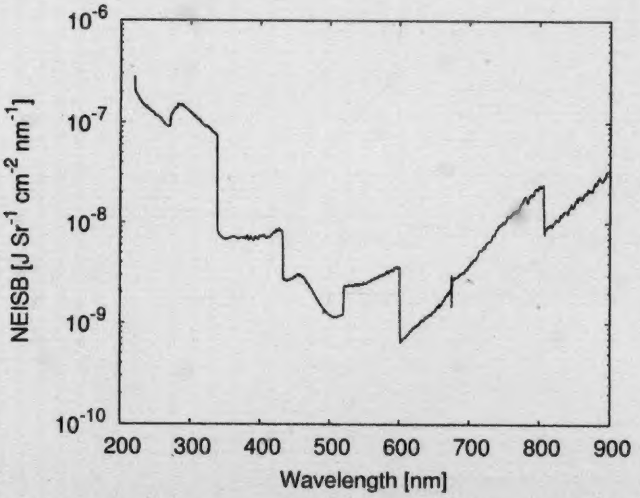

Figure 4.21. *NEISB for the multichannel CCD prototype. For this system the grating and entrance aperture are fixed. The entrance aperture is controlled by the combination of the fiber aperture and the slit size, and is* $\sim 6 \cdot 10^{-5}$ *cm*^{2} *in this case. Use of a different fiber bundle would affect these results. The narrow spikes near channel boundaries are due to imperfect wavelength matching between the channels.*

Table 4.4. Comparison of NEISB results and contributing parameters for minimum operating gain.

System	Minimum NEISB [J Sr^{-1} cm^{-2} nm^{-1}]	$\mathcal{L}$ [Sr cm^2 nm μm^{-1}]	Maximum Responsivity [Counts Photon^{-1}]
IPDA/Czerny-Turner	$3 \cdot 10^{-9}$	$5 \cdot 10^{-7}$	$1.7 \cdot 10^{-5}$
ICCD/Czerny-Turner	$3 \cdot 10^{-13}$	$1.3 \cdot 10^{-6}$	$1.4 \cdot 10^{-1}$
ICCD/Echelle	$6 \cdot 10^{-8}$	$7 \cdot 10^{-10}$	$5 \cdot 10^{-3}$
Multichannel CCD	$7 \cdot 10^{-10}$	$\approx 10^{-9}$	$1.3 \cdot 10^{-2}$

eter, resulting in competitive overall performance. The system with the highest NEISB is the ICCD/Echelle system, due to the relatively low responsivity and low luminosity of the system.

One important point about the NEISB values is the influence of intensifier gain. In general, an moderate increase in gain will not lead to a strong increase in the background variability, until the onset of cathode noise spikes described in Sec. 4.5.2. Up to this point, as the gain is increased the NEISB will drop. As a result, the performance of the intensified systems can be improved significantly. The increase in performance can be predicted by combining the intensifier gain results presented in Fig. 4.2 with the NEISB results presented in Fig. 4.18 through Fig. 4.20.

The influence of integration time must also be considered. Under long-lived, but low intensity, light conditions a very long gate at low gain would be the correct choice. However, the NEISB results presented above are not expected to be valid at arbitrarily large gate widths, as dark current will increase with integration time. This characterisation has not been performed for the intensified systems studied here, but the multichannel CCD system shows no increase in variability up to a gate time of 100 ms.

4.6.2 Noise-Equivalent Spectral Brightness at Maximum Gain

The analysis for the regime in which cathode noise spikes were observed is presented in Fig. 4.22 through Fig. 4.24. In all cases, the maximum gain was used. The minimum NESB, luminosity and maximum responsivity at maximum gain are tabulated in Tab. 4.5.

Overall the NESB is lowest for the ICCD/Czerny-Turner system. The ICCD/Echelle system is a factor of ~ 110 noisier, while the IPDA/Czerny-Turner system is another factor of ~ 17 noisier still. In this case, the extremely

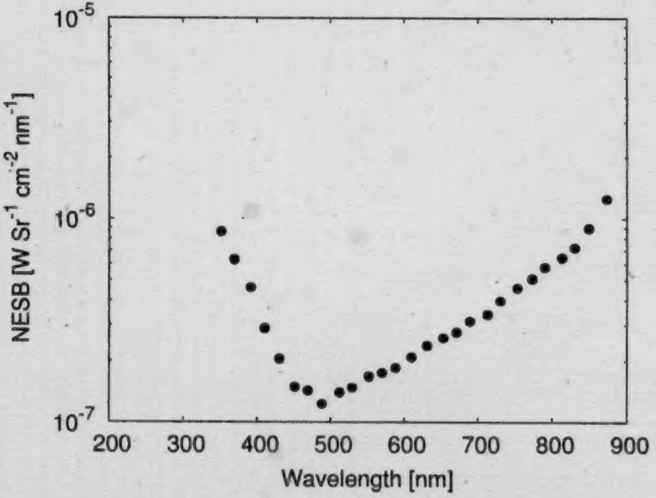

Figure 4.22. NESB for the IPDA/Czerny-Turner system at maximum gain, with a 150 l/mm grating and slit area of $2.5 \cdot 10^{-3}$ cm^2. A different grating or entrance slit would affect these values.

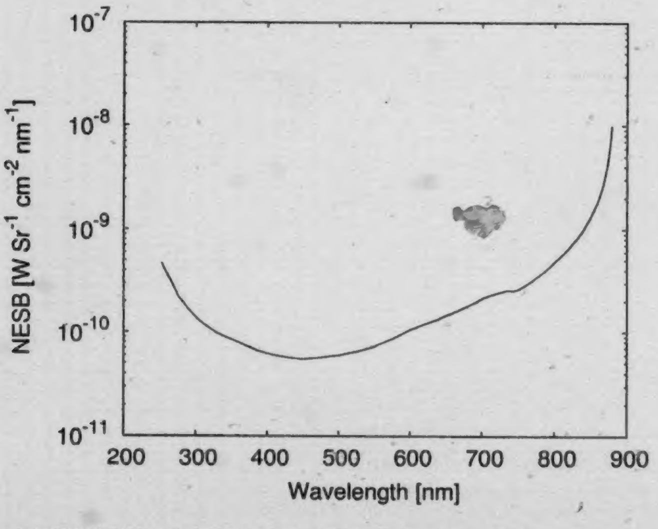

Figure 4.23. NESB for the ICCD/Czerny-Turner system at maximum gain, with a 600 l/mm grating and slit area of $4.0 \cdot 10^{-3}$ cm^2. A different grating or entrance slit would affect these values.

Table 4.5. Comparison of NESB results and contributing parameters.

System	Minimum NESB [W Sr^{-1} cm^{-2} nm^{-1}]	$\mathcal{L}$ [Sr cm^2 nm µm^{-1}]	Maximum Responsivity [Counts Photon^{-1}]
IPDA/Czerny-Turner	$1.2 \cdot 10^{-7}$	$5 \cdot 10^{-7}$	$4.2 \cdot 10^{-1}$
ICCD/Czerny-Turner	$6 \cdot 10^{-11}$	$1.3 \cdot 10^{-6}$	$2.7 \cdot 10^{1}$
ICCD/Echelle	$7 \cdot 10^{-9}$	$7 \cdot 10^{-10}$	$6.6 \cdot 10^{0}$

good performance of the ICCD in the ICCD/Echelle system offsets the low luminosity of the Echelle system to yield good overall performance. As discussed earlier, the performance of the ICCD/Czerny-Turner system would be improved with an ICCD with similar characteristics to that in the ICCD/Echelle system.

However, it is important to remember that for typical µLIBS measurements, the gate width will be in the range of 1 µs or less. Under these conditions, the performance of the ICCD/Echelle is better described with the NEISB results, scaled for ICCD gain and the gate width of acquisition. Naturally, the same improvements would be obtained with an upgraded ICCD/Czerny-Turner system. The NESB results found here can be scaled for MCP gain using the results presented in Sec. 4.5.

4.7 Conclusion

In this paper, a theory of LIBS detector systems has been developed, and used to define responsivity, NESB and NEISB in terms useful for the LIBS experimentalist. Using this treatment, four LIBS detection systems have been characterised for responsivity, NESB and NEISB. A detailed noise characterization of the intensified systems has been carried out. The cathode noise spikes have been characterised for arrival rate, area and width. Using the noise characterization and the absolute responsivity of the systems, the performance of the four LIBS detection systems has been evaluated.

Of the systems studied here, the ICCD/Czerny-Turner has the best responsivity and luminosity. In terms of luminosity, the ICCD/Czerny-Turner is followed closely by the IPDA/Czerny-Turner system, with both the ICCD/Echelle system and the Multichannel CCD spectrometer system exhibiting much lower luminosities. In terms of responsivity, the ICCD/Czerny-Turner system is closely followed by the ICCD/Echelle, with the IPDA/Czerny-Turner and Multichannel CCD spectrometer exhibiting much lower respon-

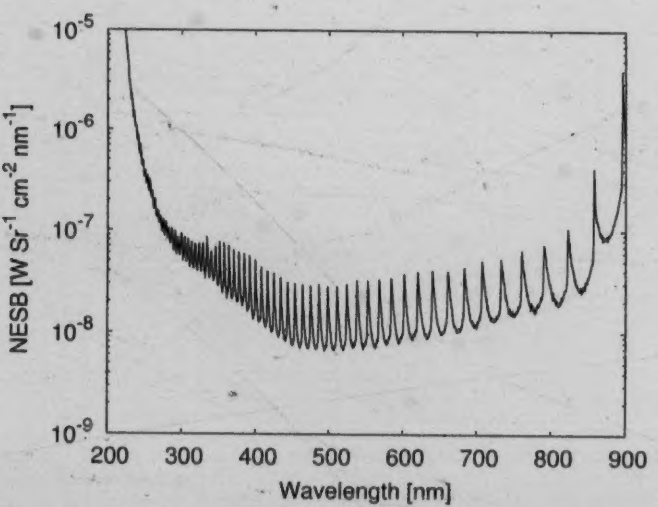

Figure 4.24. *NESB for the ICCD/Echelle system at minimum gain. For this system the grating and entrance aperture are fixed. The entrance aperture is controlled by choice of fiber, and is at the maximum allowable value of* $19.6 \cdot 10^{-6}$ *cm*^{2} *in this case.*

sivities. However, the Multichannel CCD spectrometer system is not intensified, so the lower responsivity is not surprising.

The detector/spectrometer characterizations performed here are only a guide to the performance of the class of instrument, and specific detector/spectrometer combinations will have different results than those reported here. In particular, the multichannel CCD spectrometer system is a prototype, and the current results may not fully reflect the capabilities of such a system.

The trade off between spectral resolution and bandwidth was not investigated in this work. In the case of the Czerny-Turner systems, a choice must be made between high resolution and high spectral bandwidth. For the ICCD/Echelle and Multichannel CCD spectrometer systems it is possible to acquire spectra with high spectral resolution and high spectral bandwidth which give additional advantages for simultaneous identification of multiple species and observation of multiple lines for the identification of individual species. These additional advantages were not considered here. It is expected that the ability to simultaneously observe the brightest emission lines from multiple elements simultaneously will increase the utility of the broadband systems for LIBS in a manner not captured by the current analysis.

Chapter 5

Quantification of the LIBS Process: Atomic Emission, Plume Expansion, and Noise Sources

5.1 Introduction

In this chapter, the hydrodynamic and emission processes of LIBS are investigated using a simple target system of elemental contaminants in water. This target system presents many advantages over solid targets, such as reduced inhomogeneity and the ease of sample preparation at arbitrary concentrations. As a result, this system presents a good subject for investigations of plume dynamics, quantitative emission levels, optimization procedures and for comparison with simple models.

The emission of radiation from the LIBS plasma is a complex function of space, time, laser pulse energy, major plasma constituent, background gas composition and pressure. It is typical practice in LIBS to use a gated detector which allows experimenters to avoid the initial strong continuum radiation while maximising the late time integration of atomic or ionic emission from the plasma. Usually, an empirical investigation of the behaviour of the LIBS plasma for a particular application is conducted to obtain a global optimization of signal to noise. Once the global optimum for the signal-to-noise ratio (SNR) has been identified, characterisation of the sensitivity and limit of detection of the technique is performed and evaluated against the requirements for a given application. However, the results presented are usually inextricably tied to the performance of the experimental system used to evaluate the technique. Therefore, the results obtained are often of limited usefulness for comparisons between experimental groups or with theory. A better understanding of the fundamental processes that govern LIBS is required in order to apply LIBS in a more general situation without having to conduct optimization studies for each application.

Modelling of the expansion behaviour and chemical or thermodynamic properties of plasma plumes such as those generated in LIBS has been studied by many groups [125–130]. Colonna et al. used a one-dimensional fluid model to describe the expansion of a plasma plume, obtaining time-dependent profiles for density, pressure and plume velocity [125]. The authors note that under the high temperature and pressures found in LIBS plasmas, chemical reactions can occur very quickly, and include the thermodynamic properties of TiO in their model. Additional work with the spectroscopy and modelling of TiO in laser produced plasma plumes is reported by Di Giacomo et al. [126]. Babushok et al. take a similar approach to that of Colonna et al. with a detailed model including the chemistry of atmospheric gases and metallic lead in a recent report [127]. In different work by Colonna et al., a collisional radiative model of a atomic hydrogen plasma is developed [128]. Significant deviations from equilibrium conditions for the distributions of species within the plasma plume are predicted for a number of initial conditions. Le et al. have studied the expansion of a laser-produced plume into different low pressure ambient gases for a better understanding of the processes involved in pulsed-laser deposition of thin films [129].

The simulation of absolute emission levels from LIBS plasmas has been studied by a few groups. Shah et al. have obtained good qualitative agreement in the temporal profiles for ionic and neutral carbon emission for early times after the laser pulse [131]. The authors assume that for times soon after the laser-matter interaction the plasma can be described using cylindrical blast wave theory as described by Sedov [42]. Ionization of the plasma is treated using the Saha equation, and the hydrodynamics of the plasma plume expansion is assumed to be independent of the ionization state as the variation of populations in various neutral and ionic species is not expected to affect the plume expansion. Shah et al. extended their work to include emission contributions from the ambient gases and predictions for temperature profiles [132]. Good absolute agreement between the model predictions and experimental measurements of temperature was observed. The investigation for both papers was limited to a single position on the longitudinal axis of the plume, focusing on the temporal profiles at one point in space.

Recent work by Gornushkin et al. [133–135] has developed a model for laser-induced plasmas which includes hydrodynamics and radiative transfers within the plasma. The model successfully generates spectra for an evolving SiC plasma in a vacuum with emission levels in terms of spectral brightness [133]. This work has been extended by Kazakov et al. [136] to include the effects of a background Ar gas. Excellent qualitative agreement between time-resolved spectra from the simulation and experimental data has been obtained. The experimental data used has not yet been calibrated in terms of quantitative emission levels for a direct comparison with simulation results.

In this chapter, the application of LIBS to the detection of elemental contaminants in water is being studied from both the theoretical and experimental standpoints. Liquid samples are very homogeneous, and arbitrary concentrations can be easily prepared. The resulting samples do not suffer from the variations in elemental composition on the 10 μm scale that are present in many solid targets [56,64,69,70]. Direct measurement of the limit of detection (LOD) can be made as samples above and below the detection limits may be easily prepared [119]. As a result, liquids make an excellent test sample for fundamental investigations of the capabilities and the underlying phenomena of LIBS. Additionally, the application of LIBS for the detection of elemental contaminants in water also has applications to the real time monitoring of effluent streams, environmental compliance monitoring, and process control. Using lower energies, it may be possible to integrate LIBS with microfluidic devices for lab on a chip applications.

In this chapter, a simple model is presented for the simulation of the LIBS process. A test case for comparison with the modelling presented here is obtained from a parametetric study of the space-time behaviour of a LIBS plasma measured in absolute units. For the work presented here, Na was studied as a trace element in water. Na exhibits bright emission in LIBS plasmas, and is a hydrogen-like atom which allows a simplified theoretical treatment of the expected emission. The expansion of the plasma plume is modelled using both ideal shock wave theory and numerical solutions to the hydrodynamic equations for a strong shock with counter pressure taken into account [41, 42, 137]. The models predict temperature, pressure, density and velocity for regions behind the shock front. The time dependent temperature and density profiles can then be used for the modelling of the time and space dependence of plasma emission.

5.2 Experimental Setup

The experimental setup is given in Figure 5.1. In these experiments a frequency-tripled Nd:YAG (Continuum 9010 Powerlite) laser generating 10 ns, 45 mJ laser pulses is used to ionize a small portion of a water jet which is used as a sample. The energy is controlled using a combination of a half wave plate and Glan-Taylor polarising prism. Pulse energy is monitored using a calorimeter calibrated for energy delivered to the target plane. Solutions of a known concentration were prepared, and circulated through a 3 mm wide by 0.5 mm thick jet onto which the laser light was focused. The resulting LIBS plasma is

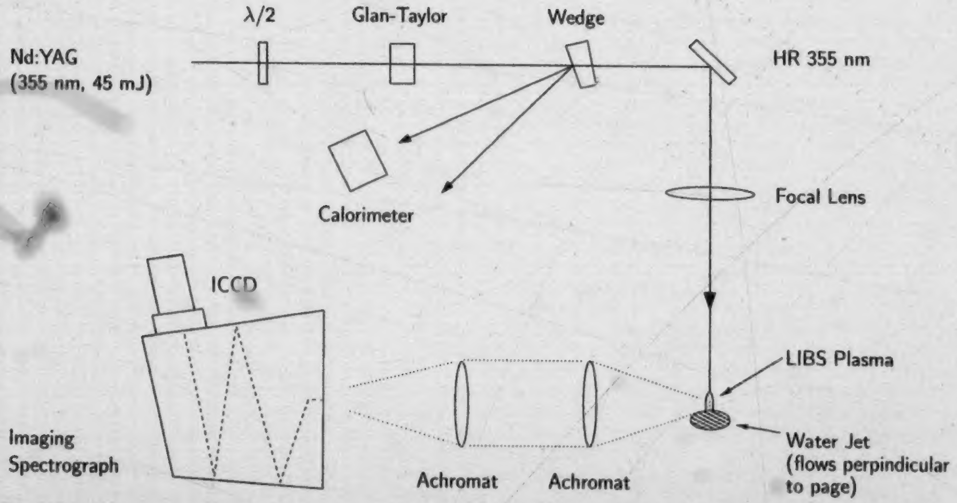
λ/2
Glan-Taylor
Wedge
Nd:YAG
(355 nm, 45 mJ)
HR 355 nm
Focal Lens
Calorimeter
ICCD
LIBS Plasma
Imaging
Spectrograph
Achromat
Achromat
Water Jet
(flows perpindicular
to page)

Figure 5.1. *Experimental setup for the detection of trace elements in water. A frequency tripled Nd:YAG (355 nm, 10 ns) is used as excitation source. Pulse energy is controlled using a half wave plate Glan-Taylor prism combination, and monitored using a calibrated calorimeter. Plasma emission is imaged 1:1 using two achromats onto the entrance slit of a 1/4 m spectrometer. Dispersed plasma light is detected with a 2D ICCD.*

viewed at right angles to the laser propagation axis, and is imaged 1:1 using two achromat lenses onto the entrance slit of a 1/4 m Czerny-Turner spectrograph (Oriel MS260i). The resolution of the imaging system is estimated at 100 μm based on measurements from a resolution test pattern. This resolution is comparable with the slit widths used in the experiment. A 2D intensified CCD (Andor iStar DH720) collects the dispersed light.

The system used has been calibrated for absolute photon emission measurements using the Hg lamp and angular calibration techniques described in Sec. 3.4.4.2. Including the manufacturer supplied sensitivity, a total of three independent calibration sources have been used to characterise the spectral response of the system. An average of these three spectral responsivities has been used for the current measurements and the absolute accuracy is estimated at ~ 40%.

The water samples used in the experiments presented here were prepared from distilled water and dissolved NaCl for the Na solutions; and $Pb(NO_3)_2$ for the Pb solutions.

5.3 Experimental Results

To characterise the emission of Na in a water solution, an extensive investigation of the plasma emission as a function of space and time was undertaken. In the plasma imaging configuration used for these experiments, the entrance slit of the spectrometer selects a vertical slice of the plasma emission which is then imaged onto the ICCD detector. This vertical slice may be moved longitudinally along the axis of laser propagation allowing the selection of different regions of space for the integration of the LIBS signal. Combining this with the temporal gating capability of the ICCD, it is possible to select any location in both space and time in the expanding plasma plume. Using a slit width of 100 μm and a gate integration width of 100 ns, a survey of plasma emission was made for a region of $\sim$ 5 mm as measured along the laser propagation axis for a period of 800 ns to 10 μs was made. For each location in space and time, the spectra are analysed for Na emission and SNR as defined in Eqn. 3.13. The results of this survey and analysis are given in Fig. 5.2 and Fig. 5.3.

The horizontal axis of Figure 5.3 refers to the position of the slit image measured from the front of the water jet. The vertical axis is the delay of the gate in time, measured from the moment the laser pulse strikes the water jet. The laser pulse enters the space-time region given in the plot from the right, and travels to the left towards the water surface located at zero. From 0 μs to 2 μs, the plasma expands quickly, stagnating at a distance of about 1.5 mm. After a brief period, the plasma starts to contract, with the signal to noise ratio dropping significantly by a time of 8 μs after the laser shot. The peak SNR is located at a distance of 1 mm from the front of the water jet, at a delay of 3 μs.

It has been previously reported [119] that in cases where the detector readout noise is the limiting factor for the limit of detection, the gate width can be increased without increasing the noise of the acquisition. Na emission, background continuum and noise equivalent power are plotted as a function of gate delay in Figure 5.4. Continuum levels approach the detector noise equivalent power in a few μs, while the Na signal continues to be measurable for many μs after the laser pulse. The SNR for Na as a function of gate delay is plotted in Figure 5.4b. The quick decay of the noise levels result in an increase in SNR up to 2.5 μs, after which further delay results in a decrease of integrated signal.

As a result of using long gate widths, it can be advantageous to choose a location in front of the water jet where the plasma emission survives for a longer time even though the peak SNR (using short gate widths) is found elsewhere. In such cases, the gate width may be opened for a much longer time than is typically used in LIBS in order to integrate the maximum num-

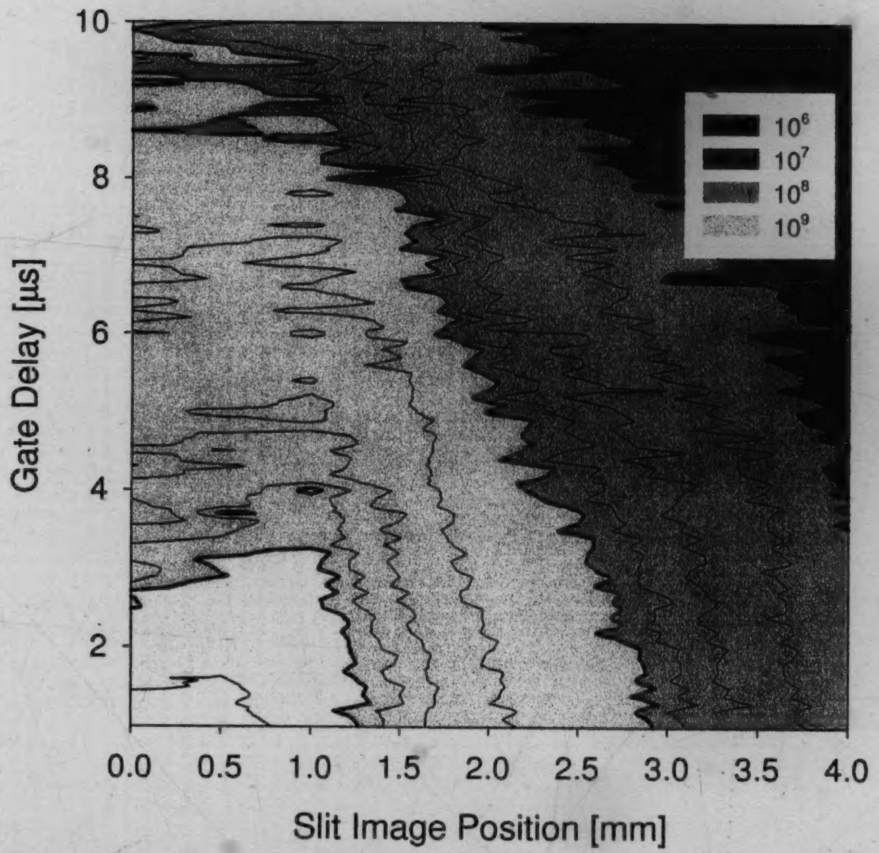

Figure 5.2. *A spacetime contour map of the integrated Na emission line strength in units of photons* Sr^{-1} cm^{-2}. *Horizontal axis refers to the position of the slit image on the longitudinal axis of laser, with zero as the front of the water jet. The vertical axis is the delay of the gate in time, with zero time as the laser striking the water jet. The laser travels from right to left. Experimental conditions:* $N_{shots} = 5$, *2200 ppm Na, Slit = 100 µm, Gate Width = 100 ns, Detector Gain = 0.81 counts/photon.*

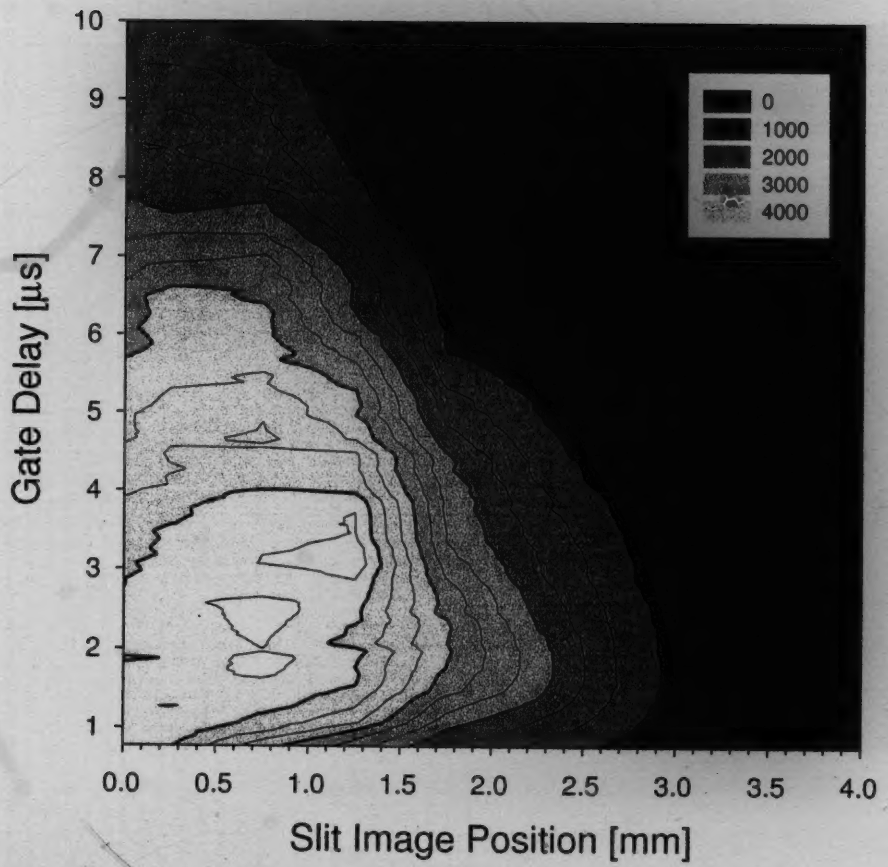

Figure 5.3. *A spacetime contour map of the Na SNR. Horizontal axis refers to the position of the slit image on the longitudinal axis of laser, with zero as the front of the water jet. The vertical axis is the delay of the gate in time, with zero time as the laser striking the water jet. The laser travels from right to left. Experimental conditions:* N_{shots} *= 5, 2200 ppm Na, Slit = 100 μm, Gate Width = 100 ns, Detector Gain = 0.81 counts/photon.*

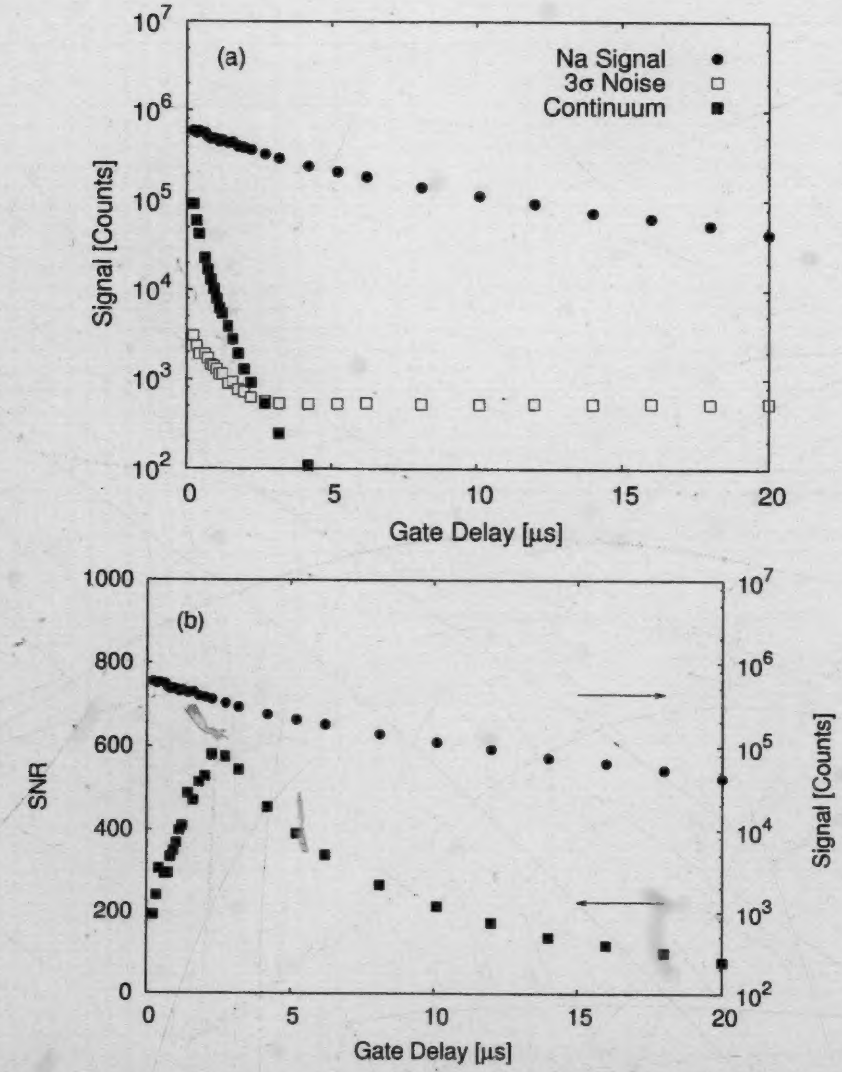

Figure 5.4. *(a) Na emission, background levels, and noise equivalent signal as a function of gate delay. Continuum levels decay below detector equivalent noise power by about 2.5 μs. (b) SNR as a function of gate delay. Optimal SNR with a long gate of 40 μs occurs with a delay of ~ 2.5 μs. Experimental Conditions:* $N_{shots} = 100$, *E = 100 mJ, 972 ppm Na in water,* $T_{gate} = 40$ *μs, Slit = 10 μm. (Reproduced with permission from Taschuk et al. [118])*

ber of photons, obtaining an integrated SNR far greater than the peak values observed in the survey data presented in Figure 5.3.

Once the optimum viewing location has been selected, the detector conditions must be optimised. The method used here is similar to that described by Treytl et al. [138], but was developed independently. In order to avoid the continuum background, the gate delay was set to 2.5 μs for the following detector condition survey. The remaining detector conditions that have the most impact on SNR are gate width and detector gain. Using a gate width step of 0.25 μs and gain steps of 1/10 of the full gain scale, every combination of gate width and gain was tested with an average of 5 shots. The results of this survey are given in Figure 5.5.

The SNR achievable increases at gains from 0.35 to ~ 8 counts/photon, as the sensitivity of the detector increases. As gain is increased beyond ~ 8 counts/photon, there is an increased contribution to the noise floor due to spikes from the cathode of the ICCD. Similarly, as the gate width is increased, more of the long-lived Na signal can be integrated, improving the SNR. However, beyond a gate width of about 20 μs, the increased width of the gate increases the number of noise spikes that are integrated into the accumulation, resulting in a rolling off of the SNR. Optimal detector conditions are found at a gain of 6.3 counts/photon and a gate width of 18.5 μs.

It is important to perform this type of scan with a relatively low concentration of the target element. Unlike the results presented in Fig. 5.5 for a concentration of 20 ppm, for the case of a scan at 2150 ppm Na in water the signal from the Na was so much larger than the noise from detector that there was no roll off in SNR as the gain and gate width were increased. As a result, it would have been possible to misidentify the optimal conditions for the detection of Na in water, and to obtain a poor LOD.

Using the optimal conditions identified in the above optimization sweeps, a LOD experiment for Na in water was undertaken. A solution of ~ 25 ppm Na was prepared, and 100 shots at 45 mJ/pulse were taken. Emission levels and NEISB as a function of Na concentration are presented in Figure 5.6. The solution was then diluted and the measurement repeated. Between measurements, the water jet apparatus was then rinsed with distilled water twice to minimise contamination. This procedure was repeated until the SNR approached a level of 3, which in this case is given by the intersection of best fit lines to the emission data points and the NEISB. The 100 shot detection limit for Na in water using the optimal conditions for viewing and detection was determined to be 24.5 ± 1.4 ppb. The same optimization procedure was performed for Pb, and a LOD experiment yielded a 100-shot detection limit of 7.54 ± 0.49 ppm for 45 mJ laser pulses. The data is presented in Fig. 5.7.

The results of this optimization procedure are competitive with previously reported results, summarised in Figure 5.8 [139–143]. All values re-

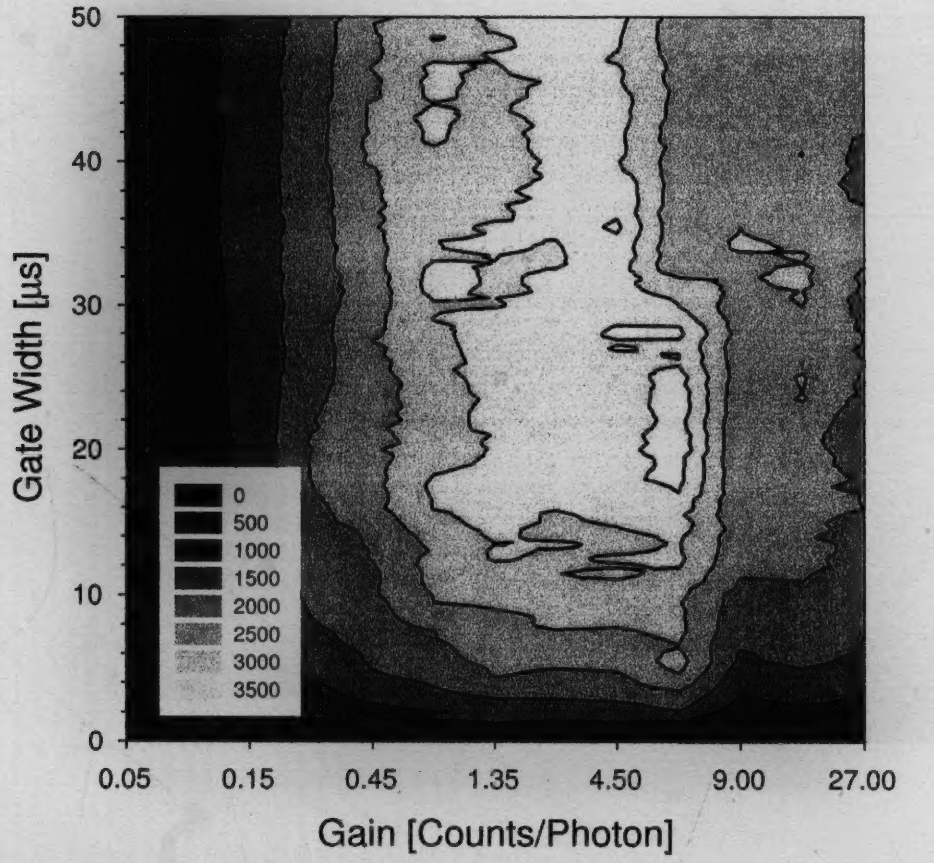

Figure 5.5. A survey of detector gain and gate width for SNR from 20 ppm Na in water. As gain increases, the increased rate of noise from the ICCD cathode causes a decrease in SNR. Similarly, as the gate width increases, more noise events from the cathode are included in the integration. These two factors combine to yield optimal detection conditions at a gain of 6.3 counts/photon and a gate width of 18.5 µs. Experimental Conditions: $N_{shots} = 5$, $E = 45$ *mJ, 20 ppm Na in water,* $T_{delay} = 2.5$ *µs*

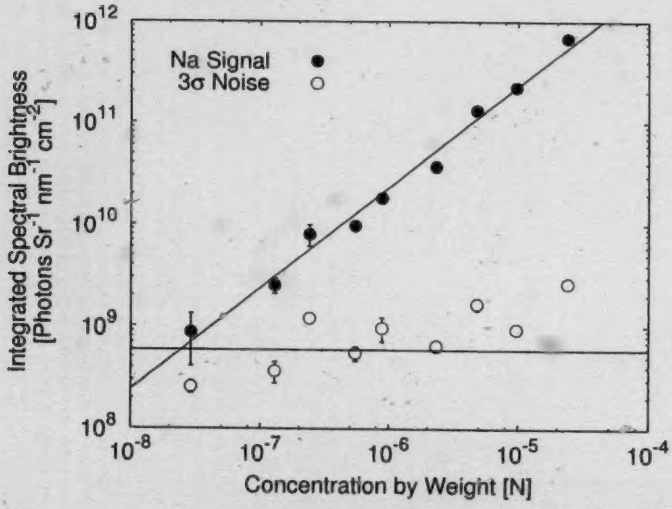

Figure 5.6. *LOD of Na in water at optimal detection conditions. The 100-shot LOD at 45 mJ for Na is ≈ 25 ppb. Experimental conditions:* N_{shots} = 100, *E* = 45 *mJ*, T_{delay} = 2.5 *μs*, T_{gate} = 18.5 *μs*, *Responsivity* = 6.3 *counts/photon.*

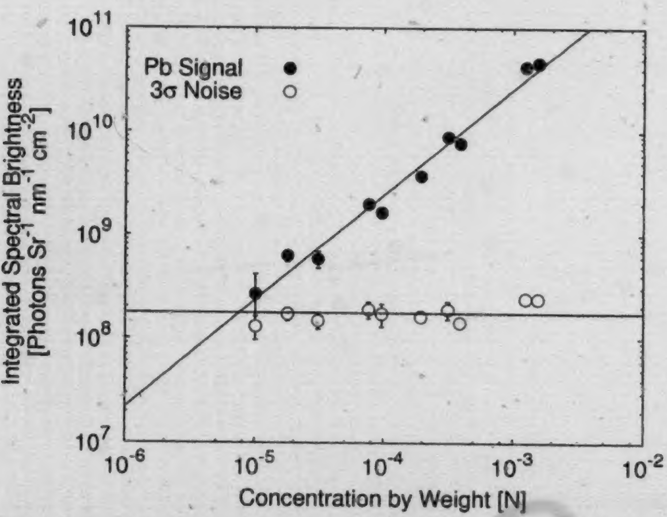

Figure 5.7. *LOD of Pb in water at optimal detection conditions. The 100-shot LOD at 45 mJ for Pb is ≈ 7 ppm. Experimental conditions:* N_{shots} = 100, *E* = 45 *mJ*, T_{delay} = 2.5 *μs*, T_{gate} = 22 *μs*, *Responsivity* = 4.5 *counts/photon.*

ported in this plot are scaled to 100 shot equivalent values using the standard $\sqrt{N_{shots}}$ from the values reported by the authors in question. In cases where a range of energies and shot number was reported, an average was used.

For the case of interactions with the surface of water, the optimization technique presented here improves the LOD achievable by about a factor of 10 over those previously reported. However, there are approaches that exceed the LODs of $\sim$ 25 ppb for Na and $\sim$ 7 ppm for Pb reported here. Knopp et al. use a laser focused into bulk water to achieve a 100-shot LOD of $\sim$ 3 ppb for Na and $\sim$ 5 ppm for Pb [140]. Lo et al. have added an absorbing agent of HCl to their water samples, improving the coupling of laser energy to the target to achieve an impressive 100-shot LOD of $\sim$ 900 ppt Na and $\sim$ 670 ppb for Pb [143]. For μLIBS, 100-shot LODs are $\sim$ 50 ppm for Na [105] and $\sim$ 75 ppm for Pb [106].

It is expected that the benefits of the optimization technique reported here will also help in the use of techniques more complicated than the simple water jet. Hence, it may be possible to improve the LODs presented both here and in the literature by combining the approaches.

5.4 Plume Expansion: Comparison with Simple Blast Wave Models

The theory of shock waves and laser-produced expansion plumes is the subject of a number of papers [41, 42, 44, 130, 144]. Two aspects of the plume expansion are considered in the current work: the value of hydrodynamic quantities as a function of expansion time, and the stagnation distance of the expansion plume. The development of a full hydrodynamic model suitable for the conditions of the LIBS plasma plume studied in these experiments is the subject of an ongoing study.

In order to model the expansion of the plasma plume, ideal shock waves and published curves from Sedov's numerical solutions to hydrodynamic equations have been used. Such models may be used to predict pressure, density and velocity for regions behind the shock front. Combined with the assumption of an ideal gas, it is possible to extract the temperature for all regions behind the shock front. As a result, these models may be used as a foundation for the modelling of plasma emission, which depends on temperature and density. In addition, the stagnation distance of the plume is compared with the model presented by Dyer et al. [44]. In the work that follows, air is approximated as pure nitrogen gas.

In the case of a strong shock where the background gas doesn't affect the propagation of a shock and where heat conduction is neglected the work of Taylor [41] and Sedov [42] is applicable. Taylor and Sedov demonstrated that

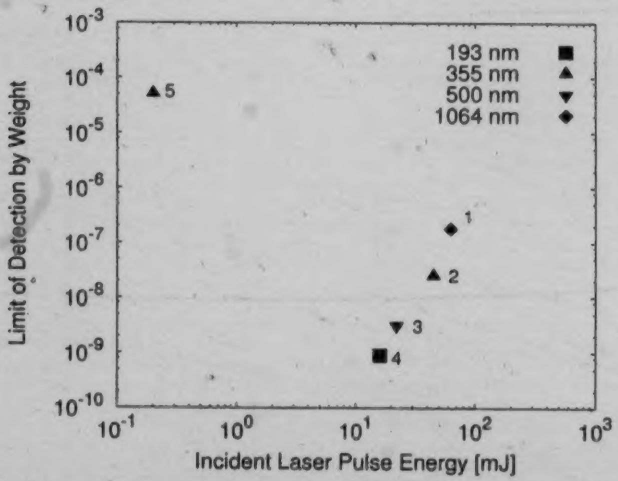

Figure 5.8. Current results compared to literature values for Na LOD as a function of energy. All values have been scaled to a 100-shot, 3σ LOD. 1 = Samek et al. [141], 2 = Present Result, 3 = Knopp et al. [140], 4 = Lo et al. [143], 5 = μLIBS result for comparison, Taschuk et al. [105].

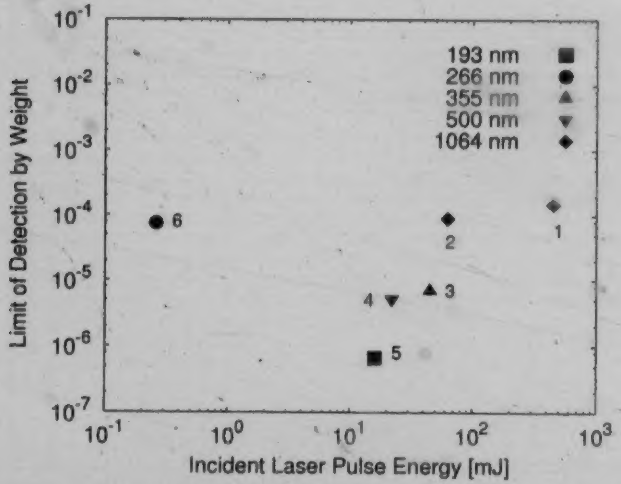

Figure 5.9. Current results compared to literature values for Pb LOD as a function of energy. All values have been scaled to 100-shot, 3σ LOD. 1 = Arca et al. [139], 2 = Samek et al. [141], 3 = Present Result, 4 = Knopp et al. [140], 5 = Lo et al. [143], 6 = μLIBS result for comparison, Godwal et al. [106].

self-similarity may be used to derive shock wave relations for a number of different geometries. In the spherical case, the radius of the shock front may be described as:

$$R(t) = s(\gamma)t^{2/5}E^{1/5}\rho_o^{-1/5} \tag{5.1}$$

where s is a function of γ, the ratio of the specific heats of the background gas, t is time measured from the initiation of the shock, E is the total energy deposited in the blast wave, and ρ_o is the density of the background gas. For an ideal diatomic gas, $\gamma = 1.4$ and $s(\gamma) \sim 1$. Further details regarding the solution of the Taylor/Sedov strong-shock model can be found in Sec. A.4.

The energy absorbed into the shock front is estimated at 30 mJ, based on measurements of transmitted and scattered UV laser light through the water jet. From the pressure and density predicted by the strong shock model, isotherms for the spacetime expansion may be generated. These isotherms may then be compared to the expansion of the plasma as given in Figure 5.3. The emission intensity of the plasma should reflect the temperature of the plasma, and so it is expected that the characteristics of the Na intensity in space and time should be correlated to the temperature isotherms. However, as can be seen in Figure 5.10, the agreement between the strong shock and the observed behaviour of the Na emission in space and time is poor. While the high emission regions for Na are bounded by the shock front, the expected correlation between the Na emission and strong shock isotherms only agrees to ≈ 2 μs. Additionally, as a result of the fact that the strong shock model does not take into account the background gas, the predicted temperature for the region directly behind the strong shock front (the region between 300 K isotherm (d) and the strong shock radius (e) in Figure 5.10.) is less than room temperature. The result clearly indicates that more physics must be included in the calculations.

The next step in increasing model complexity may be found in the work of Sedov [42], in which the case of a point explosion with a non-zero background gas is considered. For comparison with the strong shock case, the two models are compared for the case of $\gamma = 1.4$ at a time of 3 μs in Figure 5.11. The numerical solution yields a shock that is significantly weaker than the ideal shock wave, but that has a higher velocity. Further, the temperature predicted by the numerical solution to the shock wave relations near the shock front exhibits more reasonable behaviour.

Using numerical results reported by Sedov [42], it is possible to calculate temperature profiles for a series of times as the shock wave expands. From the profiles, temperature isotherms have been generated and overlaid on the Na emission map in Figure 5.12. The weak shock front propagates more quickly than the strong shock front (e). The isotherms predicted by the numerical solution lag the shock front, stagnating after about 2 μs. Quali-

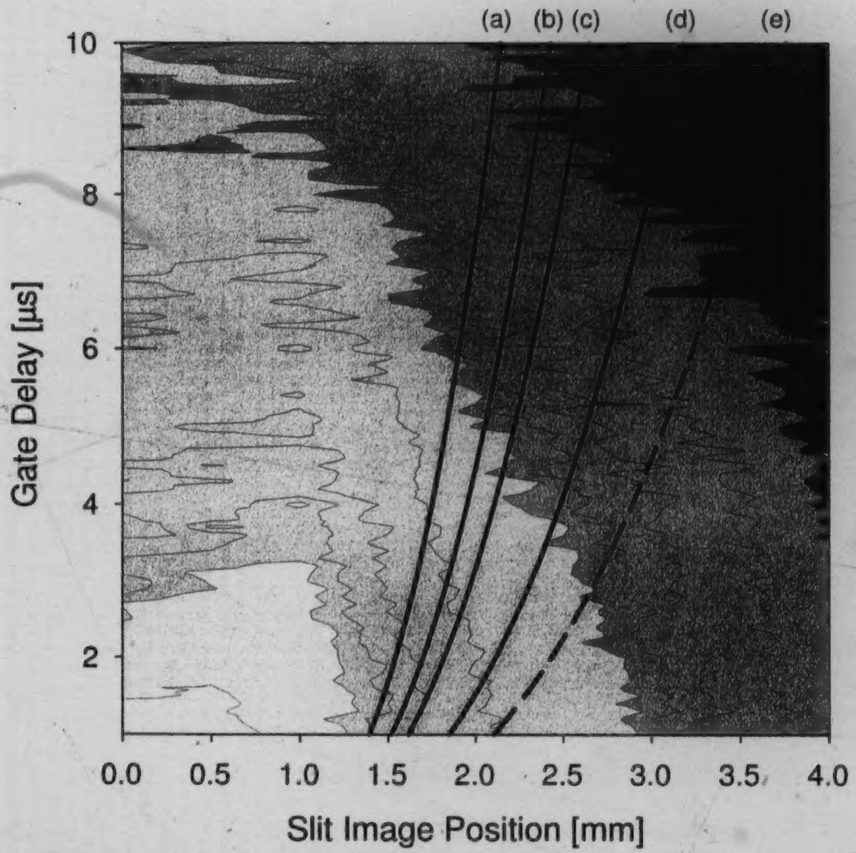

Figure 5.10. *Predicted temperature isotherms from Taylor/Sedov strong shock theory overlaid on Na emission spacetime map. The overlaid curves represent (a) 20000 K, (b) 5000 K, (c) 2000 K, and (d) 300 K strong shock isotherms. Curve (e) is the radius of the strong shock. The regions with high Na emission are bounded by the shock front, but are not correlated with strong shock isotherms.*

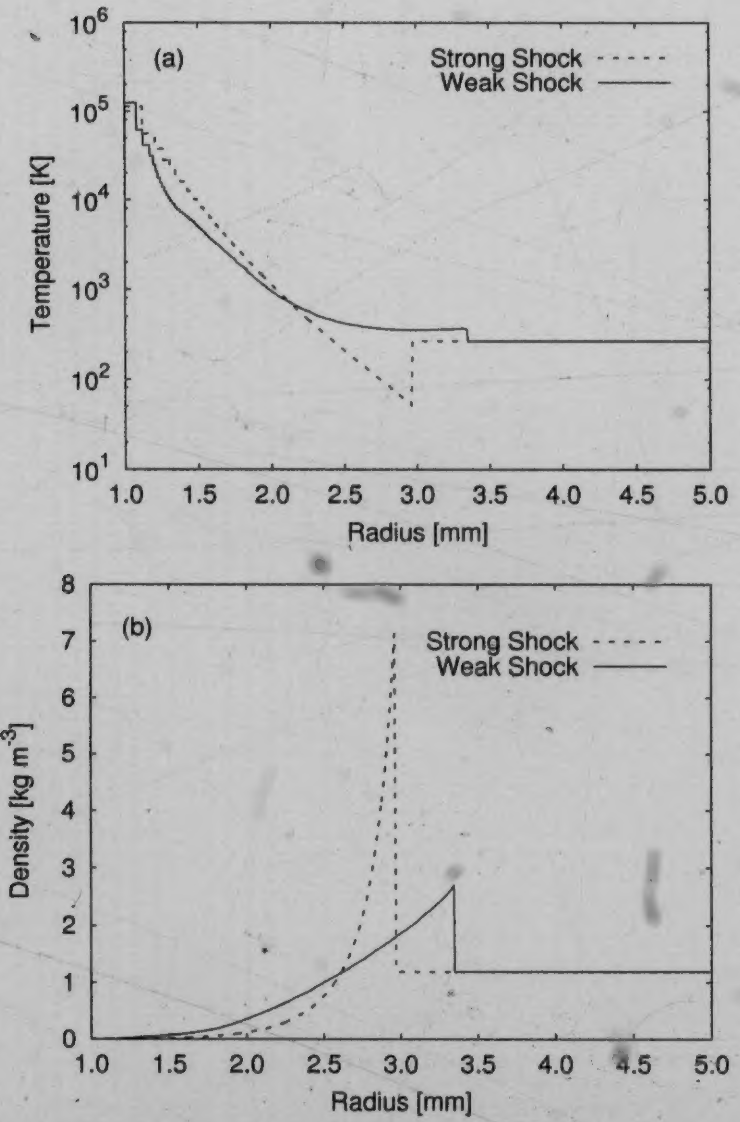

Figure 5.11. *Comparison between strong and weak shock models for (a) temperature and (b) density for an ideal gas at a time of* $\sim 3\ \mu s$. *The numerical solution to the weak shock model predicts a larger radius than the strong shock for all time. The model also predicts physically reasonable temperatures near the shock front, a clear improvement over the strong shock case. Discretization noise occurs in the temperature for the strong and weak shock due to numerical and digitisation errors in the very low densities, respectively.*

tatively, the agreement between the spacetime location of the isotherms and the high Na SNR regions is reasonable. However, at times greater than ≈ 5 μs, there starts to be significant deviation between the predicted location of the temperature isotherms and the location of the region with high Na SNR. The numerical solution to the weak shock front does not include heat conduction, as in the case of the strong shock model. As a result, the hot core of the region behind the shock wave never cools, resulting in a overestimation of the temperature for those regions near the site of the original laser matter interaction. This discrepancy grows worse at later times for which the effects of conduction would be more significant.

The plume stagnation distance has also been studied by Dyer et al. [44] for application to pulsed laser deposition experiments. The authors consider an adiabatic expansion of a plasma plume with a conical expansion geometry. In such a case, the stagnation distance L of the plume was found to be:

$$L = A[(\gamma - 1)E]^{1/3\gamma} P_o^{-1/3\gamma} V_i^{(\gamma-1)/3\gamma} \tag{5.2}$$

where A is a geometric factor which depends on the expansion geometry of the plume. In this case, the plume is assumed to be expanding in a cone with angle θ, capped with a hemispherical tip, such that:

$$A = (1 + 1/tan\theta)[3tan\theta/(\pi + 2\pi tan\theta)]^{1/3} \tag{5.3}$$

This model has been applied for the current case and a number of expansion angles, and is compared to the spacetime expansion data in Figure 5.13. Approximate agreement is found between the stagnation distance and an expansion cone angle of ~ 80° for the high intensity region.

5.5 Plume Emission

To model the plume emission, the isotherms calculated for the previous comparison between Sedov's weak shock calculations and the experimental data presented in Figure 5.12 are used. From Figure 5.12 the region around 3 μs exhibits reasonable agreement in the spatial extend of the observed emission, and the isotherms predicted by the weak shock theory. For the experimental conditions, a delay time of 3 μs and 6.8 μs corresponds to Sedov's L4 and L7 curves [42]. From the curves for pressure and density, it is possible to calculate temperature as a function of radius for the ideal gas.

Thermal equilibrium in the plasma is assumed. In addition, the plasma is assumed to be optically thin at the wavelength in question. The concentration of Na in water was 2000 ppm in this case, which may violate this assumption of optical transparency. However, no saturation of the line emission was observed in previous Na in water experiments for concentrations up to 1000

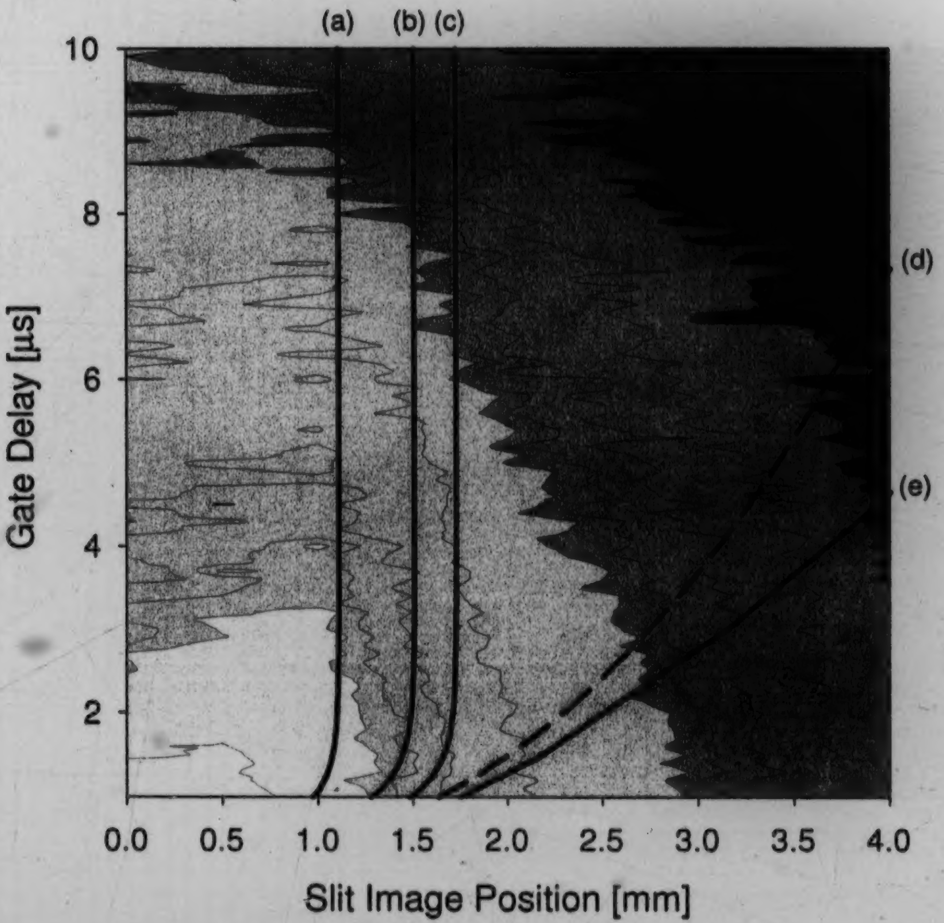

Figure 5.12. *Predicted temperature isotherms from numerical solutions to the weak shock wave case overlaid on Na emission spacetime map. The overlaid curves represent (a) 20000 K, (b) 5000 K, (c) 2000 K, (d) the strong shock radius and (e) the weak shock radius. The temperature isotherms lags the weak shock wave, and stagnates after approximately 2μs. The correlation between the weak shock isotherms and the regions of high Na emission is better than the strong shock model, but deviation occurs at ≈ 3 µs.*

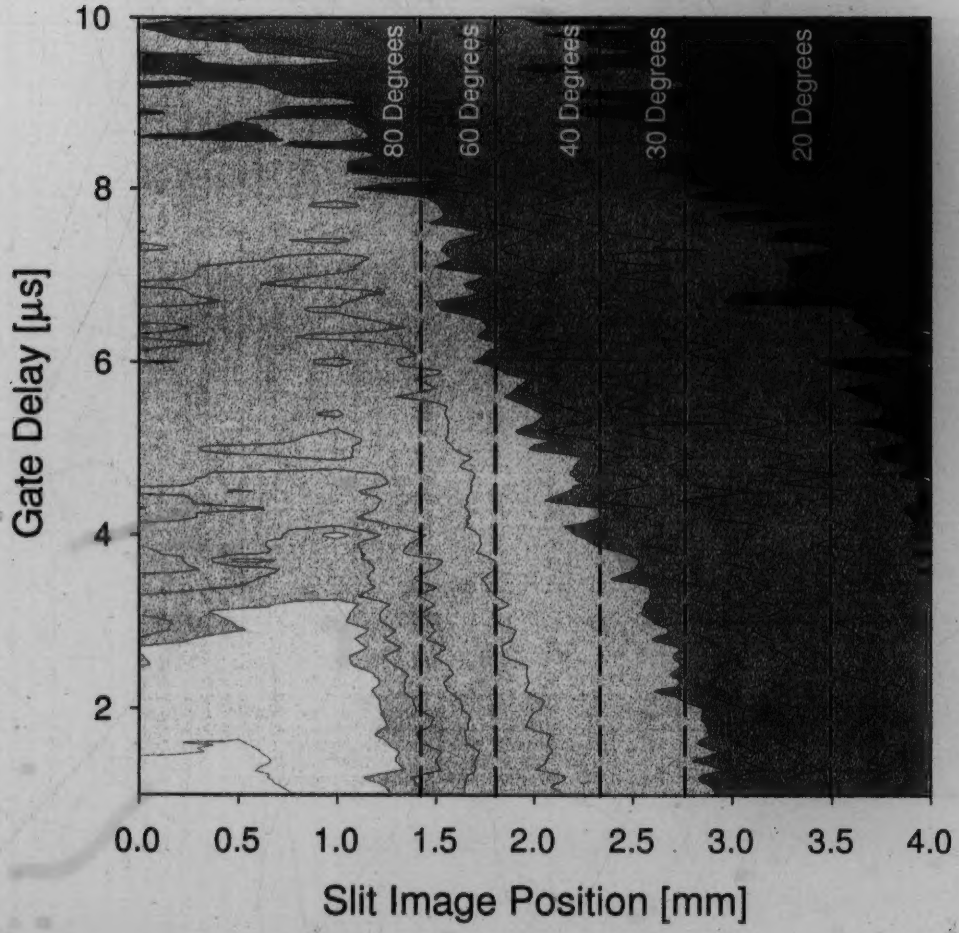

Figure 5.13. *Predicted stagnation distances from the model by Dyer et al. [44] overlaid on the Na emission spacetime map. A number of expansion angles θ are compared to the space time expansion of the plasma plume produced in these experiments.*

Table 5.1. *Simplified Na atomic model. Values obtained from the NIST Atomic Spectra Database (Version 2.0)*

λ [nm]	Upper Energy [eV]	g_n [N]	A $[10^8\ \mathrm{s}^{-1}]$
568	4.283502	4	$1.03 \cdot 10^{-1}$
	4.283502	4	$2.10 \cdot 10^{-2}$
569	4.283498	6	$1.20 \cdot 10^{-1}$
589	2.104430	4	$6.22 \cdot 10^{-1}$
	2.102298	2	$6.18 \cdot 10^{-1}$
615	4.116360	2	$2.60 \cdot 10^{-2}$
	4.116360	2	$5.20 \cdot 10^{-2}$
1138	3.191353	2	$8.40 \cdot 10^{-2}$
	3.191353	2	$1.76 \cdot 10^{-1}$

ppm [118]. The equation describing the emitted power in units of W Sr^{-1} cm^{-3} for a particular line λ is given as [45]:

$$I = \frac{hc}{4\pi\lambda}\frac{n\,(r)\,gA}{Z(T)}exp\left(-\frac{E}{k_BT}\right) \tag{5.4}$$

where the first factor distributes the energy of the emitted photons isotropically into 4π Sr, $n\,(r)$ is the number density of candidate atoms per volume as a function of position, $Z(T)$ is the partition function of the atoms, and E is the energy of the upper level for the transition in question. The spectroscopic parameters g and A are the degeneracy and the spontaneous emission coefficient of the transition of interest respectively. The atomic partition function is given as [45]:

$$Z_n(T) = \sum_n g_n exp\left(-\frac{E_n}{k_BT}\right) \tag{5.5}$$

The atomic model of Na was constructed using the emission lines given in Table 5.1, obtained from the NIST Atomic Spectra Database (Version 2.0). With this data, the partition function as defined in Equation 5.5 can be calculated as a function of temperature. As a result, the partition function is now effectively known as a function of radius from the center of the blast wave, which will allow the calculation of emission as a function of radius once the number density of candidate atoms is known.

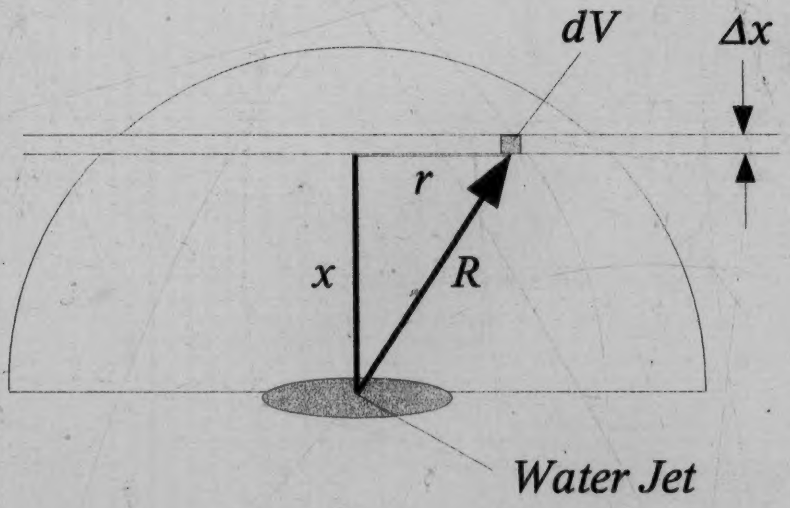

Figure 5.14. A schematic top view of the hemispherical expanding plasma plume with the planar chord viewed by the entrance slit of the spectrometer. The numerical model calculates the properties of dV as a function of R. The cylindrically symmetric integration for emitted energy for a slit width Δx is given by equation 5.6.

The focal spot size on the water jet is approximately 40 μm in diameter. Assuming a hemisphere the size of the focal spot is liberated by the laser pulse, and knowing the concentration of Na in the water jet, it is possible to derive the number of atoms released into the plasma plume. Total mixing is assumed behind the shock front such that the Na atoms will be in the same fractional concentration throughout the blast wave region. The concentration of Na atoms will then depend only on the density as calculated by the Sedov weak shock curves.

At this point it is possible to use Equation 5.4 to calculate the total emission per unit solid angle and unit volume as a function of radius. However, the optics described in Figure 5.1 integrate a planar chord across the expanding hemispherical plasma plume as shown in Figure 5.14. If the emission $P(R)$ is known as a function of radius R, it is possible to calculate the expected integrated energy as a function of slit position, slit width and gate width:

$$E = 2\pi\tau_{gate}\Delta_x \int P(\sqrt{x^2 + r^2})rdr \tag{5.6}$$

The parameter x represents the slit position, as measured from the front of the water jet along the axis of laser propagation. This parameter corresponds exactly to the horizontal axis in Figure 5.3. The variable r is cylindrical radius, also measured from the axis of laser propagation. Gate delay does not come into the equation since each of the Sedov curves correspond to a specific time.

The results of this calculation are presented in Figure 5.15. The results have been converted to units of photons Sr^{-1} cm^{-2} for both the theoretical prediction and experimentally obtained values as the total line emission is the quantity of interest. While the spatial extent of the emission areas for simulation and experiment agree reasonably well for the case of 3 μs, but the absolute emission levels do not. The numerical model due to Sedov does not include heat conduction or consideration of the propagation of material within the blast wave radius, which may explain the deviation between the model and the experimental results.

The lack of heat conduction results in a hot void at the origin of the blast wave that doesn't fill in as the blast wave expands. As a result, the plasma emission model currently overestimates emission close to the surface of the water jet. Further, the effects of the presence of the water jet at a distance of zero have not been considered in the model. For this preliminary work, it was assumed that the Na atoms mix completely with the material behind the shock front in order to account for the spatial dilution of the Na as the blast wave expands. This does not allow for the fact that new air is entrained into the leading edge of the shock plume and thus the sodium atoms will only mix up to a radius that will lag the leading edge of the shock front. In addition, no radiative losses are accounted for in the model, which will become a more significant error as time goes on.

It is clear from these results that a simple blast wave model combined with a simple emission model is not sufficient to explain the experimental observations in detail. Refinements of both the hydrodynamic modelling and emission models would be required to make full use of the experimental data set acquired during the course of these experiments. While approximate agreement has been obtained, it is my feeling that it is fortuitous agreement, rather than an indication that the model is of good quality.

5.6 Conclusion

The expansion dynamics of high-energy LIBS has been investigated in detail, and a high resolution characterisation of absolute emission levels has been performed. Combined with a global detector optimization, this study has allowed the identification of the absolute optimum location in space, time, gate delay, gate width and detector gain for the detection of Na and Pb in water.

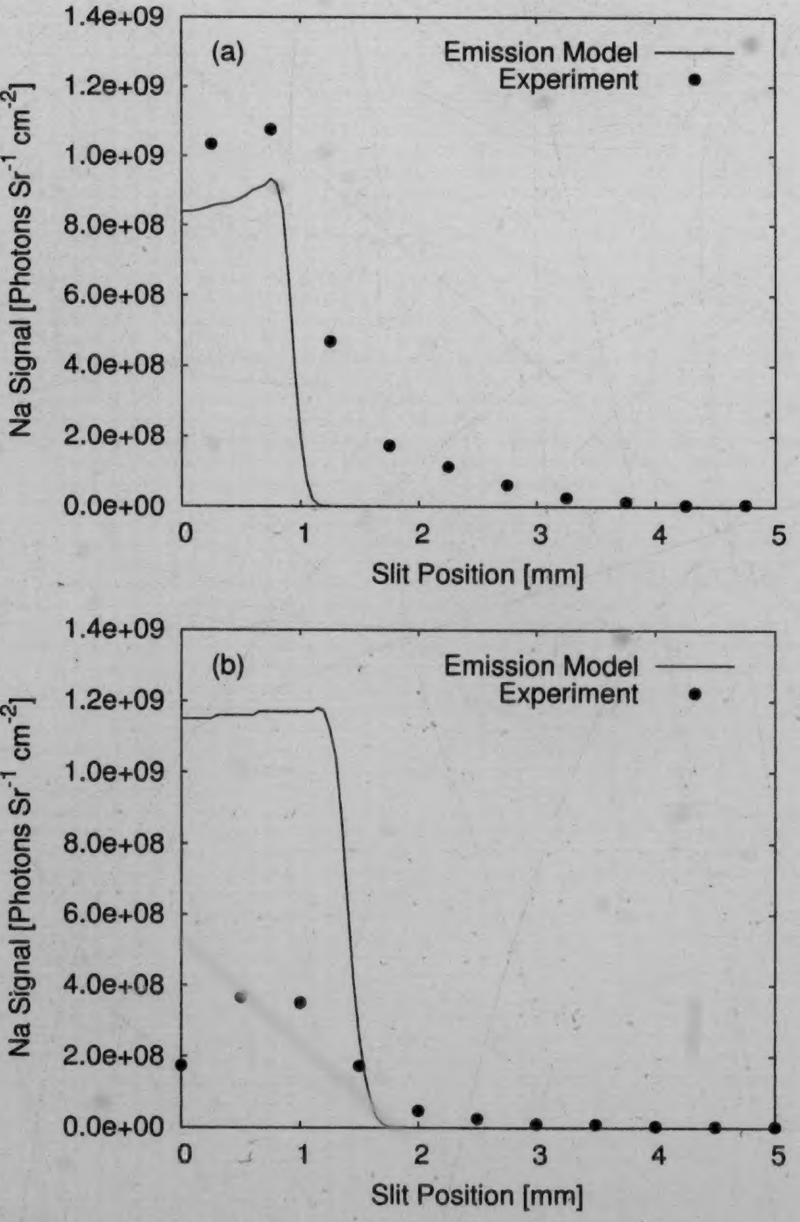

Figure 5.15. *Comparison between a simple emission model and the corresponding experimental data for a time of (a) 3 μs and (b) 6.8 μs after the laser arrives at the water jet.*

At the optimum locations, LOD experiments for Na and Pb have been carried out, and 100-shot LODs of 24.5 ± 1.4 ppb and 7.54 ± 0.49 ppm, respectively, have been obtained. These results compare favourably to literature values for similar experimental setups. Additional optimization opportunities exist in choice of laser wavelength and treatment of the water jet sampling system to enhance absorption of the laser light, as demonstrated by other groups. It is possible that those results would be enhanced by the optimization process presented here.

The expansion dynamics of the plasma plume have been compared to simple blast wave models. Sedov's model of a point explosion with counterpressure has been scaled to the conditions used here, and used to predict temperature, pressure and density for the expanding plume. Combined with a simple model for the spectral emission of the Na atoms, this has allowed a comparison of the quantitative experimental results with theory. While reasonable agreement is obtained for the spatial extend of the plasma, the emission levels do not agree well, especially for later times. The increasing discrepancy in time is likely due to the fact that heat conduction and radiative losses were not included in the model. It is clear that the model doesn't capture the full behaviour of the expanding LIBS plasma, and that further work will be required to make full use of the experimental data set.

Chapter 6

Scaling LIBS to μJ Energies: Microplasma Emission, Ablation Efficiency and Emission Efficiency

6.1 Introduction[1]

In this chapter, the properties of LIBS microplasmas are studied as the pulse energy is reduced below 100 μJ. Absolute emission levels, ablation efficiency and emission efficiency are studied as functions of laser pulse width and wavelength. Laser pulse widths used are 10 ns, 50 ps and 130 fs; wavelengths are 248, 266, 400 and 800 nm. The target samples are Al alloys, a 100 nm Cu layer on Si, and a bare Si wafer. The experimental setups used and analysis procedures are discussed.

It is found that for energies well above the breakdown threshold, laser pulse width is less important to the overall LIBS emission than the energy coupled into the target. Laser wavelength plays a stronger role, but small variations in target reflectivity do not appear to significantly affect the absolute intensity of LIBS emission.

Ablation efficiency is investigated, and is used to quantify the emission efficiency of μLIBS plasmas. It will be shown that the number of atoms ablated from the target is much greater than the number of photons emitted for the strong emission lines observed. The distribution of emitting atoms in the ablation crater is investigated using the Cu thin film targets. For fs μLIBS the emitting region is shallower than the ablation crater, though precise limits were not obtained.

---

[1] Large portions of Sec. 6.2 have been published in [65, 94]

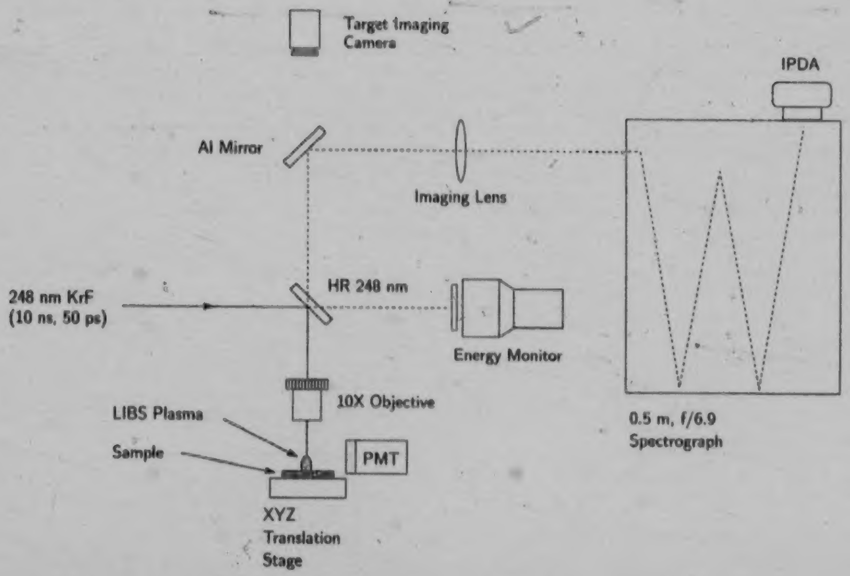
Target Imaging Camera
IPDA
Al Mirror
Imaging Lens
248 nm KrF (10 ns, 50 ps)
HR 248 nm
Energy Monitor
10X Objective
LIBS Plasma
Sample
PMT
XYZ Translation Stage
0.5 m, f/6.9 Spectrograph

Figure 6.1. *Experimental set-up for nanosecond and picosecond results. KrF pulses at 10 ns and 50 ps are focused onto the target using 10X objective. The LIBS emission is captured by the same objective, and imaged onto the entrance slit of the 0.5 m spectrometer. LIBS emission is also measured using a PMT with various interference filters.*

6.2 Experimental Setup

Two setups were used for the experimental data presented in this chapter, one for the nanosecond and picosecond results, and another for the femtosecond results. The experimental set-up for longer ns and ps pulse widths is given in Fig. 6.1. The KrF-excimer laser operates at 248 nm (Excimer 540, Lumonics Corp.) and emits pulses of 10 ns (FWHM) duration when operated at low energies. It can also be seeded with single frequency doubled short pulses from a dye laser (FL 4000, Lambda Physik) yielding 50 ps pulses at energies of up to several millijoules. A saturable absorber was used to ensure clean single pulses [145]. The picosecond data presented here are due to clean single pulses from the normal laser system. The pulse shape was monitored on an oscilloscope for every shot and shots with imperfect pulse shapes were not considered for analysis.

The laser pulses are focused on the samples with a microscope objective (Optics For Research, 15 mm working distance, 10X, N.A. = 0.25 or Carl Zeiss, 10X, N.A. = 0.2) that is also used for collecting the radiation emitted by the plasma. The samples used for the experiments were commercially polished silicon wafers and hand polished aluminum plates. The silicon samples had a highly smooth and polished surface down to the submicron scale level. The aluminum samples, while visibly shiny, still had micron scale surface roughness. Only a small fraction of the full KrF laser beam is selected by an aperture of 3 mm diameter and then expanded with a telescope to 10 mm in order to slightly overfill the microscope objective and to provide a relatively homogeneous laser spot. The focal spot size measured in the plane of the target surface in a knife-edge experiment is approximately 5 μm limited by the quality of the laser beam for both objectives used.

A 0.5 m, f/6.9 spectrometer (Spectra Pro 500, Acton Research) with an intensified multichannel array detector (OMA 1455 G, Princeton Instruments) is used for spectrally resolved light detection. A high resolution grating (1200 lines mm^{-1}) blazed at 500 nm is used for the nanosecond and picosecond experiments described here. Note that this grating is different than the one characterized for this system in Chapter 4. The responsivity, NESB and NEISB results reported there will change as a result of the change of grating. The gate width of the OMA detector is 200 ns and no gate delay is used in experiments with laser energies below 10 μJ; at higher energies delay times of 100 200 ns are used.

The plasma emission was also measured using a PMT coupled with an interference filter. In the case of silicon, a solar blind PMT (Hamamatsu R821) fitted with an interference filter (289 nm, 10 nm FWHM) is used to detect the Si I 288 nm line emission. Additionally, three 1 mm thick WG 280 filters (Schott Glass) were used to filter the laser radiation. In the case of aluminum the two strongest aluminum lines at 394.4 and 396.2 nm are selected by a different interference filter (400 nm, 25 nm FWHM) and are monitored on a PMT (RCA 7265) that has a high sensitivity at 400 nm. A glass window is used in front of the filter to block all UV radiation from the laser. The collection cone angle is $\sim$ 0.4 Sr in both cases. Peak and FWHM values of the PMT traces were measured using an oscilloscope.

All experiments were conducted in air. The target can be exactly positioned using a camera alignment system and a high-precision mechanical translation stage. All experimental results presented in this paper are based on single laser pulses on fresh target spots. The energy of each laser pulse is monitored using a calibrated photodiode (Hamamatsu R1193U-02).

The experimental setup used to characterise the femtosecond plamsas is presented in Fig. 6.2. A Ti:Sapphire is used as the excitation source for the microplasmas investigated here, and the characteristics of the three harmonics used are summarised in Table 6.1. The laser light is focused with a 10X objective or a 10 cm lens. Pulse energy delivered to the target is controlled with both a half-wave plate / Glan-Taylor prism combination and a series of

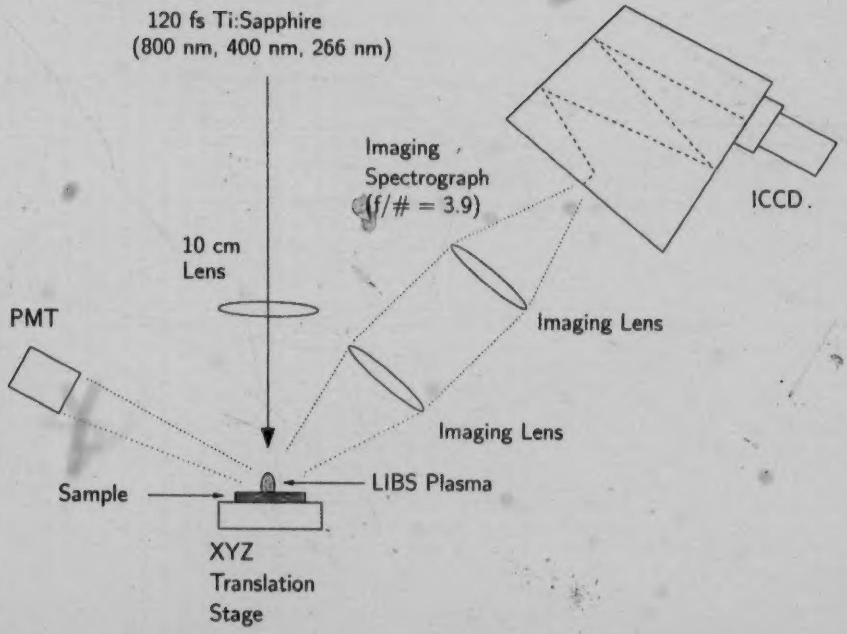

Figure 6.2. Experimental setup used for quantitative characterisation of emission levels from femtosecond laser-induced microplasmas. The fundamental (800 nm), 2nd harmonic (400 nm) and 3rd harmonic (266 nm) are delivered to the setup collinearly. Plasma emission is collected simultaneously by a PMT coupled with interference filters for the wavelength of interest, and a imaging spectrograph and ICCD combination.

calibrated filters. A photodiode (FND-100) has been calibrated with a power meter (SpectraPhysics 407A) for energy delivered to the target plane and is used as a shot to shot energy monitor.

The precision of the energy calibration factors has been monitored for all wavelengths over the course of the experiments reported here. The estimated accuracy for the incident pulse energies reported in the paper are also reported in Table 6.1, having combined the day to day precision with the accuracy of the power meter standard. The high value for 266 nm is due to the fact that the overall energies are much lower, and precise readings with the power meter become more difficult.

The targets used in these experiments are an aluminum alloy (Al 5052), a 100 nm thick film of Cu on Si wafers, and a bare Si wafer. The reflectivity of each of these targets is given in Table 6.2. For the Cu and Si targets, the reflectivity was measured for the various excitation wavelengths used here.

Table 6.1. Femtosecond Laser Characteristics

Laser Wavelength	800 nm	400 nm	266 nm
Maximum Energy	350 μJ	110 μJ	25 μJ
Focal Spot (FWHM)	17.8 ± 0.2 μm[a]	8.7 ± 0.1 μm[a]	5.8 ± 0.2 μm[b]
Pulse Width (FWHM)	~ 130 fs	~ 130 fs	~ 130 fs
Energy Calibration Accuracy	6%	8%	18%

[a] Focal spot imaged onto calibrated CCD

[b] Focal spot obtained from D^2 method [146]

Table 6.2. Target Reflectivities and Observation Wavelengths

	Laser Wavelength			Observation	Observation
Target	266 nm	400 nm	800 nm	Wavelength	Bandwidth
Al 5052 Alloy	~ 0.7	N/A	~ 0.7	400 nm	25 nm
Cu (100 nm on Si)	0.29	0.39	0.97	326 nm	10 nm
Si Wafer	0.67	0.48	0.33	288 nm	10 nm

In the case of the Al target, the surface was too rough to get a good specular reflection. For another aluminum alloy sample (Al 2024), a specular reflection was obtained, and that value is used here as an estimate.

The emission from the microplasmas is monitored by a photomultiplier tube (PMT) coupled to interference filters, and with a 1/4 m, f/3.9 spectrometer (Oriel MS260i) coupled to an intensified CCD (Andor iStar DH720). PMT signals were measured for peak and full-width at half-maximum (FWHM) to estimate the area under the curve. The PMT used for the femtosecond experiment has been calibrated using a pulsed laser together with a barium sulphate diffuser plate to provide a known intensity source with an absolute error of ± 15%. The spectrometer/ICCD combination has also been calibrated with the same source, as well as with a Hg lamp with known brightness [113], and compared to the manufacturer specifications. The three calibration sources for the spectrometer/ICCD agree to within about 40%, and the absolute error in spectral intensity values is estimated at that value. Interference filters were used to reduce the response of the PMT to background continuum from the microplasma. Observation wavelengths and filter bandwidths are given in Table 6.2.

6.3 Absolute Emission Scaling of μLIBS Plasmas

6.3.1 Laser Pulse Width Scaling: Experimental Results

The pulse width scaling of Si and Al has been investigated using UV laser pulses with 10 ns, 50 ps and 130 fs pulse widths. The 10 ns and 50 ps data used KrF pulses at 248 nm, and the 120 fs data used a frequency-tripled Ti:Sapphire at 266 nm. While this difference in laser wavelength is not ideal, it is not expected that the material response will vary significantly over this limited range. In these experiments, the absolute emission levels from Al and Si microplasmas are characterised as a function of energy, and plasma emission thresholds are quantified.

The emission scaling for Si microplasmas is presented in Fig. 6.3 and Fig. 6.4. In the case of the 10 ns and 50 ps data, the vertical scale does not directly correspond to photons Sr^{-1}. Above $\sim 3 \cdot 10^7$, the PMT used began to saturate, responding nonlinearly to increased emission. Below $\sim$ 3 μJ, emission rolls off at different rates for the two pulse widths. The emission generated by 10 ns pulses approaches the noise floor of the PMT at an energy of $\sim$ 1 μJ; the 50 ps pulses at an energy of $\sim$ 0.1 μJ. The Si microplasma emission scaling for femtosecond UV pulses is given in Fig. 6.4. For pulse widths of $\sim$ 120 femtoseconds, the emission is at levels similar to those observed for the 10 ns pulses; the emission thresholds also agree. For both the Al and Si emission, the noise floor of the PMT used for the femtosecond data is off the plot, at $\sim 10^3$ photons Sr^{-1}.

The behaviour of Al microplasmas was found to be similar to that of Si, though the scatter is significantly greater. The increased variability may be due to the greater surface roughness of the target as compared to the Si wafers. Nanosecond and picosecond results for Al microplasmas are presented in Fig. 6.5; femtosecond results in Fig. 6.6. In this case the emission for 10 ns and 50 ps pulses begins to separate at $\sim$ 2 μJ. The emission due to 10 ns pulses decreases to the noise floor at an energy of $\sim$ 1 μJ; the 50 ps pulses at an energy of $\approx$ 0.1 μJ. Significant scatter exists in the picosecond data, with emission observed with energies as low as $\sim$ 10 nJ. As observed in the Si data, for pulse widths of $\sim$ 120 fs the emission threshold has increased above the $\sim$ 0.1 μJ emission threshold of the 50 ps pulses.

6.3.2 Laser Pulse Width Scaling: Discussion

Based upon heat diffusion arguments, a $\sim \sqrt{\tau}$ dependence of the ablation threshold fluence on laser pulse width is expected for the range between 1 ps and $\sim$ 1 ns. The ablation fluence threshold is therefore expected to drop by about a factor of 14 as one moves from 10 ns pulses to 50 ps pulses. In Fig. 6.3, a factor of 10 decrease in the plasma emission threshold is noted. The

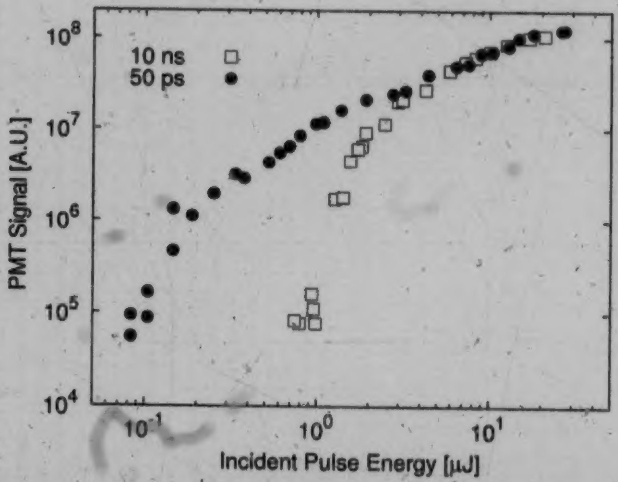

Figure 6.3. Time integrated emission of Si I 288 nm as measured with a photomultiplier. For signals below approximately $3 \cdot 10^7$ on the vertical axis the arbitrary units correspond to total photons emitted per steradian. (Reprinted from Rieger et al. [65] with permission from Elsevier)

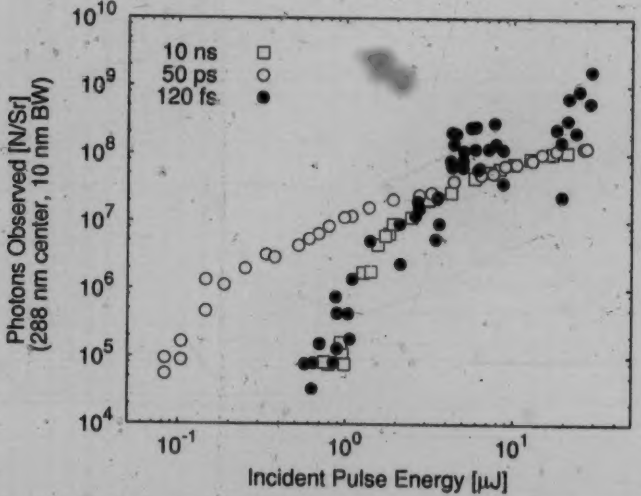

Figure 6.4. Time integrated emission of Si I 288 nm as measured with a photomultiplier for femtosecond pulses. The longer pulse data from Fig. 6.3 is plotted for comparison. The femtosecond data is similar to the nanosecond data.

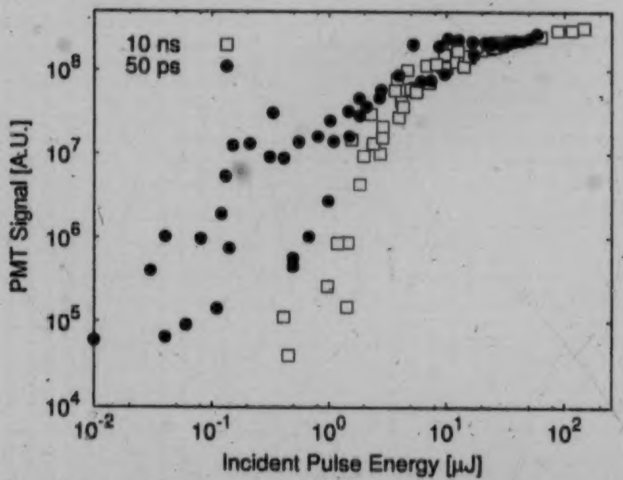

Figure 6.5. Time integrated emission of Al I (394.4, 396.2 nm) as measured with a photomultiplier. For signals below ≈ $4 \cdot 10^7$ on the vertical axis the arbitrary units correspond to total photons emitted per steradian. (Reprinted from Rieger et al. [65] with permission from Elsevier)

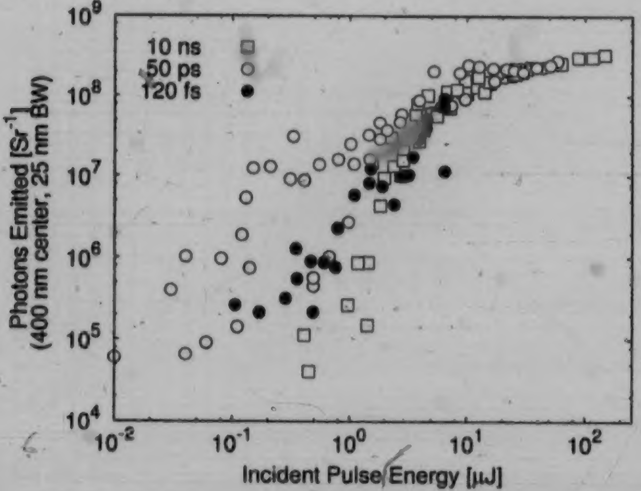

Figure 6.6. Time integrated emission of Al I (394.4, 396.2 nm) as measured with a photomultiplier for femtosecond pulses. The longer pulse data from Fig. 6.5 is plotted for comparison.

data is not as clear for Al due to the larger scatter observed.

As the pulse width of the laser decreases below the response time of the material in question (on the order of 1 ps), the $\sqrt{\tau}$ scaling will not continue. Nevertheless, the ablation threshold is not expected to increase at lower pulse widths, but instead remain constant. Thus, another mechanism must be responsible for the change in plasma emission threshold as one moves from 50 ps to 120 fs pulse widths. As a result, we may conclude that the ablation fluence threshold and the plasma emission threshold are different, and that the difference is a function of pulse width. The discrepancy between the expected ablation threshold scaling and the observed plasma emission threshold may be due to the fact that there is limited laser-plasma interaction in the case of the femtosecond pulse. In the case of nanosecond and picosecond plasmas, laser energy can be absorbed directly by the plasma, causing an increase in plasma temperature. While the ablation threshold (in terms of pulse energy) should decrease with the pulse width, it may be that the lack of a plasma heating mechanism at shorter pulse widths causes an increase in the plasma emission threshold. In this case, higher energies would be required to excite the emission of the species which are ablated from the surface.

An alternative explanation is the limited interaction depth of femtosecond LIBS, which will be introduced in Sec. 6.6. It is expected that the aluminum target would exhibit a surface oxide layer, and a similar layer may exist on the Si wafer as no special cleaning treatment was performed. As will be discussed in Sec. 6.6, the layer that contributes to LIBS emission is a fraction of the total ablated depth. In cases where a surface oxide layer exists, the bulk material will have a reduced contribution to the LIBS emission, which may explain the behaviour observed in the previous section.

In most cases, LIBS is performed at intensities much greater than the ablation threshold. Above an energy of a few μJ, the emission strength for all pulse widths is similar, suggesting that for most cases in LIBS the pulse energy used will be more important than the pulse width of the laser.

6.3.3 Laser Wavelength Scaling

The quantitative scaling of emission of Al, Cu and Si microplasmas excited by 800 nm, 400 nm and 266 nm femtosecond laser light with incident pulse energies from 100 μJ down to 100 nJ is presented. Using 800 nm, the emission from the solid targets is compared with the emission from air breakdown with the target removed.

The energy scaling of microplasma emission using 800 nm laser pulses is presented in Fig. 6.7 through 6.9 for Si, Cu and Al respectively. For the microplasma emission, single shot data was acquired at various energies. For Al and Cu a 10 cm lens was used to focus the laser light, while in the case

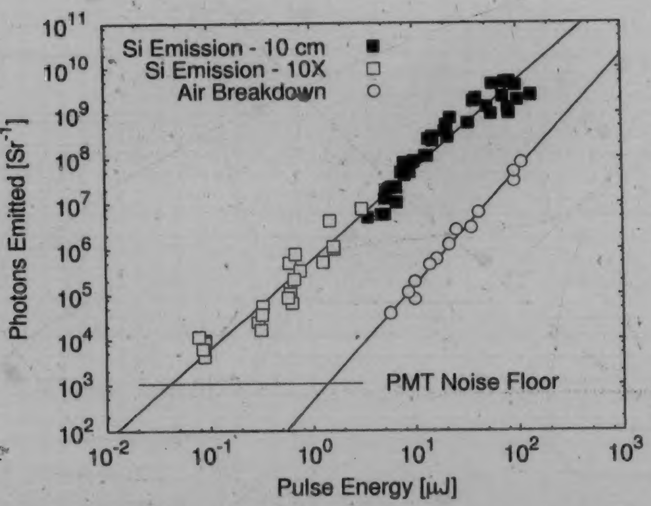

Figure 6.7. *Quantitative emission levels from Si plasmas induced by 800 nm pulses. The solid lines are power law fits. Si data points are single shot, while air breakdown points are an average of 16 shots. The horizontal line represents the noise equivalent intensity of the PMT at 290 nm. (Reproduced with permission from Taschuk et al. [94])*

of Si both a 10 cm lens and a 10X objective were used. For measurements of the emission from air breakdown, 16 shot averages were taken with the target removed from focus using the 10X objective in all cases. In all cases, the air breakdown is significantly less than the emission observed when a solid target is present at the laser focus.

In the case of Si microplasmas, the energy scaling is preserved across the transition from the 10 cm lens to the 10X objective. There is no difficulty detecting the Si microplasma down to $\sim$ 100 nJ per pulse where the emission trend approaches the noise floor of the PMT. The solid angle observed by the PMT is $\sim 9 \cdot 10^{-3}$ Sr, so a noise floor of $\sim 10^3$ photons Sr^{-1} corresponds to a detection limit of $\sim$ 9 photons. The noise floor varies with observation wavelength due to the quantum efficiency of the PMT and the transmission of the interference filters used.

The emission levels per unit energy for Cu (Fig. 6.8) and Al (Fig. 6.9) are much lower than that of Si. In both cases, the higher noise limit of the PMT is met even before the 10X objective can be used. In addition, if the emission trends for Al and Cu were to continue across a transition to the 10X objective, one would expect to start having difficulty differentiating the microplasma signal from the background air breakdown. This effect was observed in ex-

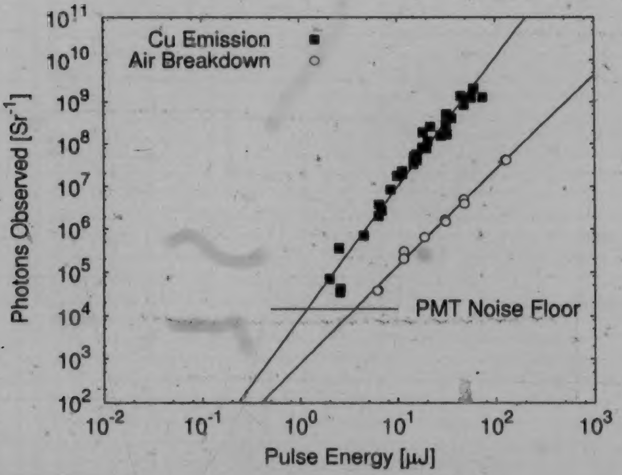

Figure 6.8. Quantitative emission levels from Cu plasmas induced by 800 nm pulses. The solid lines are power law fits. Cu data points are single shot, while air breakdown points are an average of 16 shots. The horizontal line represents the noise equivalent intensity of the PMT at 324 nm. (Reproduced with permission from Taschuk et al. [94])

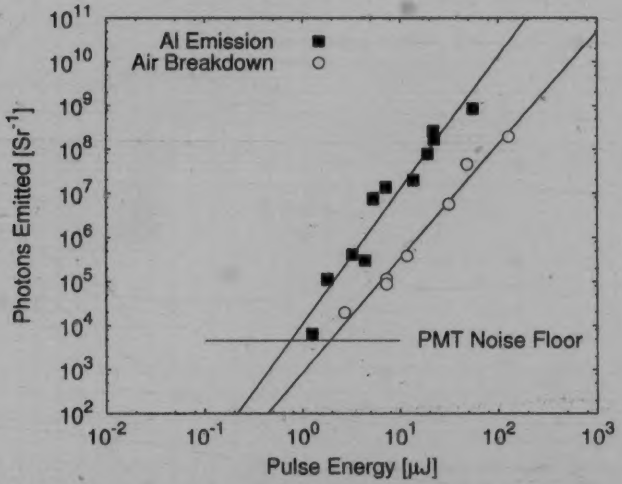

Figure 6.9. Quantitative emission levels from Al plasmas induced by 800 nm pulses. The solid lines are power law fits. Al data points are single shot, while air breakdown points are an average of 16 shots. The horizontal line noise equivalent intensity of the PMT at appropriate 400 nm. (Reproduced with permission from Taschuk et al. [94])

periments with the 10X objective for Cu emission, where it was not possible to reliably differentiate between microplasma emission and air breakdown.

One possible explanation for the enhanced emission of the Si microplasma when compared to the Al and Cu microplasmas may be the large difference in reflectivities. In order to further investigate the reflectivity, the wavelength scaling of emission from the same targets has been investigated. The absolute emission from Cu as different wavelengths is given in Fig. 6.10. As seen in Table 6.2, the reflectivity of Cu drops significantly as one moves from 800 nm to 400 nm and 266 nm. To first order, one would expect that more energy would be coupled as the reflectivity drops. As seen in the pulse width scaling, the energy used to initiate a LIBS plasma has a very strong effect on the absolute emission levels. The absolute emission is expected to follow the absorbed energy, and the results presented in Fig. 6.10 agree with this interpretation.

Since the observation wavelength for Al targets includes 400 nm, it is not possible to use the second harmonic of the Ti:Sapphire without severely damaging the PMT. Thus, only 800 nm and 266 nm were used, and the emission results are presented in Fig. 6.11. The Al target used here was too rough to get a specular reflection, and the reflectivity was not measured. Using another alloy with a polished surface produced reflectivities of ~ 0.7 for 800 nm and 266 nm.

For the 800 nm results, the Al emission begins to roll off as the pulse energy used is reduced below ~ 6 μJ. The Al emission for 800 nm laser pulses decreases to the noise floor of the PMT at ~ 1 μJ, suggesting that the breakdown threshold has been reached. Since the 266 nm pulses have a smaller beam waist, the intensity is larger. Therefore, despite the similar reflectivities, the 266 nm emission results continue the emission scaling down to an energy of ~ 100 nJ. The solid line is a power law fit to the 266 nm data and the 800 nm data above 10^6 photons Sr^{-1}.

Finally, the wavelength scaling of Si microplasmas is presented in Fig. 6.12. In this case there is not much variation with the laser wavelength used, despite the factor of two change in reflectivity. While the change in reflectivity is large, it is much less than the reflectivity change in Cu as one moves from 800 nm to 266 nm. From the results presented in this section, it is clear that reflectivity of the target plays a role in determining the overall emission strength of LIBS plasmas. However, the results do not exactly follow the small signal reflectivities presented in Fig. 6.2, suggesting that a more detailed understanding of the reflectivity is required. The behaviour of target reflectivity during laser-matter interactions has been shown to be complicated, depending on incident fluence [147] and target thickness [148]. Further work would be required to evaluate these effects for the results presented here.

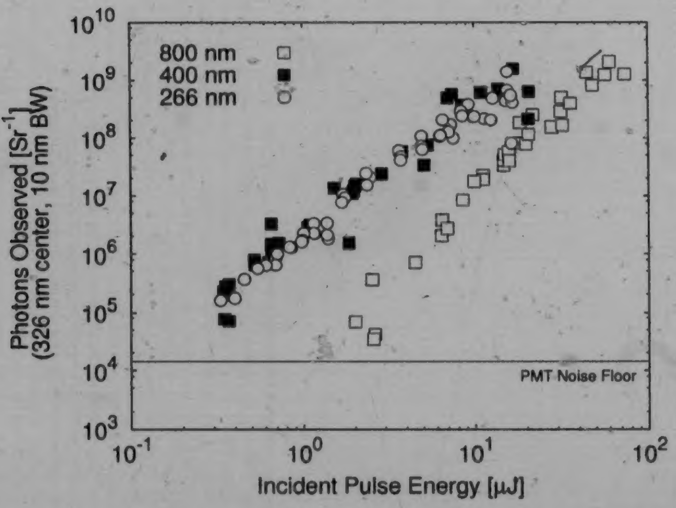

Figure 6.10. *Wavelength dependence of Cu microplasmas. A strong dependence on the linear reflectivity is observed, with increased absorption yielding higher emission levels at lower incident pulse energies.*

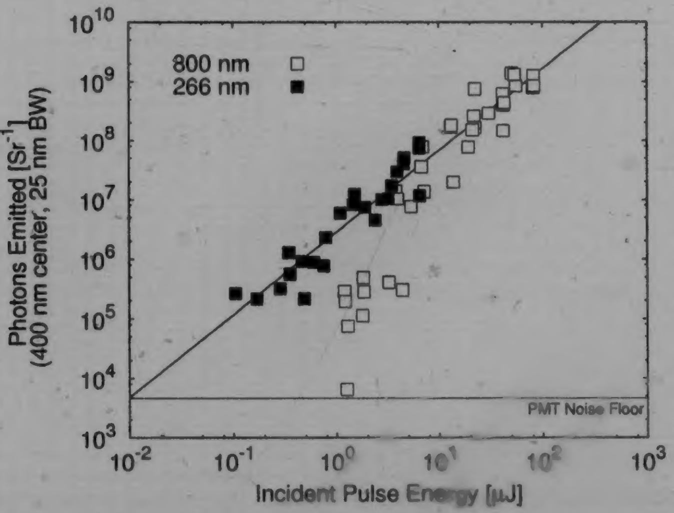

Figure 6.11. *Wavelength dependence of Al microplasmas. Overall behaviour of the emission scaling is similar, except for the emission threshold for 800 nm being reached by about 1 μJ. As the focal spot for the UV pulses is smaller, the incident fluence is higher, allowing the energy scaling of emission to continue to ∼ 100 nJ.*

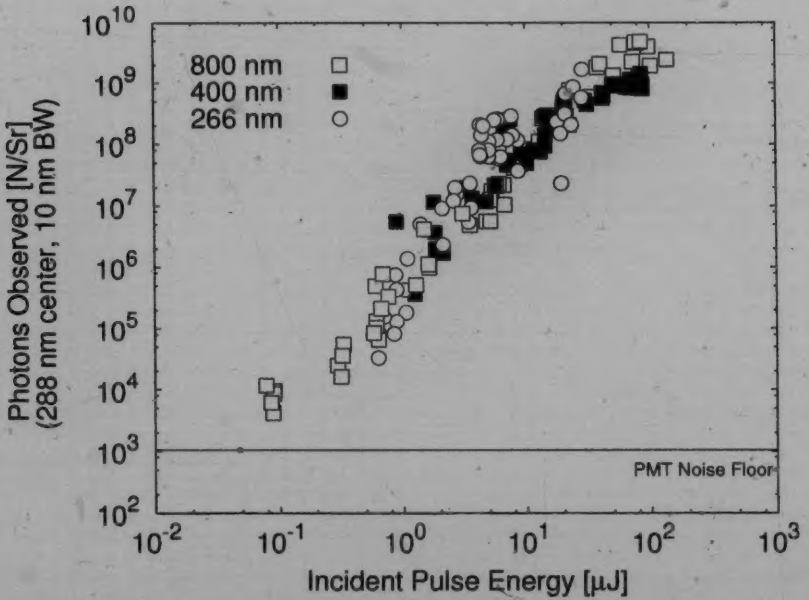

Figure 6.12. *Wavelength dependence of Si microplasmas. The changes in incident reflectivity do not appear to affect the overall emission levels observed here.*

6.4 Ablation Efficiency of μJ Laser Pulses

The sample volume of μLIBS is one of the parameters that will impact the overall performance of the technique. As the laser pulse energy used is reduced, the ablation volume will decrease, limiting the number of atoms liberated from the target. In this section, ablation efficiency is studied as a function of incident laser energy and wavelength. Ablation efficiency is defined in terms of volume ablated per unit energy, with units of $\mu m^3\ \mu J^{-1}$. A Si wafer ablated with 130 fs laser pulses at 800 nm, 400 nm and 266 nm with pulse energies between 100 nJ and 100 μJ is used as the sample. It was not possible to locate the Al craters ablated by femtosecond pulses because the surface roughness of the target was too great, so they are excluded from this study. The Cu targets used in the previous section are also excluded, because the pulse energies used here ablated through the 100 nm Cu thin film into the Si substrate. This effect will be discussed further in Sec. 6.6.

Ablation craters were measured using an optical profilometer (Zygo New View 5000). This instrument is capable of measuring a 2D surface profile through white light inteferometery. Two orthogonal line outs per crater were taken from the 3D surface plot for each crater. Crater line outs were fit with a

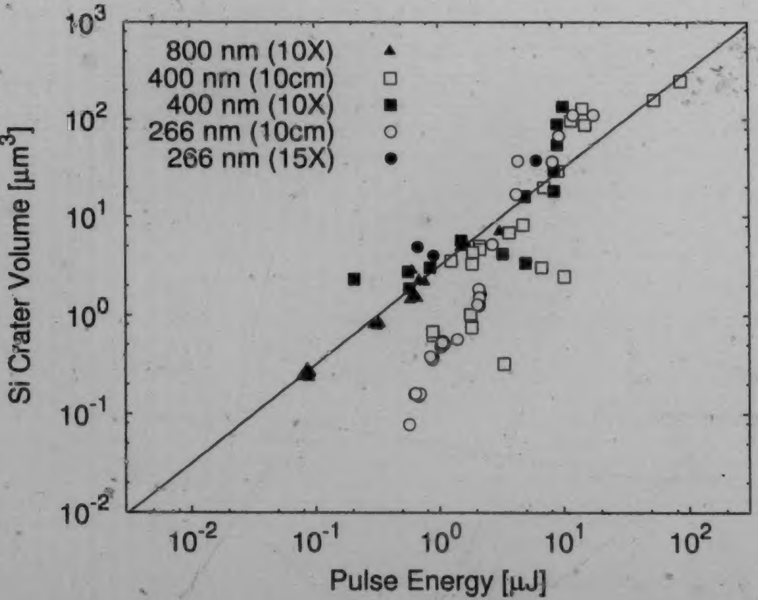

Figure 6.13. *Si crater volumes for a variety of conditions. Open symbols were taken with a 10 cm lens; closed with a microscope objective. 10 cm lens data is rolling off below a pulse energy of ~ 2 μJ. The solid line is a best fit, described in the text.*

modified Gaussian function as given in Equation 6.1, where D is the nominal depth, x_0 is the center of the crater, σ is a width parameter, and d is a parameter which governs the flatness of the peak region of the modified Gaussian function.

$$y = -Dexp(-\frac{(x-x_o)^d}{2\sigma^d}) + y_o \tag{6.1}$$

Each crater was fit using the modified Gaussian function, which was then numerically integrated to provide an estimate of the total volume ablated from the Si wafer. Each trace was inspected to evaluate the quality of the fit, and only those which exhibited good agreement were used for the results are plotted in Fig. 6.13.

A wide variety of conditions for Si ablation volume are presented in Fig. 6.13. This data set is composed of shots at all of the wavelengths used, and with different focal lenses. Open symbols were taken with a 10 cm lens; closed used a microscope objective. As the energy decreases below ~ 2 μJ, the open symbols for 266 nm and 400 nm begin to roll off as the breakdown threshold is approached. Data for both 266 nm and 400 nm taken with microscope objectives yield a higher ablation volume compared to the data taken with the 10 cm lens for energies below 2 μJ, further supporting the conclusion that the 10 cm data is approaching the breakdown threshold.

In previous reports [56, 61, 62, 94], and in the aluminum data presented above, ablation volume was found to be linear with pulse energy. The solid line in Fig. 6.13 is a best linear fit to the data, with the 10 cm data approaching the breakdown threshold having been excluded. This fit can be used to estimate the ablation efficiency for femtosecond laser pulses well above the ablation threshold. Under these conditions, the ablation efficiency for Si is $\approx 3\ \mu\text{m}^3\mu\text{J}^{-1}$. There is significant scatter in the current Si data set, so this value must be considered preliminary.

6.5 Emission Efficiency of μLIBS Plasmas

This section will combine the absolute efficiency data with the ablation rates to given an estimate of the emission efficiency of the LIBS process. Emission efficiency is defined in terms of photons emitted per atom ablated, and gives some insight into the performance of a μLIBS plasma as a spectroscopic source. A Si wafer ablated with 130 fs laser pulses at 800 nm, 400 nm and 266 nm with pulse energies below 100 μJ is used as a target sample.

A few assumptions are made in order to use the data presented in Fig. 6.12 and 6.7. The plasma emission is assumed to be isotropic, and to emit over the 2π Sr emission angle not blocked by the Si wafer. Having obtained an estimate of the total number of emitted photons, the ablation efficiency scaling derived in the previous section may be used to estimate the number of atoms liberated from the target. The results of this analysis are presented in Fig. 6.14.

Data with energies below 2 μJ for the 10 cm data were not plotted in this figure as the fit presented in Fig. 6.13 will not be valid. The solid line is a power law fit with a dependence of 1.85 ± 0.05. Overall, the number of photons emitted is far less than the number of atoms ablated from the target. At energies of ~ 100 nJ, less than 1 atom in 10^5 emits. The emission efficiency increases to ~ 1 atom in 10^3 for pulse energies of 100 μJ.

The PMT used to acquire the LIBS signal for these experiments integrates in time the total emission for the spectral bandwidth given in Table 6.2. The data presented in Fig. 6.14 can be explained by the small number of atoms which leave the target in an excited state compared to the number of of atoms which leave the target as neutrals, clusters, liquid droplets or solid fragments. Other energy loss mechanisms include continuum emission, other atomic emission lines and the transfer of energy to hydrodynamic expansion.

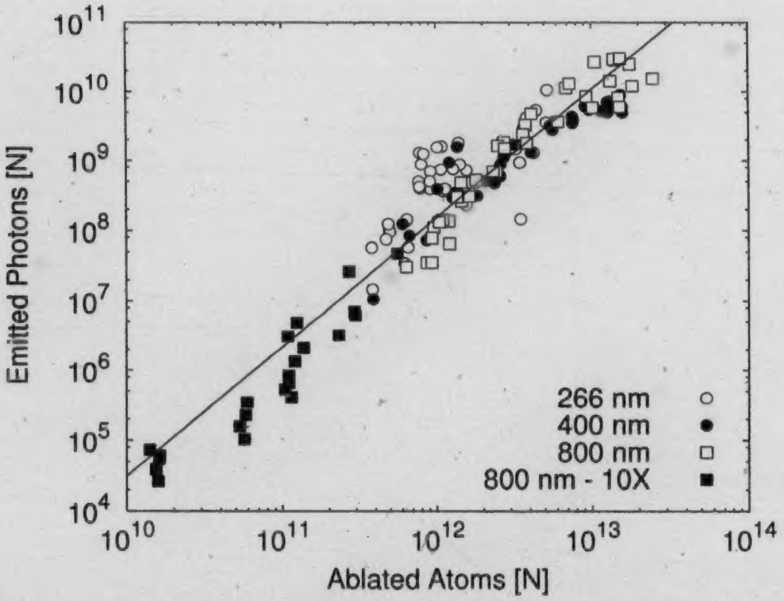

Figure 6.14. *Si emission efficiency for different laser wavelengths and focal conditions. The solid line is a power law fit with a dependence of 1.85 ± 0.05.*

The overall conclusions will hold, despite the scatter in the ablation efficiency data. A more accurate picture of the overall scaling could be obtained with further work. Also of interest would be an extension of this work to high energies, to determine the emission efficiency under more traditional LIBS conditions.

6.6 Interaction Depth of fs μLIBS

The previous section has shown that the number of photons emitted from a LIBS plasma is much less than the number of atoms liberated from the target. This section will investigate the distribution of emitting atoms from the ablated volume by investigating the ablation craters and emission behaviour of the Cu thin films used in this study. The Cu targets used in this work were fabricated using thin film deposition on Si substrates. The Cu thickness was ~ 100 nm. The ablation craters that were produced on the Cu targets penetrated into the Si substrate when pulses of sufficient energy were used. Depth profiles of the two ablation craters are presented in Fig. 6.15.

Despite the fact that the Si substrate is ablated by the time a pulse energy

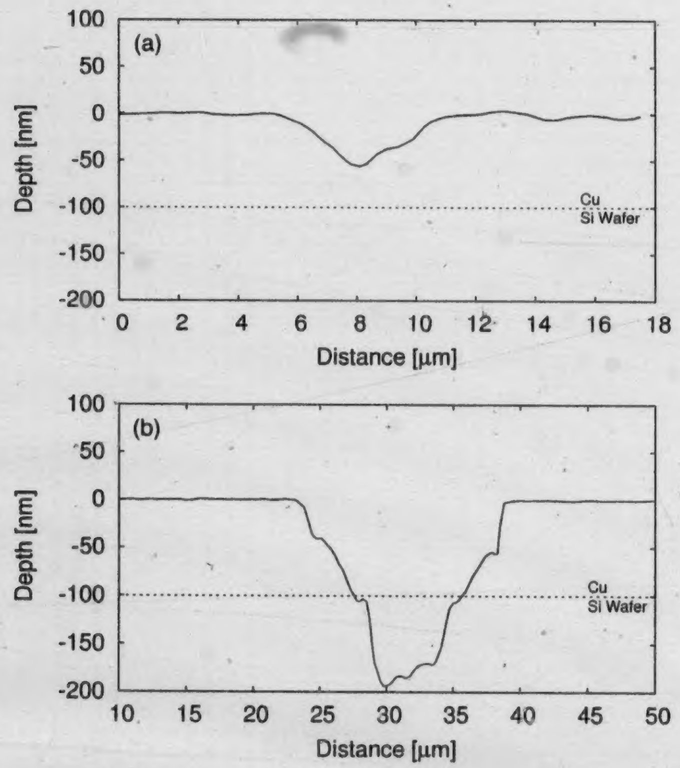

Figure 6.15. Depth profiles of ablation craters in 100 nm of Cu on a Si wafer using (a) 0.60 µJ and (b) 3.72 µJ. The penetration energy for the 266 nm pulses is ~ 1.5 µJ.

beyond ~ 1.5 µJ is used, the emission trend of the Cu microplasma is unperturbed. If every atom which was ablated contributed to the emission, one would expect an emission saturation in the Cu signal at energies comparable to the penetration depth. Since this effect is not observed, it suggests that the emission observed in fs LIBS is due to a layer shallower than the ablation depth of the crater.

Using data from the spectrometer which was viewing the experiment, it was possible to observe a range in which both Cu and Si emission lines would be expected. A sample spectra from a single 266 nm with 25.1 µJ pulse energy on the Cu target is presented in Fig. 6.17. There exists a strong Si I line at 288.2 nm, but no such line is observed in this spectra.

At this time, it is not clear how deep the emitting layer is. In related experiments, a saturation behaviour in the Cu emission at high energies was

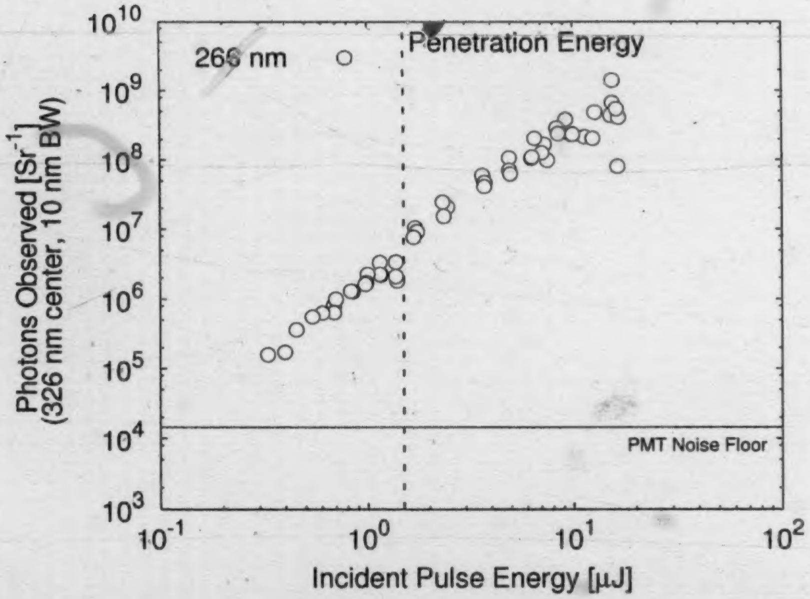

Figure 6.16. *Cu emission due to 266 nm, 130 fs laser pulses. The Si substrate is ablated for energies above ∼ 1.5 μJ, yet the trend of the Cu emission continues unperturbed. This implies that the sensitivity depth of fs LIBS is significantly shallower than the crater depth.*

observed with the spectrometer. However, due to the geometry of the imaging optics, it is not clear if the saturation is due to a lack of Cu atoms, or if the emitting volume of the plasma was moving outside of the focal volume. Further work with a wider range of targets and alternative viewing geometries will be required to quantify this effect. Despite these short comings, it is clear from the present experimental data that the sensitivity depth of fs μLIBS is less than the ablation depth. This effect has important consequences for all potential applications of μLIBS, and will need to be explored in detail.

6.7 Comparison with sub-millijoule results

During the course of this thesis, some preliminary work was performed with nanosecond and picosecond laser pulses, but at higher energies than most of the work presented in this thesis. As a comparison with the femtosecond ablation efficiency and emission efficiency results presented above, some results are given here.

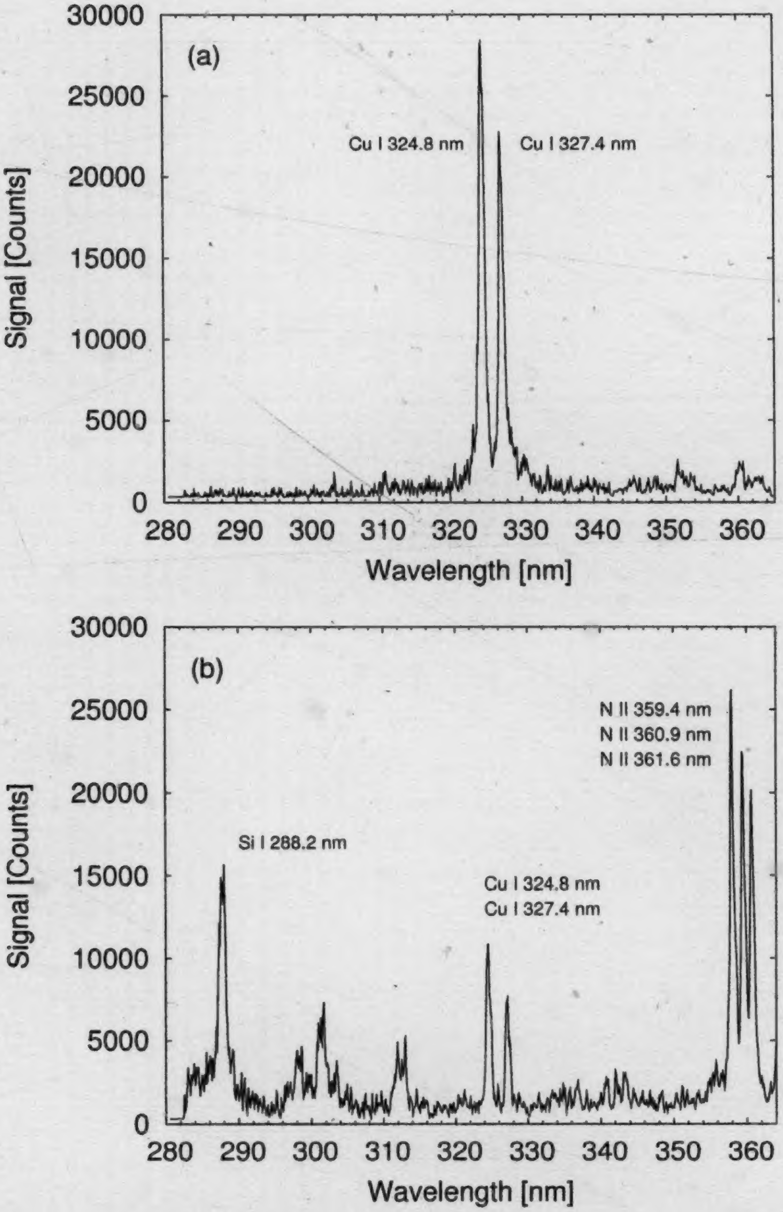

Figure 6.17. *Spectra obtained from the (a) first and (b) seventh shot on a Cu target using 25.1 μJ pulses at 266 nm. The energy used is well above the single-shot penetration energy for this laser wavelength, but no signal from the Si substrate is observed for the first shot (a).*

6.7.1 Ablation Efficiency

Unlike the femtosecond results, it was possible to find and measure the aluminum ablation craters. The crater diameter and depth were measured with an optical microscope. The depth resolution of the optical microscope was estimated at 1 μm. The craters were assumed to be ellipsoidal in shape for volume calculations. The crater volumes are plotted in Fig. 6.18 as a function of energy for the (a) 10 ns and (b) 50 ps pulses. In the case of the 10 ns data, there is a reduction in the crater volume ablated above 300 μJ, attributed to plasma shielding of the incident laser light. This effect is not observed in the picosecond data. It is possible that the plasma shielding is less pronounced due to the reduced laser-plasma interaction at picosecond pulse widths. However, due to the very small data set, any firm conclusions would be premature.

The solid lines in Fig. 6.18 are best linear fits to the data sets. In the case of the 10 ns data, two fits are performed to capture the different behaviours visible in Fig. 6.18a. The first fit is restricted to the values between 25 μJ and 300 μJ (low-energy), capturing the high efficiency behaviour. The second fit is restricted to energies between 300 μJ and 500 μJ (high-energy). Craters which appear to only partially shielded are rejected by restricting crater volumes to below $\sim 3000\ \mu m^3$ at 300 μJ and $\sim 5000\ \mu J^3$. While a qualitative approach, I feel that this more accurately reflects the behaviour of the data.

Ablation efficiency can be estimated from these linear fits. For the nanosecond data, the slopes of $30.61 \pm 0.90\ \mu m^3\ \mu J^{-1}$ for the low energy data, and $17.6 \pm 1.3\ \mu m^3\ \mu J^{-1}$ for the high energy data. In the case of the low energy data, the intercept is not significantly removed from zero, and it is reasonable to report the slope as the ablation efficiency. However, in the case of the data between 300 μJ and 500 μJ, the intercept is ~ 250 μJ, and more care must be taken. If one were to assume a value of zero for the intercept, the ablation efficiency in the high energy range would be $\sim 7\ \mu m^3\ \mu J^{-1}$. Table 2.1 is reproduced here as Table 6.3 to facilitate further discussion.

A value of $\sim 7\ \mu m^3\ \mu J^{-1}$ is in reasonable agreement with the value reported by Geertsen et al. [56] and one of the values reported Semerok et al. [62]. The different values reported by Semerok are taken with different lasers which exhibit different mode structure. The laser is single-mode for the $6\ \mu m^3\ \mu J^{-1}$ value, and multi-mode for the $29.3\ \mu m^3\ \mu J^{-1}$ value. It seems that the multi-mode value was taken for a pulse energy of 60 μJ [61]. Unfortunately, the exact energy for the single-mode result is not clearly specified, but is in the range of 10 to 100 μJ.

The KrF laser used for my results did not have a high quality beam, and the low energy results give reasonable agreement to the ablation efficiency reported by Semerok for the multi-mode case. When compared to the KrF laser, the single-mode case reported by Semerok would have higher intensities due to the higher quality beam and shorter pulse width for the same pulse en-

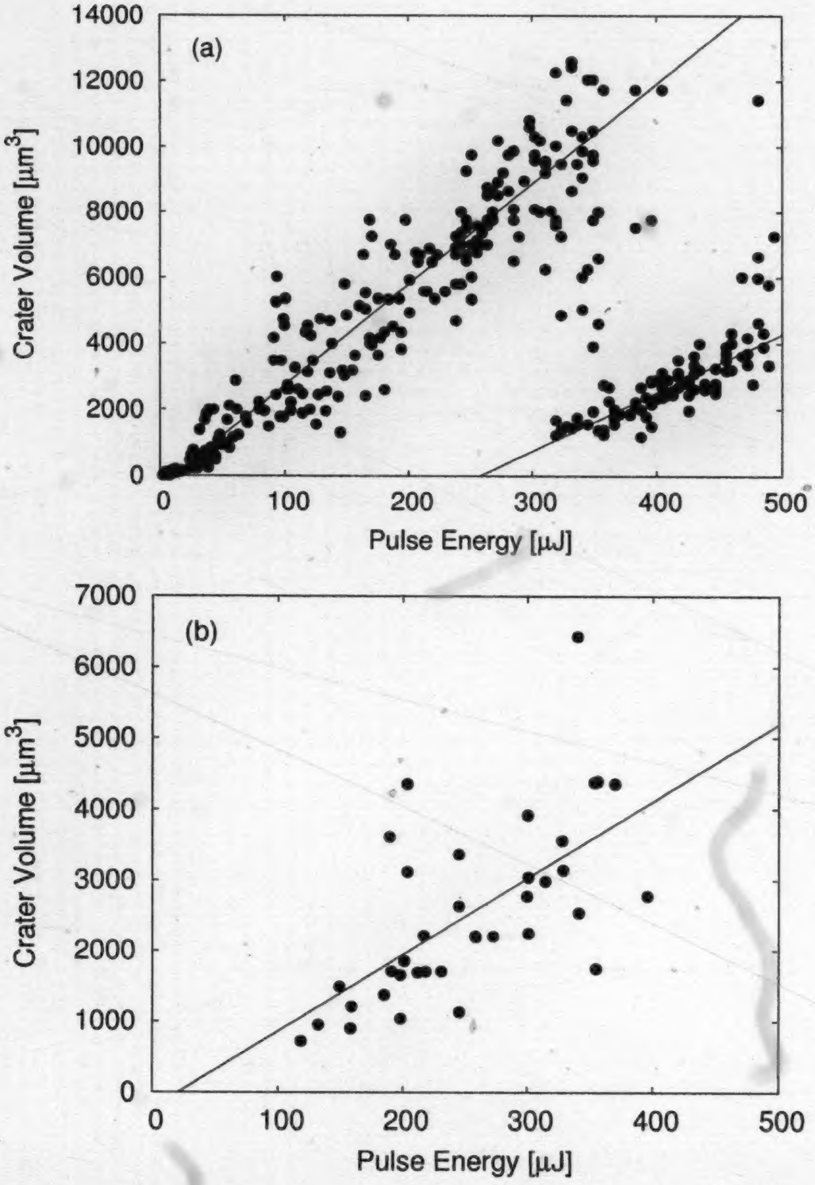

Figure 6.18. *Al crater volume for KrF laser pulses with (a) 10 ns and (b) 50 ps pulse width, using a 10X objective. In the case of the 10 ns pulses, a significant decrease in ablation efficiency above 300 μJ is observed, and is attributed to plasma shielding. The solid lines are best linear fits to the data sets, described in the text.*

Table 6.3. *Nanosecond Ablation Efficiencies [$\mu m^3\ \mu J^{-1}$]*

Author	λ	Pulse Width	Al	Cu	Fe	Ni	Pb	Mo
Taschuk[a] [Sec. 6.7]	248 nm	10 ns	31 ± 1					
Taschuk[b] [Sec. 6.7]	248 nm	10 ns	18 ± 1					
Geertsen [56]	266 nm	6 ns	9.8					
Semerok [61]	266 nm	4 ns	29.3	6.5	3.1		45.7	
Semerok [62]	266 nm	6 ns	6	2	1	3	9	1.4
Salle [60]	532 nm	6 ns	4.9	1.93			6.11	
Semerok [61]	532 nm	4 ns	12.4	3.1	1.5		18.6	
Semerok [62]	532 nm	6 ns	5	2			6	
Gornushkin [66]	1064 nm	550 ps					200	
Semerok [62]	1064 nm	6 ns	5	2	0.9	0.7	6	0.6

[a] 25 μJ ≤ E ≤ 300 μJ

[b] 300 μJ ≤ E ≤ 500 μJ, see text.

ergy. It is possible that the high energy results were taken in a similar range to the single-mode results reported by Semerok. The high-energy ablation efficiency results from the KrF and the single-mode ablation efficiency reported by Semerok also give reasonable agreement.

Geertsen et al. used a frequency-quadrupled Nd:YAG, but do not comment on the mode structure of their laser. However, a 25X reflecting objective was used, which would tend to produce a smaller focal spot than the 10X objective used in my case. It is plausible that the conditions under which Geertsen et al. were operating correspond to the high energy conditions reported above. The ablation efficiencies in the experiments of Geertsen et al. agree with the high energy conditions reported here.

The differences described here may account for the discrepancies in the literature, but this has been done for only one element. Further work would be required to confirm these effects, both for aluminum and for the other metals reported in Tab. 6.3. The picosecond data either lacks the difficulties observed in the nanosecond data, or insufficient data was collected. For the data presented here, an ablation efficiency of 10.8 ± 2.2 $\mu m^3\ \mu J^{-1}$ is estimated.

6.7.2 Emission Efficiency

For the data set presented in Fig. 6.18, the IPDA/Czerny-Turner system described in Ref. [64] was used to observe the LIBS signal during the crater ablation studies. Unfortunately, at this point it is not possible to properly account for all of the factors needed in order to present the acquired spectra in

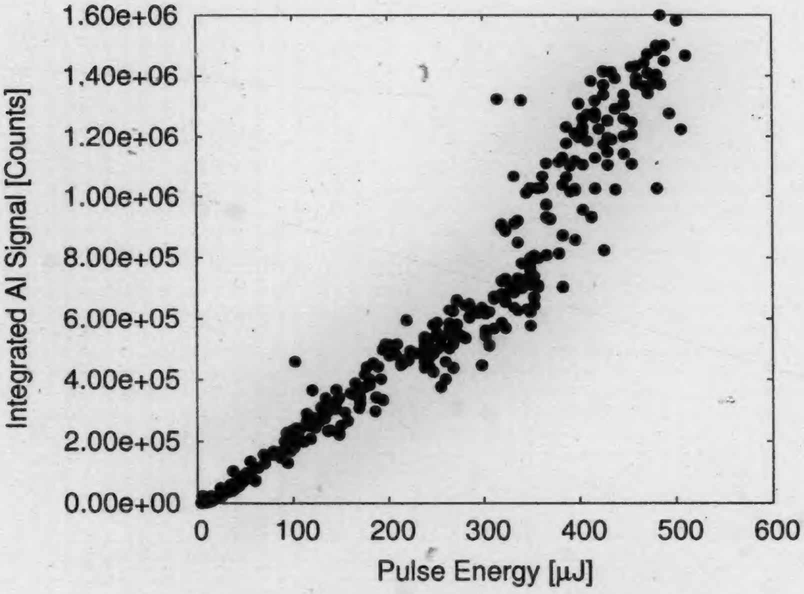

***Figure 6.19.** Integrated Al signal as a function of energy.*

absolute units. So, unlike the emission efficiencies reported earlier, it will not be possible to report in terms of photons atom^{-1}.

The integrated signal from the Al doublet at 394/396 nm is presented in Fig. 6.19. A significant increase in the emission strength is observed as the energy gets to the 300 μJ to 500 μJ. This is the same region in which the ablation efficiency is dropping, as shown in Fig. 6.18. This result strengthens the interpretation of this effect as plasma shielding, as the increase in emission would be expected if more energy were to be absorbed by the plasma.

Overall, this indicates that the question of emission efficiency for LIBS in general will be more complicated for longer pulse widths. Further work will be required to confirm the preliminary emission efficiency results presented here, and to develop a more complete picture of the emission behaviour in this regime.

6.8 Conclusion

In this chapter, the scaling of absolute emission levels with laser pulse width and laser wavelength has been investigated. For energies well above the ablation threshold, the pulse width of the laser is less important than the energy coupled into the target. For energies near the ablation threshold, the mechanisms by which laser energy is coupled to the target become important. For 10 ns and 50 ps pulses, an approximate agreement with the expected $\sqrt{\tau}$ scaling was observed, as the emission threshold dropped about 10 times for a change in pulse width from 10 ns to 50 ps.

However, as the laser pulse width was decreased further to 130 fs, the emission threshold returned to a value similar to the nanosecond case. As the ablation threshold is expected to remain approximately constant below a laser pulse width of $\sim$ 1 ps, another mechanism must be responsible for the observed increase. One possible explanation is the cooler plasma generated by femtosecond laser pulses requires a higher energy than required by picosecond or nanosecond pulses to excite the atoms to the required emission level.

The scaling of absolute plasma emission with incident laser wavelength was investigated using the harmonics of a femtosecond laser beam. Strong changes in absorbitivity ($\geq$ 10 times for Cu) had a large effect on the overall emission levels, but moderate changes ($\sim$ 2 times for Si) had little effect. It is known that the reflectivity of a target can change during the laser pulse [147,148]. This will affect the amount of laser light coupled to the target, and thus the total emission levels. Further work will be required to quantify the transient reflectivity effect for these targets, and the overall effect this might have on μLIBS.

The ablation efficiency of Si was investigated, and combined with the absolute emission levels of Si microplasmas to quantify the emission efficiency. It was found that the number of ablated atoms is much greater than the number of emitted photons for the strong emission lines observed here. Further work with the Cu targets revealed that the emitting atoms come from a layer shallower than the ablation crater. These results impact the overall capabilities of LIBS, and will need to be investigated further.

The ablation efficiency of Al has been compared with preliminary higher energy results for nanosecond and picosecond pulses. It is clear that the situation becomes more complicated with the increase in pulse width, and that further work will be required to extend some of the quantitative results presented in this chapter to the higher energies typically used in LIBS.

Chapter 7

μLIBS Applications

7.1 Introduction[1]

In this chapter, two selected applications of the μLIBS technique performed during the course of this thesis are described. Advances in the 2D mapping technique for Al alloy surfaces is described. The pulse energy required for 2D mapping has been reduced by nearly an order of magnitude to ~ 0.9 μJ, using ~ 130 fs pulses at 266 nm. The 2D mapping technique is also applied to the imaging of latent fingerprints, using ~ 84 μJ, ~ 130 fs pulses at 400 nm. A 2D image of a 1 mm by 5 mm area of a latent fingerprint from my right thumb was collected.

7.2 Surface mapping of Al alloys by μLIBS

One application area for μLIBS is measuring surface microstructure and composition. Due to the small energies used in μLIBS, the crater size from a single shot can be as small as a few microns, varying with target composition [46,70]. Aluminum alloys are a good test case for evaluating the capabilities of μLIBS for 2D surface mapping, as their microstructure varies significantly on the micron scale. During the course of this thesis, a 2D mapping technique that detects and classifies aluminum alloy composition in a single LIBS shot was developed [69,70,98].

In this section, the most recent work on μLIBS surface mapping is presented. A brief introduction to the composition and structure of the Al 2024 target is given, and a review of the 2D mapping methodology developed during the thesis work is presented. The energy required to produce a 2D surface map has been reduced to 0.87 μJ using 266 nm, 130 fs pulses focused with a 15X Scwartzchild objective. A 200 μm by 1 mm region of a commercially available Al 2024 alloy has been mapped, with successful single-shot detection and discrimination of precipitates.

---

[1] Section 7.3 in this chapter has been published as Ref. [149]

7.2.1 Introduction to Al Alloys

In aluminum alloys, minor constituent elements form precipitates with different chemical compositions from the alloy matrix. These precipitates range in size from 2 - 20 μm diameter. Details of the formation and processing of Al alloys significantly influence morphology, density, size and composition of precipitates, and hence on the alloy properties in service [150–153]. Two precipitate types, consisting of particles of insoluble Al_6(Cu,Fe,Mn) and soluble undissolved Al_2CuMg are known to form in Al 2024 during annealing [150, 152, 153].

A SEM micrograph of an Al 2024 sample, taken in electron backscatter mode, was taken to characterise the surface composition. The sample is from the same sheet as the 2D mapping target used in the current experiments. The results are presented in presented in Fig. 7.1, in which intensity corresponds to atomic weight. The dark area corresponds to the aluminum alloy matrix, while the high-density elements which exist preferentially in precipitates show up as bright spots. Analysis of the image presented in Fig. 7.1 indicates that precipitates cover $\sim 4\%$ of the surface. Precipitate size in Fig. 7.1 varies from ≈ 2 μm to ~ 370 μm; size distribution is presented in Fig. 7.2. The distribution is highly biased towards small precipitates, with 90% of precipitates having an area smaller than 36 μm^2. At the lower end, measurement precision is limited by the image pixel size, and may not represent a true lower limit on precipitate size for this alloy.

Measurement of the matrix and precipitate composition for a different sample of Al 2024 has been performed using the same X-ray microprobe [69], and are reported in Table 7.1. It can be seen that the concentration of minor elements in the precipitates is about an order of magnitude greater than in the background matrix. This large change in composition is detectable in a single LIBS shot, as described in the following section.

7.2.2 2D Mapping Methodology

For LIBS experiments, it has been found that the high concentrations of minor alloy elements found in precipitates will be detectable as an increase in the corresponding line intensity for each element found in the precipitate. Using a target imaging system, it was possible to target precipitates on an Al 2024 sample [69]. Single-shot LIBS data obtained in this experiment are presented in Fig. 7.3. The different spectra show enhancement of the various elements in the precipitates. In Fig. 7.3a, a typical matrix spectra is given as a reference. Fig. 7.3b shows a single shot on an Al_6(Cu,Fe,Mn) precipitate,

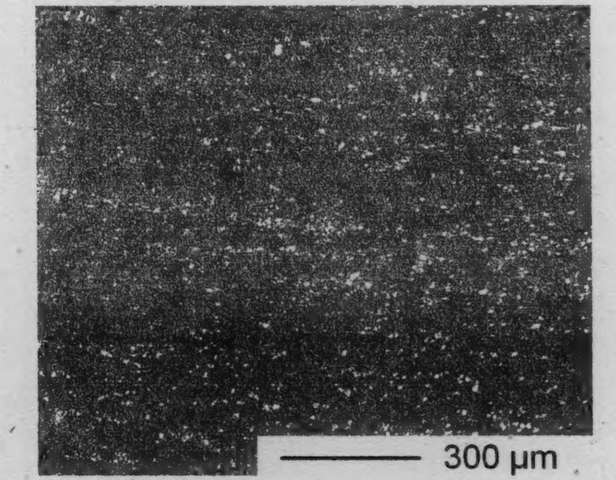

Figure 7.1. SEM image of an Al 2024 alloy surface taken in electron backscatter mode. The bright areas correspond to both precipitate types with high concentrations of high Z elements such as Cu, Mn, Fe compared with aluminum matrix (grey area). The black areas may correspond to surface defects such as holes or scratches.

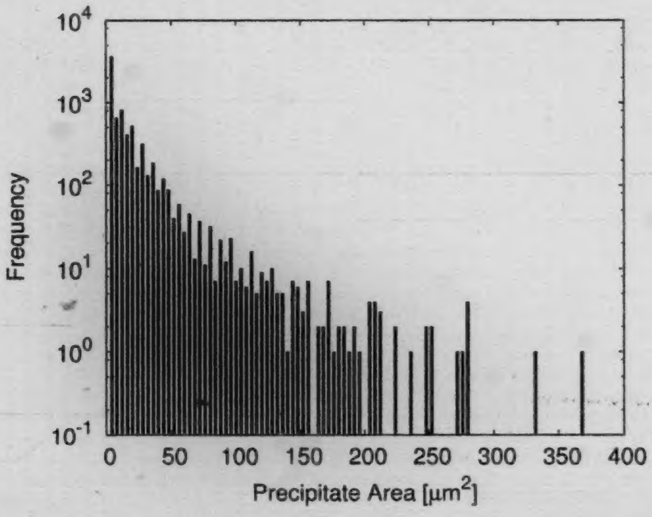

Figure 7.2. Histogram of precipitate area for the image presented in Fig. 7.1. Precipitate areas range from ~ 2 μm to ~ 370 μm for the area sampled here, with precipitates below 36 μm^2 making up 90% of the total.

Table 7.1. *Weight % of elements in different phases of an Al 2024 sample. Values are averages and standard deviations from 16 measurements on the matrix material, 3 for each of the precipitate types. (Reproduced with permission from [69].)*

Element	Matrix	Al_6(Cu,Fe,Mn)	Al_2CuMg
Al	93.6 ± 0.5	56.7 ± 1.4	43.1 ± 2.7
Cu	43.1 ± 2.7	24.84 ± 5.68	40.28 ± 1.15
Fe	0.04 ± 0.02	10.77 ± 1.73	0.11 ± 0.13
Mg	1.42 ± 0.04	0.11 ± 0.05	15.26 ± 0.62
Mn	0.61 ± 0.03	7.07 ± 2.01	0.15 ± 0.15
Si	0.04 ± 0.01	1.26 ± 0.61	0.37 ± 0.23

with corresponding enhancement in the Cu lines at 324 nm and 327 nm, Fe lines between 350 nm and 380 nm, and an enhanced signal from the 403 nm Mn lines. Similarly, Fig. 7.3c shows a single shot on an Al_2CuMg precipitate, with similar Cu enhancement and a strong increase in the Mg emission lines near 383 nm.

Using this single-shot capability, an analytic process to distinguish between precipitate types has been developed [70]. Using signals from elements exhibiting higher concentrations in the precipitate, statistical thresholds for distinguishing between matrix and precipitates were developed. A histogram of Mg SNR (as defined in Sec. 3.6.2.7) is given in Fig. 7.4. To derive a threshold, a Gaussian function was fit to the entire data set, using the Marquardt-Levenberg algorithm as implemented in GnuPlot 4.0 (see Appendix A.1.1). This approach is a nonlinear fitting method, and avoids biasing the final results with the outliers that represent the precipitates. Once the fit is complete, it is possible to identify a statistical threshold for anomalous events, based on sample size and desired degree of certainty. In this particular case, a threshold of 3σ above the average SNR was used, as only 300 data points are under study.

If more spots are sampled for the 2D map, the threshold should be increased if false positives are a concern. Evaluation more than one emission signal will also reduce the number of false positives. In [70], a region was identified as a precipitate if and only if emission thresholds were exceeded for each element making up the precipitate. Thus, in the case of the Al_2CuMg precipitates, both Cu and Mg emission levels were required to exceed the 3σ thresholds for a spot to be identified as a precipitate. Similarly, for Al_6(Cu,Fe,Mn) precipitates, anomalous emission levels for all three elements were required.

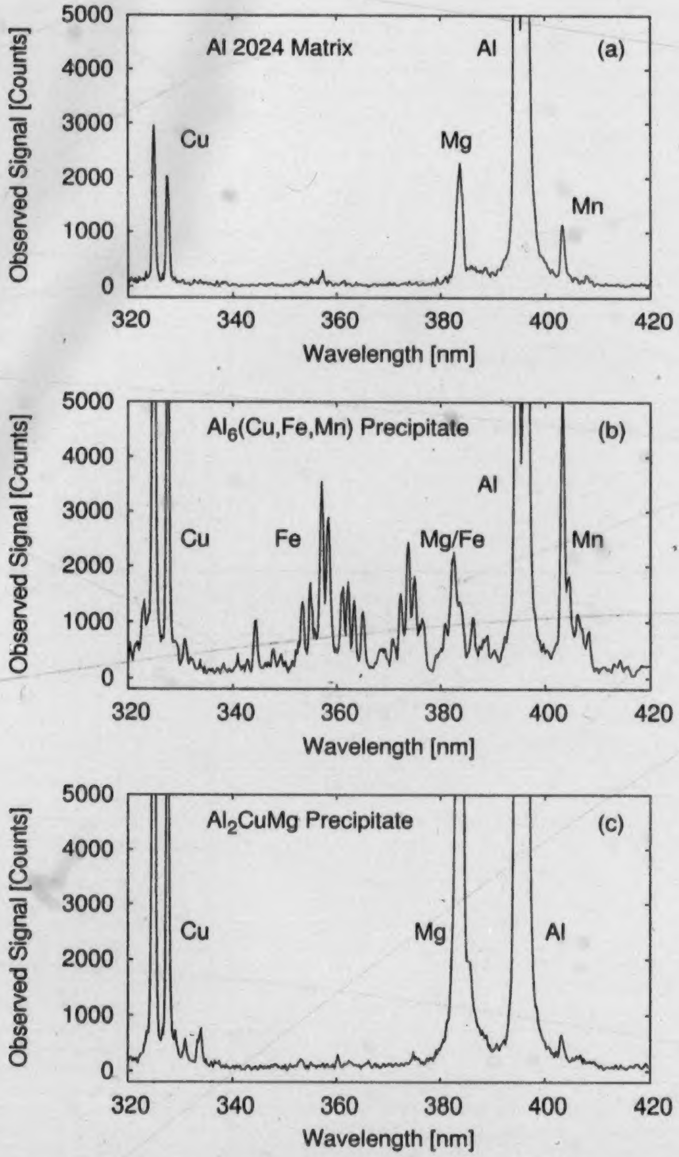

Figure 7.3. *Representative single-shot spectra from (a) Al 2024 matrix, (b) Al_6(Cu,Fe,Mn) precipitate, and (c) Al_2CuMg precipitate regions of an aluminum surface. A single ~ 7 μJ, 7 ns shot at 266 nm was used in each case. Clear differences between the spectra are observed, allowing definitive classification of region type.*

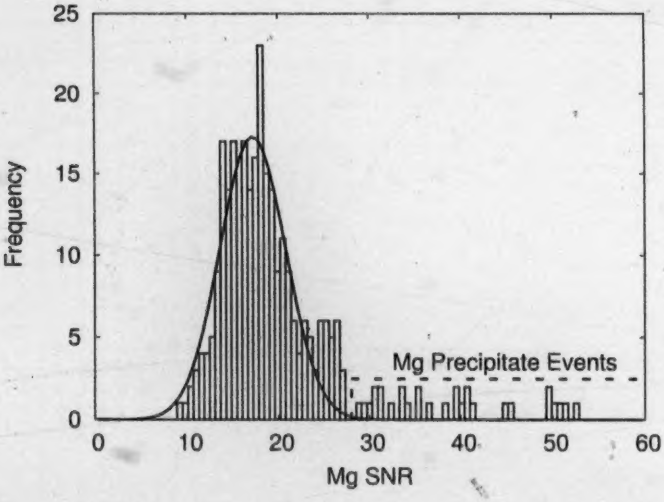

Figure 7.4. Histogram of Mg SNR using ~ 7 μJ, ~ 130 fs pulses at 800 nm. The solid line is a nonlinear fit to the distribution, while the dashed line delineates precipitates with Mg signals greater than 3σ above the average. (Reproduced with kind permission of Springer Science and Business Media from Fig. 10 of Cravetchi et al. [98])

The emission threshold technique was used to produce a 2D map of the surface of an Al 2024 sample [70]. In this case, 8 μJ, 7 ns laser shots at 266 nm were used. The map's step size was 10 μm, chosen to ensure that damage from a previous shot did not interfere with subsequent shots. A map showing the spatial distribution of Al_2CuMg and $Al_6(Cu,Fe,Mn)$ precipitates was generated and is given in Fig. 7.5. White squares indicate the location of $Al_6(Cu,Fe,Mn)$ precipitates; black squares indicate the location of Al_2CuMg precipitates.

If we take each LIBS shot to represent the composition of a 10 μm by 10 μm pixel on the surface, surface coverage of the precipitates can be estimated. Using this approach the calculated surface area covered by precipitates is ~ 5% of the total scanned surface area, ~ 2.6% by Al_2CuMg precipitates and ~ 2.3% by $Al_6(Cu,Fe,Mn)$ precipitates. Literature on the coverage of Al 2024 alloy surface by precipitates is somewhat inconsistent, with one reference quoting 2.7% coverage by the Al_2CuMg precipitates and approximately 1% coverage by the $Al_6(Cu,Fe,Mn)$ precipitates [152], while a second reference gives 1% and 2.8%, respectively, for the same precipitates [153].

Assigning an entire pixel area to a precipitate type should overestimate coverage as average precipitate size is smaller than 100 μm^2, as seen in Fig. 7.2. Taking this into account, the coverage reported by this technique is ex-

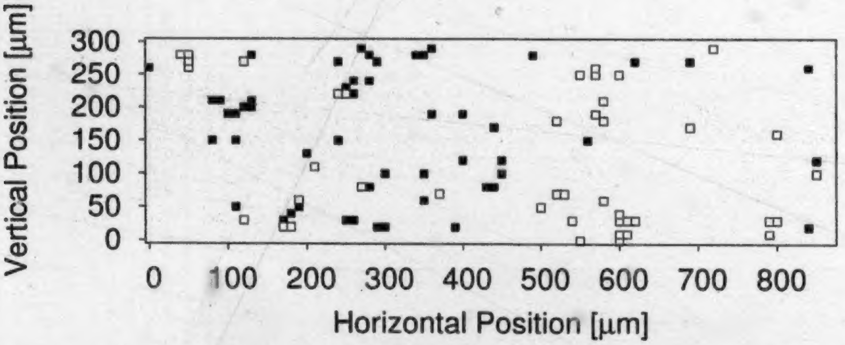

Figure 7.5. *Precipitate map on the Al 2024 alloy surface: black squares represent* Al_2CuMg *precipitates; white squares represent* $Al_6(Cu,Fe,Mn)$ *precipitates.* 3σ *criterion is applied for all constituent elements except Al. Reproduced with permission from [70].*

pected to overestimate the percentage of the surface covered by precipitates, bringing our results closer into line with the previously reported literature values.

7.2.3 Experimental Setup

The schematic layout of the experimental LIBS setup used for the present study is shown in Fig. 7.6. A frequency-tripled Ti:Sapphire (Spectra-Physics Hurricane) produces ~ 120 fs pulses at 266 nm, with a maximum energy of ~ 7 µJ on target. A total of four dielectric 266 nm mirrors at 45 degrees were used to separate the harmonics and direct the laser light to the target. The laser was focused with a 15X Schwartzchild objective.

Spectral purity was measured at the entrance of the setup, after the 4 dielectric mirrors, with a calibrated photodiode and coloured glass filters (Schott Glass). Under conditions where ~ 20 µJ at 266 nm was delivered to the setup, ≈ 35 pJ at 800 nm was measured. Light at 400 nm was not measurable, which indicates a maximum energy of ≈ 140 pJ. The spectral contrast ratio for the current experiments is at least 10^5. This leakage is not expected to affect the results presented here, even though the residual light from the harmonic conversion will be focused at the same point as the 266 nm light.

Pulse energy was controlled with a combination of a half-wave plate and a Glan-Taylor prism in the fundamental beam before the tripling operation. The Ti:Sapphire laser has a pre-pulse with a polarisation slightly rotated from the main pulse. The pre-pulse ratio of the beam is therefore a function of the half-wave plate, decreasing as the half-wave plate angle increases. In

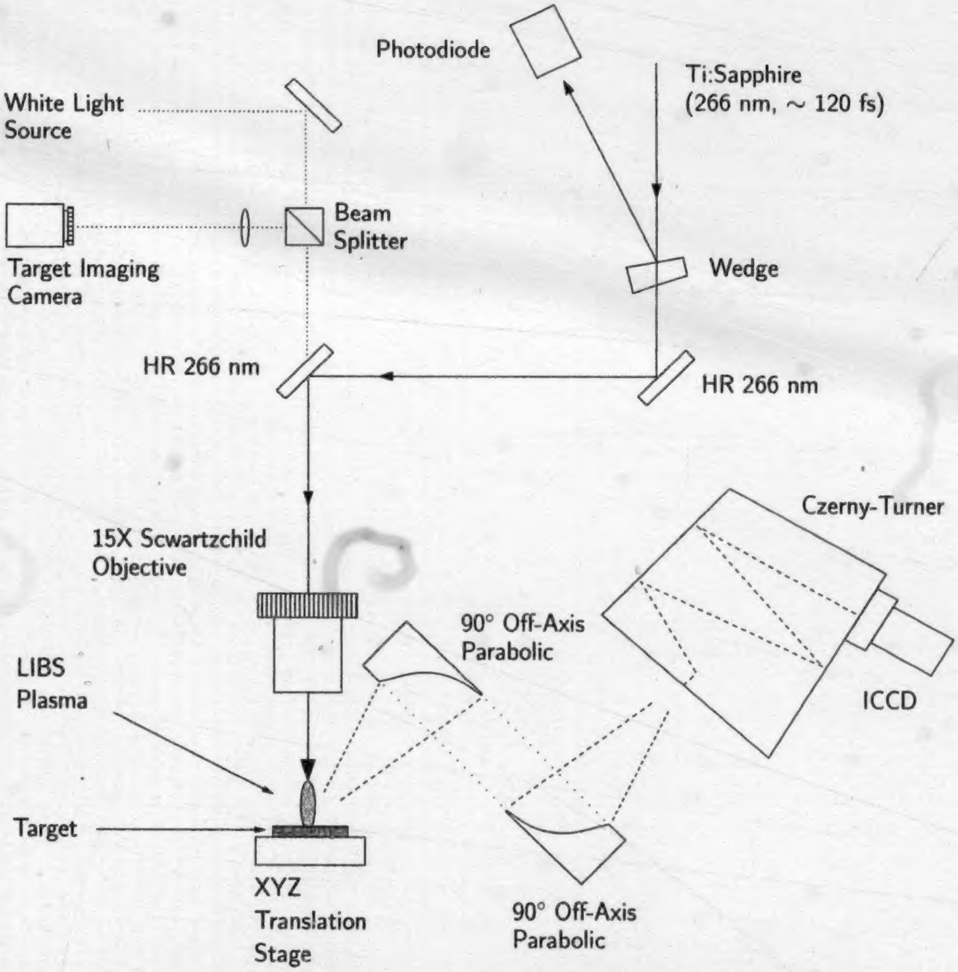
Photodiode
Ti:Sapphire
(266 nm, ~ 120 fs)
White Light
Source
Beam
Splitter
Target Imaging
Camera
Wedge
HR 266 nm
HR 266 nm
Czerny-Turner
15X Scwartzchild
Objective
90° Off-Axis
Parabolic
LIBS
Plasma
ICCD
Target
XYZ
Translation
Stage
90° Off-Axis
Parabolic

Figure 7.6. *Experimental setup for low-energy 2D mapping. A frequency tripled Ti:Sapphire beam (266 nm, ~ 120 fs FWHM) produces pulses with energies up to ~ 7 μJ on the target surface. Pulse energy is controlled with λ/2 plate combined with a Glan-Taylor prism (not shown). The LIBS emission is imaged 1:1 with achromatic 90° off-axis parabolic mirrors. A real-time imaging system allows positioning of the LIBS sample spot on the target with a precision of ~ 1 μm.*

order to keep a high contrast ratio, attenuation filters were also used to reduce the energy, reducing the angle required for the half-wave plate. The pulse energy was monitored with a photodiode, calibrated for energy delivered to the target plane using a power meter (SpectraPhysics 405A). Power meter accuracy is 5%, and energy calibration precision was ≈ 16%. The absolute error in the energy values presented here is estimated at 17%.

The plasma was imaged 1:1 onto the spectrometer's entrance slit with 90° off-axis parabolics. The off-axis parabolics were aligned to view the plasma at an angle of 45° from the incident laser light. Two 1 mm WG280 filters (Schott Glass) were used to prevent stray 266 nm laser light from entering the spectrometer. LIBS emission was measured using a 1/4 m, f/3.9 imaging spectrometer (Oriel MS260i) combined with an intensified CCD (ICCD). A 600 lines mm^{-1} grating with a blaze angle of 400 nm was used, giving a reciprocal linear dispersion of 0.168 nm channel^{-1}. The spectrometer's entrance slit was 100 μm for all experiments. A wavelength calibration of the spectrometer was carried out using a Hg lamp (Oriel 6035) as a standard [112]. Spectra were recorded using an ICCD (Andor iStar DH720-25mm). The setup was calibrated for absolute radiometric response using procedures described in Sec. 3.4.4; ICCD timing was calibrated using the procedures described in Sec. 3.4.2.

A real-time target imaging system was constructed from a white-light source, a beam splitter and a CCD camera. This system viewed the target through the last dielectric mirror in the laser path, and provided real-time feedback on target position and focus quality. With this system, it was possible to place the target with a lateral precision of ∼ 1 μm, and observe the laser-matter interaction in real-time.

Commercially available Al 2024 alloy was used as a specimen sample. The alloy was obtained in a 1′ by 1′ sheet with a thickness of about 0.375″. The only sample preparation was cleaning with ethanol.

7.2.4 Low Energy 2D Mapping of Al Alloys

A pulse energy of ∼ 0.87 μJ was used for the experiments presented here. At this energy, the craters produced had an inner diameter of ∼ 5 μm and lips which extended to a diameter of ≈ 7 μm. To ensure that subsequent shots did not fire on previously damaged Al alloy surface, a step size of 10 μm was used.

The system was optimised for using the Al doublets at 308.2 nm / 309.3 nm and at 394.4 nm / 396.2 nm simultaneously. This approach gives simultaneous feedback at two wavelengths separated by ∼ 85 nm, ensuring correct alignment of the achromatic plasma imaging optics. Due to the low emission levels for the 0.87 μJ pulse used here, the ICCD was run at maximum gain.

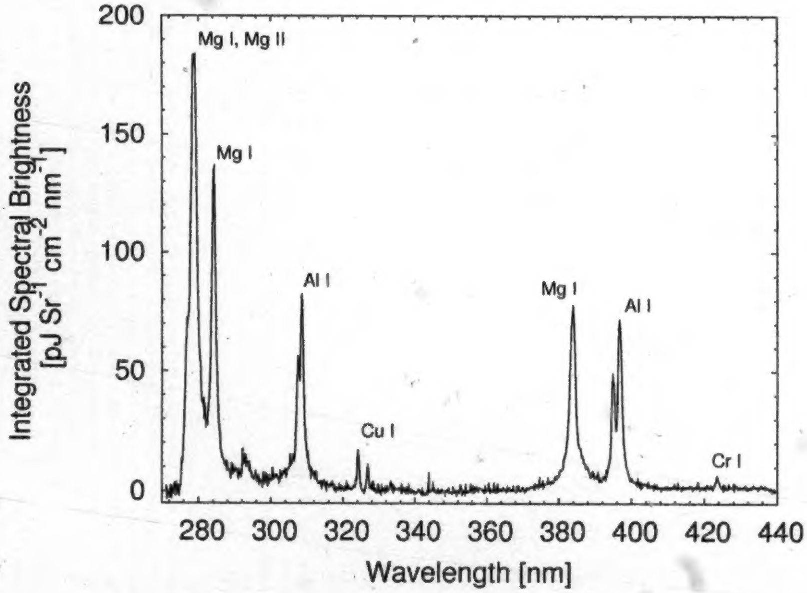

***Figure** 7.7. 100-shot average spectrum from Al 2024 sample, using 0.87 μJ laser pulses. Each shot was on a fresh surface. Emission levels observed here are low, with an average of ∼ 4500 photons observed in the Al doublet at 394.4 nm and 396.2 nm.*

No attempt to remove cathode noise spikes was made. The optimum gate delay was found to be indistinguishable from the arrival of the laser pulse, and was set to zero. The emission from the Al 394.4 nm / 396.2 nm doublet decreased to near zero by 70 ns after the laser pulse. The gate width was set to 100 ns. The 2D map was taken under these conditions. An average of 100 shots from the 2D mapping experiment is presented in Fig. 7.7.

Continuum radiation is visible towards the UV end of the spectrum below 320 nm as a result of the short gate delay. Some lines of interest for precipitate analysis are clearly visible in Fig. 7.7, including the unresolved Mg I lines near 383 nm, the Cu lines at 324.7 nm and 327.4 nm. There are also Mg lines below 300 nm: Mg I lines at 285.2 nm and near 280 nm, and an Mg II line at 280.3 nm. In the average spectrum, the Mn lines previously used near 403 nm are not visible, and other strong Mn lines are masked by nearby Mg lines around 280 nm. The signal near 280 nm is assigned to Mg rather than the strong Mn lines in the same region as the signal strengths are correlated with the Mg lines at 383 nm. If the signal at 280 nm were due to Mn it should be anti-correlated with the Mg signal at 383 nm, as expected from the composition of Al 2024 (Table 7.1) and earlier experiments [69]. This result is consistent with earlier observations of Al alloys, in which Mn was not visible on average for 130 fs pulses at 800 nm with energies below ~ 5 μJ [98]. Overall, emission levels are low, with an average of ~ 4500 photons distributed in 35 channels for the Al 394.4 / 396.2 nm doublet.

The current target presents a rougher surface than in previous work, where the target was polished [69]. As a result, the laser energy coupled into the target may vary significantly if a scratch or other surface defect is encountered during the scan. To compensate, an internal spectral normalisation method is used during analysis. As a measure of the overall coupling efficiency between laser and target, emission from the Al 308.2 nm / 309.3 nm doublet is used to normalise spectral emission. The peak area analysis technique described in Sec. 3.6.2.5 was used.

The emission from the Mg I line at 285.2 nm and the Mg I lines near 383 nm is correlated in Fig. 7.8. The area of each line has been integrated, and the number of photons observed is reported in Fig. 7.8a. However, this result is unsatisfactory, as the expected signature from the Mg precipitates is not present here. The improvement achieved by using the normalisation technique can be seen in Fig. 7.8b, where the presence of precipitates can be inferred from the outliers extending to the upper right of the plot. The normalisation technique is used for the work presented in the remainder of this section.

The two Mg lines used in this technique verification are clearly observed at these energy levels. As seen in Fig. 7.7, the lines for Cu are barely observable, and the lines for Fe and Mn are not observable even in a 100-shot average. Detecting and identifying precipitates depends on these elements, and on being able to establish thresholds for anomalous events. However, due to the low signal levels here, it becomes difficult to establish reliable thresholds. As an illustration, correlation for two Cu I lines and two Mg I lines is presented in Fig. 7.9.

The solid ellipses in Fig. 7.9 are the 3σ radius from a fit of the bivariate Gaussian distribution to the datasets [154]. The bivariate distribution contains a cross term which allows it to rotate to fit the distribution, as seen in Fig. 7.9b. Points outside the 3σ radius are statistically significant. The overall correlation coefficient between the Cu 324.7 and 327.4 nm lines is 0.19, and drops to -0.38 for data outside the 3σ ellipse. The Mg data has an overall correlation coefficient of 0.56, which drops to -0.03 for data outside the ellipse (excluding those data points closer to the plot origin than the ellipse origin).

Since the overall Cu emission is weakly correlated with itself, and the outliers are strongly anti-correlated, it is inappropriate to include it as an indicator of precipitates for this analysis. Similar behaviour was observed for Fe. Because the emission from Mn was quite weak, and only one unresolved

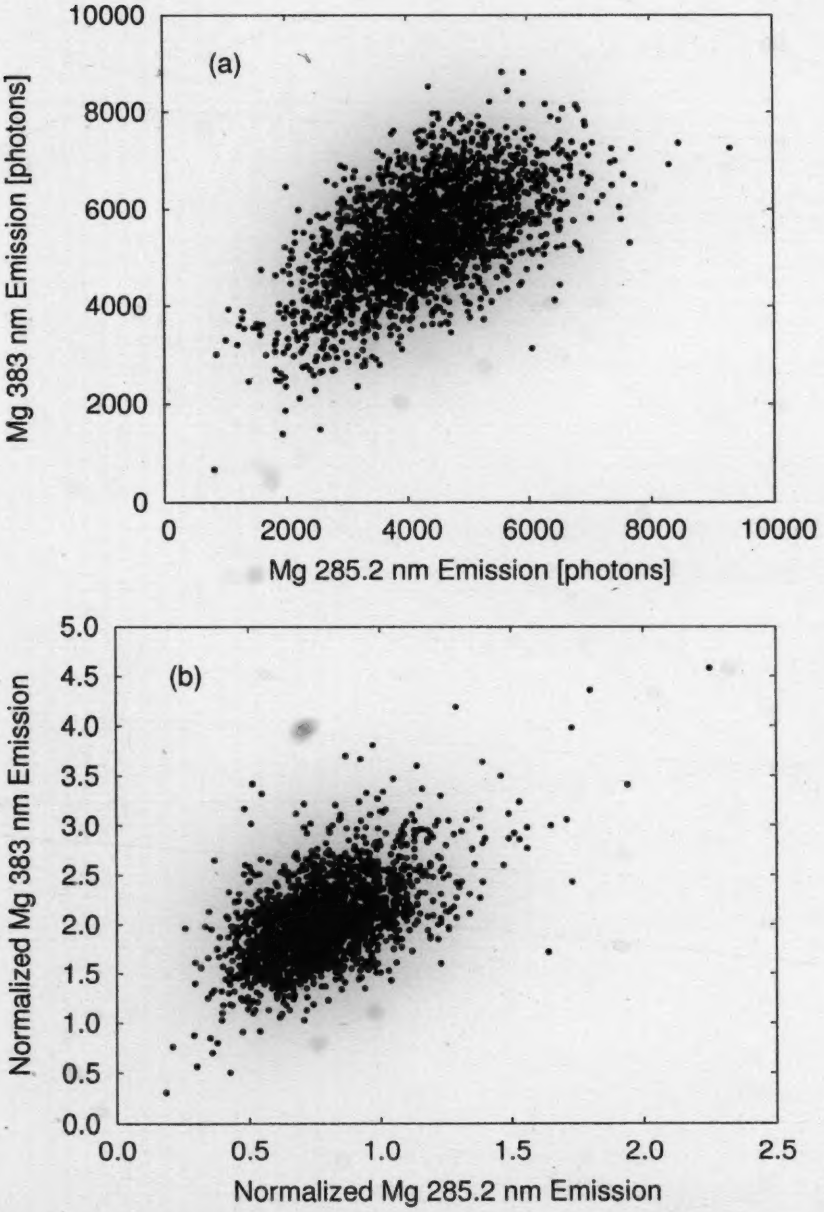

Figure 7.8. *Effect of normalisation of spectral emission on correlation between two emission lines of the same species. (a) Emission strength for two Mg I lines. (b) The expected signature from the Mg precipitates is visible when the Mg lines are normalized to the Al doublet at 308.2 nm / 309.3 nm.*

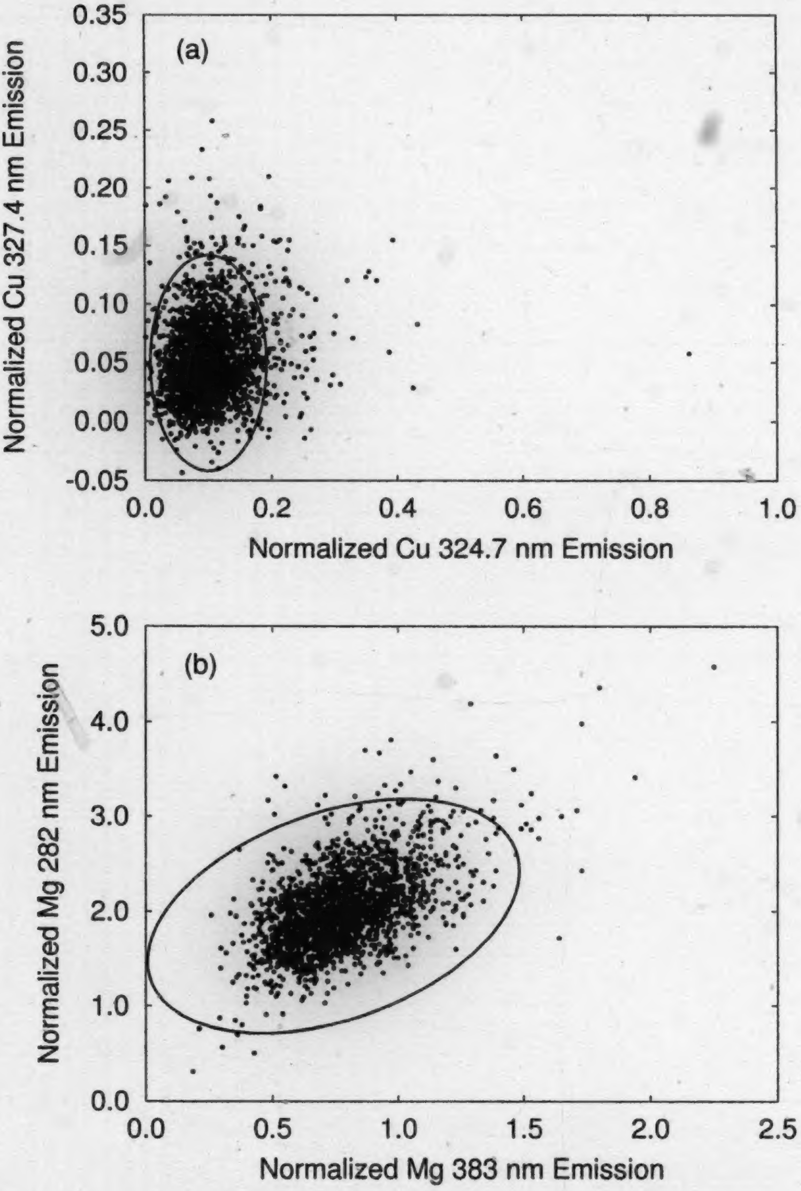

Figure 7.9. *Correlation of the (a) Cu 324.7 nm and Cu 327.4 nm lines, and the (b) Mg 285.2 nm and unresolved Mg lines near 383 nm. The solid ellipses represents the 3 σ level for a fit of a bivariate Gaussian distribution to the dataset. Data points outside the ellipse can be deemed statistically significant. In the case of the two Cu lines, the data outside the ellipse is strongly anti-correlated.*

set of lines near 403 nm was observed in the current spectral window, the multivariate approach can not be used for Mn.

Since the multivariate approach is unavailable for three of the four elements of interest (Cu, Fe and Mn) and only moderate successful in the case of Mg, it was not be used in the current analysis. The timing optimisation process described above used the Al 394 nm / Al 396 nm doublet, and the optimum gate delay obtained reflects the low noise in that region of the spectra as compared to the region below 300 nm. As a result, the current analysis uses the unresolved Mg lines near 383 nm and the unresolved Mn lines near 403 nm and the univariate approach described previously.

Histograms for the normalized Mg and Mn signals are presented in Fig. 7.10. Each histogram was fit with a Gaussian distribution and detection thresholds obtained, using a 3σ criteria. Precipitate events are indicated for Al_2MgCu and $Al_6(Cu,Fe,Mn)$ in Fig. 7.10a and Fig. 7.10b respectively. These thresholds are used to produce the 2D map in Fig. 7.11. The grey background is the alloy matrix, where no significant event was detected. Dark squares represent Al_2CuMg precipitates; white squares represent $Al_6(Cu,Fe,Mn)$ precipitates. Regions which had significant signals for both Mg and Mn are identified as containing both precipitate types, and are indicated with a checkered square.

In previous experiments, signals from two precipitates adjacent to one another were not detected. The crater diameter for the 0.8 μJ pulses used here was ~ 5 μm, suggesting that the area sampled was ~ 20 μm^2. As seen from the precipitate size distribution in Fig. 7.2, many precipitates are smaller than the expected probe spot size. In addition, precipitates of different types are sometimes found adjacent to one another (e.g. Plate 2039 of [150]). Thus, it is conceivable that precipitates of different types could be found within a single-shot sample volume.

A total of 2205 shots were taken for the 2D scan presented in Fig. 7.11. For the 3σ criterion, ≈ 3 false positives are expected for each precipitate type in a sample set of this size. Including the locations identified as containing both precipitate types, 35 spots were identified as Al_2MgCu precipitates, while 56 spots were identified as $Al_6(Cu,Fe,Mn)$ precipitates. This corresponds to an areal coverage of 1.6% for Al_2CuMg precipitates, and 2.5% for $Al_6(Cu,Fe,Mn)$ precipitates, and a total coverage of 4.1%. The overall coverage agrees with the analysis of the electron backscatter image presented in Fig. 7.1. In terms of the relative fractions of precipitate type, the results presented here give reasonable agreement with Blanc et al. [153], but disagree with Buchheit et al. [152]. It is expected that variations in the annealing process will vary the size distribution of these precipitates for different samples, which may explain this discrepancy [150].

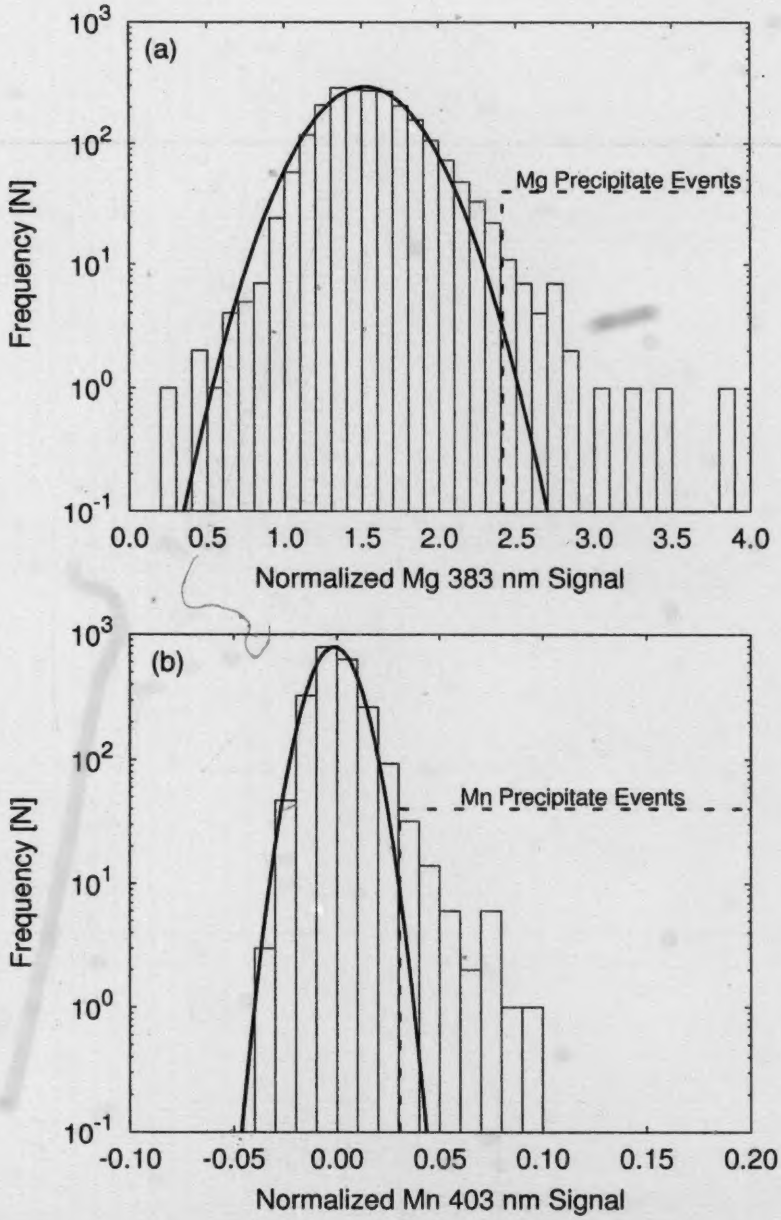

Figure 7.10. *Histograms of normalized (a) Mg signals, and (b) Mn signals. The solid line is a best fit of a Gaussian distribution to the data set, and the dashed lines represent detection thresholds for the* Al_2MgCu *and* $Al_6(Cu,Fe,Mn)$ *precipitates.*

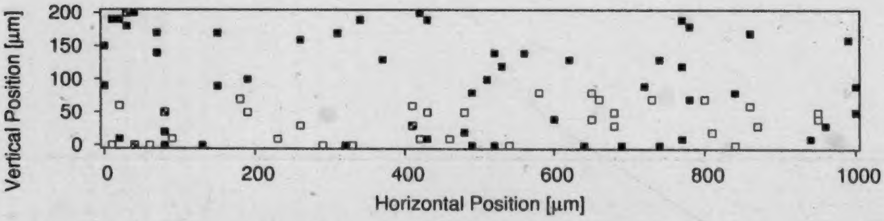

Figure 7.11. *2D precipitate map of a 200 µm by 1 mm region of an Al 2024 sample with a step size of 10 µm. The background alloy matrix is grey, while* Al_2CuMg *precipitates are black squares,* $Al_6(Cu,Fe,Mn)$ *precipitates are white squares and locations identified as both are represented with a checkered square.*

7.2.5 Discussion and Future Work

A few issues have been raised by the 2D mapping work performed as part of this thesis and in the recent work presented above: optimum gate conditions in achromatic systems, lack of accurate standards on the µm scale, redeposition of ablated material during intensive surface scans, and reduction in the number of available photons at extremely low energies. Each of these is discussed below.

In the case of broadband systems, achromatic imaging optics are advantageous since they maximise the coupling efficiency for the broad range of wavelengths observed. However, as seen in Fig. 7.7, noise can be a function of wavelength. This effect can be due to the varying radiometric sensitivity of the observing system, as well as fundamental differences in background emission as functions of wavelength. In practice, this means that optimum gate delay and width may not be the same for all of the lines observed. For example, in the current case, it might have been advantageous to use a longer gate delay. This would have reduced emission strength from the lines observed here, but the reduction in noise in the UV portion of the spectrum may have improved the usefulness of the lines below 300 nm. A procedure that optimises some overall average of the SNR of the various elements would be preferred to maximise the use of the LIBS process. The impact of this type of effect will depend strongly on the application and performance of the available instrumentation. Thus, the correct approach will likely have to be evaluated on a case by case basis in future work.

In previous work by us and many other groups redeposition of ablated material has been observed, as discussed in Section 2.6.2. Previous work on Al alloys has uncovered a 'shock-cleaning' effect, in which redeposited material is removed from the surface for a radius a few times greater than the map step size. While the amount of material ablated is reduced as energy

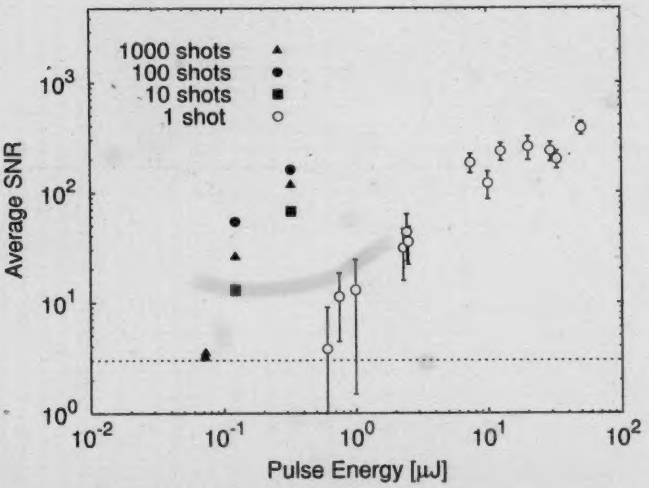

Figure 7.12. SNR scaling as a function of shot number for the Al doublet at 394 nm / 396 nm. Accumulating a number of shots reduces the energy required to get reasonable SNR. (Reproduced with kind permission of Springer Science and Business Media from Fig. 12 of Cravetchi et al. [98])

is decreased, it is expected that the radius which is 'shock-cleaned' will also decrease with energy. Further work will be required to ascertain the effect of redeposition for low energy 2D mapping in light of these competing processes.

One possibility for improving emission levels, and thus the performance of μLIBS for 2D surface mapping, is increasing the number of shots while significantly reducing the energy. In previous work, a preliminary investigation of this approach was made, and is presented in Fig. 7.12. By increasing the number of shots per spectrum to an accumulation of 10 shots, it is possible to reduce the energy required to achieve a SNR of 10 for the Al doublet at 394 nm / 396 nm from ~ 0.8 μJ to ~ 0.15 μJ. A similar approach could be taken for the 2D mapping work presented here, provided that low-energy shots do not ablate through a precipitate within 10 shots. Further work will be required to ascertain whether this approach can be applied to 2D mapping with μLIBS.

7.2.6 Conclusion

In this section, the possibility of 2D mapping aluminum alloy surfaces with pulse energies below 1 μJ has been explored. The Al 2024 target has been characterised, and the 2D mapping methodology that has been developed during the course of the thesis work was introduced. Multivariate techniques were explored to use the multiple emission lines available in the current setup, but were not found to be useful for the low signal levels observed for Cu, Fe and Mn. It is possible that an analysis which makes use of the cathode spike analysis techniques presented in Sec. 3.7.2 would improve the results, and may allow multivariate techniques to be used. In the present work, univariate techniques were used for the the unresolved Mg I lines and Mn I lines at at 383 nm and 403 nm, respectively. Single-shot detection and discrimination of Al_2MgCu and $Al_6(Cu,Fe,Mn)$ precipitates has been demonstrated, and a 2D map of a 200 μm by 1 mm region has been performed.

7.3 Fingerprint Detection and Imaging

In this section, detection of latent fingerprints on a Si wafer by Laser-Induced Breakdown Spectroscopy (LIBS) is demonstrated using $\sim$ 120 fs pulses at 400 nm with energies of 84 ± 7 μJ. The presence of a fingerprint ridge is found by observing the Na emission lines from the transfered skin oil. The presence of the thin layer of transferred oil was also found to be sufficient to suppress the LIBS signal from the Si substrate, giving an alternative method of mapping the latent fingerprint using the Si emission. A 2D image of a latent fingerprint can be successfully collected using these techniques.

7.3.1 Introduction

Fingerprints are a highly reliable method of identifying humans, as they have been found to be unique to each individual [155]. Objects that have been touched often have transferred fingerprints that can be used in criminal investigations or security applications. Fingerprints found at crime scenes are classified into three types: visible prints such as those made when an ink-coated finger touches a surface and leaves a print, plastic prints which are a mechanical impression in soft materials such as wax, and latent prints which result from a transfer of oils from finger to surface [155]. The traditional method for detecting and collecting latent fingerprints is to lightly dust a suspect surface with fingerprint powder which will tend to stick to the latent fingerprint. The dusted print can then be lifted from the surface with an adhesive plastic sheet for later evaluation [155].

Detection of fingerprints using lasers was first demonstrated by Dalrymple et al. who excited the fluorescence of fingerprint oils using an argon ion laser [156]. Two major challenges in fingerprint detection with laser techniques are low emission levels from the fingerprint oils, and interference from the fluorescent signal from the background substrate. Strategies for improving the emission signal from fingerprint oils include selection of laser wavelength [157], as well as chemical treatments to tag the fingerprint for enhanced fluorescence response [158,159]. Elimination of background interference has been the focus of much work in this area [160–163]. Hooker et al. used a 0.3 m f/4 monochromator to spectrally resolve the fluorescence to optimise the choice of fluorescent dye agents and filters for photography of fingerprints [160]. An alternative technique is to use gated acquisition of the fluorescent fingerprint image to avoid ambient light. Work by Wenchong et al. uses ICCD detection to eliminate contributions from highly illuminated substrates such as exterior walls during daylight [161]. Recent work by Dinish et al. [162,163] makes use of phase-resolved fluorescence from fingerprint samples. This technique modulates the illumination laser at several MHz to induce a phase shift between the substrate background and the latent fingerprint signals that can be used to detect the print.

LIBS offers an alternative to the traditional optical methods for fingerprint detection as it directly detects the elemental signature of latent fingerprints. In many cases, the substrate on which the latent fingerprint is found will have only trace amounts of the elements found in the fingerprint. Recent work by Lopez-Moreno et al. has demonstrated detection of human fingerprints at a distance of 30 m using the fundamental of a Nd:YAG with 350 mJ laser pulses [164]. The fingerprints used as samples for their work were composed of the natural skin oils, various explosive residues and other samples. Successful discrimination between fingerprints of different compositions was achieved.

In the current section, a preliminary investigation of the capabilities of μLIBS not only for detection but also for imaging of latent fingerprints is reported. Lower pulse energies are required to minimise damage to the fingerprint during the mapping process. As shown in the present results, with low-energy femtosecond pulses the sensitivity depth is reduced to a depth comparable to the fingerprint film. This phenomena reduces the effect of the substrate in fingerprint detection and imaging. Characteristics of the elemental optical emission of latent fingerprint on a Si substrate have been measured and are presented below.

7.3.2 Experimental Setup

The experimental setup used for LIBS fingerprint detection and mapping is given in Fig. 7.13. A Ti:Sapphire (Spectra-Physics Hurricane) laser which produces ~ 120 fs (FWHM) at 800 nm pulses is frequency doubled using a LBO crystal. The doubled beam is at 400 nm and gives a maximum pulse energy of ~ 90 μJ on target. The pulse width of the doubled beam is estimated at ~ 120 fs (FWHM) on target. A total of four dielectric 400 nm mirrors at 45 degrees are used to separate the fundamental and second harmonic beams. The spectral purity of the excitation beam was measured before the focal lens with a calibrated photodiode and a OG570 glass filter (Schott Glass) to block the 400 nm laser light. The residual 800 nm laser light energy was ~ 40 nJ/pulse when the 400 nm light was ~ 90 μJ/pulse for a spectral contrast ratio of about 2200. This level of 800 nm leakage light is not expected to be a significant factor for the experiments presented here, especially considering that the 800 nm light would be out of focus for the conditions used here.

The pulse energy was controlled with a combination of a half-wave plate and Glan-Taylor prism in the fundamental beam before the doubling operation. An energy-monitoring photodiode has been calibrated for pulse energy using a power meter. The precision of the calibration factor is 6% and the absolute error of the power meter is 5%. For the laser pulse energies reported in this paper, the absolute error is estimated at ~ 8%. The laser pulse has a Gaussian spatial profile, and was focused to a 9 ± 1 μm (FWHM) spot on the sample surface using a 10 cm focal length lens. For an 80 μJ pulse, the peak irradiance on the target is $\sim 3 \cdot 10^{15}$ W cm^{-2}.

The LIBS emission was measured using a 1/4 m, f/3.9 imaging spectrometer (Oriel MS260i) combined with an intensified CCD (ICCD). A grating with 600 lines mm^{-1} and a blaze angle of 400 nm was used, giving a reciprocal linear dispersion of 0.168 nm channel^{-1} or 6.5 pm μm^{-1}. The entrance slit of the spectrometer was 100 μm for all experiments. A spectral calibration of the spectrometer was carried out using a Hg lamp (Oriel 6035) as a wavelength standard [112]. The Hg lamp calibration was combined with the wavelength calibration provided by the manufacturer for the work presented here.

Spectra were recorded using an ICCD (Andor iStar DH720-25 mm). Due to the low pulse energies used in μLIBS, short delay times are necessary to achieve an optimum signal to noise ratio (SNR) [65]. The delay time was calibrated using the technique described in Sec. 3.4.2. With this approach, it was possible to establish an absolute zero reference time with a precision of ~ 1 ns. A gate delay of ~ 5 ns was chosen for the initial studies presented here. The gate width used was 1 μs, which is long enough to capture all available emission without accumulating significant detector noise for the gain conditions used here.

In the case of 2D surface mapping, it is necessary to extract as much information as possible from each shot, as the surface properties may change after the first laser pulse. In previous work, it has been shown that it is possible to estimate SNR from a single shot using neighbouring regions of the spectrum which are spectrally quiet [65] . For an initial analysis of the results presented here a single-channel definition of SNR is used, as described in Sec. 3.6.2.4. In the work presented here, a linear model was fit to the background to account for the general trend of the background in the region of interest.

The fingerprints used as samples in this paper were taken from my right thumb. First, a Si substrate was rinsed with ethanol and wiped clean with

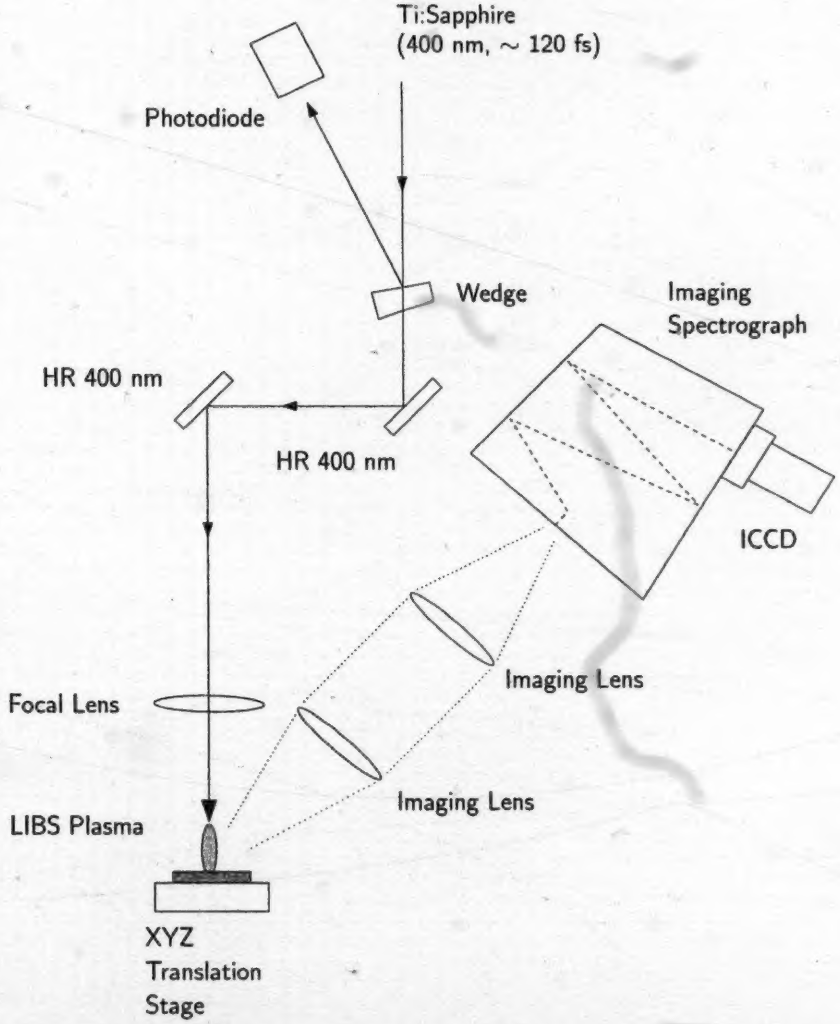
Ti:Sapphire
(400 nm, ~ 120 fs)
Photodiode
Wedge
Imaging
Spectrograph
HR 400 nm
HR 400 nm
ICCD
Imaging Lens
Focal Lens
Imaging Lens
LIBS Plasma
XYZ
Translation
Stage

***Figure* 7.13.** *Experimental setup for latent fingerprint detection and mapping. A frequency doubled Ti:Sapphire beam (400 nm, ~ 120 fs FWHM) produces pulses up to ~ 90 μJ on target. Pulse energy is controlled using a combination of a half-wave plate and Glan-Taylor prism (not shown). One reflection from the wedge is measured with a photodiode to monitor the pulse energy delivered to the target. LIBS emission is observed at an angle of 45 degrees from the laser axis. (Reproduced with permission from Taschuk et al. [149])*

lens paper prior to fingerprint deposition. The fingerprints were prepared by brushing my thumb against my forehead, and then lightly rolling the ball of my thumb against a cleaned Si substrate. The preparation of suitable fingerprints is a challenge: too much pressure smears the fingerprint, reducing definition; too little pressure yields an incomplete fingerprint. Only fingerprints which looked complete and were clearly visible in the reflected image of fluorescent room lights on a Si wafer were used for the experiments described below.

7.3.3 Experimental Results

Initial trials for fingerprint detection by LIBS were undertaken using a fingerprint left on a Si wafer. It is expected that the oils which are transfered to surfaces in latent fingerprints contain Na [165], which is a good candidate for LIBS detection using the doublet line at 589.0 nm and 589.6 nm. Si provides a smooth surface for the latent fingerprint and has strong emission in the observed spectral region. For each shot, Na and Si SNR were calculated using Eq. 3.10. In the work presented here, two spectrally quiet regions were used for background corrections: the first from 570.4 nm to 573.7 nm, and the second from 592.2 nm to 595.5 nm. These background regions were used for both Na and Si signals. In the case of Na, the peak wavelength used was 589.2 nm, and for Si the peak wavelength used was 576.2 nm. The wavelengths quoted for the background and peak regions correspond to channel centers, and thus do not necessarily agree with handbook values for observed lines.

The Si line observed here was identified as the 288.16 nm line in the second order. This was confirmed by placing a GG395 glass filter (Schott Glass) in front of the slit, which strongly filters wavelengths below 380 nm. This test removed the Si signal entirely, ruling out the possibility that the 575.4 nm, 576.3 nm, or 577.2 nm neutral Si lines contributed to the Si signal observed here. Fig. 7.14 gives sample spectra from a fingerprint ridge (Fig. 7.14a), and from a region between fingerprint ridges (Fig. 7.14b). Both spectra are single-shot acquisitions taken with 84 μJ pulses at 400 nm. These spectra indicate that the presence of a fingerprint ridge can be sufficient to shield the substrate from the laser pulse, as no Si signal is observed in Fig. 7.14a. In this case, a fingerprint ridge must be thick enough that the ablated layer which contributes to the LIBS signal does not penetrate into the Si substrate.

A 1D LIBS scan of a latent fingerprint sample is given in Fig. 7.15. A step size of ~ 50 μm was used for a 100-shot series along the surface for a total mapped distance of 5 mm for all scans. For each location on the target, SNR was calculated for both Na and Si. Both signals have a period of ~ 750 μm, but are out of phase. Si signals are lower in regions where a strong Na signal was obtained, suggesting that fingerprint ridges are sufficient to suppress the

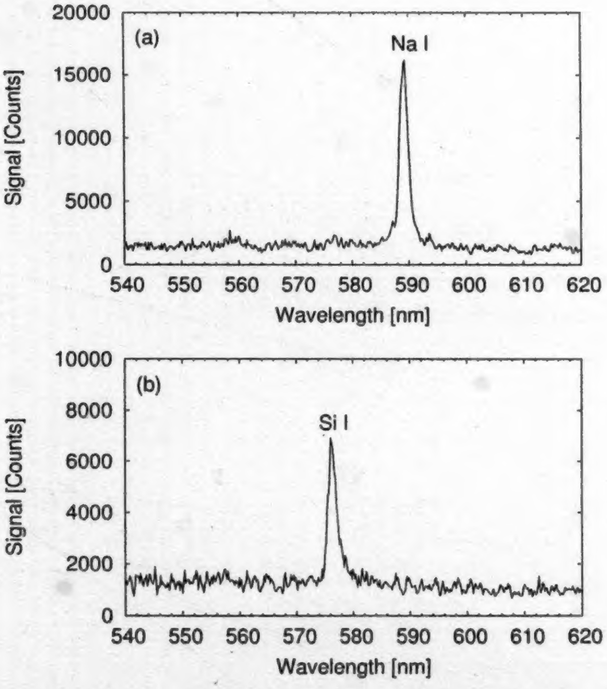

Figure 7.14. *Sample spectra with no background correction from a fingerprint scan. (a) A strong Na signal is visible in a shot located on a fingerprint ridge. (b) Second-order signal from the Si substrate from a shot taken between fingerprint ridges. Both spectra were generated with a single 84 μJ pulse at 400 nm with a gate delay of ~ 5 ns and a gate width of 1 μs. (Reproduced with permission from Taschuk et al. [149])*

LIBS signal from the Si substrate.

As a further investigation of the suppression of the Si signal, a Si wafer with a latent fingerprint was rinsed with ethanol and wiped with lens paper: the ethanol was dripped onto the substrate and the lens paper was gently drawn over the substrate. This procedure was performed twice, and a 1D LIBS scan was made of the cleaned region. However, as can be seen in Fig. 7.16a, this procedure left Na on the wafer at concentrations which were still detectable by LIBS. The washing procedure was repeated twice more, for a total of 4 wash-and-wipe cycles. Another 1D LIBS scan of the surface was made, and the average Na SNR was below the 99% confidence detection limit (Fig. 7.16b). However, Na was still detected at a few locations in the 1D scan, indicating that fragments of the print have survived the cleaning pro-

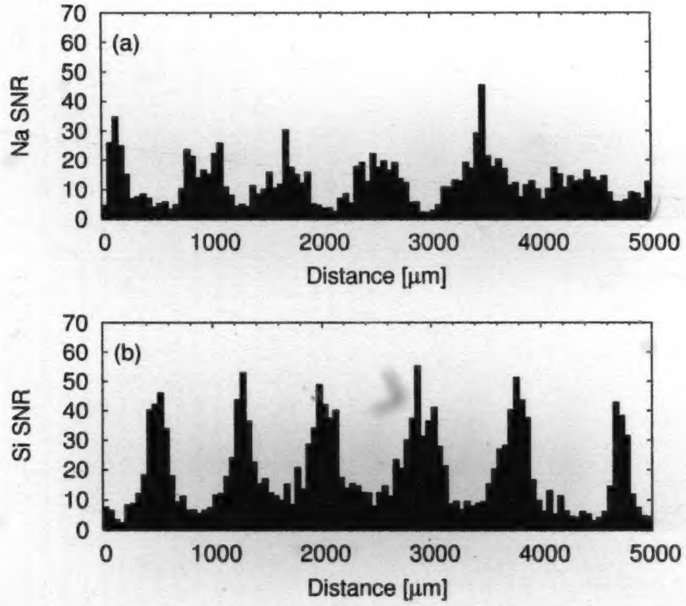

Figure 7.15. *1D scan of a latent fingerprint on a Si wafer using single-shot 84 μJ pulses at 400 nm and ~ 50 μm spacing between shots. Na signals (a) and Si signals (b) are periodic in space with a period of ~ 750 μm. Si signal levels are lower where a strong Na signal is observed, suggesting that the presence of a fingerprint is sufficient to suppress the LIBS signal from the Si substrate. (Reproduced with permission from Taschuk et al. [149])*

cess. In both the twice-cleaned sample and the quadruple-cleaned sample, Si was visible at all locations, and at an average SNR of ~ 30. These signal levels are somewhat consistent with those observed in the 1D fingerprint scan presented in Fig. 7.15b indicating that the fingerprints prepared here do not cover the entire surface and that the laser pulse is interacting with a mostly bare Si substrate between fingerprint ridges.

A 2D scan of a 1 mm by 5 mm region of a latent fingerprint from my right thumb was performed using laser pulses with energies of 84 μJ. The spatial step size was ~ 50 μm in both dimensions. SNRs for Na and Si as a function of position are presented in Fig. 7.17. The distribution of Na SNR values has a small number of outliers with SNR values above 60. To highlight the technique's mapping capability, the 2D map of Na SNR presented in Fig. 7.17a is limited to a maximum SNR of 50. Fingerprint ridges are visible in the Na image (7.17a), and gaps between ridges are visible in the Si image (7.17b).

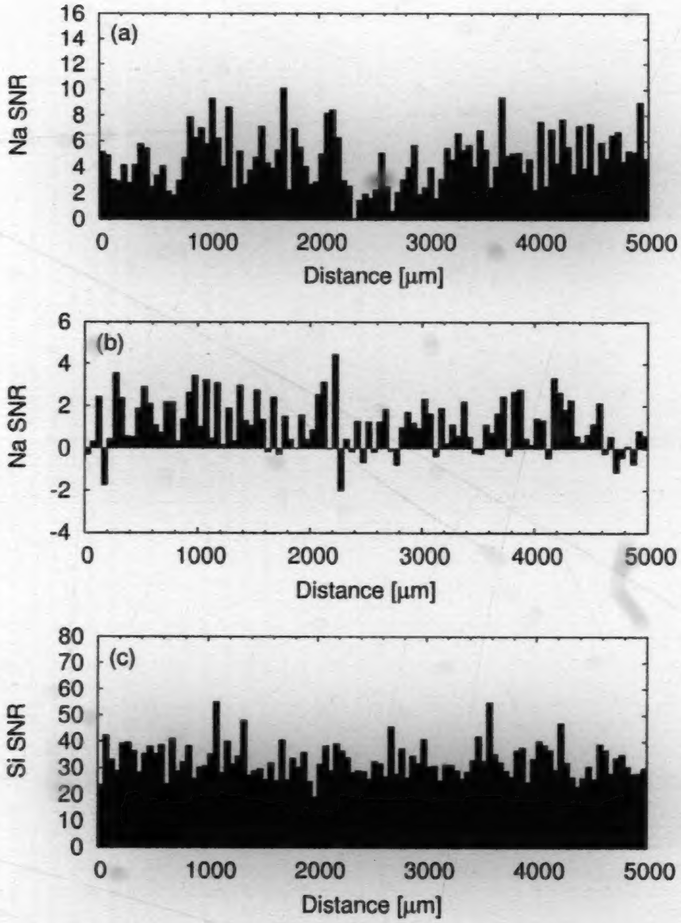

Figure 7.16. *1D LIBS scans of control samples. Sample were imprinted with a fingerprint as described in the text. Sample was then rinsed with ethanol and wiped with lens paper. (a) After repeating the cleaning procedure twice Na was still detected at reduced levels, though fingerprint structure had been destroyed. (b) After a total of 4 cycles of the cleaning procedure, Na is no longer reliably detectable on average. On both the twice washed and quadruple washed sample (c) Si is visible at all spatial locations at SNR levels similar to those observed in the gaps in the fingerprint observed in Fig. 7.15b. (Reproduced with permission from Taschuk et al. [149])*

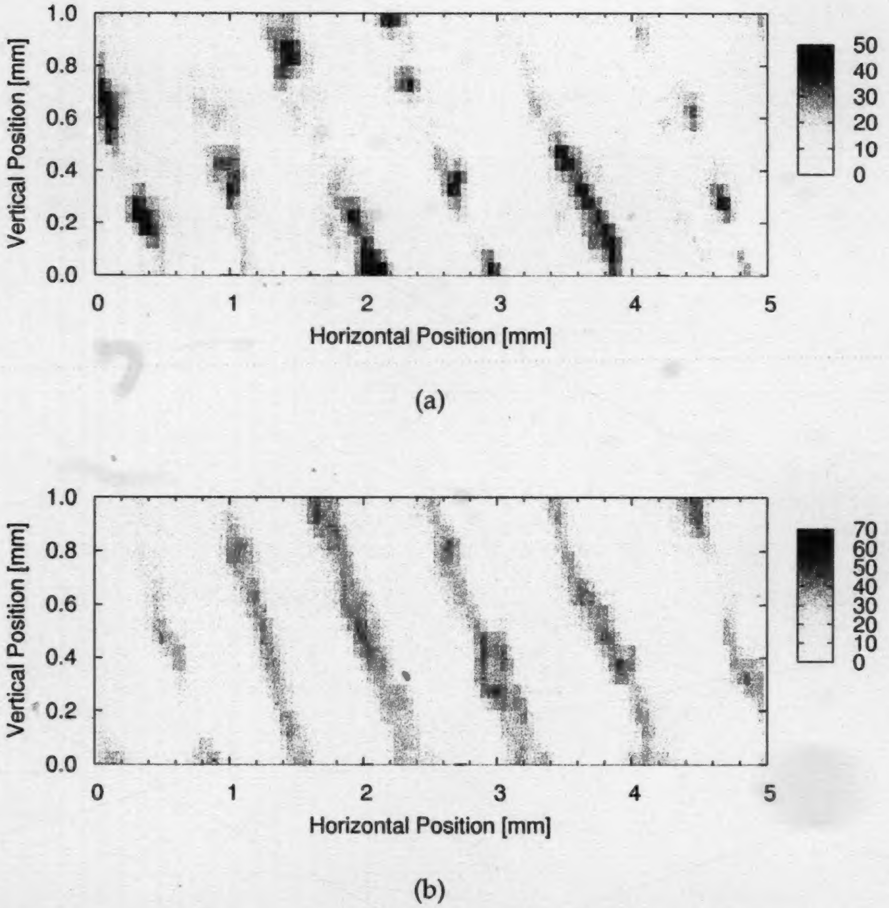

Figure 7.17. *2D LIBS scan of a 1 mm by 5 mm area of a latent fingerprint from the right thumb of one of the authors using 84 μJ pulse energies. Ridges are clearly visible in both (a) Na SNR and (b) Si SNR signals. (Reproduced with permission from Taschuk et al. [149])*

Using optical microscopy, redeposited material surrounding the mapped area is visible. This effect has been the subject of some study [68,70,71], and in principle may affect the quality of any mapping process performed by LIBS. It is known that in some cases the shock wave launched by the LIBS ablation process can clean the redeposited material such that a fresh surface is available for 2D mapping [70]. In the current case, the clarity of the fingerprint maps presented in Fig. 7.17 suggests that redeposition did not significantly affect the results presented here. However, further investigation of the degree to which redeposited material can affect fingerprint mapping for both the current sample type and other substrate materials will be required to quantify the effect.

7.3.4 Discussion

While detection and mapping of a latent fingerprint using 400 nm 84 μJ, 120 fs laser pulses has been demonstrated, many issues remain. These include the time required to acquire a fingerprint image, the level of damage to the latent fingerprint, difficulty in preparing consistent fingerprint samples, the effect of redeposition of ablated material during a mapping process and the detection of reliable fingerprint signal on different surface materials.

The time taken to acquire the image presented in Fig. 7.17 was $\sim$ 20 minutes of laser firing at 2 Hz. This image represents $\sim$ 1% of a total thumb print area of $\sim$ 6 cm^2. The acquisition time could be improved significantly by moving to the multi-kHz repetition rates possible with fiber or microchip lasers. Significant changes to the experimental setup for controlling direction of the laser beam and signal acquisition would be required. It is expected that with acousto-optic or galvano-metric deflectors and photo-multiplier tube data acquisition would be possible at kHz repetition rates, which would allow the acquisition of a full print in a reasonable time. In addition, the step size used here for preliminary testing may be unneccesarily small for fingerprint mapping.

Another difficulty is the possibility of unacceptable damage to the fingerprint. LIBS is generally considered a non-destructive technique, but in the case of small structures that are similar in scale size to the probe spot this is no longer the case. In the current scans, there is significant damage to the print, though the overall structure remains visible. At pulse energies of $\sim$ 80 μJ crater diameters are $\sim$ 50 μm. If step size were increased to 100 μm only $\sim$ 25 % of the print would be damaged by the LIBS mapping process. With even lower energies, it may be possible to further reduce the damage to the print to the point that a substantial fraction of the fingerprint survives the LIBS measurement process. Further work will be required to ascertain the compatibility of the LIBS fingerprint scanning process with the requirements of law enforcement and security applications.

Additional complications arise from the preparation of the latent fingerprint itself, which is a difficult standardisation challenge. As a result, it is not certain that the conditions used here are optimal for the overall distribution of latent fingerprints that might be observed using this technique. Additional optimisation opportunities exist in the choice of wavelength [157]. Use of the third harmonic of the Ti:Sapphire laser at 266 nm may reduce the energies necessary to produce good SNR due to increased absorption in the fingerprint oils.

Redeposition of ablated material was observed for the current 2D mapping process. Based on the quality of the fingerprint image acquired in the present work, it is not believed that the redeposited material is a limiting factor in the acquisition of fingerprint images. However, further work will be required to quantify this effect. In addition, to test the utility of the technique, fingerprint samples on a variety of different substrates will need to be investigated.

Despite the difficulties discussed above, this technique has potential to provide an alternative to the current fluorescent fingerprint imaging techniques. While the Si substrates used here do not contribute any Na emission to the signal, other substrate materials may contribute emission in the Na band. However, in those cases where Na is found in the substrate, it may be possible to use the substrate signal suppression effect observed here to distinguish between Na emission from a latent fingerprint and contributions from the substrate. By observing other elemental lines from the substrate, the substrate signal suppression effect may help identify regions covered by fingerprint ridges. However, further work will be required to ascertain the feasibility of this approach.

Gornushkin et al. and Freedman et al. have demonstrated that microchip lasers can be used to obtain useful LIBS data [66, 91]. With further optimisation of the fingerprint detection operating parameters and the expected increases in the output of microchip lasers, it may be possible to design a portable device capable of detection and mapping fingerprints. By increasing the shot spacing to 200 μm and the increase in repetition rate to ~ 5 kHz which would be possible with a microchip laser, a 6 cm^2 fingerprint could be imaged in ~ 3 seconds. Such a device may reduce the time required to process a crime scene by providing near real time feedback to forensic investigators.

7.3.5 Conclusion

A preliminary investigation of the capabilities of femtosecond μLIBS for detection and mapping of latent fingerprints has been conducted. Detection and mapping of latent fingerprint structure has been demonstrated using 400 nm, 84 μJ pulses. The presence of a latent fingerprint has been shown to suppress the line emission from the Si substrate in regions covered with a fingerprint ridge, indicating that the sensitivity depth for femtosecond pulses is similar to the thickness of the fingerprint. The substrate signal suppression effect may make it possible to detect the fingerprint pattern by monitoring the suppression of other substrate emission lines rather than the Na emission. A 2D image of a 1 mm by 5 mm region of a fingerprint has been successfully collected. Further study is expected to reduce the energy requirements for fingerprint detection. A multi-kHz laser, high speed scanners and improved data acquisition should significantly reduce the current time required to acquire a fingerprint image.

Chapter 8

Conclusions

8.1 Summary of Thesis Results

One of the key obstacles in LIBS research at this time is the lack of quantitative results in the literature. This lack makes it difficult to compare results between different lab groups, and only qualitative comparisons can be made with theory. The available results often include detector characteristics, which can make it difficult to develop a detailed understanding of the underlying physics of the LIBS process. To address this problem, this thesis has focused on quantifying LIBS detection systems, quantifying the behaviour of LIBS at millijoule energies, and determining the scaling laws governing LIBS performance as one moves to the μJ regime.

A theory of LIBS detector systems has been developed, and used to define NEISB and NESB in a manner more useful for the LIBS experimentalist. Using this approach, four LIBS detection systems have been characterised for responsivity, NEISB and NESB. A detailed noise characterisation of the intensified systems has been carried out, characterising cathode noise spikes for spatial distribution, arrival rate, intensity and width.

The laser ablation plume dynamics and absolute emission levels from a traditional LIBS system were examined in detail to quantify the behaviour and allow comparison with simple physical models. The plume dynamics were compared to shock wave expansion and stagnation models, and reasonable agreement was found. A simple model for the emission was compared with the absolute emission levels of the LIBS plasma. While approximate agreement was obtained for early times, the model diverged from experimental observations at later times. Given the lack of heat conduction and radiation loss mechanisms in the model, this discrepancy is expected. In order to take full advantage of the quantitative data set that was collected, a more detailed model with better physics will be required.

The scaling of LIBS emission down to μJ pulse energies was investigated as a function of laser pulse width and wavelength for three targets: Al, 100 nm Cu on Si, and Si. The ablation efficiency of Si was investigated in detail for femtosecond laser pulses. When combined with the absolute emission levels, it was possible to characterise the emission efficiency of the μLIBS plasmas in terms of emitted photons per atom. The number of photons emitted was found to be a small fraction of the number of atoms ablated from the target for the energy range between 100 nJ and 100 μJ. Using the 100 nm Cu on Si targets, it was found that the ablated region which contributes to the LIBS emission is restricted to a layer much shallower than the ablation crater.

Finally, a few applications of the μLIBS technique were presented. Surface mapping of Al alloys with sub-microjoule laser pulses was demonstrated. It was also shown that latent fingerprints can be detected and imaged using the μLIBS technique.

8.2 Outlook for Future Work

> *Science never solves a problem without creating ten more.*
> George Bernard Shaw

8.2.1 μLIBS LOD Capabilities

Though not presented in full detail in this thesis, it has been shown that the LODs achievable with μLIBS are comparable to those achieved in traditional LIBS. This work was performed at relatively high energies and using nanosecond pulses. The current experimental setup is well suited to extending this work to pulse energies well below 100 μJ, which will allow an experimental verification of the results presented by Freedman et al., who used 14 μJ pulses and an unintensified system [91]. The scaling of the achievable LOD to lower energies is of importance in the design and implementation of portable LIBS systems. This work would also represent an opportunity to test the detector performance characterisation presented in this thesis.

8.2.2 Detector Characterisations

The detector performance characterisation should be used to fully predict the performance of one of the systems for a case that wasn't done during the course of this thesis. This would require an absolute characterisation of the emission levels from a new material. This test would determine what, if any, factors are missing from the detector theory developed during the course of this thesis work. The model could be extended to include noise contributions from continuum emission, to more fully model the LIBS process. In addition, the effect of signal shot noise should be explored in more detail. Since noise from the signal is neglected for the current analysis, the full behaviour of the system has not been captured.

8.2.3 LIBS Modelling

The absolute emission data collected during the course of this thesis could be used test models or numerical simulations of the LIBS process.

8.2.4 μLIBS Physics

In terms of the overall performance of the μLIBS technique, the issue of emission efficiency will be critical. Further quantification of both the emission efficiency and the region of the ablated zone which contributes to μLIBS emission is required. The emission efficiency should be continued to higher energy levels for femtosecond laser pulses, and for the longer pulse width lasers which have a significant laser-plasma interaction. Eventually, this will need to be done for the traditional LIBS pulse energies.

The issue of depth sensitivity is of great importance for μLIBS and traditional LIBS alike. With the use of layered targets of different thicknesses, this effect could be quantified in detail. As in the case of the emission efficiencies, this should also be done for conventional LIBS pulse energies in order to clarify the possibilities for LIBS depth profiling.

8.2.5 μLIBS Applications

For the sub-microjoule 2D mapping work, the first aspect which should be addressed is the possibility of cathode spike removal. Since the number of photons available is so low, every potential avenue for improving SNR must be explored to help the performance of μLIBS at these energy levels. After that, it is expected that the use of multiple shots for each target site will also improve the performance of the technique since the damage to the target per shot is low.

The application of μLIBS to fingerprint analysis has many promising avenues of investigation. The investigation of the detection of fingerprints on more complicated substrates is the next step for the overall usefulness of the technique. If some strategies for detection of fingerprints on more realistic substrates can be developed, it should be possible to decrease the time required to acquire a fingerprint image to a few seconds using high repetition-rate laser systems.

8.3 Conclusion

This thesis has helped move the understanding of LIBS forward by quantifying the LIBS process, developing the understanding of the scaling laws of LIBS as one scales to microjoule energies, and quantifying the performance of LIBS detection systems. The understanding developed of the capabilities of μLIBS indicates that it should be possible to develop small, portable LIBS systems using microjoule laser systems.

References

[1] E.F. Runge, R.W. Minck, F.R. Bryan. Spectrochemical analysis using a pulsed laser source. *Spectrochimica Acta*, 20:733 – 736, 1964.

[2] R. Noll, V. Sturm, M. Stepputat, A. Whitehouse, J. Young, P. Evans. Industrial applications of LIBS. In A.Z. Miziolek, V. Palleschi and I. Schechter, editor, *Laser-Induced Breakdown Spectroscopy (LIBS): Fundamentals and Applications*, pages 400 – 439. Cambridge University Press, 2006.

[3] D.A. Cremers and L.J. Radziemski. *Handbook of Laser-Induced Breakdown Spectroscopy*. John Wiley & Sons, Ltd., 2006.

[4] A.Z. Miziolek, V. Palleschi and I. Schechter, editor. *Laser-Induced Breakdown Spectroscopy (LIBS): Fundamentals and Applications*. Cambridge University Press, 2006.

[5] J.P. Singh, S.N. Thakur, editor. *Laser-Induced Breakdown Spectroscopy*. Elsevier Science B.V., 2007.

[6] F. Brech, L. Cross. Optical microemission stimulated by ruby maser. *Applied Spectroscopy*, Vol. 16:59, 1962.

[7] Anonymous. Lasers Boost Spectrography Utility. *Chemical & Engineering News*, Vol. 40, No. 36:52, 1962.

[8] S.D. Rasberry, B.F. Scribner, M. Margoshes. Laser Probe Excitation in Spectrochemical Analysis. I: Characteristics of the Source. *Applied Optics*, Vol. 6:81 – 86, 1967.

[9] E.S. Beatrice, I. Harding-Barlow, D. Glick. Electric Spark Cross-Excitation in Laser Microprobe-Emission Spectroscopy for Samples of 10 - 25 μ Diameter. *Applied Spectroscopy*, Vol. 23:257 – 259, 1969.

[10] N.A. Peppers. A Laser Microscope. *Applied Optics*, Vol. 4:555 – 558, 1965.

[11] R.C. Rosan. On the Preparation of Samples for Laser Microprobe Analysis. *Applied Spectroscopy*, Vol. 19:97 – 98, 1965.

[12] I. Harding-Barlow, E.S. Beatrice and D. Glick. Laser Microprobe Emission Spectroscopy of Picogram Quantities of Cations in Tissue. *Federation Proceedings*, Vol. 26:780.

[13] E.H. Piepmeier, H.V. Malmstadt. Q-Switched Laser Energy Absorption in the Plume of an Aluminum Alloy. *Analytical Chemistry*, Vol. 41:700 – 707, 1969.

[14] J.W. Daiber, J.G. Winans. Radiation from Laser-Heated Plasmas in Nitrogen and Argon. *Journal of the Optical Society of America*, Vol. 58:76 – 80, 1968.

[15] R.H. Scott, A. Strasheim. Laser Induced Plasmas for Analytical Spectroscopy. *Spectrochimica Acta B*, Vol. 25:311 – 332, 1970.

[16] R.H. Scott, A. Strasheim. Time-resolved direct-reading spectrochemical analysis using a laser source with a medium pulse-repetition rate. *Spectrochimica Acta B*, Vol. 26:707 – 719, 1971.

[17] W.J. Treytl, J.B. Orenberg, K.W. Marich, D. Glick. Photoelectric Time Differentiation in Laser Microprobe Optical Emission Spectroscopy. *Applied Spectroscopy*, Vol. 25:376 – 378, 1971.

[18] T. Ishizuka. Laser Emission Spectrography of Rare Earth Elements. *Analytical Chemistry*, Vol. 45:583 – 541, 1973.

[19] D. Glick, K.W. Marich. Potential for Clinical Use of the Analytical Laser Microprobe for Element Measurement. *Clinical Chemistry*, Vol. 21:1238 – 1244, 1975.

[20] W.J Treytl, K.W. Marich, J.B. Orenberk, P.W. Carr, D.C. Miller, D. Glick. Effect of Atmosphere on Spectral Emission from Plasmas Generated by the Laser Microprobe. *Analytical Chemistry*, Vol. 43:1452 – 1456, 1971.

[21] H.S. Kwong, R.M. Measures. Trace Element Laser Microanalyzer with Freedom from Chemical Matrix Effect. *Analytical Chemistry*, Vol. 51:428 – 432, 1979.

[22] R.M. Measures, H.S. Kwong. TABLASER: trace (element) analyzed based on laser ablation and selectively excited radiation. *Applied Optics*, Vol. 18:281 – 286, 1979.

[23] C.D. Allemand. Spectroscopy of single-spike laser-generated plasmas. *Spectrochimica Acta B*, Vol. 27:185 – 204, 1972.

[24] T.R. Loree, L.J. Radziemski. Laser-Induced Breakdown Spectroscopy: Time-Integrated Applications. *Plasma Chemistry and Plasma Processing*, Vol. 1:271 – 279, 1981.

[25] L.J. Radziemski, T.R. Loree. Laser-Induced Breakdown Spectroscopy: Time-Resolved Spectrochemical Applications. *Plasma Chemistry and Plasma Processing*, Vol. 1:281 – 293, 1981.

[26] D.A. Cremers, L.J. Radziemski. Detection of Chlorine and Fluorine in Air by Laser-Induced Breakdown Spectrometry. *Analytical Chemistry*, Vol. 55:1252 – 1256, 1983.

[27] L.J. Radziemski, T.R. Loree, D.A. Cremers, N.M. Hoffman. Time-Resolved Laser-Induced Breakdown Spectrometry of Aerosols. *Analytical Chemistry*, Vol. 55:1246 – 1252, 1983.

[28] G. Chen and E.S. Yeung. Acoustic Signal as an Internal Standard for Quantitation in Laser-Generated Plumes. *Analytical Chemistry*, Vol. 60:2258 – 2263, 1988.

[29] K.J. Grant and G.L. Paul. Electron Temperature and Density Profiles of Excimer Laser-Induced Plasmas. *Applied Spectroscopy*, Vol. 44:1349 – 1354, 1990.

[30] K.J. Grant, G.L. Paul, J.A. O'Neill. Time-Resolved Laser-Induced Breakdown Spectroscopy of Iron Ore. *Applied Spectroscopy*, Vol. 44:1711 – 1714, 1990.

[31] K.J. Grant, G.L. Paul, J.A. O'Neill. Quantitative Elemental Analysis of Iron Ore by Laser-Induced Breakdown Spectroscopy. *Applied Spectroscopy*, Vol. 45:701 – 705, 1991.

[32] Z.W. Hwang, Y.Y. Teng, K.P. Li and J. Sneddon. Interaction of a Laser Beam with Metals. Part I: Quantitative Studies of Plasma Emission. *Applied Spectroscopy*, Vol. 45:435 – 441, 1991.

[33] Y.I. Lee and J. Sneddon. Ambient Gas Breakdown Behaviour in an Excimer Laser-Ablated Plasma. *Microchemical Journal*, Vol. 50:235 – 243, 1994.

[34] C.M. Davies, H.H. Telle, D.J. Montgomery, R.E. Corbett. Quantitative analysis using remote laser-induced breakdown spectroscopy (LIBS). *Spectrochimica Acta B*, Vol. 50:1059 – 1075, 1995.

[35] Laser Diagnostics of Painted Artworks: Laser-Induced Breakdown Spectroscopy in Pigment Identification. D. Anglos, S. Couris, C. Fotakis. *Applied Spectroscopy*, Vol. 51:1025 – 1030, 1997.

[36] J.M. Vadillo, J.J. Laserna. Depth-resolved Analysis of Multilayered Samples by Laser-Induced Breakdown Spectrometry. *Journal of Analytical Atomic Spectrometry*, Vol. 12:859 – 862, 1997.

[37] M.T. Taschuk, I.V. Cravetchi, Y.Y. Tsui and R. Fedosejevs. MicroLIBS. In J.P. Singh, S.N. Thakur, editor, *Laser Induced Breakdown Spectroscopy*. Elsevier Science B.V., 2007.

[38] W.S. Fann, R. Storz, H.W.K. Tom and J. Bokor. Electron thermalization in gold. *Physical Review B*, Vol. 46:13592 – 13595, 1992.

[39] F.F. Chen. *Introduction to Plasma Physics and Controlled Fusion (Volume 1: Plasma Physics)*. Plenum Press, 2nd edition, 1984.

[40] D. Bäuerle. *Laser Processing and Chemistry*. Springer-Verlag, Third, Revised and Enlarged edition, 2000.

[41] G. Taylor. The formation of a blast wave by a very intense explosion I. Theoretical discussion. *Proceedings of the Royal Society of London. Series A, Mathematical and Physical Sciences*, Vol. 21:159–174, 1950.

[42] L.I. Sedov. *Similarity and Dimensional Methods in Mechanics*. CRC Press, 10th edition edition, 1993.

[43] P.E. Dyer and J. Sidhu. Spectroscopic and fast photographic studies of excimer laser polymer ablation. *Journal of Applied Physics*, Vol. 64:4657 – 4663, 1988.

[44] P.E. Dyer, A. Issa and P.H. Key. Dynamics of excimer laser ablation of superconductors in an oxygen environment. *Applied Physics Letters*, Vol. 57:186 – 188, 1990.

[45] H.R. Griem. *Principles of Plasma Spectroscopy*. Cambridge University Press, 1997.

[46] D. Menut, P. Fichet, J-L. Lacour, A. Rivoallan and P. Mauchien. Micro-laser-induced breakdown spectroscopy technique: a powerful method for performing quantitative surface mappingon conductive and non-conductive samples. *Applied Optics*, Vol. 42:6063 – 6071, 2003.

[47] B. Al Ali, D. Bulajic, M. Corsi, G. Cristoforetti, S. Legnaioli, L. Masotti, V. Palleschi, A. Salvetti and E. Tognoni. MicroLIBS/MicroRaman Spectroscopic Analysis of Pigments in a Roman Fresco. *SPIE 4402*, pages 25 – 31, 2001.

[48] John J. Zayhowski and A. Mooradian. Single-Frequency microchip Nd Lasers. *Optics Letters*, Vol. 14:24 – 26, 1989.

[49] John J. Zayhowski. Q-switched operation of microchip lasers. *Optics Letters*, Vol. 16:575 – 577, 1991.

[50] John J. Zayhowski. Ultraviolet generation with passively Q-switched microchip lasers. *Optics Letters*, Vol. 21:588 – 590, 1996.

[51] J. Bloch, B. Johnson, N. Newbury, J. Germain, H. Hemond, J. Sinfield. Field Test of a Novel Microlaser-Based Probe for in situ Fluoresence Sensing of Soil Contamination. *Applied Spectroscopy*, Vol. 52:1299 – 1304, 1998.

[52] John J. Zayhowski. Passively Q-switched Nd:YAG microchip lasers and applications. *Journal of Alloys and Compounds*, 303 - 304:393 – 400, 2000.

[53] J. Limpert, A. Liem, M. Riech, T. Schreiber, S. Nolte, H. Zellmer, A. Tünnermann, J. Broeng, A. Petersson,C. Jakobsen. Low-nonlinearity single-transverse-mode ytterbium-doped photonic crystal fiber amplifier. *Opt. Express*, Vol. 12:1313 – 1319, 2004.

[54] M. Laroche, A.M. Chardon, J. Nilsson, D.P. Shepherd, W.A. Clarkson. Compact diode-pumped passively Q-switched tunable Er-Yb double-clad fiber laser. *Opt. Lett.*, Vol. 27:1980 – 1982, 2002.

[55] H. Häkkänen and J.E.I. Korppi-Tommola. Uv-laser plasma study of elemental distributions of paper coatings. *Applied Spectroscopy*, Vol. 49:1721 – 1728, 1995.

[56] C. Geertsen, J-L Lacour, P. Mauchien, L. Pierrard. Evalution of laser ablation optical emission spectrometery for microanalysis in aluminum samples. *Spectrochimica Acta B*, Vol. 51:1403 – 1416, 1996.

[57] M. Hidalgo, F. Martin and J.J. Lasernai. Laser-induced breakdown spectrometry of titanium dioxide antireflection coatings in photovoltaic cells. *Analytical Chemistry*, Vol. 68:1095 – 1100, 1996.

[58] W.F. Ho, C.W. Ng and N.H. Cheung. Spectrochemical Analysis of Liquids Using Laser-Induced Plasma Emissions: Effects of Wavelength. *Applied Spectroscopy*, Vol. 51:87 – 91, 1997.

[59] B. Sall e, C. Chaléard, V. Detalle, J.L. Lacour, P. Mauchien, C. Nouvellon, A. Semerok. Laser Ablation efficiency of metal samples with UV laser nanosecond pulses. *Applied Surface Science*, Vol. 138 - 139:302 – 305, 1999.

[60] B. Sall e, M.N. Libenson, P. Mauchien, G. Petite, A. Semerok, and J-F. Wagner. Laser Plasma limiting effects at nanosecond laser microablation. SPIE 3822, pages 56 – 67, 1999.

[61] A. Semerok, C. Chal eard, V. Detalle, J-L. Lacour, P. Mauchien, P. Meynadier, C. Nouvellon, B. Salle e,P. Palianov, M. Perdix, G. Petite. Experimental investigations of laser ablation efficiency of pure metals with femto, pico and nanosecond pulses. *Applied Surface Science*, Vol. 138-139:311 – 314, 1999.

[62] A. Semerok, B. Sall e, J-F. Wagner, G. Petite, O. Gobert, P. Meynadier, M. Perdrix. Microablation of Pure Metals: Laser Plasma and Crater Investigations. SPIE 4423, pages 153 – 164, 2001.

[63] D. Kossakovski and J.L. Beauchamp. Topographical and Chemical Microanalysis of Surfaces with a Scanning Probe Microscope and Laser-Induced BreakdownSpectroscopy. *Analytical Chemistry*, Vol. 72:4731 – 4737, 2000.

[64] G.W. Rieger, M. Taschuk, Y.Y. Tsui and R. Fedosejevs. Laser Induced Breakdown Spectroscopy for Microanalysis using Sub-millijoule UV Laser Pulses. *Applied Spectroscopy*, Vol. 56:689 – 698, 2002.

[65] G.W. Rieger, M. Taschuk, Y.Y. Tsui and R. Fedosjevs. Comparative study of laser-induced plasma emission from microjoule picosecond and nanosecond KrF-laser pulses. *Spectrochimica Acta B*, Vol. 58:497 – 510, 2003.

[66] I.B. Gornushkin, K. Amponsah-Manager, B.W. Smith, N. Omenetto, J.D. Winefordner. Microchip Laser-Induced Breakdown Spectroscopy: A Preliminary Feasibility Investigation. *Applied Spectroscopy*, Vol. 71:762 – 769, 2004.

[67] J.M. Vadillo, S. Palanco, M.D. Romero, and J.J. Laserna. Applications of laser-induced breakdown spectrometry (LIBS) in surface analysis. *Fresenius Journal of Analytical Chemistry*, Vol. 355:909 – 912, 1996.

[68] D. Romero and J.J. Laserna. Multielemental Chemical Imaging Using Laser-Induced Breakdown Spectrometry. *Analytical Chemistry*, Vol. 69:2871 – 2876, 1997.

[69] I. Cravetchi, M. Taschuk, G.W. Rieger, Y.Y. Tsui and R. Fedosejevs. Spectrochemical Microanalysis of Aluminum Alloys by Laser Induced Breakdown Spectroscopy: Identification ofPrecipitates. *Applied Optics*, Vol. 42:6138 – 6147, 2003.

[70] I. Cravetchi, M. Taschuk, Y.Y. Tsui and R. Fedosejevs. Scanning microanalysis of Al alloys by laser-induced breakdown spectroscopy. *Spectrochimica Acta B*, 59:1439 – 1450, 2004.

[71] H. Häkkänen, J. Houni, S. Kaski, and J.E.I. Korppi-Tommola. Analysis of paper by laser-induced plasma spectroscopy. *Spectrochimica Acta B*, Vol. 56:737 – 742, 2001.

[72] N.H. Cheung, C.W. Ng, W.F. Ho and E.S. Yeung. Ultra-micro analysis of liquids and suspensions based on laser-induced plasma emissions. *Appl. Surf. Sci.*, Vol. 127 - 129:274 – 277, 1998.

[73] J.J. Zayhowski. Microchip lasers. *Lincoln Laboratory Journal*, 3:427 – 446, 1990.

[74] J.J. Zayhowski and J.A. Keszenheimer. Frequency Tuning of Microchip Lasers Using Pump-Power Modulation. *IEEE J. Quantum Electron.*, Vol. 28:1118 – 1122, 1992.

[75] J.J. Zayhowski and C. Dill III. Diode-pumped passively Q-switched picosecond microchip lasers. *Opt. Lett.*, Vol. 19.:1427 – 1429, 1994.

[76] John J. Zayhowski. Passively Q-switched Microchip Lasers and Applications. *Laser Review*, Vol. 26:841 – 846, 1998.

[77] D. Taverner, D.J. Richardson, L. Dong, J.E. Caplen, K. Williams, R.V. Penty. 158 μJ pulses from a single-transverse-mode large-mode-area erbium-doped fiber amplifier. *Opt. Lett.*, Vol. 22:378 – 380, 1997.

[78] H.L. Offerhaus, N.G. Broderick, D.J. Richardson, R. Sammut, J. Caplen and L. Dong. High-energy single-transverse-mode Q-switched fiber laser based on a multimode large-mode-area erbium-dopedfiber. *Opt. Lett.*, Vol. 23:1683 – 1685, 1998.

[79] C.C. Renaud, H.L. Offerhaus, J.A. Alvarez-Chavez, J. Nilsson. W.A. Clarkson, P.W. Turner, D.J. Richardson, A.B. Grudinin. Characterisitics of Q-Switched Cladding-Pumped Ytterbium-Doped Fiber Lasers with DifferentHigh-Energy Fiber Designs. *IEEE J. Quantum Electron.*, Vol. 37:199 – 206, 2001.

[80] A. Galvanauskas. Mode-Scalable Fiber-Based Chirped Pulse Amplification Systems. *IEEE Journal on Selected Topics in Quantum Electronics*, Vol. 7:504 – 517, 2001.

[81] J. Limpert et al. 100-W average-power, high-energy nanosecond fiber amplifier. *Applied Physics B*, Vol. 75:477 – 479, 2002.

[82] R. Fluck, R. Häring, R. Paschotta, E. Gini, H. Melchior and U. Keller. Eyesafe pulsed microchip laser using semiconductor saturable absorber mirrors. *Applied Physics Letters*, Vol. 72, No. 25:3273 – 3275, 1998.

[83] G.J. Spühler, R. Paschotta, M.P. Kullberg, M. Graf, M. Moser, E. Mix, G. Huber, C. Harder, U. Keller. A passively Q-switched Yb:YAG microchip laser. *Applied Physics B*, Vol. 72:285 – 287, 2001.

[84] R. Feldman, Y. Shimony, Z. Burshtein. Passive Q-switching in Nd:YAG/Cr^{4+}:YAG monolithic microchip laser. *Optical Materials*, Vol. 24:393 – 399, 2003.

[85] G. Karlsson, V. Pasiskevicius, F. Laurell, J.A. Tellefsen. Q-switching of an Er-Yb:glass microchip laser using an acousto-optical modulator. *Optics Communications*, Vol. 217:317 – 324, 2003.

[86] F. Druon, F. Balembois, P. Georges and A. Brum. High-repetition-rate 300-ps pulsed ultraviolet source with a passively Q-switched microchip laser and a multipassamplifier. *Optics Letters*, Vol. 24, No. 7:499 – 501, 1999.

[87] B. Braun, F.X. Kärtner, U. Keller, J.-P. Meyn, G. Huber. Passive Q-switched 180-ps Nd:$LaSc_3(BO_3)_4$ microchip laser. *Opt. Lett.*, Vol. 21:405 – 407, 1996.

[88] R. Fluck, B. Braun, E. Gini, H. Melchior, and U. Keller. Passively Q-switched 1.34-μm Nd:YVO_4 microchip laser with semiconductor saturable-absorber mirrors. *Opt. Lett.*, Vol. 22:991 – 993, 1997.

[89] Björn T. Hansson and Ari T. Friberg. Eye-safe actively Q-switched microchip laser with an electro-absorbing semiconductor modulator. *Optics Letters*, Vol. 26, No. 14.:1057 – 1059, 2001.

[90] John J. Zayhowski. Passively Q-switched Microchip Lasers and Applications. *Journal of the Communications Research Laboratory*, Vol. 46, No. 3:385 – 398, 1999.

[91] A. Freedman, F.J. Iannarilli Jr., J.C. Wormhoudt. Aluminum alloy analysis using microchip-laser induced breakdown spectroscopy. *Spectrochimica Acta B*, Vol. 60:1076 – 1082, 2005.

[92] J. Wormhoudt, F.J. Iannarilli Jr., S. Jones, K.D. Annen and A. Freedman. Determination of Carbon in Steel by Laser-Induced Breakdown Spectroscopy Using a Microchip Laser and Miniature Spectrometer. *Applied Spectroscopy*, Vol. 59:1098 – 1102, 2005.

[93] D. Taverner, P. Britton, P.G.R. Smith, D.J. Richardson, G.W. Ross, D.C. Hanna. Highly efficient second-harmonic and sum-frequency generation of nanosecond pulses in a cascaded erbium-dopedfiber:periodically poled lithium niobate source. *Opt. Lett.*, Vol. 23:162 – 164, 1998.

[94] M.T. Taschuk, S.E. Kirkwood, Y.Y. Tsui and R. Fedosejevs. Quantitative emission from femtosecond microplasmas for laser-induced breakdown spectroscopy. *Journal of Physics: Conference Series*, (In Press), 2007.

[95] G.W. Rieger, M. Taschuk, Y.Y. Tsui and R. Fedosejevs. Laser Induced Breakdown Spectroscopy with Low Energies. SPIE 4087, pages 1127 – 1136, 2000.

[96] M. Sabsabi and P. Cielo. Quantitative Analysis of Aluminum Alloys by Laser-Induced Breakdown Spectroscopy and PlasmaCharacterization. *Applied Spectroscopy*, Vol. 49:499 – 507, 1995.

[97] D. Romero and J.J. Laserna. Surface and tomographic distribution of carbon impurities in photonic-grade silicon using laser-induced breakdownspectrometry. *Journal of Analytical Atomic Spectrometry*, Vol. 13:557 – 560, 1998.

[98] I.V. Cravetchi, M.T. Taschuk, Y.Y. Tsui and R. Fedosejevs. Evaluation of femtosecond LIBS for spectrochemical analysis of aluminum alloys. *Anal. Bioanal. Chem.*, 385, 287 - 294.

[99] D. Romero and J.J. Laserna. A microanalytical study of aluminum diffusion in photovoltaic cells using imaging-mode laser-inducedbreakdown spectrometry. *Spectrochimica Acta B*, Vol. 55:1241 – 1248, 2000.

[100] M.P. Mateo, L.M. Cabalín and J.J. Laserna. Automated Line-Focused Laser Ablation for Mapping of Inclusions in Stainless Steel. *Applied Spectroscopy*, Vol. 57:1461 – 1467, 2003.

[101] M.P. Mateo, L.M. Cabalín, J.M. Baena, J.J. Laserna. Surface interaction and chemical imaging in plasma spectrometry induced with a line-focused laser beam. *Spectrochimica Acta B*, Vol. 57:601 – 608, 2002.

[102] K.T. Rodolfo et al. Capabilities of Surface Composition Analysis Using a Long Laser-Induced Breakdown Spectroscopy Spark. *Applied Spectroscopy*, Vol. 58:367 – 375, 2004.

[103] Nai-Ho Cheung and Edward S. Yeung. Single-Shot Elemental Analysis of Liquids Based on Laser Vaporization at Fluences Below Breakdown. *Appl. Spectrosc.*, Vol. 47:882 – 886, 1993.

[104] Nai-Ho Cheung and Edward S. Yeung. Distribution of Sodium and Potassium Within Individual Human Erythrocytes by Pulsed-Laser Vaporization in aSheath Flow. *Anal. Chem.*, Vol. 66:929 – 936, 1994.

[105] M.T. Taschuk, Y.Y. Tsui and R. Fedosejevs. Optimization of laser-induced breakdown spectroscopy for liquid samples at millijoule pulse energies. *2002 Laser Induced Breakdown Spectroscoy, Orlando, USA, Sept. 24 - 28th,* 2002.

[106] Y. Godwal, S.L. Lui, M.T. Taschuk, Y.Y. Tsui and R. Fedosejevs. Detection of Elemental Contaminants in Water with Dual-Pulse μLIBS. *2006 Laser Induced Breakdown Spectroscoy, Montreal, Canada, Sept. 5th - 8th,* 2006.

[107] E. Hecht. *Optics*. Addison-Weslay Longman, Inc., 3rd edition, 1998.

[108] M. Born and E. Wolf. *Principles of Optics*. Cambridge University Press, 7th (expanded) edition, 1999.

[109] S. Brodersen. Slit-Width Effects. *Journal of the Optical Society of America*, Vol. 44:22 – 25, 1954.

[110] J.R. Janesick. *Scientific Charge-Coupled Devices*. SPIE Press, 2001.

[111] G.F. Knoll. *Radiation Detection and Measurement*. John Wiley & Sons, Inc., 3rd edition. edition, 2000.

[112] C.J. Sansonetti et al. Wavelengths of spectral lines in mercury pencil lamps. *Applied Optics*, Vol. 35:74–77, 1996.

[113] C.J. Sansonetti J. Reader and J.M. Bridges. Irradiances of spectral lines in mercury pencil lamps. *Appl. Opt.*, Vol. 35:78 – 83, 1996.

[114] B.P. Lathi. *Signal Processing and Linear Systems*. Berkeley Cambridge Press, Carmichael, California, 1998.

[115] R.A. Multari, L.E. Foster, D.A. Cremers and M.J. Ferris. Effect of Sampling Geometry on Elemental Emissions in Laser-Induced Breakdown Spectroscopy. *Applied Spectroscopy*, Vol. 50:1483 – 1499, 1996.

[116] C. Aragon and J.A. Aguilera. Two-Dimensional Spatial Distribution of the Time-Integrated Emission from Laser-Produced Plasmas in Air at Atmospheric Pressure. *Applied Spectroscopy*, Vol. 51:1632 – 1638, 1997.

[117] M. Milan and J.J. Laserna. Diagnostics of silicon plasmas produced by visible nanosecond laser ablation. *Spectrochimica Acta B*, Vol. 56:275 – 288, 2001.

[118] M.Taschuk, I. Cravetchi, Y.Y. Tsui and R. Fedosejevs. Scaling to millijoule energies for laser induced breakdown spectroscopy of water samples. In *Proceedings of the 2002 IQEC/LAT*, SPIE 5149, pages 239–250, 2002.

[119] M. Taschuk, Y.Y. Tsui and R. Fedosejevs. Optimization of Laser-Induced Breakdown Spectroscopy for Liquid Samples at Millijoule Pulse Energies. In *Laser Induced Plasma Spectroscopy and Applications*, volume 81 of *OSA Trends in Optics and Photonics (TOPS)*, 2002.

[120] M.T. Taschuk, Y. Godwal, Y.Y. Tsui, R. Fedosejevs, M. Tripathi, B. Kearton. Absolute Characterization of LIBS Detection Systems. *Spectrochimica Acta B*, (Submitted Dec. 15th, 2006).

[121] J.F. James, R.S. Sternberg. *The Design of Optical Spectrometers*. Chapman and Hall Ltd., 1969.

[122] E.L. Dereniak, D.G. Crowe. *Optical Radiation Detectors*. John Wiley & Sons, 1984.

[123] S.B. Howell. *Handbook of CCD Astronomy*. Cambridge University Press, 2000.

[124] J.R. Taylor. *An Introduction to Error Analysis*. University Science Books, 2nd edition, 1997.

[125] G. Colonna, A. Casavola, M. Capitelli. Modelling of libs plasma expansion. *Spectrochimica Acta B*, Vol. 56:567 – 586, 2001.

[126] A. De Giacomo, V.A. Shakhatov, O. De Pascale. Optical emission spectroscoy and modeling of plasma produced by laser ablation of titanium oxides. *Spectrochimica Acta B*, Vol. 56:753 – 776, 2001.

[127] V.I. Babushok, F.C. DeLucia Jr., P.J. Dagdigian, M.J. Nusca and A.W. Miziolek. Kinetic modeling of the laser-induced breakdown spectroscopy plume from metallic lead. *Applied Optics*, Vol. 42:5947 – 5962, 2003.

[128] G. Colonna, L.D. Pietanza, M. Capitelli. Coupled solution of a time-dependent collisional-radiative model and boltzmann equation for atomic hydrogen plasmas:possible implications with libs plamas. *Spectrochimica Acta B*, Vol. 56:587 – 598, 2001.

[129] H.C. Le, D.E. Zeitoun, J.D. Parisse, M. Sentis, W. Marine. Modeling of gas dynamics for a laser-generated plasma: Propagation into low-pressure gases. *Physical Review E*, Vol. 62:4152 – 4161, 2000.

[130] N. Arnold, J. Gruber, J. Heitz. Spherical expansion of the vapour plume into ambient gas: an analytical model. *Applied Physics A*, Vol. 69:S87 – S93, 1999.

[131] P. Shah, R.L. Armstrong, L.J. Radziemski. Modeling of time-dependent laser-induced plasma spectra formed on a carbon surface. *Journal of Applied Physics*, Vol. 65:2946 – 2950, 1989.

[132] P. Shah, A. Biswas, R.L. Armstrong, L.J. Radziemski. On the coupling of blast wave theory with atomic excitation in low-energy laser-induced plasmas formed in gases. *Journal of Applied Physics*, Vol. 68:3809 – 3813, 1990.

[133] I.B. Gornushkin, A.Ya. Kazakov, N. Omenetto, B.W. Smith, J.D. Winefordner. Radiation dynamics of post-breakdown laser induced plasma. *Spectrochmica Acta B*, Vol. 59:401 – 418, 2004.

[134] I.B. Gornushkin, A.Ya. Kazakov, N. Omenetto, B.W. Smith, J.D. Winefordner. Experimental verification of a radiative model of laser-induced plasma expanding into vacuum. *Spectrochimica Acta B*, Vol. 60:215 – 230, 2005.

[135] I.B. Gornushkin, S.V. Shabanov, N. Omenetto, J.D. Winefordner. Non-isothermal asymmetric expansion of laser induced plasmas into vacuum. *Journal of Applied Physics*, Vol. 100:073304, 2006.

[136] A.Ya. Kazakov, I.B. Gornushkin, N. Omenetto, B.W. Smith, J.D. Winefordner. Radiative model of post-breakdown laser-induced plasma expanding into ambient gas. *Applied Optics*, Vol. 45:2810 – 2820, 2006.

[137] G. Taylor. The formation of a blast wave by a very intense explosion II. The atomic explosion of 1945. *Proceedings of the Royal Society of London. Series A, Mathematical and Physical Sciences*, Vol. 21:174 – 186, 1950.

[138] W.J. Treytl, J.B. Orenberg, K.W. Marich, A.J. Saffir, D. Glick. Detection Limits in Analysis of Metals in Biological Materials by Laser Microprobe Optical Emission Spectrometery. *Analytical Chemistry*, Vol. 44:1903 – 1904, 1972.

[139] G. Arca, A. Ciucci, V. Palleschi, S. Rastelli, E. Tognoni. Detection of Pollutants in Liquids by Laser Induced Breakdown Spectroscopy Technique. *IEEE Geoscience and Remote Sensing Symposium*, pages 520 – 522, 1996.

[140] R. Knopp et al. Laser induced breakdown spectroscopy (libs) as an analytical tool for the detection of metal ions in aqueous solutions. *Fresenius Journal of Analytical Chemistry*, Vol. 355:16 – 20, 1996.

[141] O. Samek et al. Application of laser-induced breakdown spectrosocpy to in situ analysis of liquid samples. *Optical Engineering*, Vol. 39:2248 – 2262, 2000.

[142] J.O. Caceres et al. Quantitative analysis of trace metals in ice using laser-induced breakdown spectroscopy. *Spectrochim. Acta, Part B*, Vol. 56:831 – 838, 2001.

[143] K.M. Lo and N.H. Cheung. Arf laser-induced plasma spectroscopy for part-per-billion analysis of metal ions in aqueous solutions. *Applied Spectroscopy*, Vol. 56:682 – 688, 2002.

[144] D. Geohegan. Fast intensified-CCD photographyo $YBa_2Cu_3O_7$ laser ablation in vacuum and ambient oxygen. *Applied Physics Letters*, Vol. 60:2732–2734, 1992.

[145] H. Nishioka, H. Kuranishi, K. Ueda and H. Takuma. UV saturable absorber for short-pulse KrF lase systems. *Optics Letters*, Vol. 14:692 – 694, 1989.

[146] J. Jandeleit, G. Urbasch, H.D. Hoffmann, H.-G. Treusch, E.W. Kreutz. Picosecond laser ablatio of thin copper films. *Applied Physics A*, Vol. 63:117 – 121, 1996.

[147] Y.Y. Tsui, R. Fedosejevs, C.E. Capjack. Interaction of 10 fs to 15 ns KrF laser pulses with metals. In *SPIE Vo. 3491*, pages 732 – 740, 1998.

[148] J. Hohlfeld, S.S. Wellershoff, J. Gudde, U. Conrad, V. Jahnke, E. Matthias. Electron and lattice dynamics following optical excitation of metlas. *Chemical Physics*, 251:237 – 258, 2000.

[149] M.T. Taschuk, Y.Y. Tsui and R. Fedosejevs. Detection and Imaging of Latent Fingerprints by Laser-Induced Breakdown Spectroscopy. *Applied Spectroscopy*, 60:1322 – 1327, 2006.

[150] R.F. Mehl et al. *Metals Handbook*, volume 7. Atlas of Microstructures of Industrial Alloys. American Society for Metals, 8th edition, 1972.

[151] C. Blanc, B. Lavelle and G. Mankowski. The role of precipitates enriched with copper on the susceptibility to pitting corrosion of the 2024 aluminum alloy. *Corrosion Science*, Vol. 39:495 – 510, 1997.

[152] R.G. Buchheit, R.P. Grant, P.F. Hlava, B. McKenzie and G.L. Zender. Local Dissolution Phenomena Associated with S Phase (Al_2CuMg) Particles in Aluminum Alloy 2024-T3. *Journal of the Electrochemical Society*, Vol. 144:2621 – 2628, 1997.

[153] C. Blanc, S. Gastaud and G. Mankowski. Mechanistic Studies of the Corrosion of 2024 Aluminum Alloy in Nitrate Solutions. *Journal of the Electrochemical Society*, Vol. 150:B396 – B404, 2003.

[154] W.H. Press, S.A. Teukolsky, W.T. Vetterling, B.P. Flannery. *Numerical Recipes in Fortran*. Press Syndicate of the University of Cambridge, 2nd edition, 1992.

[155] R. Saferstein. *Criminilistics: An Introduction to Forensic Science*. Prentice-Hall, Englewood Cliffs, N.J., 4th edition, 1990.

[156] B.E. Dalrymple, J.M. Duff and E.R. Menzel. Inherent Fingerprint Luminescence - Detection by Laser. *Journal of Forensic Sciences*, 22:106 – 115, 1976.

[157] S.K. Bramble, K.E. Creer, W. Gui Qiang and B. Sheard. Ultraviolet luminescence from latent fingerprints. *Forensic Science International*, 59:3 – 14, 1993.

[158] C.E. Allred, T. Lin and E.R. Menzel. Lipid-Specific Latent Fingerprint Detection: Fingerprints on Currency. *Journal of Forensic Science*, Vol. 42:997 – 1003, 1997.

[159] E.R. Menzel, S.M. Savoy, S.J. Ulvick, K.H. Cheng, R.H. Murdock and M.R. Sudduth. Photoluminescent Semiconductor Nanocrystals for Fingerprint Detection. *Journal of Forensic Science*, 45:545 – 551, 2000.

[160] R.H. Hooker, K.E. Creer and J.S. Brennan. Microspectrophotometry in the development and photography of fluorescing marks. *Forensic Science International*, 51:297 – 304, 1991.

[161] Li Wenchong, Ma Chunhua, Jiang Hong, Wu Chengbai, Lu Zhiming, Wang Bangrui and Lu Bingqun. Laser Fingerprint Detection Under Background Light Interference. *Journal of Forensic Sciences*, 37:1076 – 1083, 1992.

[162] U.S. Dinish, L.K. Seah, V.M. Murukeshan, L.S. Ong. Theoretical analysis of phase-resolved fluorescence emission from fingerprint samples. *Optics Communications*, Vol. 223:55 – 60, 2003.

[163] U.S. Dinish, Z.X. Chao, L.K. Seah, A. Singh and V.M. Murukeshan. Formulation and implementation of a phase-resolved fluorescence technique for latent-fingerprint imaging:theoretical and experimental analysis. *Applied Optics*, Vol. 44:297 – 304, 2005.

[164] C. Lopez-Moreno, S. Palanco, J.J. Laserna, F. DeLucia, A.W. Miziolek, J. Rose, R.A. Waters and A.I. Whitehouse. Test of a stand-off laser-induced breakdown spectroscopy sensor for the detection of explosive residues on solid surfaces. *J. Anal. At. Spectrom.*, Vol. 21:55 – 60, 2006.

[165] R.D. Olsen. The Chemical Composition of Palmar Sweat. *Fingerprint and Identification Magazine*, 53:3 – 23, 1972.

Appendix A

Analysis Code

A.1 Introduction

This appendix documents the major codes developed as part of the thesis work. The codes presented here are:

1. Spectra: a spectral analysis library with client scripts
2. Taylor-RK: a script using the Runge-Kutta method to solve the strong shock equations
3. Emission: a library for the simple emission model used to simulate Na emission in a weak shock

A.1.1 Code Requirements

The code was developed for a Debian GNU/Linux system, but should work on any GNU/Linux distribution, provided the following programs are available.

1. Python 2.3.5
2. Numeric 24.2-6
3. GnuPlot 4.0 patchlevel 0
4. GNU Make 3.81

Spectra and **Taylor-RK** have been written with a number of test cases, so if the above exact versions can not be obtained satisfied exactly, the behaviour of the code can still be thoroughly tested to verify correct operation. In addition, the client scripts have been written to be fairly helpful in their error messages, so if all else fails, try it and see what the script suggests.

A.2 Spectra

A.2.1 Introduction

The Spectra module is a python module that is split up into the following sections: background.py, gnuplot.py, integrate.py, noise.py and utilities.py. The spectra module has two major client scripts, *spectraintegrate and* plotspectra. A brief description of each component is given below.

background.py handles fitting and removal of average, linear and parabolic backgrounds from spectra.

gnuplot.py handles the interaction with GnuPlot, which is used for some of the more sophisticated fitting functionality of Spectra.

integrate.py implements the various integration methods that are described in the thesis, as well as some diagnostic methods for noise levels and line widths.

noise.py handles analysis of the noise in a spectra.

utilities.py contains various routines for parsing the spectra into a form useable by the other modules.

A.2.2 File Listing

The Spectra code can be found in my archive under ~/projects/code/spectra. This directory will look like:

```
CVS  Makefile  bin  build  doc  setup.py  spectra
```

CVS is an archival directory and can be ignored here and in all subdirectories. **Makefile** will compile and test the code. The listing of **Makefile** is quite simple:

```
# $Id: Makefile,v 1.3 2006-06-01 20:24:14 mtt Exp $
default: test

clean:
    rm -f ‘find . -name ’*.py[co]’‘

    test:
        PYTHONPATH=. ./spectra/test/integrate.py
        PYTHONPATH=. ./spectra/test/noise.py
        PYTHONPATH=. ./spectra/test/utilities.py
        PYTHONPATH=. ./spectra/test/background.py
```

The only other important directory is ./spectra, which has:

```
CVS           background.py  integrate.py  test
__init__.py   gnuplot.py     noise.py      utilities.py
```

The *.py files are listed in the following section, and contain the implementation of the Spectra module. The next directory is ./test, which contains the scripts and test cases used to test the code. There's far too much material for a full code listing, but it can be found in my archive. In order to test the code, you need all of the files, which are:

```
CVS                          shot105.asc
analysis                     shot106.asc
background.py                shot107-background-removed.txt
channels.txt                 shot107-linear-removed.txt
integrate.py                 shot107.asc
noise.py                     shot108-background-removed.txt
shot-list.txt                shot108-linear-removed.txt
shot100-csv.asc              shot108.asc
shot100.asc                  shot109.asc
shot101.asc                  shot110.asc
shot103-average-removed.asc  shot111.asc
shot103-corrected.asc        spectraplottemp.gnuplot
shot103.asc                  trial.eps
shot104.asc                  utilities.py
```

A.2.3 Testing the Code

The code is tested by using the Makefile in the uppermost directory. A testing run will look like:

```
darthmaul:spectra/:make
PYTHONPATH=. ./spectra/test/integrate.py
...........
--------------------------------------------
Ran 11 tests in 2.585s

OK
PYTHONPATH=. ./spectra/test/noise.py
...
--------------------------------------------
Ran 3 tests in 0.174s

OK
PYTHONPATH=. ./spectra/test/utilities.py
```

```
........
---------------------------------------------
Ran 8 tests in 0.146s

OK
PYTHONPATH=. ./spectra/test/background.py
.....
---------------------------------------------
Ran 5 tests in 0.575s

OK
```

The periods under each 'PYTHONPATH' are indicators of successful tests. If a test fails, the code will notify you which test failed, and what the failure was. If you can't debug it, try contacting me.

A.2.4 Spectra Code Listing

A.2.4.1 background.py

```
#!/usr/bin/env python
""" spectra/background

bakcground analysis funcions for spectral files

"""

__version__ = '$Id: background.py,v 1.1 2006-06-01 20:25:15 mtt Exp $'

from __future__ import division
from math import sqrt
import sys

from spectra.utilities import *

def removeparabola(background, channels):
    """
    Takes a parsed spectra file, and fits a parabola
    to the background specified by the channels.  The
    channel vector must define the area of interest:

        channels[0] = noise1low, channels[1] = noise1high
        channels[2] = signallow, channels[3] = signalhigh
        channels[4] = noise2low, channels[5] = noise2high

    The channels are specified in the Andor iStar style,
    with the range from 1 < N < 1024.

    The background vector must be in the following form,
    not including the column headings presented here.:

        Channel     Signal
        0           345
        ...         ...
        N           348

    The function returns a spectra file that has had the
    parabolic fit subtracted from the entire range of
    channels.
    """
    back1 = background[channels[0]-1:channels[1],:]
    back2 = background[channels[4]-1:channels[5],:]
    a, b, c = parabolafit(back1, back2)

    corrected = zeros((len(background), 2), Float)
    corrected[:, 0] = background[:, 0]          # copy channel numbers
    corrected[:, 1] = background[:, 1] - \
                      a*background[:, 0]*background[:, 0] - \
                      b*background[:, 0] - c
    return corrected

def removelinear(background, channels):
    """
    Takes a parsed spectra file, and fits a line
    to the background specified by the channels.  The
    channel vector must define the area of interest:
        channels[0] = noise1low, channels[1] = noise1high
        channels[2] = signallow, channels[3] = signalhigh
        channels[4] = noise2low, channels[5] = noise2high

    The channels are specified in the Andor iStar style,
    with the range from 1 < N < 1024.

    The background vector must be in the following form,
    not including the column headings presented here.:

        Channel     Signal
        0           345
        ...         ...
        N           348

    The function returns a spectra file that has had the
    linear fit subtracted from the entire range of
    channels.
    """
    back1 = background[channels[0]-1:channels[1],:]
    back2 = background[channels[4]-1:channels[5],:]
    m, b = linearfit(back1, back2)

    corrected = zeros((len(background), 2), Float)
    corrected[:, 0] = background[:, 0]          # copy channel numbers
    corrected[:, 1] = background[:, 1] - m*background[:, 0] - b
    return corrected

def removeaverage(background, channels):
    """
    Takes a spectra file, and takes the average of
    the background regions specified by channels. The
    channel vector must define the area of interest:

        channels[0] = noise1low, channels[1] = noise1high
        channels[2] = signallow, channels[3] = signalhigh
        channels[4] = noise2low, channels[5] = noise2high

    The channels are specified in the Andor iStar style,
    with the range from 1 < N < 1024.

    The background vector must be in the following form,
    not including the column headings presented here.:

        Channel     Signal
        0           345
        ...         ...
        N           348

    The function returns a spectra file that has had the
    average value of the background regions removed from
    the entire spectra.
    """
    back1 = background[channels[0]-1:channels[1], 1]
    back2 = background[channels[4]-1:channels[5], 1]
    baseline = 0.5*(average(back1) + average(back2))

    corrected = zeros((len(background), 2), Float)
    corrected[:, 0] = background[:, 0]          # copy channel numbers
    corrected[:, 1] = background[:, 1] - baseline
    return corrected

def parabolafit(back1, back2):
    """
    Takes two segments of a spectra file, and fits them
    to a parabola. Returns the best fit coefficients,
    using the linear regression algorithm for minimizing
    the residuals.

    This function wants zero indexed channel numbers,
    not the Andor iStar channel numbers. Should be
    relevant only in the test suite, not from the
    user perspective.
    """
    dataset = zeros((len(back1) + len(back2), 2), Float)
    for i in range(len(back1)):
        dataset[i, :] = back1[i, :]
    for i in range(len(back2)):
        dataset[i + len(back1), :] = back2[i, :]
    Y = sum(dataset[:, 1])
    X = sum(dataset[:, 0])
    X2 = sum(dataset[:, 0]*dataset[:, 0])
    X3 = sum(dataset[:, 0]*dataset[:, 0]*dataset[:, 0])
    X4 = sum(dataset[:, 0]*dataset[:, 0]*dataset[:, 0]*dataset[:, 0])
    XY = sum(dataset[:, 0]*dataset[:, 1])
    X2Y = sum(dataset[:, 0]*dataset[:, 0]*dataset[:, 1])
    N = len(dataset)

    delta = X4*(X*X - N*X2) + X3*(N*X3 - 2*X2*X) + X2*X2*X2
    a = (X3*(N*XY - Y*X) + X2*(X2*Y - N*X2Y - X*XY) + X*X*X2Y)/delta
    b = (X2*(X2*XY - X2Y*X - X3*Y) + X4*(Y*X - N*XY) + N*X3*X2Y)/delta
    c = (X4*(X*XY - X2*Y) + X3*(X3*Y - X*X2Y - X2*XY) + X2*X2*X2Y)/delta

    return a, b, c

def linearfit(back1, back2):
    """
    Takes two segments of a spectra file, and fits them
    to a line. Returns the best fit coefficients,
    using the linear regression algorithm for minimizing
    the residuals.

    Treats linear equation as m*x + b
    """
    dataset = zeros((len(back1) + len(back2), 2), Float)
    for i in range(len(back1)):
        dataset[i, :] = back1[i, :]
    for i in range(len(back2)):
        dataset[i + len(back1), :] = back2[i, :]
    Y = sum(dataset[:, 1])
    X = sum(dataset[:, 0])
    X2 = sum(dataset[:, 0]*dataset[:, 0])
    XY = sum(dataset[:, 0]*dataset[:, 1])
    N = len(dataset)


    delta = N*X2 - X*X
    b = (X2*Y - X*XY)/delta
    m = (N*XY - X*Y)/delta
```

```
#print >> sys.stderr , X
#print >> sys.stderr , X2
#print >> sys.stderr , Y
#print >> sys.stderr , XY
#print >> sys.stderr , N
#print >> sys.stderr , delta

return m, b
```

A.2.4.2 gnuplot.py

```
#!/usr/bin/env python
""" spectra/gnuplot

Handles interface with gnuplot

"""

__version__ = '$Id: gnuplot.py,v 1.1 2006-06-01 20:25:15 mtt Exp $'

import sys
import os.path

from Numeric import *

def generategaussplot(a, b, c, lambdaconstraint, sigmaconstraint):
    """
    Generate all files needed for Gnuplot fitting of line
    function.
    """
    # Write GnuPlot file
    file = open('./gauss-fit-temp/gaussfit.gnuplot', 'w')
    print >> file, 'a = %s' % a

    if lambdaconstraint:
        print >> file, 'b = %s' % float(lambdaconstraint)
    else:
        print >> file, 'b = %s' % b
    if sigmaconstraint:
        print >> file, 'c = %s' % float(sigmaconstraint)
    else:
        print >> file, 'c = %s' % c

    print >> file, 'f(x) = a*exp(-(0.5)*((x - b)/c)**2)'
    print >> file, 'FIT_LIMIT = 1e-6'

    if lambdaconstraint and sigmaconstraint:
        print >> file, 'fit f(x) \'./gauss-fit-temp/segment.spectra\'' + \
                 ' using 1:2 via a'
    elif lambdaconstraint:
        print >> file, 'fit f(x) \'./gauss-fit-temp/segment.spectra\'' + \
                 ' using 1:2 via a, c'
    elif sigmaconstraint:
        print >> file, 'fit f(x) \'./gauss-fit-temp/segment.spectra\'' + \
                 ' using 1:2 via a, b'
    else:
        print >> file, 'fit f(x) \'./gauss-fit-temp/segment.spectra\'' + \
                 ' using 1:2 via a, b, c'
    file.close()

def generategausssupport(back1, back2, peak):
    """
    Generate spectra segment, and parameter stripping file
    """
    # Write spectra segment
    file = open('./gauss-fit-temp/segment.spectra', 'w')
    for line in back1:
        print >> file, '%s \t %s' % (line[0], line[1])
    for line in back2:
        print >> file , '%s \t %s' % (line[0], line[1])
    for line in peak:
        print >> file , '%s \t %s' % (line[0], line[1])
    file.close()

    # Write parameterstrip script
    file = open('./gauss-fit-temp/parameterstrip', 'w')
    print >> file , 'sed -n "/^=/,/^corr/p" $1 |sed -n "/[+\/-]/p" |awk ' + \
                    '\'{print $1 "\\t" $3 "\\t" $5}\''
    file.close()
    os.popen('chmod a+x ./gauss-fit-temp/parameterstrip')
    return

def executegaussplot(lambdaconstraint, sigmaconstraint):
    """
    A method for execution of Gnuplot file with appopriate data.
    """
    commandstring = 'gnuplot \'./gauss-fit-temp/gaussfit.gnuplot\''
    sysin, sysout, syserr = os.popen3(commandstring)
    syserr.readlines()
    sysout.readlines()
    syserr.close()
    sysout.close()
    sysin.close()
    commandstring = './gauss-fit-temp/parameterstrip ./fit.log > ' + \
                    './gauss-fit-temp/values.txt'
    os.popen(commandstring)
    commandstring = 'rm ./fit.log'
    os.popen(commandstring)

    parametervector = []
    file = open('./gauss-fit-temp/values.txt', 'r')
    for line in file:
        name, param, error = line.split()
        parametervector.append((float(param), float(error)))
    file.close()

    if lambdaconstraint and sigmaconstraint:
        a, da = parametervector[0]
        b = float(lambdaconstraint)
        c = float(sigmaconstraint)
    elif lambdaconstraint:
        a, da = parametervector[0]
        b = float(lambdaconstraint)
        c, dc = parametervector[1]
    elif sigmaconstraint:
        a, da = parametervector[0]
        b, db = parametervector[1]
        c = float(sigmaconstraint)
    else:
        a, da = parametervector[0]
        b, db = parametervector[1]
        c, dc = parametervector[2]

    return a, b, c
```

A.2.4.3 integrate.py

```
#!/usr/bin/env python
""" spectra/integrate

Integration functions for spectra files.

Fixmes - refactor this for:
        - single input output
        - less meddling with passed parameters
        - reuse of earlier calculations
"""

__version__ = '$Id: integrate.py,v 1.20 2006-06-26 23:41:15 mtt Exp $'

from __future__ import division
import sys

from spectra.utilities import *
from spectra.noise import *
from spectra.background import *
from spectra.gnuplot import *

from Numeric import *
import os.path

class BackgroundMethod(Exception):
    pass

class ChannelError(Exception):
    pass

def linenoise(inputfile, channels, backmethod, lambdaconstraint, \
    sigmaconstraint):
    """
    Returns the standard deviation of the noise from a gaussian
    line fit to spectral data.
    """
    data = parse(inputfile)
    if backmethod == 'average':
        corrected = removeaverage(data, channels)
    elif backmethod == 'linear':
        corrected = removelinear(data, channels)
    elif backmethod == 'parabolic':
        corrected = removeparabola(data, channels)

    back1, peak, back2 = spectraslice(corrected, channels)

    a, b, c = gaussianfit(back1, back2, peak, \
                lambdaconstraint, sigmaconstraint)

    residual = zeros(len(peak), Float)

    for i in range(len(peak)):
        try:
            predicted = a*exp(-(0.5)*((peak[i,0] - b)/abs(c))**2)
        except OverflowError:
            predicted = 0.0
        actual = peak[i,1]
        residual[i] = actual - predicted
    noise = stdev(residual)

    return noise

def linewidth(inputfile , channels , backmethod , lambdaconstraint , \
    sigmaconstraint ):
    """
    Returns the 1 sigma value from a gaussian line
    fit to spectral data.
    """
    data = parse(inputfile)
    if backmethod == 'average ':
        corrected = removeaverage(data , channels)
    elif backmethod == 'linear ':
        corrected = removelinear(data , channels)
    elif backmethod == 'parabolic ':
        corrected = removeparabola(data , channels)

    back1 , peak , back2 = spectraslice(corrected , channels)

    a, b, c = gaussianfit(back1 , back2 , peak , \
            lambdaconstraint , sigmaconstraint)

    return abs(c)

def intgaussiansnr(inputfile , channels , backmethod , N, \
    lambdaconstraint , sigmaconstraint ):
    """
    Integrate a gaussian fit to a signal from a spectra file.
    Uses the deviation between the observed spectra and the
    fit to estimate the noise in the spectral width..

    Takes as arguments a file object containing spectra to
    be integrated , and a six entry long list of channel numbers
    defining the regions of interest:

        channels[0] = noise1low , channels[1] = noise1high
        channels[2] = signallow , channels[3] = signalhigh
        channels[4] = noise2low , channels[5] = noise2high

    The required portions of the file are obtained by
    utilities/parse , and are used to calculate the area
    under the curve , using a simple average of two noise
    regions defined by the user.

    N is a factor for the linewidth , in units of 1/e. The
    noise used for the snr calcultions is scaled by this factor.
    Lambdaconstraint and sigmaconstraint restrict the fitting
    process performed by GnuPlot.
    """
    data = parse(inputfile)
    if backmethod == 'average ':
        corrected = removeaverage(data , channels)
    elif backmethod == 'linear ':
        corrected = removelinear(data , channels)
    elif backmethod == 'parabolic ':
        corrected = removeparabola(data , channels)

    back1 , peak , back2 = spectraslice(corrected , channels)
    a, b, c = gaussianfit(back1, back2, peak, \
                lambdaconstraint, sigmaconstraint)

    residual = zeros(len(peak), Float)

    for i in range(len(peak)):
        try:
            predicted = a*exp(-(0.5)*((peak[i,0] - b)/abs(c))**2)
        except OverflowError:
            predicted = 0.0
        actual = peak[i,1]
        residual[i] = actual - predicted

    noise = stdev(residual)
    width = 2*abs(c)*sqrt(2*N)

    area = a*abs(c)*sqrt(2*pi)         # fit is to abs(c), so negatives creep in
    gaussiansnr = area/(noise*sqrt(width))

    return gaussiansnr

def intgaussian(inputfile, channels, backmethod, lambdaconstraint, \
    sigmaconstraint):
    """
    Integrate a gaussian fit to a signal from a spectra file.
    Returns the area.

    Takes as arguments a file object containing spectra to
    be integrated, and a six entry long list of channel numbers
    defining the regions of interest:

        channels[0] = noise1low, channels[1] = noise1high
        channels[2] = signallow, channels[3] = signalhigh
        channels[4] = noise2low, channels[5] = noise2high

    The required portions of the file are obtained by
    utilities/parse, and are used to calculate the area
    under the curve, using a simple average of two noise
    regions defined by the user.
    """
    data = parse(inputfile)
    if backmethod == 'average':
        corrected = removeaverage(data, channels)
    elif backmethod == 'linear':
        corrected = removelinear(data, channels)
    elif backmethod == 'parabolic':
        corrected = removeparabola(data, channels)

    back1, peak, back2 = spectraslice(corrected, channels)

    a, b, c = gaussianfit(back1, back2, peak, \
                lambdaconstraint, sigmaconstraint)

    area = a*abs(c)*sqrt(2*pi)         # fit is to abs(c), so negatives creep in

    return area

def gaussianfit(back1, back2, peak, lambdaconstraint, sigmaconstraint):
    """
    Uses Gnuplot to fit a gaussian to a particular segment
    from a spectra file. The gaussian fit has two modes,
    one in which the wavelength or channel number is unconstrained,
    and another in which it is constrained.
    """
    a = max(peak[:, 1])         # Crude initial guesses for GnuPlot
    b = (0.5)*(peak[0, 0] + peak[-1, 0])
    c = abs(peak[0,0] - peak[-1, 0])/6

    os.popen('mkdir ./gauss-fit-temp')
    generategausssupport(back1, back2, peak)
    generategaussplot(a, b, c, lambdaconstraint, sigmaconstraint)
    a, b, c = executegaussplot(lambdaconstraint, sigmaconstraint)
    os.popen('rm -Rf ./gauss-fit-temp')

    return a, b, c

def intsnrarea(inputfile, channels, backmethod):
    """Integrate a signal from a spectra file, and calculate the
    signal to noise ratio between the integrated signal and the
    pixel to pixel noise scaled to the integration width.

    Takes as arguments a file object containing spectra to be
    analyzed, and a six entry long list of channel numbers
    defining the regions of interest:

        channels[0] = noise1low, channels[1] = noise1high
        channels[2] = signallow, channels[3] = signalhigh
        channels[4] = noise2low, channels[5] = noise2high

    The channels are specified in the Andor iStar style,
    with the range from 1 < N < 1024. The flag backmethod
    specifies the background removal methodology, either
    an average or parabolic fit to the background.
    """
    data = parse(inputfile)
    if backmethod == 'average':
        corrected = removeaverage(data, channels)
    elif backmethod == 'linear':
        corrected = removelinear(data, channels)
    elif backmethod == 'parabolic':
        corrected = removeparabola(data, channels)

    back1, signal, back2 = spectraslice(corrected, channels)

    noise1 = stdev(back1[:, 1])
    noise2 = stdev(back2[:, 1])
    sigma = 1.5*(noise1 + noise2)           # 1.5 for 3 times average noise
    signallen = len(signal[:, 1])
    back1 = average(back1[:, 1])
    back2 = average(back2[:, 1])

    area = sum(signal[:, 1]) - signallen*(back1 + back2)/2
    snr = area/(sigma*sqrt(signallen))
    return snr

def intareaback(inputfile, channels, backmethod):
    """Integrates a signal from a spectra file. Returns the
    background corrected area, normalized to the total integrated
    background signal. Intended to normalize the peak area to
    the total emission intensity.

        channels[0] = noise1low, channels[1] = noise1high
        channels[2] = signallow, channels[3] = signalhigh
        channels[4] = noise2low, channels[5] = noise2high

    The required portions of the signal are obtained by
    utilities/parse, and are used to calculate the peak.
    """
    data = parse(inputfile)
    if backmethod == 'average':
        corrected = removeaverage(data, channels)
    elif backmethod == 'linear':
        corrected = removelinear(data, channels)
    elif backmethod == 'parabolic':
        corrected = removeparabola(data, channels)

    back1, signal, back2 = spectraslice(corrected, channels)

    # detector background correction
    background = data[:, 1] - average(data[0:20, 1])

    back1 = average(back1[:, 1])
    back2 = average(back2[:, 1])
    area = sum(signal[:, 1]) - len(signal)*(back1 + back2)/2
    background = sum(background)
    return area/background

def intarea(inputfile, channels, backmethod):
    """
    Integrate a signal from a spectra file. Returns the area.

    Takes as arguments a file object containing spectra to
    be integrated, and a six entry long list of channel numbers
    defining the regions of interest:

        channels[0] = noise1low, channels[1] = noise1high
        channels[2] = signallow, channels[3] = signalhigh
        channels[4] = noise2low, channels[5] = noise2high

    The required portions of the file are obtained by
    utilities/parse, and are used to calculate the area
    under the curve, using a simple average of two noise
    regions defined by the user.
    """
    data = parse(inputfile)
    if backmethod == 'average':
        corrected = removeaverage(data, channels)
    elif backmethod == 'linear':
        corrected = removelinear(data, channels)
    elif backmethod == 'parabolic':
        corrected = removeparabola(data, channels)

    back1, signal, back2 = spectraslice(corrected, channels)
    area = sum(signal[:, 1])

    return area

def intsnrpeak(inputfile, channels, backmethod):
    """
    Integrates a signal from a spectra file.  Returns the
    ratio of the peak value within the signal region divided
    by 3 times the average standard deviation of the noise
    region.

        channels[0] = noise1low, channels[1] = noise1high
        channels[2] = signallow, channels[3] = signalhigh
        channels[4] = noise2low, channels[5] = noise2high

    The required portions of the signal are obtained by
    utilities/parse, and are used to calculate the peak.
    """
    data = parse(inputfile)
    if backmethod == 'average':
        corrected = removeaverage(data, channels)
    elif backmethod == 'linear':
        corrected = removelinear(data, channels)
    elif backmethod == 'parabolic':
        corrected = removeparabola(data, channels)

    back1, signal, back2 = spectraslice(corrected, channels)

    noise1 = stdev(back1[:, 1])
    noise2 = stdev(back2[:, 1])
    sigma = 0.5*(noise1 + noise2)

    if channels[2] != channels[3]:
        exceptionstring = 'spectra.integrate.intpeak: peak method requires' + \
                          ' channels signal to be identical'
        raise ChannelError(exceptionstring)
    else:
        peak = signal[0, 1]

    return peak/sigma

def intpeakback(inputfile, channels, backmethod):
    """
    Integrates a signal from a spectra file.  Returns the
    peak background corrected value, normalized to the total
    integrated background signal.  Intended to normalize the
    peak signal to the total emission intensity.

        channels[0] = noise1low, channels[1] = noise1high
        channels[2] = signallow, channels[3] = signalhigh
        channels[4] = noise2low, channels[5] = noise2high

    The required portions of the signal are obtained by
    utilities/parse, and are used to calculate the peak.
    """
    data = parse(inputfile)
    if backmethod == 'average':
        corrected = removeaverage(data, channels)
    elif backmethod == 'linear':
        corrected = removelinear(data, channels)
    elif backmethod == 'parabolic':
        corrected = removeparabola(data, channels)

    back1, signal, back2 = spectraslice(corrected, channels)
    detectorback1 = average(data[0:20, 1])
    detectorback2 = average(data[1003:1023, 1])
    background = data[:, 1] - 0.5*(detectorback1 + detectorback2)
    background = sum(background)

    if channels[2] != channels[3]:
        exceptionstring = 'spectra.integrate.intpeak: peak method requires' + \
                          ' channels signal to be identical'
        raise ChannelError(exceptionstring)
    else:
        peak = signal[0, 1]

    return peak/background

def intpeak(inputfile, channels, backmethod):
    """
    Integrate a signal from a spectra file. Returns the
    background corrected peak signal.

    Takes as arguments a file object containing spectra to
    be integrated, and a six entry long list of channel numbers
    defining the regions of interest:

        channels[0] = noise1low, channels[1] = noise1high
        channels[2] = signallow, channels[3] = signalhigh
        channels[4] = noise2low, channels[5] = noise2high

    The required portions of the signal are obtained by
    utilities/parse, and are used to calculate the peak.
    """
    data = parse(inputfile)
    if backmethod == 'average':
        corrected = removeaverage(data, channels)
    elif backmethod == 'linear':
        corrected = removelinear(data, channels)
    elif backmethod == 'parabolic':
        corrected = removeparabola(data, channels)

    back1, signal, back2 = spectraslice(corrected, channels)

    if channels[2] != channels[3]:
        exceptionstring = 'spectra.integrate.intpeak: peak method requires' + \
                          ' channels signal to be identical'
        raise ChannelError(exceptionstring)
    else:
        peak = signal[0, 1]
    return peak
```

A.2.4.4 noise.py

```
#!/usr/bin/env python
""" spectra/noise

noise analysis funcions for spectral files

"""

__version__ = '$Id: noise.py,v 1.5 2006-06-01 20:25:15 mtt Exp $'

from __future__ import division
from math import sqrt
import sys

from spectra.utilities import *
from spectra.background import *

class DataLength(Exception):
    pass

def backgroundnoise(inputfile, channels, backmethod):
    """
    Reports the 1 sigma noise in the background areas.
    """
    data = parse(inputfile)
    if backmethod == 'average':
        corrected = removeaverage(data, channels)
    elif backmethod == 'linear':
        corrected = removelinear(data, channels)
    elif backmethod == 'parabolic':
        corrected = removeparabola(data, channels)

    back1, signal, back2 = spectraslice(corrected, channels)
    noise1 = stdev(back1[:, 1])
    noise2 = stdev(back2[:, 1])

    noise = 0.5*(noise1 + noise2)

    return noise

def stdev(data):
    """Take the Standard Deviation of a series of numbers.

    Uses the definition due to Taylor (1997) Pg. 100:

    Sigma_x = sqrt(Sum( (x-meanx)^2)/(N-1))
    """
    # n, sigma, xbar, sum = 0, 0, 0, 0
    n, sigma, xbar = 0, 0, 0
    n = len(data)                          # calculate number of data points
    if n == 0:
        raise DataLength("Invalid data vector: no data")
    elif n == 1:                           # special case of 1 data point
        sigma = 0.0
    else:
        xbar = average(data)               # find average of data points
        # for q in data:
        #     sum = sum + (xbar - q)*(xbar - q)
        residual = sum((data - xbar)*(data - xbar))
        sigma = sqrt(residual/(n-1))          # calculate standard deviation
    return sigma
```

A.2.4.5 utilities.py

```
#!/usr/bin/env python

########################################################################
# spectra/utilities.py
#
# Common functionality for the spectra package.
#
# Functions:    Parse - extracts spectral data from a spectra file
#                       by channel number
#
#               KineticParse -  extracts spectral data from a kinetic
#                               series file, and transfers it to a
#                               Numeric array
#
#               Fixme - add remainder of functions
#
########################################################################

__version__ = '$Id: utilities.py,v 1.7 2006-06-01 20:25:15 mtt Exp $'

from __future__ import division
from math import sqrt
from Numeric import *
import sys

class ShotNumber(Exception):
    pass

class KineticSliceBounds(Exception):
    pass

class ParseBounds(Exception):
    pass

class ParseDelimiter(Exception):
    pass

def spectraslice(spectra, channels):
    """
    Return requested subsets of a spectra for subsequent
    analysis. Used to check data integerity, and reduce
    duplicated code in the spectral integration methods.

    Offset in first index of slice is to take into account
    switch to zero-index list. Lack of an offset in the
    second index of slice is to take into account Python
    slice behaviour.
    """
    for i in range(len(channels)):
        if channels[i] > 1024 or channels[i] < 0:
            raise ParseBounds
    back1 = spectra[channels[0] - 1:channels[1]]
    signal = spectra[channels[2] - 1:channels[3]]
    back2 = spectra[channels[4] - 1:channels[5]]
    return back1, signal, back2

def calibrate(quantity, factor):
    """Takes a value, and multiplies it by a calibration
    factor.  Returns the new value in new units.

    Fixme - consider adding awareness of units

    """
    return quantity*factor

def shotnumber(filename, delimiter=None):
    """Scans a filename generated by the Andor autonaming
    sequence, and extracts the number of the shot.  The shot
    must be of the following form, or the algorithm will fail:

    xxxxxxx_ShotNumber.xxxxxx

    The routine uses the '.asc' to strip the last half off, and
    then uses the '_' to extract the shot number.  The routine
    will also pick off shot numbers of the following form:

    xxxxxxx_ShotNumber-shotnumber.xxxxx

    to support the use of /bin/spectraintegrate by automated
    analysis routines.  Specific ordering of splitting for '_'
    and then '-' is required for backcompatibility.  Needs
    a clearer view of the problem, I think.

    FIXME:  should be able to pass in the delimiter to
            force the parse in a certain way.

    """
    shotnum = None
    if len(filename.split('/')) > 1:                    # strip /dir/
        dirsplit = len(filename.split('/'))
        filename = str(filename.split('/')[-1:][0])
    if len(filename.split('.')) > 1:                    # strip .***.*** suffix
        filename = str(filename.split('.')[:1][0])
    if len(filename.split('_')) > 1:
        filename = str(filename.split('_')[-1:][0])
    if len(filename.split('-')) > 1:
        filename = str(filename.split('-')[-1:][0])
    try:
        shotnum = int(filename)
        shotnum = str(shotnum)
    except ValueError:
        raise ShotNumber("Invalid File Name: can't parse")
    return shotnum

def kineticslice(kineticarray, col):
    """Returns a specific spectra from a kinetic series.
    Always returns a M by 2 array, with M being the number of
    channels.  First column will be the channel identifier of
    the kinetic series, either channel number or wavelength.
    Second column will be the signal of interest, referenced
    by zero-indexed column number.
    """
    rows, cols = kineticarray.shape
    if col < 0 or col > cols - 1:
        raise KineticSliceBounds("KineticSlice: Bound Error")
    identifier = kineticarray[:,0]
    signal = kineticarray[:,col]
    outputarray = zeros([rows,2], Float)
    for i in range(rows):
        outputarray[i,0] = identifier[i]
        outputarray[i,1] = signal[i]
    return outputarray

def kineticparse(fileobj):
    """Parse a kinetic series file:

    A kinetic series with M channels and N shots looks like:

        1,34,89,98,.....N
        2,45,34,56,.....N
          .....
       M,34,56,89,.....N

    The fields will be seperated by a comma or a tab, and the
    column number indicates shot number in the kinetic series.

    This function will read a kinetic series file into an array
    for further analysis. The first column will be maintained,
    as in some cases it will be a wavelength and noninteger.
    """
    channels = list(splitfields(fileobj))
    rows = len(channels)
    cols = len(channels[0])
    kineticarray = zeros([rows,cols], Float)        # make array of rows x cols
    for x, fields in enumerate(channels):
        for y, datum in enumerate(fields):
            kineticarray[x,y] = float(datum)        # transfer to array
    return kineticarray

def parse(inputfile):
    """Parse a spectra file.

    The data looks like this:
        232.563,150139
        232.605,149892
        232.647,149655
        232.69,149950
        ...

    Two fields separated by a comma or a tab, the second value an
    integer. The function attempts to ascertain which delimeter is
    being used for this particular spectra file.

    The function will return a numeric array.
    """
    firstline = inputfile.readline()
    if len(firstline.split(',')) >= 2:
        delimiter = ','
    elif len(firstline.split('\t')) >= 2:
        delimiter = 'whitespace'
    elif len(firstline.split(' ')) >= 2:
        delimiter = 'whitespace'
    else:
        raise ParseDelimiter("where the hell's my delimiter?")

    inputfile.seek(0)
    parsed = []

    if delimiter == 'whitespace':
        for line in inputfile:
            channel, counts = line.split()
            [illegible]ed.append((float(channel), float(counts)))
    else:
        for line in inputfile:
            channel, counts = line.split(delimiter)
            parsed.append((float(channel), float(counts)))

    data = array(parsed)
    return data

def kineticsize(fileobj, delimiter):
    """Detects size of a kinetic series file.
    Returns number of channels (rows), and number of shots (cols)
    """
    rows = 0
    cols = 0
    fileobj.seek(0)
    firstline = fileobj.readline()
    cols = len(firstline.split(delimiter))
    fileobj.seek(0)
    for line in fileobj:
        rows = rows + 1
    return rows, cols

def detectdelimiter(fileobj):
    """Function to find the delimiter to be used for a particular
    spectra file, or kinetic series file.
    """
    firstline = fileobj.readline()
    if len(firstline.split(',')) >= 2: delimiter = ','
    elif len(firstline.split('\t')) >= 2: delimiter = '\t'
    elif len(firstline.split(' ')) >= 2: delimiter = ' '
    else: raise ParseDelimiter("DetectDelimiter: No Delimiter?")
    return delimiter

# def sum(values):
    # sum = 0
    # for val in values:
    #     sum = sum + val
    # return sum(values)

def average(values):
    return sum(values)/len(values)

def splitfields(fileobj):
    """This function lifted from spectra.utilities.kineticparse,
    was written by sjt, and is not fully understood.  It is
    included here to protect this function from changes made to
    the spectra code.

    [mtt] 20040127: there has been a slight change to this
    function in the handling of the whitespace delimiters.  For
    some reason, I changed the passing of '\t' and ' ' to just
    a default argument to string.split().  This was done to ease
    trouble in later functions which tripped up on a trailing
    '\r\n' when trying to convert to floats.  Better is to bullet
    proof the parsing functions, but this hasn't happenned yet.

    [mtt] 20060523: I've removed this function from the actual
```

```
excecuted code, replacing it in parse with my own code.  The
current version passes all tests, so it looks good.
"""
lines = iter(fileobj)
firstline = lines.next()
if len(firstline.split(',')) >= 2:
    delimiter = ','
elif len(firstline.split('\t')) >= 2:
    delimiter = 'whitespace'
elif len(firstline.split(' ')) >= 2:
    delimiter = 'whitespace'
else:
    raise ParseDelimiter("where the hell's my delimiter?")
if delimiter == 'whitespace':
    yield firstline.split()
    for line in lines:
        yield line.split()
else:
    yield firstline.split(delimiter)
    for line in lines:
        yield line.split(delimiter)
```

A.3 Spectra Client Scripts

This section contains scripts that use the code listed in the previous section. These scripts interate with the user, and are only accessible on the command line. **peakfit** is less friendly, and should be used with care. **spectraintegrate** and **plotspectra** respond to –help:

```
spectraintegrate --help
```

or

```
plotspectra --help
```

A.3.1 The Linefile

The client scripts are built to use a linefile, which has the following format:

```
name, noisellow, noiselhigh, signallow,
    signalhigh, noise2low, noise2high
```

Note that the linebreak is to prevent going into the margin. The actual linefiles are all one line. The first entry is a name used to identify the line the settings are for, and the remaining entries specify the two noise regions, and the signal region. The entries must be integers.

A.3.2 Spectra Client Script Code Listing

A.3.2.1 spectraintegrate

```
#!/usr/bin/env python
""" spectraintegrate.py

 Takes a two column text file of numerical data
 and sums the second column across a given range

 Currently:  delimiter = ',' only
             report of shot number hard coded
             integrates one spectral line per file only

 To Fix:     Add smarter shot number detection

"""
__version__ = '$Id: spectraintegrate,v 1.14 2006-07-26 14:36:01 mtt Exp $'

from __future__ import division

import os.path
import sys
import getopt

from string import lower

from spectra.utilities import *
from spectra.integrate import *

class IntMethod(Exception):
    pass

class LineFileError(Exception):
    pass

def usage():
    """Emits usage comments on sys.stderr"""
    print >> sys.stderr, 'Usage: spectraintegrate [options] source_files'
    print >> sys.stderr, '\tTry spectraintegrate —help for more details'

def detailed_usage():
    """Emits detailed usage comments on sys.stderr"""
    command = 'Usage: spectraintegrate -c | —channels channel_file' +\
              ' [options] source_files'
    print >> sys.stderr, command
    print >> sys.stderr, 'Numerically integrate a region of a spectra',
    print >> sys.stderr, 'as specified in channel_file'
    print >> sys.stderr, ''
    print >> sys.stderr, 'Options: [-i | —integrate] integration method'
    print >> sys.stderr, '         [-b | —background] background fit type'
    print >> sys.stderr, '         [-l | —lambda] constrained wavelength'
    print >> sys.stderr, '         [-s | —sigma] constrained sigma'
    print >> sys.stderr, '         [-n | —width] width in 1/e units for '
    print >> sys.stderr, '                       noise scaling'
    print >> sys.stderr, ''
    print >> sys.stderr, 'Note:  constraining options (-l | -s) will only'
    print >> sys.stderr, '       operate with gaussian and gaussiansnr'
    print >> sys.stderr, '       option -n will only work with gaussiansnr'
    print >> sys.stderr, ''
    print >> sys.stderr, 'Channel File Format:'
    print >> sys.stderr, '\tSee spectra.py source or manual'
    print >> sys.stderr, 'Integration Methods:'
    print >> sys.stderr, '\tnoise:\t\treturns 1 sigma noise in background area'
    print >> sys.stderr, '\tgaussiansnr:\tgaussian divided by sigma*sqrt(2*1/e)'
    print >> sys.stderr, '\tgaussian:\tintegrate a gaussian fit to line'
    print >> sys.stderr, '\tarea:\t\tintegrate area under curve'
    print >> sys.stderr, '\tareaback:\tarea divided by total light'
    print >> sys.stderr, '\tpeak:\t\tpeak signal in region of interest'
    print >> sys.stderr, '\tpeakback:\tpeak divided by total light'
    print >> sys.stderr, '\tsnrarea:\tarea divided by 3*sigma*sqrt(width)'
    print >> sys.stderr, '\tsnrpeak:\tpeak divided by 3*sigma'
    print >> sys.stderr, 'Background Fit Types'
    print >> sys.stderr, '\taverage:\taverage of two background regions'
    print >> sys.stderr, '\tlinear:\t\tlinear fit to two background regions'
    print >> sys.stderr, '\tparabolic:\tparbolic fit to two background regions'
    print >> sys.stderr, 'Default Choices:'
    print >> sys.stderr, '\tIntegration Method:\tArea'
    print >> sys.stderr, '\tBackground Fit Type:\tAverage'

def getline(linefile):
    """
    Analyzes a linefile for the channels, and any possible
    constraints. This may break previous use of this client
    script, though an effort has been made to catch the legacy
    channel file type.

    Legacy:

    name, noise1low, noise1high, signallow, signalhigh, noise2low,
          noise2high

    The new format will accept any of the following lines. The lines
    are comma seperated, and the first one should not be case sensitive.

    name, linename
    channels, channelvalues (6 in all)
    lambdaconstraint, value
    sigmaconstraint, value
    width, value

    """
    channels = None                     # placeholders
    linename = None
    lambdaconstraint = None
    sigmaconstraint = None
    width = None

    lineinput = file(linefile)
    linecount = 0
    for line in lineinput:
        linecount = linecount + 1
        line = line.split(',')
        identifier = lower(line[0])
        if identifier == 'name':
            linename = line[1]
            linename = linename[1:-1]            # trim spaces and \n
        elif identifier == 'channels':
            channels = []                        # initialize channels
            try:
                for i in range(6):
                    channels.append(int(line[i+1]))
            except:
                errorstring = 'spectraintegrate: malformed channel ' + \
                                          'specification in %s' % linefile
                raise LineFileError(errorstring)
        elif identifier == 'lambdaconstraint':
            lambdaconstraint = float(line[1])
        elif identifier == 'sigmaconstraint':
            sigmaconstraint = float(line[1])
        elif identifier == 'width':
            width = float(line[1])
        elif len(line) == 1:                    # detect & ignore whitespace
            pass
        else:
            # this trys to catch legacy channelfiles
            channels = []                       # initialize channels
            try:
                for i in range(6):
                    channels.append(int(line[i+1]))
            except:
                errorstring = 'spectraintegrate: line %d in %s malformed' + \
                    % (int(linecount), linefile)
                raise LineFileError(errorstring)
    lineinput.close()

    return channels, linename, lambdaconstraint, sigmaconstraint, width

def report(channels, linename, intmethod, backmethod, inputfilenames, \
            lambdaconstraint, sigmaconstraint, width):
    """Print a report reporting the integrated line strength
    of the channels specified in linefile, for all files listed
    in inputfilenames.  Currently, limited to one line integration
    at a time - needs further work for multiple line integration
    implemented in this function.

    linefile is expected to be in the following format for
    every line to be integrated (same meaning as given for
    spectra/integrate):

    linename, noise1low, noise1high, signallow, signalhigh,
        noise2low, noise2high
    [optional] FIXME peak wavelength constraint
    [optional] FIXME sigma wavelength constraint

    src files are expected to be ascii converted .sif files,
    with the autonumber characteristics from the Andor files.
    The shot number should be surrounded by '_' and '.' or the
    hot number stripping routine will fail.  Uses the utility
    function 'shotnumber' for this work.
    """
    outputfile = sys.stdout

    print >> outputfile, 'Filename Shot# %s' % linename

    for filename in inputfilenames:
        #shotnum = shotnumber(filename)        # get shot number from filename
        fileobj = open(filename)
        if intmethod == 'area':
            result = intarea(fileobj, channels, backmethod)
        elif intmethod == 'areaback':
            result = intareaback(fileobj, channels, backmethod)
        elif intmethod == 'peak':
            result = intpeak(fileobj, channels, backmethod)
        elif intmethod == 'peakback':
            result = intpeakback(fileobj, channels, backmethod)
        elif intmethod == 'snrarea':
            result = intsnrarea(fileobj, channels, backmethod)
        elif intmethod == 'snrpeak':
            result = intsnrpeak(fileobj, channels, backmethod)
        elif intmethod == 'gaussian':
            result = intgaussian(fileobj, channels, backmethod, \
                        lambdaconstraint, sigmaconstraint)
        elif intmethod == 'gaussiansnr':
            result = intgaussiansnr(fileobj, channels, backmethod, \
                        width, lambdaconstraint, sigmaconstraint)
        elif intmethod == 'noise':
            result = intnoise(fileobj, channels, backmethod)
        else:
            raise IntMethod("Invalid integration method")
        #print >> outputfile, '%s %s %f' % (filename, shotnum, result)
        print >> outputfile, '%s %f' % (filename, result)
        fileobj.close()

if __name__ == '__main__':

    linefile = None             # default arguments, placeholders
    intmethod = 'area'
    backmethod = 'average'
    lambdaconstraint = None
    sigmaconstraint = None
    width = None

    # Parse command line arguments
    try:
        opts, args = getopt.getopt(sys.argv[1:], "hc:i:b:l:s[illegible]", ["help", \
                        "channels=", "integrate=", "background=", "lambda=" \
                        "sigma=", "width="])
    except getopt.GetoptError:
        usage()
        sys.exit(2)
    for o, a in opts:
        if o in ("-h", "--help"):
            detailed_usage()
            sys.exit(2)
        if o in ("-c", "--channels"):
            linefile = a
        if o in ("-i", "--integrate"):
            intmethod = a
        if o in ("-b", "--background"):
            backmethod = a
        if o in ("-l", "--lambda"):
            lambdaconstraint = a
        if o in ("-s", "--sigma"):
            sigmaconstraint = a
        if o in ("-n", "--width"):
            width = float(a)

    try:
        channels, linename, lambdaline, sigmaline, widthline = getline(linefile)
```

```
except IOError:
    print >> sys.stderr, 'spectraintegrate: channel file %s missing'\
                         % linefile
    sys.exit(2)
except LineFileError, inst:
    print >> sys.stderr, inst.args[0]
    sys.exit(2)

# Check for duplicate specifications of constraints
if lambdaconstraint and lambdaline:
    print >> sys.stderr, 'spectraintegrate: lambdaconstraint ' + \
                         'specified twice'
    sys.exit(2)
elif lambdaconstraint == None:
    lambdaconstraint = lambdaline

if sigmaconstraint and sigmaline:
    print >> sys.stderr, 'spectraintegrate: sigmaconstraint ' + \
                         'specified twice'
    sys.exit(2)
elif sigmaconstraint == None:
    sigmaconstraint = sigmaline

if width and widthline:
    print >> sys.stderr, 'spectraintegrate: width specified twice'
    sys.exit(2)
elif width == None:
    width = widthline

# Check to see if sufficient information acquired
if linefile == None:
    print >> sys.stderr, 'spectraintegrate: must specifiy channel file'
    sys.exit(2)
if intmethod == 'gaussiansnr' and width == None:
    print >> sys.stderr, 'spectraintegrate: must specify width when ' + \
                         'using gaussiansnr'
    sys.exit(2)

files = sys.argv[2*len(opts) + 1:]

# print >> sys.stdout, linefile
# print >> sys.stdout, intmethod
# print >> sys.stdout, backmethod
# print >> sys.stdout, len(sys.argv[1:])
# print >> sys.stdout, files
# print >> sys.stdout, 2*len(opts)

try:
    report(channels, linename, intmethod, backmethod, files, \
           lambdaconstraint, sigmaconstraint, width)
except IntMethod:
    print >> sys.stderr, 'spectraintegrate: invalid integration method'
    sys.exit(2)
sys.exit(0)
```

A.3.2.2 plotspectra

```
#!/usr/bin/env python
""" plotspectra

    A python script which configures and executes GnuPlot scripts
    for the plotting of a spectra file.

"""
__version__ = '$Id: plotspectra,v 1.15 2006-06-24 20:03:33 mtt Exp $'

from __future__ import division

import os.path
import sys
import getopt

from Numeric import *
from spectra.utilities import parse, spectraslice
from spectra.integrate import *

def usage():
    """Emits usage comments on sys.stderr"""
    print >> sys.stderr, 'Usage: plotspectra [options] spectrafile '
    print >> sys.stderr, '\tTry spectraintegrate —help for more details '

def detailed_usage():
    """Emits detailed usage comments on sys.stderr"""
    print >> sys.stderr, 'Usage: plotspectra [options] spectrafile '
    print >> sys.stderr, 'Plots spectra with a variety of options'
    print >> sys.stderr, ''
    print >> sys.stderr, 'Options: [-b | —background] background fit type'
    print >> sys.stderr, '         [-c | —channels] channel vector'
    print >> sys.stderr, '         [-a | —all] display fit and channels'
    print >> sys.stderr, '         [-g | —gaussian] fit gaussian to channels'
    print >> sys.stderr, '         [-l | —lambda] fixes center of gaussian'
    print >> sys.stderr, '         [-s | —sigma] fixes sigma of gaussian'
    print >> sys.stderr, ''
    print >> sys.stderr, 'Channel File Format:'
    print >> sys.stderr, '\tSee spectra.py source or manual'
    print >> sys.stderr, '\tHere, place in quotes on the command line:'
    print >> sys.stderr, '\t\t\'N, N, N, N, N, N\''
    print >> sys.stderr, 'Background Fit Types:'
    print >> sys.stderr, '\taverage:\taverage of two background regions'
    print >> sys.stderr, '\tlinear:\t\tlinear fit to background regions'
    print >> sys.stderr, '\tparabolic:\tparabolic fit to background regions'
    print >> sys.stderr, ''
    print >> sys.stderr, 'Note: specifying background will require channels'

def channelplot(spectrafile, channels):
    """
    Creates a script for plotting the spectra, with the integration
    channels indicated.
    """
    fileobj = open(spectrafile)
    data = parse(fileobj)
    fileobj.close()
    lownoise1 = data(channels[0] - 1, 1)      # get y values of spectra
    highnoise1 = data(channels[1] - 1, 1)     # at relevant points
    lowsignal = data(channels[2] - 1, 1)
    highsignal = data(channels[3] - 1, 1)
    lownoise2 = data(channels[4] - 1, 1)
    highnoise2 = data(channels[5] - 1, 1)

    file = open('./spectraplottemp.gnuplot', 'w')
    preamble(file)
    low
    plotline = 'plot "' + spectrafile + '" with lines ls 1'
    print >> file, plotline
    file.close()

def fitparabolicplot(spectrafile, channels, gaussianflag, \
        lambdaconstraint, sigmaconstraint):
    """
    Creates a script for plotting the spectra, with a parabolic
    fit applied.
    """
    fileobj = open(spectrafile)
    data = parse(fileobj)
    fileobj.close()
    back1 = data[channels[0]-1:channels[1],:]
    back2 = data[channels[4]-1:channels[5],:]
    peak = data[channels[2]-1:channels[3],:]

    rangelow = min(channels)
    rangehigh = max(channels)

    a, b, c = parabolafit(back1, back2)
    if gaussianflag:
        corrected = removeparabola(data, channels)
        back1corr = corrected[channels[0]-1:channels[1],:]
        back2corr = corrected[channels[4]-1:channels[5],:]
        peakcorr = corrected[channels[2]-1:channels[3],:]
        d, e, f = gaussianfit(back1corr, back2corr, peakcorr, \
                        lambdaconstraint, sigmaconstraint)

    file = open('./spectraplottemp.gnuplot', 'w')
    preamble(file)
    plotline = 'plot "' + spectrafile + '" with lines ls 1, \\'
    print >> file, plotline
    if gaussianflag:
        fitline = '\t(x>' + str(rangelow) + ' && x<' + str(rangehigh) + \
                ') ?' + str(a) + '*x*x + ' + str(b) + '*x + ' + \
                str(c) + ' + ' + str(d) + '*exp(-(0.5)*((x - ' + str(e) + \
                ')/' + str(f) + ')**2): 0/0 with lines ls 2'
    else:
        fitline = '\t' + str(a) + '*x*x + ' + str(b) + '*x + ' + \
                str(c) + ' with lines ls 2'
    print >> file, fitline
    file.close()

def fitlinearplot(spectrafile, channels, gaussianflag, \
        lambdaconstraint, sigmaconstraint):
    """
    Creates a script for plotting the spectra, with a linear
    fit applied.
    """
    fileobj = open(spectrafile)
    data = parse(fileobj)
    fileobj.close()
    back1 = data[channels[0]-1:channels[1],:]
    back2 = data[channels[4]-1:channels[5],:]
    [illegible]k = data[channels[2]-1:channels[3],:]

    rangelow = min(channels)
    rangehigh = max(channels)

    m, b = linearfit(back1, back2)
    if gaussianflag:
        corrected = removelinear(data, channels)
        back1corr = corrected[channels[0]-1:channels[1],:]
        back2corr = corrected[channels[4]-1:channels[5],:]
        peakcorr = corrected[channels[2]-1:channels[3],:]
        d, e, f = gaussianfit(back1corr, back2corr, peakcorr, \
                        lambdaconstraint, sigmaconstraint)

    file = open('./spectraplottemp.gnuplot', 'w')
    preamble(file)
    plotline = 'plot "' + spectrafile + '" with lines ls 1, \\'
    print >> file, plotline
    if gaussianflag:
        fitline = '\t(x>' + str(rangelow) + ' && x<' + str(rangehigh) + \
                ') ?' + str(m) + '*x + ' + \
                str(b) + ' + ' + str(d) + '*exp(-(0.5)*((x - ' + str(e) + \
                ')/' + str(f) + ')**2): 0/0 with lines ls 2'
    else:
        fitline = '\t' + str(m) + '*x + ' + str(b) + ' with lines ls 2'
    print >> file, fitline
    file.close()

def fitaverageplot(spectrafile, channels, gaussianflag, \
        lambdaconstraint, sigmaconstraint):
    """
    Creates a script for plotting the spectra, with a background
    fit applied.
    """
    fileobj = open(spectrafile)
    data = parse(fileobj)
    fileobj.close()
    back1, signal, back2 = spectraslice(data, channels)
    back1 = average(back1)
    back2 = average(back2)
    background = str(0.5*(back1 + back2))

    rangelow = min(channels)
    rangehigh = max(channels)

    if gaussianflag:
        corrected = removeaverage(data, channels)
        back1corr = corrected[channels[0]-1:channels[1],:]
        back2corr = corrected[channels[4]-1:channels[5],:]
        peakcorr = corrected[channels[2]-1:channels[3],:]
        d, e, f = gaussianfit(back1corr, back2corr, peakcorr, \
                        lambdaconstraint, sigmaconstraint)

    file = open('./spectraplottemp.gnuplot', 'w')
    preamble(file)

    plotline = 'plot "' + spectrafile + '" with lines ls 1, \\'
    print >> file, plotline
    if gaussianflag:
        fitline = '\t(x>' + str(rangelow) + ' && x<' + str(rangehigh) + \
                  ') ?' + str(background) + ' + ' + str(d) + \
                  '*exp(-(0.5)*((x - ' + str(e) + \
                  ')/' + str(f) + ')**2): 0/0 with lines ls 2'
    else:
        fitline = '\t' + str(background) + ' with lines ls 2'
    print >> file, fitline

    file.close()

def simpleplot(spectrafile):
    """
    Creates a script for plotting the spectra, with no extra
    analysis or information.
    """
    file = open('./spectraplottemp.gnuplot', 'w')
    preamble(file)
    plotline = 'plot "' + spectrafile[0] + '" with lines ls 1'
    print >> file, plotline
    file.close()

def preamble(fileobj):
    """
    Emits the common elements for the files to fileobj.
    """
    print >> fileobj, 'set terminal postscript eps color "Arial" 30'
    print >> fileobj, 'set size 1.25, 1.33'
    print >> fileobj, 'set pointsize 1'
    print >> fileobj, 'set nokey'
    print >> fileobj, 'set xrange [0:1000]'
    print >> fileobj, 'set mxtics 4'
    print >> fileobj, 'set line style 1 linetype 1 linewidth 1'
    print >> fileobj, 'set line style 2 linetype -1 linewidth 3'
    print >> fileobj, 'set xlabel "Channel [N]"'
    print >> fileobj, 'set ylabel "Signal [Probably Counts]"'

def parsearguments():
    """
    A method for parseing and checking the input arguments.
    All of the complaining regarding the input arguments occurs
    here, and this method can terminate the program.
    """
    if sys.argv[1:] == []:
        usage()
        sys.exit(2)
    try:
        opts, args = getopt.getopt(sys.argv[1:], "hb:c:agl:s:", ["help", \
                     "background=", "channels=", "all", "—gaussian", \
                     "lambda=", "sigma="])
    except getopt.GetoptError:
        print >> sys.stderr, 'spectraplot: unrecognized flag?'
        sys.exit(2)

    inputchannels = None
    channels = []
    backmethod = None
    spectrafile = None
    bothflag = False
    gaussianflag = False
```

```
lambdaconstraint = None
sigmaconstraint = None
argcount = 0

for o, a in opts:
    if o in ("-h", "—help"):
        detailed_usage()
        sys.exit(2)
    if o in ("-b", "—background"):
        backmethod = a
        argcount = argcount + 2
    if o in ("-c", "—channels"):
        inputchannels = a
        argcount = argcount + 2

        try:                            # check to see if it's a file
            print inputchannels
            file = open(inputchannels)
            line = file.readline()
            channeldata = line.split(',')
            channeldata = channeldata[1:]   # strip off label in file
            file.close()
        except IOError:
            channeldata = inputchannels.split(',')

        if len(channeldata) == 6:
            for i in range(6):
                try:
                    channels.append(int(channeldata[i]))
                except ValueError:
                    message = 'plotspectra: malformed channel vector?'
                    print >> sys.stderr, message
                    sys.exit(2)
        else:
            print >> sys.stderr, 'plotspectra: malformed channel vector?'
            sys.exit(2)
    if o in ("-a", "—all"):
        bothflag = True
        argcount = argcount + 1
    if o in ("-g", "—gaussian"):
        gaussianflag = True
        argcount = argcount + 1
    if o in ("-l", "—lambda"):
        lambdaconstraint = a
        argcount = argcount + 2
    if o in ("-s", "—sigma"):
        sigmaconstraint = a
        argcount = argcount + 2

if sys.argv[argcount + 1:] == []:
    print >> sys.stderr, 'plotspectra: must specify a file to plot'
    sys.exit(2)
elif len(sys.argv[argcount + 1:]) > 1:
    print >> sys.stderr, 'plotspectra: can only plot one file at a time'
    sys.exit(2)
else:
    spectrafile = sys.argv[argcount + 1:]

if backmethod != None:
    if channels == []:
            print >> sys.stderr, 'plotspectra: must specify channels for fit'
            sys.exit(2)

    return channels, backmethod, spectrafile, bothflag, gaussianflag, \
        lambdaconstraint, sigmaconstraint

def executegnuplot():
    """
    A method for accessing the shell and executing gnuplot.
    Lauches a ghostview viewer for the ouptput plot.
    """
    commandstring = 'gnuplot spectraplottemp.gnuplot > trial.eps'
    os.popen(commandstring)
    displaystring = 'gv trial.eps&'
    os.popen(displaystring)
    return


if __name__ == '__main__':

    channels, backmethod, spectrafile, bothflag, lineflag, \
        lambdaconstraint, sigmaconstraint = parsearguments()
    #print channels
    #print backmethod
    #print spectrafile
    #print bothflag
    #print lineflag
    #print lambdaconstraint
    #print sigmaconstraint

    if backmethod == None:
        simpleplot(spectrafile)
    elif backmethod == 'average':
        fitaverageplot(spectrafile[0], channels, lineflag, \
            lambdaconstraint, sigmaconstraint)
    elif backmethod == 'linear':
        fitlinearplot(spectrafile[0], channels, lineflag, \
            lambdaconstraint, sigmaconstraint)
    elif backmethod == 'parabolic':                # accept both as same
        fitparabolicplot(spectrafile[0], channels, lineflag, \
            lambdaconstraint, sigmaconstraint)
    elif backmethod == 'parabola':
        fitparabolicplot(spectrafile[0], channels, lineflag, \
            lambdaconstraint, sigmaconstraint)
    else:
        print >> sys.stderr, 'spectraplot: bad background method requested?'

    executegnuplot()

    sys.exit(0)
```

A.3.2.3 peakfit

```
#!/usr/bin/env python

from __future__ import division

import os.path
import sys
import getopt

from string import lower

from spectra.utilities import *
from spectra.integrate import *

from Numeric import *

def peakreport(backstart, peakstart, peakfinish, backfinish):

    channels = [backstart, peakstart, peakstart, \
                peakfinish, peakfinish, backfinish]

    corrected = removeaverage(spectra, channels)
    back1, peak, back2 = spectraslice(corrected, channels)

    try:
        a, b, c = gaussianfit(back1, back2, peak, None, None)
        print >> sys.stdout, i,
        print >> sys.stdout, 0.5*(peakstart + peakfinish),
        print >> sys.stdout, a,
        print >> sys.stdout, b,
        print >> sys.stdout, c,
        print >> sys.stdout, a*abs(c)*sqrt(2*pi)
    except:
        print >> sys.stdout, i,
        print >> sys.stdout, 0.5*(peakstart + peakfinish),
        print >> sys.stdout, 'gaussianfit-fails'

    return

def parse(inputfile):
    """Parse an input file. The data is expected to be in
    the following format:

            X Column Heading    Y Column Heading
                [float]             [float]
                  ...                 ...
                [float]             [float]

    Output will be two lists.
    """
    if inputfile == None:
        input = sys.stdin
    else:
        input = open(inputfile, 'r')

    spectra = []
    for line in input:
        if len(line.split()) != 2:
            raise LineError()
        else:
            x, y = line.split()
            try:
                isinstance(float(x), float)
                isinstance(float(y), float)
            except:
                raise ValueError()
            spectra.append((float(x), float(y)))

    return array(spectra)

if __name__ == '__main__':

    backmean = 204.3
    backsigma = 1.697522                            # gain 250
    threshold = backmean + 4*backsigma

    for i in sys.argv[1:]:
        spectra = parse(i)

        peakflag = False
        count = 1

        backstart = count
        startflag = True
        backflag = False
        peakflag = False

        while count < 1024:
            if startflag:                             # only at start
                if spectra[count, 1] > threshold:
                    startflag = False
                    peakflag = True
                    peakstart = count               # update peak region
                count = count + 1
            elif peakflag:
                if spectra[count, 1] < threshold:
                    peakflag = False
                    backflag = True
                    peakfinish = count              # finish peak region
                count = count + 1
            elif backflag:
                if spectra[count, 1] > threshold:   # end of back2 found
                    peakflag = True
                    backflag = False
                    backfinish = count
                    peakreport(backstart, peakstart, peakfinish, backfinish)
                    backstart = peakfinish          # reset for new line
                    peakstart = backfinish
                count = count + 1

        if backflag:
            backfinish = count - 1
            peakreport(backstart, peakstart, peakfinish, backfinish)
```

A.4 Taylor-RK

A.4.1 Introduction

This section is intended to provide an overview of the efforts to generate a numerical model duplicating the work of Taylor's 1950 blast wave paper. The Runge-Kutta numerical method for three coupled equations is used. The numerical resu lts are compared to those reported by Taylor in his paper.

A.4.2 Numerical Model

The numerical model was derived from an examination of Taylor's 1950 paper by Sanjay Singh. For the case of $\gamma = 1.4$, his work yields equations A.1 through A.3. This is the form of the equations given to me on August 22nd, and implemented in a Python Runge-Kutta solver, listed in Sec. A.4.5.1.

$$\frac{dy_1}{d\eta} = \frac{y_1\left[3.7y_2 - 3\eta - 2\gamma\left(y_2^2/\eta\right)\right]}{\left(\eta - y_2\right)^2 - y_1/y_3} \tag{A.1}$$

$$\frac{dy_2}{d\eta} = \frac{1}{\eta - y_2}\left[\frac{dy_1}{d\eta}\frac{0.714}{y_3} - 1.5y_2\right] \tag{A.2}$$

$$\frac{dy_3}{d\eta} = \frac{y_3}{\left(\eta - y_2\right)^2}\left[\frac{dy_1}{d\eta}\frac{0.714}{y_3} - 1.5y_2\right] + \frac{2y_2y_3}{\eta\left(\eta - y_2\right)} \tag{A.3}$$

In the above equations all of the physical quantities are normalized in some fashion. The radius η is normalized to the radius of the blast wave at any given point in time. The fluid quantities y_1 (pressure) and y_3 (density) are normalized to the ambient values, and y_2 (velocity) is normalized to the speed of sound in the local media.

A.4.3 Runge-Kutta Equations

The fourth-order Runge-Kutta method was used to solve the above equations. There are three functions that are functions of a total of 5 variables, including γ. In the current incarnation we are taking the case of an ideal gas, which gives us a value of 1.4 for γ. The generalized Runge-Kutta method may be written for i equations of j dependent variables. The step size in the independent variable is written as h. In the following, the independent variable will be written as z, to distinguish it from the coupled variables x_i.

$$x_{i,j,N+1} = x_{i,j,N} + \frac{h}{6}\left[k_{i,1} + 2k_{i,2} + 2k_{i,3} + k_{i,4}\right] \tag{A.4}$$

$$k_{i,1} = hy_i\left(z_N, x_{j,N}\right) \tag{A.5}$$

$$k_{i,2} = hy_i\left(z_N + h/2, x_{j,N} + k_{i,1}\delta_{ij}/2\right) \tag{A.6}$$

$$k_{i,3} = hy_i\left(z_N + h/2, x_{j,N} + k_{i,2}\delta_{ij}/2\right) \tag{A.7}$$

$$k_{i,4} = hy_i\left(z_N + h, x_{j,N} + k_{i,3}\delta_{ij}\right) \tag{A.8}$$

The above description of the Runge-Kutta method should be extendable to any number of coupled equations, and can be applied to the case at hand defined in equations A.1 through A.3.

A.4.4 Comparison with Taylor

Presented in the following few figures is the current best the Python code can do for the output, compared with the respective data from Taylor's paper. The step size used is $20 \cdot 10^{-6}$ normalized radius units, which takes a total execution time of 1.5 seconds, using the normal Python compiler. Improvements in runtime would be possible using the specializing compiler 'psyco', but it has not yet been attempted, given the reasonable runtime requirements at the present time.

As can be seen in Fig. A.1 the agreement with Taylor's numerical results is reasonable. Taylor is not using a Runge-Kutta method for his numerical solution, and there are not a lot of details ab out the actual methodology used by Taylor. At this time, the agreement obtained is deemed to be reasonable for further work to proceed. One possible cause for concern is the existence of a singularity at a normalized radius of zero in the normalized velocity plot, the origin of which is uncertain.

Future work includes:

- Running with different γ values
- Literature search for other test cases
- Convergence testing
- Testing with 'psyco' compiler for improved runtimes

A.4.5 Conclusion

A numerical model for the strong shock wave due to Taylor has been presented. A Runge-Kutta code has been implemented in Python, and tested. Agreement between the RK results and Taylor's original numerical solution

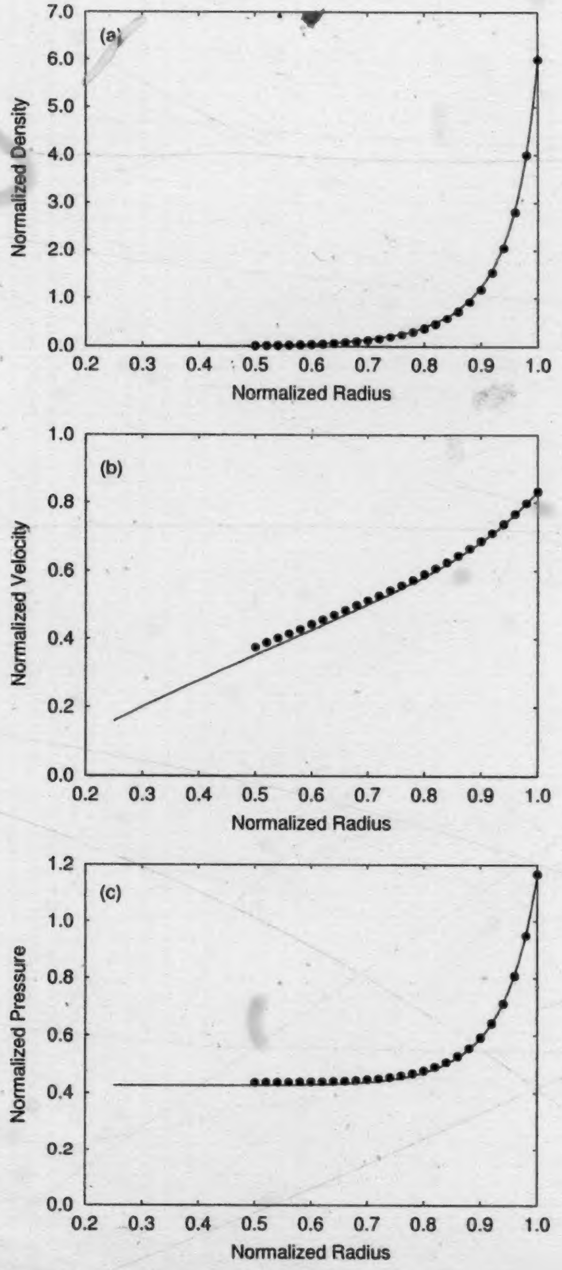

Figure A.1. *Comparison of current results (line) with Taylor [41] (circles) for (a) normalized density, (b) normalized velocity and (c) normalized pressure. Dots from Taylor, line from Python RK.*

to his equations is reasonable. Future work will include running with different γ values, and a literature survey for different test cases. Additional work for the numerical methodology should be performed: convergence testing, unittest implementation, and work with the 'psyco' specializing compiler for improved runtimes.

A.4.5.1 Taylor RK Code Listing

```
#!/usr/bin/env python

"""Taylor-Sedov Shockwave Solver by Runge-Kutta Method.


"""
__version__ = '$Id: taylor_rk.py,v 1.1.1.1 2004/09/05 17:47:02 mtt Exp $'

from __future__ import division
from math import floor
import sys

def Taylor(r, p, v, d, g, h):
        """Returns the parameters from the Taylor Model for strong shock.
        Expects: Taylor(r, p, v, d, g, h)
                r = radius
                p = pressure
                v = velocity
                d = density
                g = gamma
                h = step size and sense
        """
        newpressure = p*(-3*r + (3+g/2)*v - 2*g*v*v/r)/((r-v)*(r-v)-(p/d))
        newvelocity = (newpressure/(g*d) - 1.5*v)/(r-v)
        newdensity = (d/(r-v))*newvelocity+(2*v*d)/(r*(r-v))
        return h*newpressure, h*newvelocity, h*newdensity

def TaylorRungeKutta(initialparameters, outputfile=None):
        """Solves the Taylor equations for strong shock.

        """
        if outputfile is None:
                outputfile = sys.stdout
        p = float(initialparameters[0])
        v = float(initialparameters[1])
        d = float(initialparameters[2])
        gamma = float(initialparameters[3])
        radiusstep = float(initialparameters[4])

        print >> outputfile, 'Taylor Blast Wave Model: Runge Kutta Method'
        print >> outputfile, 'Initial Parameters:'
        print >> outputfile, '\tPressure:\t%f' % (p)
        print >> outputfile, '\tVelocity:\t%f' % (v)
        print >> outputfile, '\tDensity: \t%f' % (d)
        print >> outputfile, '\tGamma:    \t%f' % (gamma)
        print >> outputfile, '\tRadius Step: \t%1.3e' % (radiusstep)
        print >> outputfile, '\nRadius \t\tPressure \tVelocity \tDensity'
        delimiter = '======================================================='
        print >> outputfile, '%s' % delimiter

        r = 1.0

        h = -1*radiusstep
        cycle = floor(-1/(h*1000))
        count = 2*cycle

        while r > 0.25:
```

```
        if count > cycle:
            print >> outputfile, '%3.7f \t%3.3f \t\t%3.3f \t\t%3.3f' \
                    % (r, p, v, d)
            count = 0

        k1, l1, m1 = Taylor(r, p, v, d, gamma, h)
        k2, l2, m2 = Taylor(r+h/2 ,p+k1/2, v+l1/2, d+m1/2, gamma, h)
        k3, l3, m3 = Taylor(r+h/2, p+k2/2, v+l2/2, d+m2/2, gamma, h)
        k4, l4, m4 = Taylor(r+h, p+k3, v+l3, d+m3, gamma, h)

        p = p + (k1/6 + k2/3 + k3/3 + k4/6)
        v = v + (l1/6 + l2/3 + l3/3 + l4/6)
        d = d + (m1/6 + m2/3 + m3/3 + m4/6)

        r = r + h
        count = count + 1

if __name__ == '__main__':
    if len(sys.argv) != 6:
        print >> sys.stderr, 'Usage: taylor_rk [initial parameters...]'
        print >> sys.stderr, '\t pressure, velocity, density, gamma' + \
      ', radiusstep'
        sys.exit(2)
    TaylorRungeKutta(sys.argv[1:])
    sys.exit(0)
```

A.5 Emission Simulation Code

The Emission module is split into the following modules:

atomicphysics contains the atomic data for Na, and could easily be extended to other atoms.

numemission contains the code for calculating the emission from a hot/ionized gas.

optics handles the integration of the emission for the 1:1 imaging optics used for the LIBS water jet experiments. This code could be extended to other setups.

utilties has some useful code for the other modules to use.

Please note that this module is not under test, and should be used with care.

A.5.1 Emission Code Listing

A.5.1.1 emission.atomicphysics

```
#!/usr/bin/env python
""" emission.atomicphysics

    A module for the atomic physics of the various atoms used in the
    emission modelling.

"""
__version__ = '$Id: atomicphysics.py,v 1.1.1.1 2004/09/05 17:43:10 mtt Exp $'

from __future__ import division

from Numeric import *

def napartition(T):
    """
    Calculates the atomic partition function for Na atoms.  The atomic
    partition function is taken from Griem (1997), equation 7.70:

        Z(T) = Sum_n [ g_n exp( - E_n/(k_BT)) ]

    with the following parameters:

        Upper Energy [eV]        g [N]
        ==============================
            0.000000             2
            2.102298             2
            2.104430             4
            3.191353             2
            3.191353             2
            4.116360             2
            4.116360             2
            4.283502             4
            4.283502             4
            4.283498             6
```

```
In addition, this function is designed to very quietly limit
the minimum temperature to 70 K, in order to keep from getting
math overflows in the exponent function.
"""
kB = 86.1738569e-6          # [kB] =  eV/K
Z = zeros(5001, Float)
mask = less(T, 70)
T = T - mask*(T - 70)       # limit T > 70 K
Z = 2 + 2*exp(-2.102298/(kB*T)) + 4*exp(-2.104430/(kB*T)) + \
        2*exp(-3.191353/(kB*T)) + 2*exp(-3.191353/(kB*T)) + \
        2*exp(-4.116360/(kB*T)) + 2*exp(-4.116360/(kB*T)) + \
        4*exp(-4.283502/(kB*T)) + 4*exp(-4.283502/(kB*T)) + \
        6*exp(-4.283498/(kB*T))
return Z
```

A.5.1.2 emission.numemission

```python
#!/usr/bin/env python
""" Numemission

    A module for the numerical calculations of emission from a
    hot/ionized gas.

"""
__version__ = '$Id: numemission.py,v 1.6 2005/01/14 18:09:48 mtt Exp $'

from __future__ import division

from Numeric import *
import sys
from math import pi

from emission.utilities import *
from emission.atomicphysics import *

def spectrumemission(numberdensity, temperature, partition,
                     spectravector):
    """
    A function for calculating the emission spectra for a particular
    set of conditions. Depends on numberdensity of emitting particles,
    the temperature and partition function at each point. Also requires
    the spectroscopic parameters for each line composing the spectrum.

    The spectravector should be composed of a list of triplets which
    contain the parameters (A_N, g_N, E_N) for as many lines as are
    to be simulated.

    This function will make use of lineemission to calculate the
    emission for a particular line. Each spectral emission line
    will get its own row in a array representing the spectral
    emission for all points in the input spatial vectors.

    The emissionarray vector will have the format of

        [lambda, emission(space)]

    So the spectra is made up of a bunch of delta functions at given
    wavelengths, and the emission vector is a function of space that
    comes from the input hydrodynamic vectors.

    No broadening is taken into account in this function, just total
    power that is expected to be emitted into a a particular line.
    """
    emissionarray = zeros([len(spectravector), len(numberdensity)], Float)
    for i in range(len(spectravector)):
        A_N, g_N, E_N = spectravector[i]
        dEmission = lineemission(numberdensity, temperature, partition, \
                                 A_N, g_N, E_N)
        emissionarray[i, :] = dEmission
    return emissionarray

def lineemission(numberdensity, temperature, partition,
                 linerate, linedegeneracy, lineenergy):
    """
    A function for calculating the emission vector for a particular
```

```
set of conditions.  Depends on number density of emitting particles,
the temperature and partition function at each point.  Also requires
the spectroscopic parameters for the line of interest:

    linerate =          A_N
    linedegeneracy =    g_N
    lineenergy =        E_N

Uses

    P = (hc)/(4*Pi*lambda)*A*g*n(R)*exp(-E/(kB*T(R)))/Z(T(R))

As function to calculate emitted power.  Units will be in W/Sr/Vol.
where Vol. is the volume contained with the numberdensity vector.

Useful facts:   160.217733e-21 J/eV
                [linerate]          s
                [lineenergy]        eV
                [linedegeneracy]    N
                kB in eV:           86.1738569e-6

All space vectors must be same length.  Output vector is a
spatial vector, with intensity at a wavelength of E_N being
the data held in vector.  The output units will be W/Sr/vol^3.

vol^3 is picked up from the numberdensity vector.
"""
kB = 86.1738569e-6
lineemission = zeros(len(numberdensity), Float)
factor = (160.217733e-21*lineenergy/(4*pi))*linerate*linedegeneracy
lineemission = factor*numberdensity*exp(-1*lineenergy/(kB*temperature))
lineemission = lineemission/partition
return lineemission
```

A.5.1.3 emission.optics

```
#!/usr/bin/env python
""" Optics

    A module for the calculation of the optically captured emission
    from a hot/ionized gas.

"""
__version__ = '$Id: optics.py,v 1.4 2005/01/14 19:57:41 mtt Exp $'

from __future__ import division

from Numeric import *
import sys
from math import pi

from emission.utilities import *
from emission.atomicphysics import *
from emission.numemission import *

def slitsweep(density, pressure, scale, gridvector):
    """
    Runs the integration for one delay time and for all slit
    positions.
    """
    space, deltaspace, time, deltatime, radius = gridvector
    # [Puke offstage] Fix this - keep same units all the way
    # through, for fuck's sake.
    volume = deltaspace*deltaspace*deltaspace*1e-18

    print >> sys.stderr, 'slitsweep: density[0]: %f' % density[0]
    T, n = makeintegrate(density, pressure, scale, time, volume, radius)
    Z = napartition(T)

    spectravector = [(6.22e7, 4, 2.104430), (6.18e7, 2, 2.102298)]
    integrated = lambdaintegrate(n, T, Z, spectravector)

    slitwidth = 100          # in units of microns
    gatewidth = 100e-9       # in units of seconds
    radius = array(range(0, 5001, 1), Float)/1e6

    energyvector = []
    for x in range(0, 5000, 50):
        dE = chordintegrate(integrated, slitwidth, x, gatewidth, radius)
        energyvector.append(dE)
        nominalradius = x*1e-6
        print >> sys.stdout, 'Radius: %1.3e [m]' % nominalradius,
        print >> sys.stdout, '\tEmitted Energy: %1.6e [J/Sr]' % dE
    return energyvector

def chordintegrate(integrated, slitwidth, slitposition, gatewidth, scale):
    """
    Integrates the total power emitted by a slit image through the
    expanding plasma plume. This function takes in an integrated
    emission array, so only has access to a spatial vector with a
    power emission defined at each spatial point. It is client's
    responsibility to maintain information about spatial vector.

    Also necessary is the slitwidth, the slit position and the gate
    width so the power can be converted to integrated energy.  Slit
    width and position must be in the same units as the underlying
    dimensionality of integrated, which is in turn specified by
    the numberdensity vector handed to the lambdaintegrate mathod.

    This method makes use of the chord integration methodology worked
    out on 20050114.  This function is coded to sweep from slitposition
    to a distance of 5 mm in steps of 1 micron.  It ignores the finite
    image height of the CCD, which may affect the results produced.

    The output vector will have units of J/Sr.

    To do:  Make a testcase
            Switch to maxR as integration limit
            Add awareness of CCD height
    """
    power = 0
    x = slitposition
    #dR = 1e-6                          # units of m.
    for i in range(x, 5001, 1):
        R = 1e-6*sqrt(i*i + x*x)        # units of m!!!!!
        if R < 5e-3:
            localP = interpolate(integrated, scale, R)
            #power = power + 2*pi*gatewidth*slitwidth*localP*R*dR
            # need 1e6 to convert back to um, which is base unit
            # of n(R) during most of this code.
            power = power + 2*pi*gatewidth*slitwidth*localP*R*1e6
    return power


def lambdaintegrate(numberdensity, temperature, partition, spectravector):
    """
    A method for integrating emission from a certain range of wavelengths
    together as would happen during experimental analysis of a particular
    line or doublet.  The function requires a spectra vector the same
    as that used in emission.numemission.spectrumemission, which is a
    list of triplets which contain the parameters (A_N, g_N, E_N) for
    the lines that are to be integrated along the lambda axis.

    Output has units of W/Sr/vol^3.
    """
    emissionarray = spectrumemission(numberdensity, temperature, partition, \
                                     spectravector)
    integrated = sum(emissionarray)
    return integrated
```

A.5.1.4 emission.utilities

```
#!/usr/bin/env python
""" emission.utilities

    A module for common utilities for the emission package.

"""

from __future__ import division

from Numeric import *
import sys

class BoundsError(Exception):
    pass

class LengthError(Exception):
    pass

def calculatetemp(density, pressure, molarmass):
    """
    Calculates the temperature for a particular set of density
    and pressure vectors, and a given molar mass of the gas in
    question.  R is the universal gas contant.

    Due to trouble with math overflows due to low temperatures
    in exponentials, the minimum temperature this function will
    report is 70 K.
    """
    R = 8.31451
    temp = (pressure*molarmass)/(density*R)
    mask = less(temp, 70)
    temp = temp - mask*(temp - 70)
    return temp

def parseinitial(filenames):
    """
    Parses initial files for the Taylor strong shock conditions,
    and breaks them into vectors for future work.  Dies a horrible,
    miserable death if anything is wrong.  Or, maybe it doesn't.
    """
    densityin, pressurein, scalein, grid = filenames

    input = file(densityin)
    densityline = getlastline(input)
    input.close()
    density = array(parseline(densityline), Float)

    input = file(pressurein)
    pressureline = getlastline(input)
    input.close()
    pressure = array(parseline(pressureline), Float)

    input = file(scalein)
    scaleline = getlastline(input)
    input.close()
    scale = array(parseline(scaleline), Float)

    input = file(grid)
    gridvector = parsegrid(input)
    input.close()

    return density, pressure, scale, gridvector

def parsegrid(fileobj):
    """
    Parses a text file specigying the grid conditions for the emission
    calculations.
    """
    fileobj.seek(0)
    gridvector = []
    for line in fileobj:
        if line[0] != '#':
            gridvector.append(float(line.split()[1]))
    return gridvector

def makeintegrate(density, pressure, scale, time, volume, radius):
    """
    Constructs a temperature and a number of particles vector
    for use in the integration of emission.  This function
    generates the vectors for the case of

        E = 30 mJ
        P = 93.55 kPa
        Ambient Density = 1.19 kg/m3
        Nitrogen Gas:    0.02802 kg/mol

    This doesn't quite work out to room temperature, but I don't
    care right now.  The time and volume are driven by the actual
    integration function.  Function currently hardcoded to solve
    for 0 - 5 mm in 1 um steps.

    """
    # removed scaling to physical units.  User should input vectors with
    # physical units.
    rho = density                           # [kg/m3]
    P = pressure                            # [Pa]
    T = calculatetemp(rho, P, 0.02802)      # [K]
    nafraction = 172.7e-09                  # [N]      L4 Sedov Curve
    #nafraction = 92.7e-09                   # [N]      L5 Sedov Curve

    # print R
    # print len(radius)
    # print radius[0]
    # print radius[-1]
    # print len(rho)
    # print len(P)
    # print len(T)
    tempvector = zeros(5001, Float)
    numvector = zeros(5001, Float)
    for i in range(5001):
        if (i*1e-6) > radius:               # background values outside R
            tempvector[i] = 264.93
            numvector[i] = 0
        else:
            tempvector[i] = interpolate(T, scale, i*1e-6)
            # 20041125: removed nafraction factor
            # 20040114: restored nafraction.  It's a hack, but out of time
            localdensity = nafraction*interpolate(rho, scale, i*1e-6)
            # 20050111: changed 0.023 with 0.02802
            # 20050114: restored to 0.023 (Na molar mass)
            numvector[i] = localdensity*volume*602.21367e21/0.023
    return tempvector, numvector

def interpolate(vector, scale, position):
    """
    Returns a single value interpolated from a vector combined with a
    scale vector and a desired position. Attempts linear interpolation
    in the cases where the desired position doesn't line up exactly with
    the scale vector.

        Do the following:    enforce scope checks
                             linear interpolation
    """
    if position < scale[0]:
        raise BoundsError("No Extrapolation: requested position exceeds" + \
                          " negative bound of scale vector.")
    elif position > scale[len(scale) - 1]:
        raise BoundsError("No Extrapolation: requested position exceeds" + \
                          " positive bound of scale vector.")
    if len(vector) != len(scale):
        raise LengthError("Vector and Scale are different lengths.")
    i = 0
    trial = scale[i]
    while position > scale[i]:
        i = i + 1
    slope = (vector[i] - vector[i - 1])/(scale[i] - scale[i - 1])
    return (vector[i - 1] + slope*(position - scale[i - 1]))

def getlastline(fileobj):
    """
    Method to return last line of a file. Suitable for initial conditions
    for the density, velocity and pressure from either true initial
    conditions, or from logfiles for resuming after a crash.
    """
    fileobj.seek(0)
    for line in fileobj:
        lastline = line
    return lastline

def parseline(line):
    """
    Splits a text line divided by tabs into a list. After that it converts
    each of the entries to a float, suitable for further numeric work.
    """
    splitline = line.split()
    vector = []
    for i in range(len(splitline)):
        vector.append(float(splitline[i]))
    return vector
```